MODELING ATMOSPHERIC PRESSURE PLASMA JETS: PLASMA DYNAMICS, INTERACTION WITH DIELECTRIC SURFACES, LIQUID LAYERS AND CELLS

by

Seth Norberg

A dissertation submitted in partial fulfillment
of the requirements for the degree of
Doctor of Philosophy
(Mechanical Engineering)
in the University of Michigan
2015

Doctoral Committee:

Professor Eric Johnsen, Chair
Professor Arvin Atreya
Professor Mark J. Kushner
Professor Kevin P. Pipe

ACKNOWLEDGEMENTS

Thank you, Lord, for the blessings you have bestowed on my life. My loving family and wonderful friends look out for me, lift my spirits, and remind me of what is important in life.

Thanks to the U.S. Army for providing the opportunity to pursue a Ph.D. in conjunction with a return assignment to the United States Military Academy. I am grateful for the new and different opportunities this path will provide upon retirement from active service.

Thanks to my wife, Susan, and our daughters, Annie and Maggie, for putting up with this lifestyle and supporting me. Thanks especially for the recommendation to listen to audio books during the commute.

Thanks to my parents for instilling an appreciation for academic endeavors.

Thanks to my dissertation committee for their support in this process. Thanks to my advisors, Professors Mark Kushner and Eric Johnsen, for their guidance, support, sympathetic ears, and friendship.

TABLE OF CONTENTS

ACKNOWLEDGEMENTS ..... **ii**
LIST OF TABLES ..... **v**
LIST OF FIGURES ..... **vi**
LIST OF APPENDICES ..... **xvii**
Chapter 1 Introduction **1**
1.1 Overview of plasma 1
1.2 Overview of atmospheric pressure plasma jets 3
1.3 Overview of plasma medicine milestones 7
1.4 Computational modeling attempts of atmospheric pressure plasma jets 10
1.5 Motivation 12
1.6 Path forward 13
1.7 Figures 15
1.8 References 21
Chapter 2 Description of the Model **25**
2.1 Introduction 25
2.2 Overview of the model 26
2.3 Overview of chemistry input 35
2.4 Overview of geometry input 37
2.5 Tables 42
2.6 Figures 45
2.7 References 51
Chapter 3 APPJ into Humid Air **53**
3.1 Introduction 53
3.2 Description of the Model 55
3.3 Dynamics of Plasma Jet 57
3.3.1 Base Case 58
3.3.2 Voltage 67
3.3.3 O2 Fraction in Gas Feed 71
3.3.4 Flow 74
3.3.5 Pulse Repetition Frequency (PRF) 77
3.4 Concluding Remarks 81
3.5 Figures 83
3.6 References 106
Chapter 4 APPJ onto Dielectric and Metal Surfaces **109**
4.1 Introduction 109
4.2 Description of the Model 111
4.3 APPJ Properties Dependent on Surface Properties 112
4.3.1 Touching the Surface 113
4.3.2 Touch + 10 ns 115

4.3.3 End of Maximum Applied Voltage 80 ns 120
4.3.4 End of Pulse (100 ns) 125
4.4 Concluding Remarks 128
4.5 Figures 129
4.6 References 140
Chapter 5 APPJ onto Water Layer 142
5.1 Introduction 142
5.2 Description of the Model 143
5.3 Touching and not-Touching Plasma Jets onto a Liquid Layer 147
5.3.1 Transport of gas phase RONS 147
5.3.2 Evolution of Aqueous Reactivity 154
5.3.3 Fluences to the Tissue 158
5.3.4 Electric Fields 159
5.4 Concluding Remarks 159
5.5 Figures 161
5.6 References 171
Chapter 6 APPJ onto Wet Cells 173
6.1 Introduction 173
6.2 Description of the model 175
6.3 Results and Discussion 178
6.3.1 Not-touching case 179
6.3.2 Touching Cases (-15 kV, -20 kV, and second pulse of -15 kV) 180
6.3.3 Water layer thickness (50 and 1000 μm) 189
6.4 Concluding Remarks 194
6.5 Table 195
6.6 Figures 196
6.7 References 216
Chapter 7 Summary and Future Work 218
7.1 Summary 218
7.2 Future Work 221
7.3 Publications 224
Appendices 227

LIST OF TABLES

Table 2.1 Critical reaction pathways to form the near-terminal RONS..... 42

Table 2.2 Comparison of mesh spacing with computational time..... 44

Table 6.1 Selected constants of the cell components..... 195

LIST OF FIGURES

Figure 1.1 Figure of the atmospheric pressure plasma jet selected as the basis for computation domains analyzed in this thesis. The electrode placement is the key variation in this type of plasma jet. The effluent emerges from the dielectric tube forming the guided ionization wave phenomenon of these types of devices.[5] 15

Figure 1.2 Formation of electron avalanche from cathode (C) toward anode (A) at two moments of time. The arrow indicates the direction of the external electric field and v_d is the velocity of the head.[4] 16

Figure 1.3 Anode-directed streamer propagating from the cathode (C) to the anode (A). (a) the negative particles in the head of the streamer radiating and creating secondary avalanches at two moments in time. (b) the electric field at the head.[4] 17

Figure 1.4 Example of atmospheric pressure plasma jet treatment of liquid covered tissue with time and spatial scales indicated. This example uses two ring electrodes to create the discharge and a gas shield to optimize production of RONS. 18

Figure 1.5 Time scales in plasma medicine.[22] 19

Figure 1.6 Violet Ray Machine (Hochfrequenzstrahlapparat) [23] produced in 1928. Examples of applications are on the left and right frames with the apparatus and example photo in the center frame.[24] 20

Figure 2.1 Block diagram of *nonPDPSIM*.[4] 45

Figure 2.2 The computational domain of the helium atmospheric pressure plasma jet into humid air. The flow moves from the nozzle (inlet) at the base to the pump (outlet) at the top... 46

Figure 2.3 Comparison of mesh refinements with 10% finer mesh than the base shown in the left frame and 10% coarser shown in the right. The refinement zones highlighted in red in the base "default" mesh case are contained in each of the compared cases. 47

Figure 2.4 Comparison of concentration profile of helium and oxygen for the -10%, base and +10% mesh refinement cases. Helium is shown on a linear scale from the annotated maximum. Oxygen is shown on a log-scale over three-decades from the maximum annotated to highlight the seed of oxygen contained within the helium channel. 48

Figure 2.5 Centerline trace showing variations in concentration and velocity for the three mesh spacing cases. (a) Helium concentration profile. (b) Velocity profile with +20% and +100% meshes. (c) Nitrogen concentration profile. (d) Oxygen concentration profile with the tube exit annotated at 0.5 cm. The blue curve represents the coarser mesh, red represents the finer mesh, and black is the base "default" mesh for each frame. 49

Figure 2.6 Comparison of radial trace taken 5 mm from the exit of the dielectric tube showing concentration and velocity changes from the centerline (y-axis) to a point of minimal change 2.5 mm away. (a) Helium concentration profile with tube width annotated at 0.08 cm. (b) Velocity profile. (c) Nitrogen concentration profile. (d) Oxygen concentration profile. The blue curve represents the coarser mesh, red represents the finer mesh, and black is the base "default" mesh for each frame. 50

Figure 3.1 Schematic of the cylindrically symmetric plasma jet. (a) The full computational domain is 10 cm by 2 cm. (b) The numerical mesh with refinement zones. (c) Enlargement of the discharge tube. 83

Figure 3.2 He, O_2, N_2 and H_2O concentrations for a flow rate of 4 slm (base case) through the tube and 4 slm in the shroud prior to discharge ignition. The O_2 concentration is over 3 decades from the maximum of 5×10^{18} cm^{-3} to highlight the seeded O_2 flowing with the He..... 84

Figure 3.3 Plasma dynamics for the base case of He/O_2 = 99.8/0.2 at 4 slm with -15 kV applied for 80 ns. a) Electron temperature T_e from left to right at 20, 50 and 80 ns on a linear scale between 0.5 – 5.5 eV. Potential contours are at 1 kV intervals. The electron impact ionization source S_e, is shown in the right frame at 50 and 80 ns using a log scale. (b) Electron density showing the propagation of the ionization wave into the effluent at 50, 65 and 80 ns. The cation density at 80 ns is the right image. Contours are on a four decade log-scale. 85

Figure 3.4 Reactant densities for the base case at 80 ns for the first discharge pulse. (a) Cation and anion densities. (b) Densities of primary excited states and radicals. Excited helium density, He^*, is the sum of $He(2^1S)$, $He(2^1P)$, $He(2^3S)$, $He(2^3P)$, He(3S), and He(3P) states. The excited molecular nitrogen, N_2^*, represents $N_2(A^3\Sigma, B^3\Pi, C^3\Pi$, and higher) and follows from the ionization wave intersecting the N_2 from the ambient diffusing into the plume. The lateral spread of $O_2(^1\Delta)$, indicates that the laterally spreading of low energy electrons. Contours are on a four decade log-scale. 86

Figure 3.5 Densities of O and O_3 at different times following the (a) first and (b) 30^{th} discharge pulse at a PRF of 10 kHz. The times selected show the environment that the next pulse would encounter at a 1 MHz, 100 kHz, and 10 kHz PRF (left to right). Contours are on a four decade log-scale. At 100 μs, the O atoms produced by the 30^{th} pulse have spread and reacted with O_2 from the ambient to form O_3. The ozone accumulates in the plume..... 87

Figure 3.6 Densities of NO and N_xO_y at different times following the (a) first and (b) 30th discharge pulse at a PRF of 10 kHz. The times selected show the environment that the next pulse would encounter at a 1 MHz, 100 kHz, and 10 kHz PRF (left to right). At a PRF of 10 kHz, the NO produced by the previous pulse(s) moves downstream at lower, but significant, densities. N_xO_y has accumulated to 1 x 10^{11} cm^{-3} over the 30 pulses in the effluent. Contours are on a three decade log-scale. 88

Figure 3.7 Densities of OH and H_2O_2 at different times following the (a) first and (b) 30th discharge pulse at a PRF of 10 kHz. The times selected show the environment that the next pulse would encounter at a 1 MHz, 100 kHz, and 10 kHz PRF (left to right). The OH density is at its maximum at the tip of the dielectric tube at 10 μs, which transitions towards the axis as the humid air diffuses into the helium jet. H_2O_2, primarily created by the reaction of two OH radicals, increases to 1 x 10^{12} cm^{-3} over the 30 pulses in the effluent following the similar spatial trend of OH. Contours are on a three decade log-scale. 89

Figure 3.8 Densities on the axis at the end of the first discharge pulse (80 ns) for voltages of -10 kV, -15 kV (base case), -20 kV, and -30 kV. (a) electrons and total cations, (b) OH, (c) $O_2(^1\Delta)$, (d) total He excited states, (e) total N_2 excited states, and (f) O atoms. The end of the tube corresponds to 0.5 cm. 90

Figure 3.9 The spatial densities of selected RONS at the end of the 30th pulse for the different voltages (-10 kV, -15 kV, -20 kV, -30 kV). The mixture is He/O_2 = 99.8/0.2 flowing at 4 slm with a 10 kHz PRF. (a) O atoms and O_3. (b) NO and N_xO_y. (c) OH and H_2O_2. Contours are on a log-scale with the number of decades shown in the frame. 91

Figure 3.10 Densities on the axis at the end of 30 pulse for a flow rate of 4 slm for voltages from -10 kV to -30 kV. (a) OH, (b) H_2O_2, (c) HNO_x, (d) O_3, (e) NO , and (f) N_xO_y. The end of the tube is at 0.5 cm. At this flow rate and elapsed time, the reactive species in the effluent reach nearly 5.5 cm from the exit of the tube. 92

Figure 3.11 Densities on the axis at the end of the first discharge pulse (80 ns) for O_2 concentrations in He of 0.1%, 0.2% (base case), 0.5%, and 1.0%. (a) electrons, (b) total cation, (c) $O_2(^1\Delta)$, (d) total He excited states, (e) total N_2 excited states, and (f) O atoms. The end of the tube is at 0.5 cm. 93

Figure 3.12 The spatial densities of selected RONS at the end of the 30th discharge pulse for O_2 concentration in He of 0.1%, 0.2%, 0.5%, and 1.0% O_2. (a) O atoms and O_3. (b) NO and N_xO_y. (c) OH and H_2O_2. Contours are on a three decade log-scale. 94

Figure 3.13 Densities on the axis at the end of the 30th discharge pulse for O_2 concentrations in He of 0.1%, 0.2% (base case), 0.3%, 0.5%, and 1.0%. (a) OH, (b) H_2O_2, (c) HNO_x, (d) O_3, (e) NO, and (f) N_xO_y. 95

Figure 3.14 The inventory (spatial integral) of selected species at the end of the 30th discharge pulse for O_2 concentrations from 0.1% to 2%. The O_3 inventory is relatively constant. The lower inventory of NO for 0.1 and 0.2% can be attributed to the higher amount of N_xO_y at the end of the 30th pulse. The NO is depleted by reactions with O to form NO_2. 96

Figure 3.15 Axial densities for flow rates of 2 slm, 4 slm (base case), 5 slm, and 7 slm 100 μs after the of the discharge pulse. (a) O, (b) N, (c) $O_2(^1\Delta)$, (d) O_3, (e) NO, and (f) OH. The end of the tube is at 0.5 cm. 97

Figure 3.16 Densities of RONS at the end of the 30th discharge pulse for flow rates of 2-7 slm with -15 kV pulses at 10 kHz and He/O_2=99.8/0.2 (a) O and O_3, (b) NO and N_xO_y, (c) OH and H_2O_2. At 2 slm, the primary reactants do not flow out of the tube before the next pulse which allows for accumulation of reactants in the tube. At 7 slm, the primary reactants flow out of the tube and the species formed by the next pulse enter a pristine environment. Contours are on a three decade log-scale from the maximum value listed in the frame. 98

Figure 3.17 Axial densities for flow rates of 2 slm, 4 slm (base case), 5 slm, and 7 slm at the end of the 30th discharge pulse. (a) OH, (b) H_2O_2, (c) HNO_x, (d) O_3, (e) NO, and (f) N_xO_y. The exit of the tube exit is at 0.5 cm. 99

Figure 3.18 O atom and O_3 densities for -15 kV, 4 slm and He/O_2=99.9/0.2. (a) Densities at the end of 5th and 10th discharge pulses for 100 kHz (left) and 10 kHz (right) PRF. The higher PRF allows O atoms to accumulate in the tube. (b) Densities at the end of the 30th discharge pulse for PRFs of 500 kHz to 10 kHz. Note the accumulation of O atoms in the tube in the high PRF cases. The O_3 plume is longer, though less dense for the low PRF cases. Contours are on a three decade log-scale from the maximum value listed on the frame. 100

Figure 3.19 NO atom and N_xO_y densities for -15 kV, 4 slm and He/O_2=99.9/0.2. (a) Densities at the end of 5th and 10th pulses for 100 kHz (left) and 10 kHz (right) PRF. (b) Densities at the end of the 30th discharge pulse for PRFs of 500 kHz to 10 kHz. The higher PRF allows NO to accumulate in the tube. For the lower PRFs, NO accumulates at lower densities further downstream. The NO accumulation is significant in the high PRF cases. Contours are on a three decade log-scale with the maximum value noted in each frame. 101

Figure 3.20 OH and H_2O_2 densities for -15 kV, 4 slm and He/O_2=99.9/0.2. (a) Densities at the end of the 5th and 10th pulses for 100 kHz (left) and 10 kHz (right) PRF. (b) Densities at the end of the 30th discharge pulse for PRFs of 500 kHz to 10 kHz. Contours are on a three decade log-scale with the maximum value noted in each frame. 102

Figure 3.21 Axial densities for PRFs of 500 kHz, 100 kHz, 50 kHz, 10 kHz, and 5 kHz at the end of their 30th discharge pulse. (a) OH, (b) H_2O_2, (c) HNO_x, (d) O_3, (e) NO, and (f) N_xO_y. The

end of the tube is at 0.5 cm. The length of the effluent is proportional to the total elapsed time after the 30 pulses at the different PRFs. 103

Figure 3.22 Axial densities for PRFs of 500 kHz, 100 kHz, 50 kHz, 10 kHz, and 5 kHz after a total elapsed time of 6 ms (corresponding to the end of the 30^{th} pulse at 5 kHz PRF case. In each case 30 pulses were computed, followed by flow without additional pulsing until a total time of 6 ms. (a) OH, (b) H_2O_2, (c) HNO_x, (d) O_3, (e) NO, and (f) N_xO_y. The end of the tube corresponds to 0.5 cm. 104

Figure 3.23 Total inventory (integral of the density over the entire volume) for different PRF. (a) Inventory immediately after the completion of the 30^{th} pulse. (b) Inventory after 30 pulses followed by additional flow for the same elapsed time of 6 ms. The additional flow time allows for the creation of O_3, H_2O_2, N_xO_y and HNO_x in the 50, 100, and 500 kHz cases. 105

Figure 4.1 The cylindrically symmetric model geometry. (a) The full computational domain is 1.95 cm by 0.88 cm. (b) The numerical mesh with refinement zones. 129

Figure 4.2 He, N_2, O_2, and H_2O concentrations for a flow rate of 4 slm He/O_2=99.8/0.2 through the tube prior to discharge ignition and humid air flowed as a shroud. Maximum values are shown in each frame (1 decade log scale). The O_2 concentration is plotted over 3 decades to highlight the 0.2% O_2 seeded in the He. 130

Figure 4.3 Plasma dynamics at the time the ionization wave arrives at the material surface. Each case has He/O_2 = 99.8/0.2 flowing at 4 slm into humid air and a -15 kV applied voltage. From left to right, the frames correspond to relative permittivities of 2, 5, 10 and 80, and metal. The time from beginning of the pulse to impact are listed for each permittivity. (a) Electron temperature T_e, (b) electron impact ionization source S_e, and (c) magnitude of the electric field with potential contours at -1 kV intervals. The maximum value or range of values are noted in each figure…. 131

Figure 4.4 Plasma dynamics at 10 ns after the ionization wave touches the material surface. From left to right, the frames correspond to relative permittivities of 2, 5, 10 and 80, and metal. The *touch + 10 ns* time is listed in each frame. (a) Electron impact ionization source S_e, (b) electron density, (c) total cation density, and (d) total anion density. Contours are on a log-scale with the maximum value and number of decades listed in the frame. 132

Figure 4.5 Production of key neutrals at 10 ns after the ionization wave touches the material surface (*touch + 10 ns*). From left to right, the frames correspond to relative permittivities of 2, 5, 10 and 80, and metal. The times listed correspond to *touch + 10 ns*. (a) He^*, (b) O atoms, (c) N_2^* and. (d) OH. Contours are on a three decade log-scale from the maximum value listed in the frame…… 133

Figure 4.6 Plasma dynamics at the end of the maximum applied voltage (80 ns). From left to right, the frames correspond to relative permittivities of 2, 5, 10 and 80, and metal. (a) Electron temperature T_e (linear scale from 1 – 3 eV), (b) electron density, (c) total cation density and (d) total anion density. Contours are on a log-scale with the maximum value and number of decades listed on the frame. 134

Figure 4.7 Production of key neutrals at the end of the maximum applied voltage (80 ns). From left to right, the frames correspond to relative permittivities of 2, 5, 10 and 80, and metal. (a) He^* decreases in density compared to *touch + 10 ns*, (b) O atoms accumulate in the channel and on the surface, (c) N_2^* also accumulates in the channel and along the surface and (d) OH. Contours are on a log-scale. 135

Figure 4.8 Magnitude of the electric field at the end of the maximum applied voltage (80 ns). From left to right or top to bottom, the frames correspond to relative permittivities of 2, 5, 10 and 80, and metal. (a) The maximum extent of the penetration of the electric field into the dielectric from and electric potential contours at -1 kV intervals. (b) Close up of the material surface showing the penetration of the electric field. Contours for the electric field are on a linear scale from 3 – 35 kV/cm. 136

Figure 4.9 Total positive and negative charge density, and resulting electric field (with voltage contours) when the applied voltage pulse returns to 0 at 100 ns. (a) ε_r = 5 (tissue-like), (b) ε_r = 80 (water-like) and (c) metal. For positive charge density, contours are on a log-scale with the maximum value and number of decades listed on the frame. For negative charge density and magnitude of the electric field, the contours are on a linear scale. 137

Figure 4.10 Magnitude of the electric field at the end of the applied voltage (100 ns). From left to right or top to bottom, the frames correspond to relative permittivities of 2, 5, 10 and 80, and metal. (a) The resulting ion matrix and surface electric fields resulting from the charge separation when the applied voltage returns to 0. Contours are on a linear scale from 3 – 35 kV/cm. The potential contours at -1 kV intervals. (b) Close up of the electric field at the material surface. Contours are on a log-scale from 5 – 100 kV/cm. 138

Figure 4.11 An enlarged view of the material surface showing total positive (top frame) and negative charge density (bottom frame) that result in a surface electric field. The time is 100 ns when the applied voltage pulse returns to 0. (a) ε_r = 5 (tissue-like), (b) ε_r = 80 (water-like) and (c) metal. Contours are on a log-scale with the maximum value and number of decades listed on the frame..... 139

Figure 5.1 Schematic of the cylindrically symmetric model geometry. (a) The total computational domain is 1.95 cm in height and 0.88 cm in radius. (b) Numerical mesh showing different refinement zones. 161

Figure 5.2 Flow profiles at 8 ms prior to initiating the discharge for (a) He, (b) O_2, (c) N_2 and (d) H_2O. The water vapor is blown from the surface of the water layer by the jet. The maximum value is noted in each frame. Contours are on a linear scale unless the number of decades for a log scale is noted. 162

Figure 5.3 Electron density for applied potentials of -10 kV, -15 kV and -20 kV at 50 ns prior to pulse termination. The electron plume for -10 kV does not touch the liquid surface and is not-touching. The electron plume for -15 kV touches at 35 ns (in contact with water and spreading for 15 ns) and the plume for -20 kV touches at 20 ns (in contact for 30 ns). Contours are on a log-scale over 4 decades. 163

Figure 5.4 Plasma dynamics -15 kV. (a) electron density, (b) electron temperature and (c) electron impact ionization source at 20, 35 and 50 ns after start of the pulse. At 20 ns the ionization wave has not touched the surface. The spread of the ionization as a surface ionization wave continues after touching. Contours are on a linear scale unless the number of decades for a log scale is noted. 164

Figure 5.5 Ozone density in the gas phase and in the liquid for -15 kV at varying times after the discharge pulse. Ozone is relatively non-reactive in both phases. . Contours are on a 5-decade log-scale. 165

Figure 5.6 OH in the gas phase and water, and H_2O_2 in the water for the -15 kV at varying times after the discharge pulse. At 1 μs, the highest OH concentration is adjacent to the water layer where the electron plume intersects the evaporating water. Over the next 200 μs the OH reacts or blows away. The evolution of OH_{aq} into H_2O_{2aq} is shown in the lower panels. Notice that the location of the high concentration of OH at 1 μs becomes the location of the highest concentration of H_2O_{2aq}. Contours are on a 5-decade log-scale. 166

Figure 5.7 N_xO_y density for -15 kV case shown at varying times after the discharge pulse in the gas and water layer. NO is the initiating molecule for N_xO_y. The comparatively low density of N_xO_y results from the effectiveness of the helium jet blocking access of NO to the water layer and the laminar flow that blows NO away. Contours are on a 4-decade log-scale. 167

Figure 5.8 The time evolution of the liquid volume average densities of aqueous ions. (a) $O_2^-{}_{aq}$ and $H_3O^+{}_{aq}$; and (b) $NO_3^-{}_{aq}$ and $ONOO^-{}_{aq}$ for the touching -15 kV and -20 kV cases. (c) Densities for the -10 kV (no-touch) case. 168

Figure 5.9 The time evolution of the liquid volume average densities of neutral aqueous species (a) H2O2aq and OH_{aq}; and (b) O3aq and HO_{2aq} for the touching -15 kV and -20 kV cases. (c) Densities for the -10 kV (no-touch) case. 169

Figure 5.10 Fluences to the tissue beneath the water over one second for not-touching (-10 kV) and touching (-15 kV, -20 kV) cases. a) ions and b) neutral species. 170

Figure 6.1 Range of electrical field effects based on pulse duration and the resulting application.[10]. 196

Figure 6.2 Schematic of the 2-D Cartesian symmetric model geometry. (a) The full computational domain is 19 mm by 9 m. (b) A closer look at the cells beneath the water layer with locations for further investigation annotated by the red dots..... 197

Figure 6.3 Helium, oxygen, nitrogen and H_2O concentrations of the He/O_2 = 99.8/0.2 flow at 4 slm and 1 slm of humid air from shroud into the ambient prior to discharge ignition. The color contours on the helium and nitrogen images represent 10% decreases from the maximum listed value. The oxygen and H_2O concentrations are over 3 decades from the maximum listed to highlight the seeded oxygen within the helium and the movement of the water vapor from the surface of the water layer. 198

Figure 6.4 Plasma dynamics for the not-touching, -10 kV, case shown at maximum potential at 40 and 50 ns and at zero applied voltage at 60 ns. (a) Electron temperature T_e from left to right at 40, 50 and 60 ns on a linear scale between 0.5 – 8 eV. (b) The electron impact ionization source S_e, at 40, 50 and 60 ns using a log-scale over five decades. (c) Electron density at 40, 50 and 60 ns from left to right using a three decade log-scale. 199

Figure 6.5 Magnitude of electric field for the not-touching, -10 kV, case shown at 40, 50 and 60 ns. (a) Electric field using a linear scale from 2 – 20 kV/cm with potential contours representing one kV changes. (b) Electric field at the air – water layer – tissue interface from top to bottom at 40, 50, and 60 ns using a log-scale over two decades. (c) Electric field magnitude at the water layer – cell membrane interface, within the cell structure, and in the tissue below the cells shown using a log-scale over two decades. 200

Figure 6.6 Plasma dynamics for the touching, -15 kV, case shown at 3 ns before touching, at touching, and 3 ns after touching. (a) Electron temperature T_e, using a linear scale from 0.5 – 9 eV with direction of the propagation shown by arrows within the frame. (b) The electron impact ionization source S_e, using a log-scale over five decades. The restrike and surface ionization wave at 35.5 ns are noticeable in both (a) and (b). (c) Electron density n_e, using a log-scale over three decades. The formation of the conduction channel is apparent at 35.5 ns..... 201

Figure 6.7 Magnitude of electric field for the touching, -15 kV, case shown at 3 ns before touching, at touching, and 3 ns after touching. (a) Electric field within the using a linear scale from 5 – 50 kV/cm with potential contours representing one kV changes. (b) Electric field at the air – water layer – tissue interface from top to bottom at 3 ns before, at, and 3 ns after touching using a log-scale from a maximum of 50 kV/cm over two decades. (c) Electric field magnitude

at water layer – cell membrane interface, within the cell structure, and in the tissue below the cells shown from a maximum of 15 kV/cm on a log-scale over two decades. 202

Figure 6.8 The discharge dynamics at the end of the pulse. Corresponding to the maximum extent of the pulse at 50 ns, the end of the pulse fall at 60 ns, and 10 ns into the afterglow at 70 ns. (a) The electron density in the left frame at 50 ns on a log-scale over four decades. The magnitude of the electric field and potential contours at 50, 60 and 70 ns. The contours represent one kV and the field is shown using a log-scale from 100 kV/cm over two decades. (b) The electric field at the air – water layer – tissue interface. (c) The magnitude of the electric field at the water layer – cell interface at the maximum extent of the pulse (50 ns), pulse fall (60 ns) and afterglow (70 ns). 203

Figure 6.9 The critical discharge dynamics of the touching, -20 kV, case. From left to right, electron temperature T_e, using a linear scale from 0.5 – 11 eV at moment guided ionization wave touches the water layer, the electron impact ionization source S_e, using a log-scale over five decades with arrows indicating direction of restrike and surface ionization wave at 3 ns after touching, and electron density n_e, using a log-scale over three decades at 3 ns after touching.. 204

Figure 6.10 The discharge dynamics of the end of the -20 kV pulse shown at the maximum extent of the pulse (50 ns) and the end of the pulse fall (60 ns). (a) The conduction channel represented by the connection of the electrons from the water layer surface to the pin electrode and the spread of the electrons across the surface of the water layer is shown in the left frame at 50 ns. The magnitude of the electric field at 50 ns shown using a log-scale from 100 kV/cm over two decades. (b) The magnitude of the electric field at the air – water layer – tissue interface highlights the formation of an electric field on the surface of the water layer at 60 ns shown using a log-scale over two decades from 100 kV/cm. (c) The magnitude of the electric field at the water layer – cell membrane interface, within the cell, and in the tissue beneath the cells from a maximum of 38 kV/cm over two decades using a log-scale at 50 ns. 205

Figure 6.11 The concentration of aqueous ions 50 ms after the completion of the first pulse and immediately prior to the second -15 kV pulse (top frame) and at the end of the second -15 kV pulse (70 ns). (a) Concentration of aqueous electrons and anions and (b) concentration of aqueous cations from 10^{14} cm^{-3} using a log-scale over four decades. 206

Figure 6.12 The critical discharge dynamics of a second -15 kV pulse touching a conductive, 200 μm thick, water layer. From left to right, electron temperature T_e, using a linear scale from 0.5 – 9 eV at the time of touch, 36 ns. the electron impact ionization source S_e, using a log-scale over five decades with arrows indicating direction of restrike and surface ionization wave at 39 ns (3 ns after touch), and electron density n_e, at 39 ns using a log-scale over three decades. 207

Figure 6.13 The discharge dynamics at the end of the second pulse. Corresponding to the maximum extent of the pulse at 50 ns and the end of the pulse fall at 60 ns. (a) The electron

density in the left frame is shown on a log-scale over four decades at lower levels than those of the first pulse at 50 ns. The magnitude of the electric field and potential contours are shown at 50 ns for the plasma region. The contours represent one kV and the field is shown using a log-scale from 100 kV/cm over two decades. (b) The electric field at the air-water layer-tissue interface highlighting the effect of surface charging and the resulting surface electric field created at 60 ns using a log-scale from 130 kV/cm over two decades. (c) The magnitude of the electric field at the water layer-cell interface at the extent of the pulse (50 ns) also using a log-scale from 25 kV/cm over two decades. 208

Figure 6.14 The magnitude of the electric field as it changes with time at four locations for the -10 kV, -15 kV (1^{st} and 2^{nd} pulses) and -20 kV cases. (a) At the surface of the water layer, 10 μm from the centerline. The locations for the membrane, cytoplasm and nucleus are indicated in Fig. 6.2(b). (b) In the membrane. (c) In the cytoplasm. (d) In the nucleus..... 209

Figure 6.15 The critical discharge dynamics of the touching, -15 kV, case touching a 1 mm thick water layer. From left to right, electron temperature T_e, using a linear scale from 0.5 – 9 eV at the moment of touching, 29 ns, the electron impact ionization source S_e, using a log-scale over five decades with arrows indicating direction of restrike and surface ionization wave at 3 ns after touching (32 ns), and electron density n_e, at 32 ns using a log-scale over three decades. 210

Figure 6.16 The discharge dynamics of the end of the -15 kV pulse onto a 1 mm thick water layer shown at the maximum extent of the pulse (50 ns) and the end of the pulse fall (60 ns). (a) The conduction channel and spread of electrons across the surface of the water layer using a log-scale from 4×10^{13} cm^{-3} over three decades. (b) The magnitude of the electric field at the air – water layer – tissue interface highlights the formation of an electric field on the surface of the water layer at 60 ns shown from 5 – 160 kV/cm using a linear-scale. (c) The magnitude of the electric field at the water layer – cell membrane interface, within the cell, and in the tissue beneath the cells at 50 ns from a maximum of 35 kV/cm over two decades using a log-scale.. 211

Figure 6.17 The critical discharge dynamics of the touching, -15 kV, case touching a 50 μm thick water layer. From left to right, electron temperature T_e, using a linear scale from 0.5 – 9 eV at the moment of touch (28.5 ns), the electron impact ionization source S_e, using a log-scale over five decades with arrows indicating direction of restrike and surface ionization wave at 3 ns after touch (31.5 ns), and electron density n_e, at 31.5 ns using a log-scale over three decades. 212

Figure 6.18 The discharge dynamics of the end of the -15 kV pulse onto a 50 μm thick water layer shown at the maximum extent of the pulse (50 ns) and the end of the pulse fall (60 ns). (a) The conduction channel and spread of electrons across the surface of the water layer using a log-scale from 1×10^{14} cm^{-3} over three decades. (b) The magnitude of the electric field at the air – water layer – tissue interface highlights the formation of an electric field on the surface of the water layer at 60 ns shown from 5 – 85 kV/cm using a linear-scale. (c) The magnitude of the

electric field at the water layer – cell membrane interface, within the cell, and in the tissue beneath the cells at 50 ns from a maximum of 26 kV/cm over two decades using a log-scale.. 213

Figure 6.19 The magnitude of the electric field as it changes with time at four locations for the 50 µm, 200 µm, and 1 mm thick water layer cases. (a) At the surface of the water layer, 10 µm from the centerline. The locations for the membrane, cytoplasm and nucleus are indicated in Fig. 6.2(b). (b) In the membrane. (c) In the cytoplasm. (d) In the nucleus..... 214

Figure 6.20 Comparing the development and propagation of the electric field in and through the tissue beneath the water layer for the 50 µm and the 1 mm thick water layer cases at 40 and 50 ns. A grounded plate exists beneath the tissue at the bottom of the computational domain. (a) 50 µm at 40 ns. (b) 50 µm at 50 ns showing the lateral spread of the electric field through the tissue but beneath the water layer forming a connection with the surface ionization wave. (c) 1 mm at 40 ns. (d) 1 mm at 50 ns showing the penetration of the field through the tissue to the ground plate and spread through the tissue. Each figure uses a linear scale showing 3 – 30 kV/cm to highlight the electric field within the tissue. 215

LIST OF APPENDICES

Appendix I List of Reactions……..227

Appendix II Author's Biography…….242

Chapter 1 Introduction

1.1 Overview of plasma

As with the formation of each preceding state of matter, the fourth state, plasma, is created by continuing to add energy to the third state, gas.[1,2] The addition of energy ionizes the gas. The presence of charged species makes the fourth state of matter electrically conductive. Plasmas can be completely ionized or weakly ionized and thermal or non-thermal. Thermal plasmas are also called "hot" plasmas and are nearly fully ionized. In those plasmas, the temperatures of the neutral species in the gas, ions and electrons are the same. Applications include: plasma torches for cutting and plasma welding. These applications are typically conducted at atmospheric (or higher) pressure.[3]

In non-thermal plasmas, or "cold" plasmas, the temperatures of the gas and ions are much lower than the temperature of the electrons.[3,4] These are also weakly ionized plasmas in which the number of charged species to neutral species is on the order of 1×10^{-6}. Initially, these plasmas were used in low pressure applications for lighting, microelectronics manufacturing, and surface functionalization. The use of dielectric coatings on electrodes as well as short voltage pulses have allowed for low temperature plasma applications at atmospheric pressure. Creating a stable discharge at atmospheric pressure has opened opportunities for functionalization of various polymers and textiles in typical industrial settings.[3]

Non-thermal plasma applications have been classified as either direct or indirect. The applications listed earlier are direct applications and have high photon and ion fluxes to the

treated surface. This is necessary for micro-fabrication of silicon wafers and plasma activation of surfaces for better wettability, for instance.[3] The indirect method is a means to remotely deliver the plasma created species to a surface potentially at a greater distance from the source with lower fluxes and, subsequently, a decreased electric field. The atmospheric pressure plasma jet (APPJ) is an example of an indirect method of application of non-thermal plasma. This method allows for the greater interaction of the plasma with the ambient air and produces significant quantities of reactive species. One of the great challenges of cold, atmospheric pressure plasma applications is the reactivity of air because of the variability of streamer formation and the multiple energy loss reaction mechanisms. Discharges formed in air are difficult to control as streamers, like mini-lightning bolts, form randomly and branch as discussed in Sec. 1.2 and 1.4.

In recent experiments, the atmospheric pressure plasma jet is comprised of a noble gas (typically helium or argon) seeded with small amounts of O_2 or H_2O.[5] The noble gas flows through the tube or capillary and exits into the ambient air forming a channel consisting dominantly of the noble gas. The effluent of the plasma jet flows into the room air and creates a channel for the plasma-produced high-energy species to travel along and then transfer their energy to or react with the ambient air as shown in Fig. 1.1.[5] The temperature in the effluent of the plasma jet is near ambient. This method has lower photon and ion flux than the direct method but creates useful amounts of reactive species. A recent push is to leverage the charged and reactive species produced in the plasma effluent, as well as the electric field effects generated, for medical treatment taking advantage of the therapeutic reactive species produced by the APPJ.

First, an overview of plasma jets will be discussed (Sec. 1.2), followed by a review of milestones in plasma medicine (Sec. 1.3), a discussion of computational modeling of plasma jets (Sec. 1.4), the motivation of my research (Sec. 1.5), and then an overview of the dissertation (Sec. 1.6).

1.2 Overview of atmospheric pressure plasma jets

Non-equilibrium APPJs provide therapeutic and sterilizing effects in the context of biomedical treatment of surfaces through delivery of fluxes of photons, charged and reactive species, and electric fields to tissue.[6-10] Although the devices are geometrically simple, the structure of the plasma in APPJs can be quite complex, as demonstrated by early observations of *plasma bullets* propagating through the plume of an APPJ which motivated significant research on the dynamics of these discharges.[11,12] The fluxes of ions and photons, and electric fields in APPJs that arrive at the surface being treated typically have lower intensities than in a dielectric barrier discharge (DBD).[13] However, the design and method of implementation of APPJs allow for more opportunity to control the reaction of the plasma produced species with the ambient air to form reactive oxygen and nitrogen species (RONS) that are beneficial for surface treatment than the typical DBD. Many of these aspects of the APPJ will be analyzed through this dissertation.

Typically, the plasma jet is a noble gas seeded with small amounts of O_2 or H_2O.[5] The noble gas flows through a capillary tube in which the discharge is formed into room air. In doing so, a rare-gas dominated channel in the air is hydrodynamically formed, through which plasma produced reactive species flow. Mixing of the reactive species in the gas plume with the ambient

air environment results in production of secondary species.[14,15] Due to the gas flow and pulse shape, the temperature in the effluent of the plasma jet is near ambient.[16,17]

The *plasma bullet* that propagates through the plasma plume is also known as a *guided ionization wave* or *guided streamer*.[11] A brief overview of the formation of streamers will be presented prior to discussing the guided aspect. Summarizing Raizer's text [4], the formation of a streamer requires an electron avalanche at the head as shown in Fig. 1.2. Streamers can be cathode or anode directed. A cathode-directed-streamer, or a streamer moving toward the cathode, is also called a positive streamer as it emanates from the positively charged anode and, conversely, the anode-directed-streamer is negative as shown in Fig. 1.3. In light of the work that will be presented in this dissertation, the negative streamer will be further discussed. The electron avalanche is produced by the repulsion of electrons from the negative voltage applied to the cathode and is true for both types of streamers. If the field and gap between the electrodes is large enough, the avalanche will transition to an anode-directed-streamer. The electrons are moving in the same direction as the streamer (away from the cathode). According to Raizer in his text from 1991, "The plasma front propagates at the expense of the electrons of the front, accelerated in the strong field, while the electrons behind the front (in a weak field) do not separate from the ions, that is, the charges form a quasineutral plasma. This resembles the propagation of an ionization wave."[4]

The structure of the guided streamer is similar to a conventional atmospheric pressure streamer where space charge produced electric field enhancement in the head of the streamer generates an electron avalanche. The guided aspect of propagation results from the E/N (electric field/gas number density) required for avalanche being lower in the rare-gas dominated plume than in the surrounding air. The avalanche is then prevented from spreading laterally into the air

and remains in the rare-gas channel. From this "guiding" of the ionization wave down the rare-gas channel, the term *guided ionization wave* or *guided streamer* was coined. The speed of the propagating front has been measured at more than 1×10^7 cm/s.[5,10,17]

As the plasma produced ions, electrons, and other excited species interact with the ambient air, other RONS are created. The RONS produced in this manner that are believed to be beneficial in biomedical applications include singlet delta molecular oxygen, $O_2(a^1\Delta_g)$, oxygen atoms (O), hydroxyl radicals (OH), ozone (O_3), hydrogen peroxide (H_2O_2) and nitric oxide (NO).[18] Each species has specific characteristics that can be used independently or to complement others, and whose production rates would ideally be separately controlled. For example, $O_2(a^1\Delta_g)$ is metastable species that is a convenient mechanism to transport activation energy from the plasma to the surface, OH is the precursor to H_2O_2 and, along with O, is an oxidizing reactive species, NO is an important cellular signaling molecule thought to be necessary in wound healing, and O_3 is convenient mechanism to transport the reactivity of the O atom to remote locations.

In plasma medicine, the desired application of APPJs is to treat cells as highlighted in Fig. 1.4. The entire treatment process of an APPJ flowing onto a liquid layer covering tissue with cellular structure beneath is shown in this figure. The first step is the creation of an electric discharge generated by a high-voltage pulse to the process gas flowing from left to right as shown in the plasma kinetics portion. The time and length scales are a critical challenge in both the experiment and the computational representation of the treatment of cells. The formation of the plasma occurs over nanoseconds within the discharge region that is a few to 10s of mm in size. Following this pulse, the next step is to generate the reactive species in the gas phase through the repetitive sequence of electric discharge formation in the capillary, flow of primary

reactive species into the rare-gas dominated plume, mixing with the ambient environment and transport to the surface, normally a few mm to a few cm away, which occurs over 10s of nanoseconds (for charged species that are formed by the ionization wave) to microseconds for neutral and excited species that move with the gas flow). In an effort to control the production of RONS by the discharge, the use of a gas shield has been reported [19,20] and is included in Fig. 1.4. The use of the shielding gas encourages formation of selected charged and excited species depending on the composition of the gas curtain. As the ionization wave propagates to the surface, the charged species move through the helium channel, strike and spread across the surface, and eventually form aqueous species.

Often the surface being treated is cellular tissue, which is covered by a thin layer of a blood serum-like liquid a few hundred microns thick.[21] Instead of directly interacting with the tissue, the plasma-produced neutral reactive species, ions and photons first react with the liquid layer. Gas phase species solvate into the liquid and undergo additional reactions before the plasma produced activation energy reaches the underlying tissue. Photolysis and photoionization from plasma-produced ultraviolet and vacuum-ultraviolet (UV/VUV) photons may directly produce active species (neutral reactive species and ions) in the top layer of the liquid that subsequently react to form other aqueous ions and neutral reactive species. As the guided ionization wave strikes the surface of the water layer, solvation of neutral and charged species and the subsequent formation of aqueous species are the next steps as the plasma created species interact with the liquid layer which is 100s of μm up to several mm thick. These reactions occur over nanoseconds (ion charge exchange reactions, photoionization and photo-dissociation) to hours as the aqueous terminal species form and reform. Through solvation, reactions, and diffusion through the liquid layer, the aqueous species then interact with the tissue below and,

over treatment periods of minutes to hours, intratissue transport, membrane kinetics, and cellular response occur on sub μm length scales. The drastic difference in timescales for the various aspects of the treatment process was highlighted in a recent paper by Sakiyama and Graves [22] and is shown as Fig. 1.5. This figure was used to explain the extreme differences in timescales for treatment by a surface-microdischarge, but also applies to the discussed scenario following Fig. 1.4. The time scales shown range from ns for the pulse excitation and discharge formation to μs for the charged species reactions to ms for neutral reactions and applied voltage to treatment times of minutes to patient recovery (cellular response times) of hours after treatment. Length scales for the plasma model in the mm/cm range treating samples up to and exceeding three orders of magnitude smaller. These extreme differences in time and length scales challenge computational modelers.

1.3 Overview of plasma medicine milestones

The scenario discussed in the previous section details the treatment of cells with an atmospheric pressure plasma jet in a field now called “Plasma Medicine”. The idea of plasma medicine can be traced back to the “Violet Ray Machine” that provided therapeutic plasma treatment [23,24] developed in Germany in 1928 by creating plasma generated ozone for various treatments as the examples show in Fig. 1.6. The use of plasma generated ozone can be traced back to Siemens in the 1850s to clean biologically contaminated water.[24] Interest was rekindled in the late 1960’s and 1970’s with the use of an argon plasma to cauterize tissue [25] and a method developed by Menashi in 1968 to sterilize materials using plasma.[26] A new era of plasma medicine was initiated as the methods to create non-thermal plasmas at atmospheric conditions were adopted in the late 1990’s. Short, high voltage pulses and the use of dielectric

coatings on electrodes enabled the use of plasma at ambient conditions without arcing. These methods were then applied to functionalize and sterilize surfaces.

Using a glow discharge at atmospheric pressure, Laroussi treated a sample placed between the two coated electrodes. The microorganisms living on the medium were destroyed but the sample was not damaged. This highlighted both the sterilizing and non-thermal effects of the application.[27] In Russia, Shekhter used plasma created by the "Plazon", a hot air plasma rapidly cooled that is known to generate proportionally high levels of NO, for wound healing on mammalian cells (rats) in 1998.[28,29] Laroussi, continuing his successful research, found that glow and corona discharges could both be used for biological decontamination in 2000 [30] and, in an effort to characterize the effects of the plasma treatment, found that plasma influences heterotrophic pathways of bacteria and their cell morphology through a modified experiment using resistive barrier discharge enclosed in a gas mixture of 97% helium and 3% oxygen in 2002.[31] The helium provided a more stable environment for the discharge. In 2003, Stoffels *et al*. treated mammalian (Chinese Hamster Ovarian) cells by an rf electrode, plasma needle, into a helium enclosed set-up with the cells covered by a 0.3 mm phosphate buffered saline solution. The cells showed no thermal or electrical damage.[32] In the early 2000's, the plasma was known to kill the cells through continued mention of bacteria inactivation and sterilization, but treatment and recovery of cells was still uncertain. Dosage, defined as the length of total treatment and included voltage and frequency of the pulse, and its effects on cell viability was a mystery.

With a requirement of low-temperature treatment with no risk of arcing and a desire to minimize ozone production, Laroussi *et al.* developed a hand-held device using helium as a carrier gas that he named the "plasma pencil".[33] It was quickly shown to inactivate

bacteria.[34] Concurrently, Yonson *et al*. developed a similar device they coined the "plasma torch" also using helium as a carrier gas. They showed that it detached cells *in vitro* and, upon transplanting them to a second dish, they continued to grow. These experiments also showed permeation of the cell membrane. Additional experiments reported in the same report demonstrated cell adhesion to surfaces functionalized by the plasma torch.[35]

While these groups were using an indirect treatment method with atmospheric pressure plasma jets, Fridman *et al.* attempted a direct approach, a floating electrode DBD, to show plasma promoted apoptosis, programmed cell death, in cancer cells.[36] Continuing with the treatment of cancer cells, in 2010, Vandamme *et al.* showed antitumor effect on cancer cells *in vivo* using a pulsed DBD system similar to that of Fridman *et al.* to treat the U87 glioma tumor grafted onto a nude mouse. The mouse was placed on a grounded silver plate to enhance its conductivity.[37] In 2011, Keidar showed selectivity of cancer cells without damage to normal cells *in vitro* and significant reduction in tumor size *in vivo* using a cold atmospheric plasma jet.[38]

Concurrently, immersing the cell sample in a liquid previously treated by plasma drew interest as a potentially gentler treatment method without the dosage concerns of treating the cell sample directly. This plasma-activated-water leveraged the effect of plasma on liquids: increasing the acidity of the liquid, increasing the hydrogen peroxide created, as well as increasing the amount of nitrite and nitrate within the liquid. By treating the liquid with plasma and then introducing the cells, antibacterial efficacy was shown for up to seven days.[39] Experiments of electrical discharges on liquids began in the bioelectrical community by Schoenbach *et al*. in 2007 to analyze electrical breakdown in water.[40] More recently, different groups have looked at the manner in which plasma jets produce reactivity in liquids, starting with

water.[41-43] The majority of these studies have used a rare-gas seeded with a small amount (usually < 1%) of a reactive gas (e.g., O_2, N_2, H_2O) as the media flowing through the plasma jet into room air and onto the liquid.

Many other extremely successful groups working to advance the field of plasma medicine have been neglected in this high level overview. In this brief review, the seminal works were discussed and referenced. Currently, there is still debate over the primary source of the plasma treatment benefits. The plasma discharge is known to create UV/VUV, radiation, charged and reactive species and electric fields. Each of these aspects is known to produce beneficial effects leveraged in the medical field. The comprehensive application of all using one device needs to be further researched and protocols established for various applications to ensure proper treatment dosage leading to the desired effects.

1.4 Computational modeling attempts of atmospheric pressure plasma jets

Computational modeling of cold atmospheric pressure plasma jets can provide vital insights into determining the "how" of plasma medicine. However, computational modeling of APPJs is limited to a few groups across the world. Initially, the models were based upon experiments. First, Brok *et al.* provided a numerical description of the discharge characteristics of Stoffel *et al.*'s plasma needle.[44,32] Later, in 2006, Sakiyama and Graves created a 2-D model of an rf-plasma needle transitioning between corona-model to the glow-mode using a finite element analysis of a discharge occurring in helium with trace nitrogen gas.[45,46] In 2012, they created a one-dimensional plug-flow model of a surface microdischarge into humid air with over 50 species and 600 reactions.[22] Another one-dimensional plug-flow model with over 2000 chemical reactions was developed by van Gaens and Bogaerts to represent an argon

atmospheric pressure plasma jet.[47] These models contained extensive reaction chemistry sets but gave limited spatial resolution.

As modelers attempted to represent the formation of the plasma bullet, the work of a previous generation of modelers provided important ground work. As discussed previously, the plasma bullet is essentially a guided ionization wave, or a guided streamer. In the 1980's, several groups were attempting to numerically represent a streamer. Dhali and Williams published a rapid communication in 1985 of a 2-D numerical simulation of streamer propagation in nitrogen at atmospheric pressure.[48] Shortly after, Kushner *et al*. created a laser triggered spark gap numerical model to describe the experimental work being conducted within the group.[49,50] In 1994, Vitello *et al*. created at a 2-D (3-D cylindrically symmetric) model to investigate parallel plane and point-to-plane geometries producing negative streamers in atmospheric pressure N_2 with the stated application being destruction of airborne toxic chemicals.[51] Shortly after, Kulikosky modeled both an anode and cathode directed streamer focusing on the dynamics in the head of the streamer using a 1-D model and, later, a 2-D model.[52,53] Naidis, who would be the first to represent the *plasma bullet* in 2-D, simulated positive streamers propagating between a wire and a plate [54], voltage and electric field dynamics of the streamer in air [55], and subsequent production of oxygen and nitrogen atoms and excited nitrogen from the positive streamer in air.[56] More recent work on streamer dynamics has been conducted by Ebert *et al*. looking in depth at the propagating front of the streamer [57] and the spontaneous branching of anode-directed-streamers.[58]

Of the first two-dimensional models that represented the formation of the plasma bullet, Naidis, building on his successful streamer modeling from the 1990's, modeled a positive streamer propagating along a helium channel containing diffused ambient air [58,60] focusing on

the discharge dynamics. He used a limited reaction set with electrons, ions, a composite excited helium state, and the $N_2(C^3\Pi)$ excited nitrogen state. As interest continued in the development of the plasma bullet and the interaction with the ambient as the bullet propagates along the helium channel, groups conducted parametric studies on the development of the structure and dynamics of the streamer.[61,62] Recently, the interaction of the plasma jet onto a dielectric surface has been modeled.[63]

As plasma medicine has received the bulk of the interest in atmospheric pressure plasma jets, two groups have reported on the plasma-biofilm and plasma-tissue interaction. One group focused on the molecular dynamics (MD) scale [64] and the other introduced typical species created by a plasma discharge and focused on the plasma chemistry between the liquid and plasma, liquid and tissue, and plasma and tissue.[65] To this point, no one has modeled the development of the flow prior to the discharge pulse, spatially tracked the development of reactive nitrogen and oxygen species (RONS) through a 2-D model, nor incorporated a potentially reactive surface into their plasma jet model. All of these important aspects are required for better understanding of the APPJ in general, as well as in the context of plasma medicine.

1.5 Motivation

The problem I will be studying is the interaction of the APPJ with cellular structure embedded in tissue beneath a thin water layer. I will focus initially on the development and propagation of the guided ionization wave into the humid ambient and the subsequent production of RONS. Upon accurately representing the plasma jet into humid air, I will look at the effect a dielectric or metal surface has on the plasma jet flow characteristics as well as the discharge

dynamics by changing the relative permittivity of the material being impacted. From there, the APPJ will interact with a water layer covering tissue in which the additional plasma chemistry of the aqueous species and their diffusion through the water layer to the tissue beneath will be considered. Lastly, cellular structure will be embedded into that tissue and the effect of varying the applied voltage, thickness and reactivity of the water layer on the electric fields within the cellular structure will be studied.

APPJs and plasma medicine are becoming more actively researched as illustrated in Kong *et al*.'s editorial on the preponderance of plasma jets and plasma bullet papers published per annum over the last decade.[12] There is good reason for the interest, the low temperature non-equilibrium APPJ provides therapeutic and sterilizing effects through fluxes of charged and reactive species to surfaces; ion and photon fluxes to cell structure; and intracellular and surface electric field effects to the treated surfaces. As Graves wrote in his 2014 tutorial review, "The use of near-room temperature ('cold') gas discharges at atmospheric pressure for various biomedical applications is now well established, although not well understood."[66] If my work in computationally modeling any aspect of the use of APPJs can be of use to the plasma medicine community, I will consider my efforts worthwhile.

1.6 Path forward

This thesis is organized in the following manner:

In Chapter 2, the computational model used as the basis for the investigations of the subsequent chapters will be discussed. This is intended to be an overarching look at the hydrodynamic model. Specific modifications to the base model will be discussed at the beginning of the applicable chapters.

In Chapter 3, an investigation on the formation of reactive oxygen and nitrogen species by repetitive negatively pulsed helium atmospheric pressure plasma jets propagating into humid air is conducted. This is a parametric study of the effects of varying voltage, flow rate, O_2 fraction and repetition rates on the production of RONS by atmospheric pressure plasma jets.

In Chapter 4, the atmospheric pressure plasma jet will impact a metal or dielectric surface. The importance of the relative permittivity of the targeted material on the discharge dynamics and the behavior of the electric field will be analyzed. The dielectric constants were selected to represent common materials in plasma medicine to include biological tissue, water, metal, and plastic.

In Chapter 5, the atmospheric pressure plasma jet will interact with liquid-covered tissue with an emphasis on the effects of whether the guided ionization wave touches the liquid surface or does not touch the liquid. One pulse will be carried through the impact and spread across the liquid surface. The discharge produced charged and reactive species then solvate or react with the aqueous species for a minutes following treatment.

In Chapter 6, the reactive liquid layer covers cellular structure embedded in tissue and the effect of the electric field produced by the discharge and surface electric field is studied while changing the thickness of the water layer as well as the effect of a second pulse onto a more conductive medium.

Lastly, in Chapter 7, concluding remarks, thoughts on the impact of this research as well as future work will be discussed.

1.7 Figures

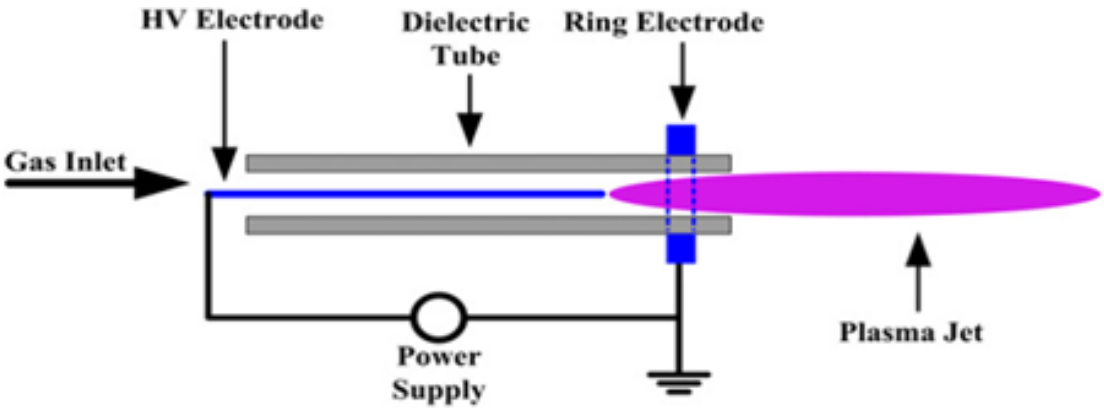

Figure 1.1 Figure of the atmospheric pressure plasma jet selected as the basis for computation domains analyzed in this thesis. The electrode placement is the key variation in this type of plasma jet. The effluent emerges from the dielectric tube forming the guided ionization wave phenomenon of these types of devices.[5]

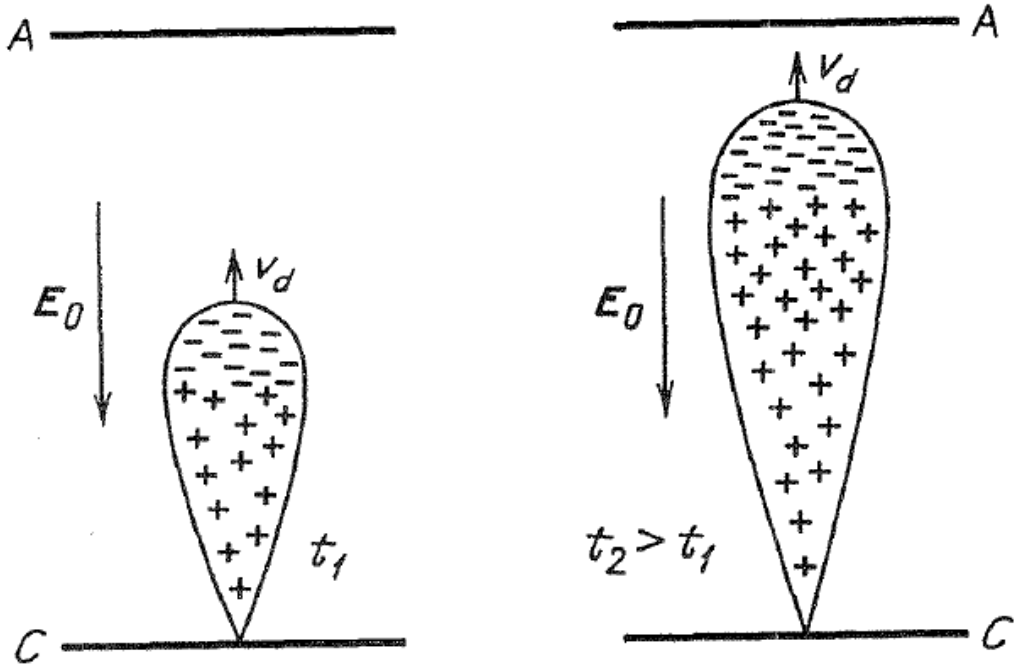

Figure 1.2 Formation of electron avalanche from cathode (C) toward anode (A) at two moments of time. The arrow indicates the direction of the external electric field and v_d is the velocity of the head.[4]

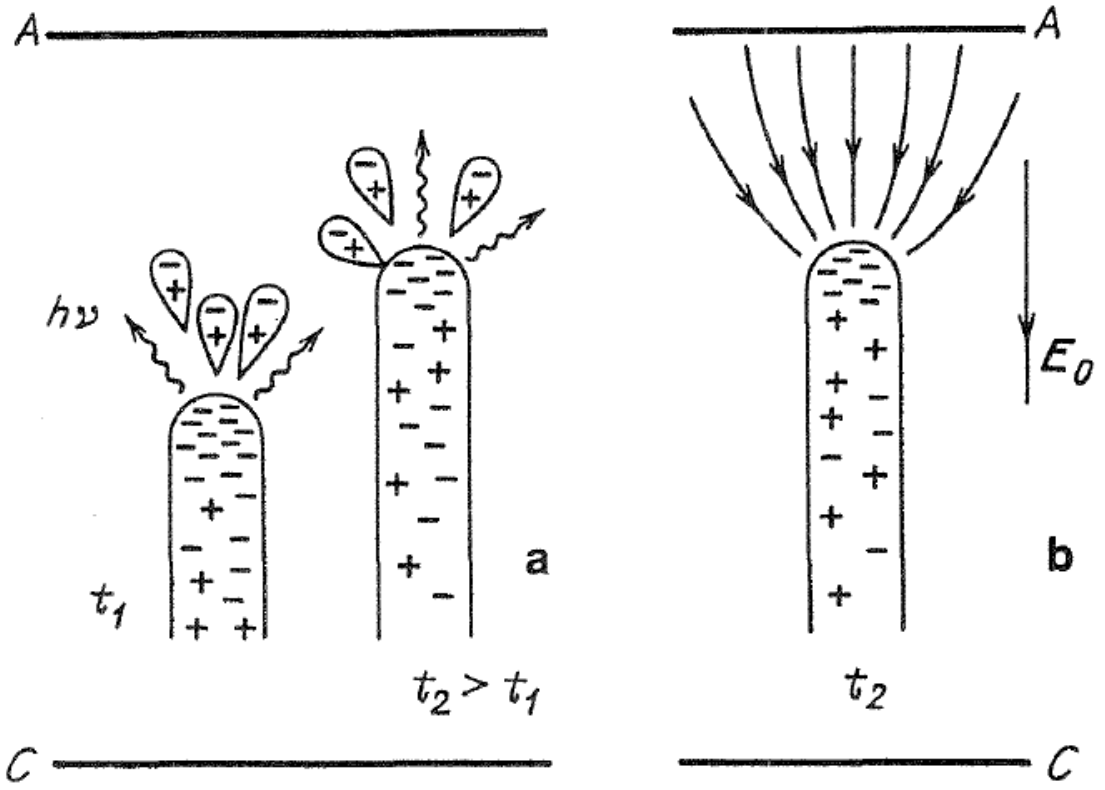

Figure 1.3 Anode-directed streamer propagating from the cathode (C) to the anode (A). (a) the negative particles in the head of the streamer radiating and creating secondary avalanches at two moments in time. (b) the electric field at the head.[4]

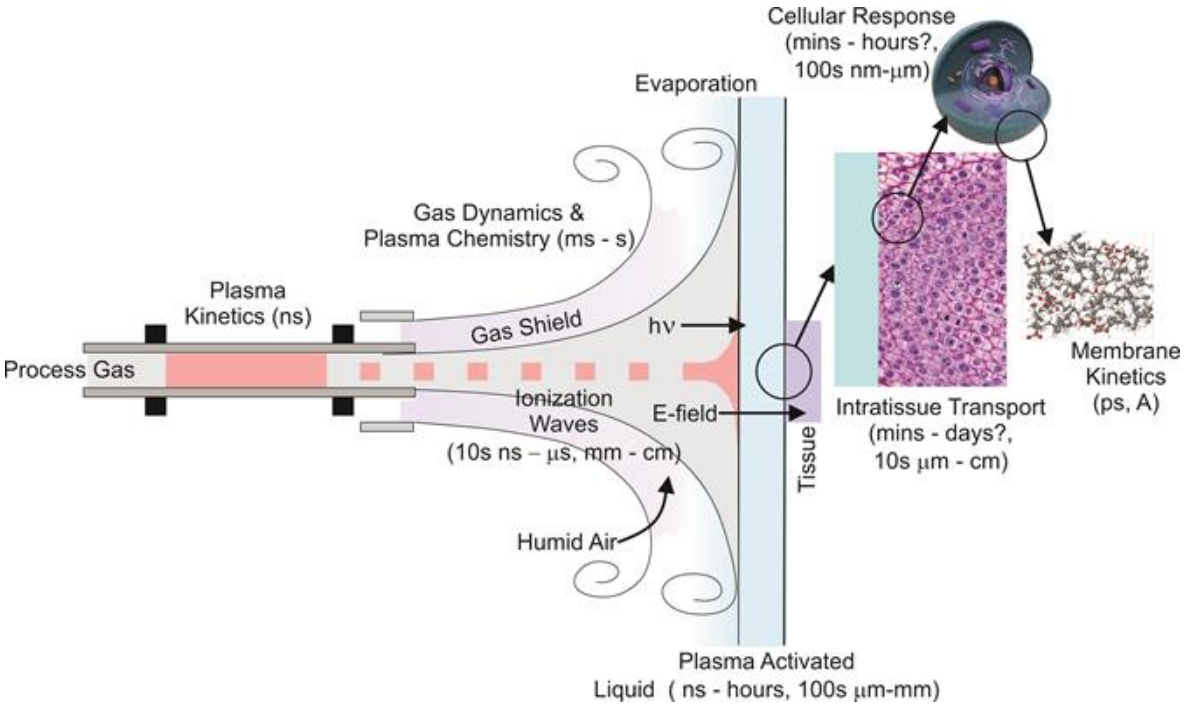

Figure 1.4 Example of atmospheric pressure plasma jet treatment of liquid covered tissue with time and spatial scales indicated. This example uses two ring electrodes to create the discharge and a gas shield to optimize production of RONS.

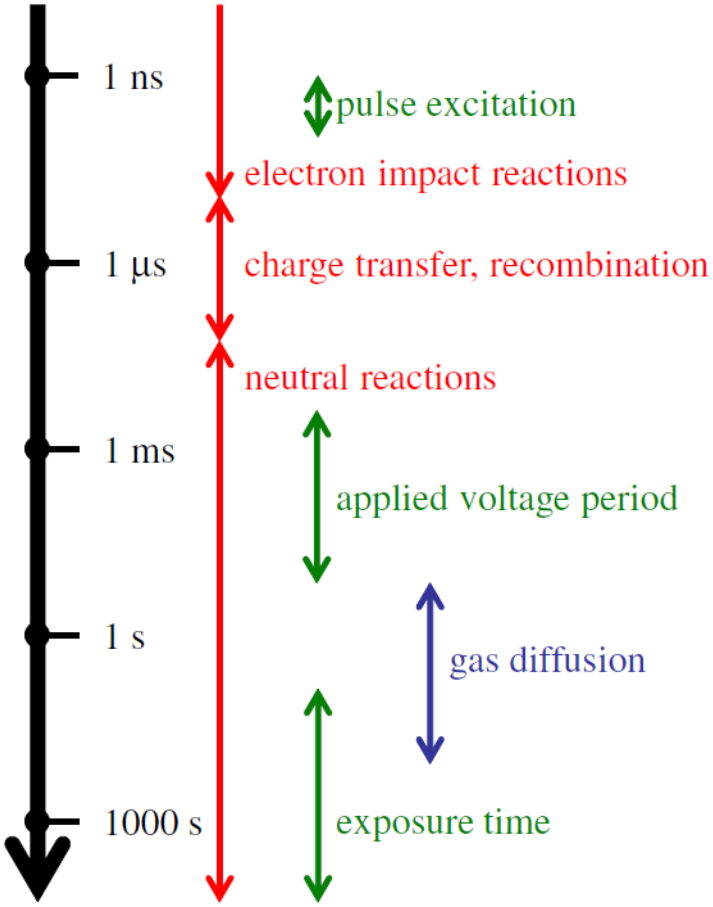

Figure 1.5 Time scales in plasma medicine.[22]

Figure 1.6 Violet Ray Machine (Hochfrequenzstrahlapparat) [23] produced in 1928. Examples of applications are on the left and right frames with the apparatus and example photo in the center frame.[24]

1.8 References

[1] I. Langmuir, "Oscillations in Ionized Gases", Proc. Nat. Acad. Sci. U.S. **14**, 628 (1928).

[2] L. Tonks and I. Langmuir, "Oscillations in Ionized Gases", Phys. Rev. **33**, 195 (1929).

[3] A. Fridman, Plasma Chemistry, Cambridge, 2008.

[4] Y.P. Raizer, Gas Discharge Physics, Springer, 1991.

[5] X. Lu, M. Laroussi, V. Puech, "On atmospheric-pressure non-equilibrium plasma jets and plasma bullets", Plasma Sources Sci. Technol. **21**, 034005 (2012).

[6] A. Schutze, J. Jeong, S. Babayan, J. Park, G. Selwyn and R. Hicks, "The Atmospheric-Pressure Plasma Jet: A Review and Comparison to Other Plasma Sources", Trans. Plasma Sci., **26**, 1685 (1998).

[7] M.G. Kong, G. Kroesen, G. Morfill, T. Nosenko, T. Shimizu, J. van Dijk, and J.L. Zimmerman, "Plasma medicine: an introductory review", New J. Phys. **11**, 115012 (2009).

[8] M. Laroussi, "Low-Temperature Plasmas for Medicine?", Trans. Plasma Sci., **37**, 714 (2009).

[9] M. Laroussi, M. Kong, G. Morfill, and W. Stolz, Plasma Medicine: Applications of Low-Temperature Gas Plasmas in Medicine and Biology, Cambridge, 2012.

[10] M. Keidar, A. Shashurin, O. Volotskova, M. Stepp, P. Srinivasan, A. Sandler, B. Trink, "Cold atmospheric plasma in cancer therapy", Phys. Plasmas **20**, 057101 (2013).

[11] M. Teschke, J. Kedzierski, E.G. Finantu-Dinu, D. Korzec, and J. Engemann, "High-Speed Photographs of a Dielectric Barrier Atmospheric Pressure Plasma Jet", Trans. Plasma Sci. **33**, 310 (2005).

[12] M. G. Kong, B. N. Ganguly, and R. F. Hicks, "Plasma jets and plasma bullets", Plasma Sources Sci. Technol. **21**, 030201 (2012).

[13] W. Tian and M. Kushner, "Atmospheric Pressure Dielectric Barrier Discharges Interacting with Liquid Covered Tissue", J. Phys. D: Appl. Phys. **47**, 165201 (2014).

[14] U. Kogelshatz, "Dielectric-barrier Discharges: Their History, Discharge Physics, and Industrial Applications", Plasma Chem. Plasma Proc. **23**, 1 (2013).

[15] I. Kossyi, A. Kostinsky, A. Matveyev, and V. Silakov, "Kinetic scheme of non-equilibrium discharge in nitrogen-oxygen mixtures", Plasma Sources Sci. Technol. **1**, 207 (1992).

[16] A. Fridman, A. Chirokov, and A. Gutsol, "Non-thermal atmospheric pressure discharges", J. Phys. D: Appl. Phys. **38**, R1 (2004).

[17] X. Lu, Z. Jiang, Q. Xiong, Z. Tang, X. Hu, Y. Pan, "An 11 cm long atmospheric pressure cold plasma plume for applications of plasma medicine", Appl. Phys. Lett. **92**, 081502 (2008).

[18] D.B. Graves, "The emerging role of reactive oxygen and nitrogen species in redox biology and some implications for plasma applications to medicine and biology", J. Phys. D: Appl. Phys. **45**, 263001 (2012).

[19] S. Reuter, H. Tresp, K. Wende, M. Hammer, J. Winter, K. Masur, A. Schmidt-Bleker, and K-D. Weltmann, "From RONS to ROS: Tailoring Plasma Jet Treatment of Skin Cells", Trans. Plasma Sci. **40**, 2986 (2012).

[20] S. Reuter, J. Winter, A. Schmidt-Bleker, H. Tresp, M. Hammer, and K-D. Weltmann, "Controlling the Ambient Air Affected Reactive Species Composition in the Effluent of an Argon Plasma Jet", Trans. Plasma Sci. **40**, 2788 (2012).

[21] R.A. Rhoades, D.R. Bell, Medical Physiology: Principles for Clinical Medicine, Williams & Wilkins, 2012.
[22] Y. Sakiyama, D.B. Graves, H-W. Chang, T. Shimizu, and G. Morfill, "Plasma chemistry model of surface microdischarge in humid air and dynamics of reactive neutral species", J. Phys. D: Appl. Phys. **45**, 425201 (2012).
[23] Bauer, Faulhaber, Kober, and Krapt, "Der Hochfrequenzstrahlapparat Sein Wesen und seine Anwendung", Verlag Dr. H. Stock, 1928.
[24] K.-D. Weltmann, M. Polak, K. Masur, T. von Woedtke, J. Winter, and S. Reuter, "Plasma Processes and Plasma Sources in Medicine", Contrib. Plasma Phys. **52**, 644 (2012).
[25] C.F. Morrison Jr., "Electrosurgical method and apparatus for initiating an electrical discharge in an inert gas flow", 1977.
[26] W.P. Menashi, "Treatment of surfaces", 1968.
[27] M. Laroussi, "Sterilization of Contaminated Matter with an Atmospheric Pressure Plasma" IEEE Trans. Plasma Sci. **24**, 1188 (1996).
[28] A.B. Shekhter, R.K. Kabisov, A.V. Pekshee, N.P. Kozlov, Y.L. Perov, "Experimental and clinical validation of plasmadynamic therapy of wounds with nitric oxide", Bull. Exp. Biol. Med. **126**, 829 (1998).
[29] G. Fridman, G. Friedman, A. Gutsol, A.B. Shekhter, V.N. Vasilets and A. Fridman, "Applied Plasma Medicine", Plasma Process. Polym. **5**, 503 (2008).
[30] M. Laroussi, I. Alexeff, and W. Kang, "Biological Decontamination by Non-Thermal Plasmas", IEEE Trans. Plasma Sci. **28**, 184 (2000).
[31] M. Laroussi, J. P. Richardson, and F. C. Dobbs, "Effects of Non-Equilibrium Atmospheric Pressure Plasmas on the Heterotrophic Pathways of Bacteria and on their Cell Morphology", Appl. Phys. Lett. **81**, 772 (2002).
[32] E. Stoffels, I.E. Kieft, and R.E.J. Sladek, "Superficial treatment of mammalian cells using a plasma needle", J. Phys. D: Appl. Phys. **36**, 2908 (2003).
[33] M. Laroussi and X. Lu, "Room Temperature Atmospheric Pressure Plasma Plume for Biomedical Applications", Appl. Phys. Lett. **87**, 113902 (2005).
[34] M. Laroussi, C. Tendero, X. Lu, S. Alla, W. Hynes, "Inactivation of Bacteria by the Plasma Pencil", Plasma Process. Polym. **3**, 470 (2006).
[35] S. Yonson, S. Coulombe, V. Leveille, and R.L Leask, "Cell treatment and surface functionalization using a miniature atmospheric pressure glow discharge plasma torch", J. Phys. D: Appl. Phys. **39**, 3508 (2006).
[36] G. Fridman, A. Shereshevsky, M.M. Jost, A.D. Brooks, A.A. Fridman, A.F. Gutsol, V.N. Vasilets, G. Friedman, "Floating electrode dielectric barrier discharge plasma in air promoting apoptotic behavior in melanoma skin cancer cell lines", Plasma Chem. Plasma Process. **27**, 163 (2007).
[37] M. Vandamme, E. Robert, S. Pesnel, E. Barbosa, S. Dozias, J. Sobilo, S. Lerondel, A. Le Pape, and J-M. Pouvesle, "Antitumor Effect of Plasma Treatment on U87 Glioma Xenografts: Preliminary Results", Plasma Process. Polym. **7**, 264 (2010).
[38] M. Keidar, R. Walk, A. Shashurin, P. Srinivasan, A. Sandler, S. Dasgupta, R. Ravi, R. Guerrero-Preston, and B. Trink, "Cold plasma selectivity and the possibility of a paradigm shift in cancer therapy", Brit. J. Cancer **105**, 1295, (2011).
[39] M.J. Traylor, M.J. Pavlovich, S. Karim, P. Hait, Y. Sakiyama, D.S. Clark, and D.B. Graves, "Long-term antibacterial efficacy of air plasma-activated water", J. Phys. D: Appl. Phys. **44**, 472001 (2011).

[40] K. Schoenbach, J. Kolb, S. Xiao, S. Katsuki, T. Minamitani, and R. Joshi, "Electrical breakdown of water in microgaps", Plasma Sources Sci. Technol. **17**, 024010 (2008).
[41] C. A. J. van Gils, S. Hofmann, B. K. H. L Boekema, R. Brandenburg, and P. J. Bruggeman, "Mechanisms of bacterial inactivation in the liquid phase induced by a remote RF cold atmospheric pressure plasma jet", J. Phys. D: Appl. Phys. **46,** 175203 (2013).
[42] P. Lukes, E. Dolezalova, I. Sisrova, M. Clupek, "Aqueous-Phase Chemistry and Bactericidal Effects from an Air Discharge Plasma in Contact with Water: Evidence for the Formation of Peroxynitrite through a Pseudo-Second-Order Post-Discharge Reaction of H_2O_2 and HNO_2", Plasma Sources Sci. Technol. **23**, 015019 (2014).
[43] H. Tresp, M. U. Hammer, J. Winter, K-D. Weltmann, and S. Reuter, "Quantitative detection of plasma-generated radicals in liquids by electron paramagnetic resonance spectroscopy", J. Phys. D: Appl. Phys. **46,** 435401 (2013).
[44] W.J. Brok, M.D. Bowden, J. van Dijk, J.J.A.M van der Mullen, and G.M.W. Kroesen, "Numerical description of discharge characteristics of the plasma needle", J. Appl. Phys. **98**, 013302 (2005).
[45] Y. Sakiyama and D.B. Graves, "Corona-glow transition in the atmospheric pressure RF-excited plasma needle", J. Phys. D: Appl. Phys. **39**, 3644 (2006).
[46] Y. Sakiyama and D.B. Graves, "Finite element analysis of an atmospheric pressure RF-excited plasma needle", J. Phys. D: Appl. Phys. **39**, 3451 (2006).
[47] W. Van Gaens and A. Bogaerts, "Kinetic modelling for an atmospheric pressure argon plasma jet in humid air", J. Phys. D: Appl. Phys. **46**, 275201 (2013).
[48] S.K. Dhali and P.F. Williams," Numerical simulation of streamer propagation in nitrogen at atmospheric pressure", Phys. Rev. A, **31**, 1219 (1985).
[49] M.J. Kushner, R.D. Milroy, and W.D. Kimura, "A Laser Triggered Spark Gap Model", J. Appl. Phys. **58**, 2988 (1985).
[50] W.D. Kimura, M.J. Kushner, E.A. Crawford, and S.R. Byron, "Laser Interferometric Measurements of a Laser Preionization Triggered Spark Column", IEEE Trans. Plasma Sci. **PS-14**, 246, (1986).
[51] P. A. Vitello, B.M. Penetrante, and J.N. Bardsley, "Simulation of negative-streamer dynamics in nitrogen", Phys. Rev. E, **49**, 5574 (1994).
[52] A.A. Kulikovsky, The structure of streamers in N_2. I. fast method of space-charge dominated plasma", J. Phys. D: Appl. Phys. **27**, 2556 (1994).
[53] A.A. Kulikovsky, The structure of streamers in N_2. II. Two-dimensional simulation", J. Phys. D: Appl. Phys. **27**, 2564 (1994).
[54] G.V Naidis, "On streamer interaction in a pulsed positive corona discharge", J. Phys. D: Appl. Phys. **29**, 779 (1996).
[55] N. Yu. Babaeva and G.V. Naidis, "Two-dimensional modelling of positive streamer dynamics in non-uniform electric fields in air", J. Phys. D: Appl. Phys. **29**, 2423 (1996).
[56] G.V. Naidis, "Modelling of plasma chemical processes in pulsed corona discharges", J. Phys. D: Appl. Phys. **30**, 1214 (1997).
[57] U. Ebert and W. van Saarloos, "Universal Algebraic Relaxation of Fronts Propagating into an Unstable State and Implications for Moving Boundary Approximations", Phys. Rev. Lett. **80**, 1650 (1998).
[58] M. Arrayas, U. Ebert, and W. Hundsdorfer, "Spontaneous Branching of Anode-Directed Streamers between Planar Electrodes", Phys. Rev. Lett. **88**, 174502 (2002).

[59] G.V. Naidis, "Modelling of streamer propagation in atmospheric-pressure helium plasma jets", J. Phys. D: Appl. Phys. **43**, 402001 (2010).
[60] G.V. Naidis, "Modelling of plasma bullet propagation along a helium jet in ambient air", J. Phys. D: Appl. Phys. **44**, 215203 (2011).
[61] D. Breden, K. Miki, and L.L. Raja, "Self-consistent two-dimensional model of cold atmospheric-pressure plasma jets/bullets", Plasma Sources Sci. Technol. **21**, 034011 (2012).
[62] J-P. Boeuf, L.L. Yang, and L.C. Pitchford, "Dynamics of a guided streamer ('plasma bullet') in a helium jet in air at atmospheric pressure", J. Phys. D: Appl. Phys. **46**, 015201 (2013).
[63] D. Breden and L.L. Raja, "Computational study of the interaction of cold atmospheric helium plasma jets with surfaces", Plasma Sources Sci. Technol. **23**, 065020 (2014).
[64] E.C. Neyts, M. Yusupov, C.C. Verlackt, and A. Bogaerts, "Computer simulations of plasma-biomolecule and plasma-tissue interactions for a better insight in plasma medicine", J. Phys. D: Appl. Phys. **47**, 293001 (2014).
[65] C. Chen, D.X. Liu, Z.C. Liu, A.J. Yang, H.L. Chen, G. Shama, M.G. Kong, "A Model of Plasma-Biofilm and Plasma-Tissue Interactions at Ambient Pressure", Plasma Chem. Plasma Process. **34**, 403 (2014).
[66] D.B. Graves, "Low temperature plasma biomedicine: A tutorial review", Phys. of Plasmas **21**, 080901 (2014).

Chapter 2 Description of the Model

2.1 Introduction

The 2-D cylindrically symmetric, plasma hydrodynamics model utilized in this investigation, *nonPDPSIM*, was initially developed by Dr. Shahid Rauf and Prof. Mark J. Kushner to simulate plasma display panel (PDP) cells [1] and has since been used for many different plasma analyses and is described in detail in Refs [2,3]. A block diagram shown in Fig. 2.1 highlights the process and computational techniques used.[4] This chapter will discuss the input files and mesh generator shown at the top of Fig. 2.1 and the corresponding source code (*nonPDPSIM*) in the following sections. The namelist file is the primary input file that calls the respective modules and sets the initial and computational conditions. In the next section, *nonPDPSIM,* as used in this dissertation, is discussed in depth. In Sec. 2.3, the chemistry file as well as the path to critical near-terminal species is reviewed. Finally, in Sec. 2.4, the production of the geometry file as well as a mesh-convergence test is discussed.

These three input files are read into the *nonPDPSIM* source code and the simulation is conducted as shown in the block diagram. For use in this dissertation, *nonPDPSIM* consists of three major modules – the plasma transport module, the radiation transport module and the fluid transport module. In the plasma transport module, Poisson's equation and continuity equations for all charged species (in the volume and on surfaces) are integrated in time using a fully implicit, 2^{nd} order, Newton-iteration technique.[3] Spatial derivatives and divergence operators are expressed in fully conservative finite-volume form. Each time step is then followed by an

implicit update of the electron energy equation for electron temperature, neutral species continuity equations and radiation transport. Transport coefficients and rate coefficients for electrons as a function of electron temperature are obtained from solutions of the stationary Boltzmann's for the electron energy distribution. These tabulated coefficients which are interpolated during execution of the model are updated on sub-nanosecond time scales to reflect changing species and mole fractions.

In the fluid module, a modified form of the Navier-Stokes equations (continuity, momentum, energy) are solved to produce the advective flow field while including body forces (e.g., momentum transfer from charged particles) and heat sources (e.g., Joule heating and change in enthalpy due to reactions) produced in the plasma transport module.[5] Since the gas constituents have large differences in atomic or molecular mass, the mass continuity equation is replaced by a number-density continuity equation and a fourth equation for the average molecular weight. These equations are simultaneously and implicitly solved using numerically derived Jacobian elements on the same unstructured mesh as the plasma calculation. The individual continuity equations for all species are simultaneously integrated using the advective flow field as a check for the average molecular weight

2.2 Overview of the model

The model, *nonPDPSIM*, uses time-slicing techniques and an unstructured triangular mesh to bridge the sub-picosecond time steps necessary to resolve the discharge dynamics on tens of micron spatial scales in the capillary tube of an APPJ during the discharge pulse, to the many microsecond timesteps over mm spatial scale up to many ms of elapsed time in the plume

between and over many discharge pulses. In the investigation of atmospheric pressure plasma jets, a series of modules are sequentially operated.

In the plasma transport module, Poisson's equation and continuity equations for charged species are solved. The equation solved is

$$\nabla(\varepsilon \nabla\Phi) = -(\sum_j q_j N_j + \rho_M), \tag{2.1}$$

where ε is the permittivity, Φ is the electrical potential, q_j is the elementary charge, N_j is the species number density, and ρ_M is the charge on surfaces and in materials. Simultaneous to solving Poisson's equation, the density of charged particles and materials charges are solved.

$$\frac{\partial N_j}{\partial t} = -\nabla\cdot\vec{\Gamma}_j + S_j + \left[\sum_m -\nabla\cdot\vec{\Gamma}_m\gamma_m + \sum_k -\nabla\cdot\phi_m\gamma_m\right]_b, \tag{2.2}$$

where the charged particle flux, Γ, is formulated using the method of Scharfetter and Gummel to discretize the drift-diffusion equation.[6] The source due to collisions is S_j. The sums in brackets apply only to electrons on the boundary of the plasmas for secondary electron emission by ions and excited species (first sum) and by photons having flux ϕ and secondary emission coefficient γ. The material charge density is solved using,

$$\frac{\partial\rho_M}{\partial t} = \left[\sum_j q_j\left(-\nabla\cdot\vec{\Gamma}_j(1+\gamma_j)\right) + \sum_k \phi_k\gamma_k\right] - \nabla\cdot(\sigma(-\nabla\Phi)), \tag{2.3}$$

where σ is conductivity of solid materials. The sums in brackets apply only to points on the surface of the material.

Eqs. 2.1-2.3 are solved implicitly using a Newton-Raphson iteration technique.[7] Jacobian elements are generated for the incremental change in variable *i* at mesh point *j* due to a change in variable *k* at mesh point *m*, $\frac{\partial N_{ij}}{\partial M_{km}}$. The mesh points for which the Jacobian elements

are produced are the local point and nearest neighbors. The Jacobian element is produced by perturbing the value of the dependent variable by a small amount. For example, the Jacobian element for the change in ion density, N_{ij}, at time t due to a perturbation of $\Delta\Phi$ in potential, Φ_m, during a time step of duration Δt is

$$\frac{\partial N_{ij}}{\partial \Phi_m}(t) = -\frac{\Delta t}{\Delta \Phi}\left(\nabla \cdot \left(\vec{\Gamma}_j\left(\Phi_m(t) + \Delta\Phi\right) - \vec{\Gamma}_j\left(\Phi_m(t)\right)\right)\right). \tag{2.4}$$

The divergence operators are expressed in finite volume format,

$$\frac{\partial N_{ij}}{\partial t} = -\nabla \cdot \vec{\Gamma}_{ij} = -\sum_m \frac{\Gamma_{ijm} A_{jm}}{V_j}, \tag{2.5}$$

where Γ_{ijm} is the flux from nearest neighbor cell m arriving into cell j, A_{jm} is the area of the face between cells j and m, and V_j is the volume of cell j. The discrete form of the partial differential equation then solved is

$$N_{ij}(t+\Delta t) = N_{ij}(t) + \Delta t\left(\sum_m \frac{\Gamma_{ijm}\left(N_j(t+\Delta t), \Phi(t)\right) A_{jm}}{V_j} + S_j(t) + \frac{\partial S_{ej}}{\partial n_e}\left(n_e(t+\Delta t) - n_e(t)\right)\right) + \sum_m \left(\frac{\partial N_{ij}}{\partial \Phi_m}(t)\left(\Phi_m(t+\Delta t) - \Phi_m(t)\right) + \frac{\partial N_{ij}}{\partial N_{im}}(t)\left(N_{im}(t+\Delta t) - N_{im}(t)\right)\right). \tag{2.6}$$

Source functions are evaluated at time t except for those involving electron impact processes which are evaluated at time $(t+\Delta t)$. Similar expressions are generated for potential and charge density. The function that is minimized during the k^{th} Newton-Raphson iteration is

$$F_{ij} = \frac{\left\lfloor N_{ij}(t+\Delta t)\right\rfloor_k - \left\lfloor N_{ij}(t+\Delta t)\right\rfloor_{k-1}}{N_{0j}}, \tag{2.7}$$

where N_{0j} is a normalization value chosen so that all normalized variables have values close to unity. The values at $(t+\Delta t)$ are obtained by solving the combined sparse matrix using a two

solver-preconditioner combination based on BiCG/ILUT. After each Newton-Raphson iteration, the Jacobian elements are re-evaluated with current values of variables.

Following the update of the electric potential and charge particle densities, the electron temperature is updated using

$$\frac{\partial}{\partial t}\left(\frac{3}{2}n_e k_B T_e\right) = S(T_e) - L(T_e) - \nabla\cdot\left(\frac{5}{2}\Gamma_e k_B T_e - \kappa(T_e)\cdot\nabla T_e\right), \tag{2.8}$$

where T_e is the electron temperature, n_e is the electron density, k_B is Boltzmann's constant, κ is the thermal conductivity, S is the source of power, in this case, Joule heating from the electric field, and L represents collisional losses or gains in energy. Eq. 2.8 is implicitly solved using the method of successive-over-relaxation (SOR). The form solved is

$$\begin{aligned} T_{ej}(t+\Delta t) = T_{ej}(t) + \frac{2\Delta t}{3k_B n_{ej}(t+\Delta t)}[& -\frac{\partial n_{ej}(t+\Delta t)}{\partial t}k_B T_{ej}(t+\Delta t) + \vec{\Gamma}_{ej}\cdot\vec{E}_j \\ & + \sum_i n_{ej}(t+\Delta t)N_{ij}\Delta\varepsilon_i\left(k_{ij}(T_{ej}(t)) + + \frac{\partial k_{ij}(T_{ej}(t))}{\partial T_e}(T_{ej}(t+\Delta t) - T_{ej}(t))\right) \\ & + \sum_m \frac{A_{jm}}{V_j}\left(\frac{5}{2}\Gamma_{ejm}(t+\Delta t)T_{ejm}(t+\Delta t) + \kappa(t+\Delta t)(T_{em}(t+\Delta t) - T_{ej}(t+\Delta t))\right)] \end{aligned}, \tag{2.9}$$

where $k_{ij}(T_e)$ is the rate coefficient for electron impact process i at mesh point j with change in energy $\Delta\varepsilon_i$ and the collision partner has density N_i. T_{ejm} indicates that the upwind value of the electron temperature is used – that is, the donor-cell method is employed. During the SOR iterations (typically hundreds of iterations are required per time step), the thermal conductivities and rate coefficients are updated every 10-20 iterations. Due to the computational expense of updating the rate coefficients on a more frequent basis, a correction to the rate coefficient for changes in T_e is accounted for by the Jacobian element $\frac{\partial k_{ij}(T_{ej}(t))}{\partial T_e}$. Convergence is determined

by values of T_e only in those cells that have an electron density greater than a minimum value, typically 10^4-10^5 cm^{-3}.

The desired value of electric field used in Eq. 2.9 is at the mesh point *j*. Since the electric potential is solved at the mesh points, the electric fields are only directly available along the chords between mesh points. The electric fields components at *j* are obtained by interpolating the values of electric potentials from the nearest neighbor mesh points to the coordinate axes above and below location *j*. Electric fields are then obtained by linear finite difference of the interpolated values. A similar technique is used to obtain gradients in number densities at the mesh point *j*.

Electron rate and transport coefficients are obtained as a function of T_e by constructing a table through solving the stationary Boltzmann's equation over a range of E/N (electric field/gas number density). The assumption for the majority of plasma nodes within the computational domain is that the local field approximation is valid. Using this approximation, the Boltzmann equation is solved for the local solution in a separate module using two-term spherical harmonic expansion for a table typically consisting of 70 entries over a range of E/N from 0.1 Td to 1000 Td (1 Td = 10^{-17} V-cm^2). The entries in the table are recorded as log values and then linearly interpolated. The tables are updated during execution of the model as mole fractions of collision partners change. Different tables are constructed for different parts of the mesh that may have significantly different gas composition. When the electric field gradient is rapidly changing (such as at the cathode fall near the pin electrode), the approximation of a local field is not valid. In this situation, the method described earlier using Eq. 2.8 is used to solve the average energy and electron temperature.

Individual neutral species diffuse within the single fluid and react with surfaces. Their densities are updated using

$$\frac{\partial N_i}{\partial t} = -\nabla \cdot (N_i \vec{v}) - \nabla \cdot \left(-D_i \nabla N_i\right) + S_i + \left[\sum_k - g_{ki} \nabla \cdot \Gamma_k\right]_{ms}, \tag{2.10}$$

where, $\vec{v}$ is the advective fluid averaged velocity, described below, D_i is the mixture dependent diffusivity, and S_i is the source or sink of that neutral species by collisions. The term in brackets accounts for the flux of species k reacting on material surfaces to produce species i with probability g_{ik}. Eq. 2.10 is also solved implicitly using the method of successive over relaxation.

$$\begin{aligned} N_{ij}(t+\Delta t) = N_{ij}(t) + \Delta t \Bigg[& \sum_m \frac{A_{jm}}{V_j} \left(D_{ijm}\left(N_{im}(t+\Delta t) - N_{ij}(t+\Delta t)\right) + v_{jm} N_{ijm}(t+\Delta t)\right) \\ & + S_i(t) + \left[\sum_{m,k} - \frac{A_{jm}}{V_j} g_{ki} \Gamma_k (t+\Delta t)\right]_m \Bigg] \end{aligned} . \tag{2.11}$$

Radiation transport and photoionization are addressed using a Green's function approach. The photoionization source for species i at location $\vec{r}_j$ is due to the integral of vacuum ultra-violet (VUV) photon emission at all other locations $\vec{r}_l$ is

$$S_{Pi}(\vec{r}_j) = N_i(\vec{r}_j) \cdot \sum_k \sigma_{ik} A_k \int N_k(\vec{r}_l\,') G_{ilk}(\vec{r}_l\,', \vec{r}_j) d^3 \vec{r}_l\,', \tag{2.12}$$

where σ_{ik} is the photoionization cross section of the species i by the photon generated by species k, A_k is the Einstein A coefficient for the transition. G_{kil} is the Greens function that provides the relative surviving flux of the photon emitted at $\vec{r}_l$ that survives to reach $\vec{r}_j$.

$$G_{kil}(\vec{r}_i, \vec{r}_l) = \frac{\exp\left(-\int_{\vec{r}_l}^{\vec{r}_i} \sum_n \sigma_{kn} N_n(\vec{r}_p\,') d\vec{r}_p\,'\right)}{4\pi \left|\vec{r}_i\,' - \vec{r}_l\right|^2}, \tag{2.13}$$

where the integral in the exponent accounts for absorption by any process of photon k by species N_n with cross section σ_{kn}. The photoionization processes used in the model for all numerical simulations conducted in support of this dissertation include the photon producing decay of the excited Helium dimer $He_2^* \rightarrow$ He + He + hν and the subsequent ionization of the oxygen molecule O_2 + hν $\rightarrow$ O_2^+ + e. In Chapter 5 and 6, photoionization and photo-dissociation of H_2O_{aq} in the liquid phase by N_2^{**} (the sum of $N_2(C^3\Pi)$ and higher states) are included. (The subscript $_{aq}$ denotes aqueous or in liquid species.)

Generating G_{kil} in the unstructured mesh in large part consists of evaluating the integral within the exponent. The integral is evaluated in the following manner. A chord is drawn between the emitting node l from which the photon originates and the absorbing node j where the photoionization occurs. The emitting node l is the *base* node. The two nodes of the nearest neighbors to l on either side of the chord are determined and the intersection of the line between the neighbors and the chord is determined. If the intersection is inside an absorbing material, then the photon is blocked and G_{kil} =0. If the intersection is inside the plasma the density of N_n is interpolated to the intersection and the integral incremented based on the distance from the base node. The nearest neighbor of the base node l to the intersection is then the new base node, and the process is repeated until node j is reached. Generating the Green's function is computationally expensive and so G_{kil} is not recomputed unless the density of absorbers significantly changes.

Using unsteady, compressible algorithms, *nonPDPSIM* updates the neutral fluid mass, momentum and energy equations using time slicing between the plasma modules using a fully implicit, sparse matrix technique.[2] Due to the significant differences in mass density resulting

from the He jet emanating into air, the traditional Navier-Stokes like equations are modified in the following manner. The continuity equations are

$$\frac{\partial N_t}{\partial t} = -\nabla \cdot (N_t \vec{v} + \sum_{k,i} \frac{f_{ki}}{A_k}), \tag{2.14}$$

$$\frac{\partial N_t M_t}{\partial t} = -\nabla \cdot (\sum_i m_i \Gamma_i N_i + \sum_{k,i} \frac{m_i f_{ki}}{A_k}), \tag{2.15}$$

where N_t is the total number density of the gas, $\vec{v}$ is the advective velocity and the sum in Eq. 2.14 is over gas inlets k have face area A_k where species i has an inlet flow rate f_{ki}. Eq. 2.15, provides the average molecular weight M_t where m_i is the molecular weight of species i having flux Γ_i and density N_i.

The momentum equation is then

$$\frac{\partial (N_t M_t \vec{v})}{\partial t} = -\nabla P - \nabla \cdot (M_t N_t \vec{v}\vec{v}) - \nabla \cdot \bar{\tau} + \sum_i q_i N_i \vec{E} + N_t M_t g \frac{\vec{v} \cdot \hat{n}}{|\vec{v}|} \tag{2.16}$$

where $\bar{\tau}$ is the viscous stress tensor, q_i is the elementary charge, g is the gravitational constant, $\hat{n}$ is the normal in the direction of gravity, $\vec{E}$ is the electric field and N_i is the number density of species i. Ideal gas properties are assumed (pressure $P = N_t k_B T$). The term with the electric field represents the net momentum transfer between charged particles accelerated by the electric field and the neutral gas.

In the conservation of energy equation,

$$\frac{\partial (N_t c_v T)}{\partial t} = -\nabla (-\kappa \nabla T + \rho \vec{v} c_v T) + P \nabla \cdot \vec{v} - \sum_m R_m \Delta H_m + \sum_i \vec{j}_i \cdot \vec{E} \tag{2.17}$$

where c_v is the specific heat, κ is the thermal conductivity, T is the gas temperature, R_m is the rate of reaction m, ΔH_m is the change in enthalpy for reaction m, and $\vec{j}_i \cdot \vec{E}$ is the Joule heating term where the sum is over ions having current density $\vec{j}_i$. Assuming no slip conditions at

atmospheric pressure, the boundary conditions are that the temperature matches the wall temperature. Although not used here, there is also the option to retain the thermal conduction term of Eq. 2.17 inside materials and compute *T* throughout materials. In this case, an additional heating term is added at surfaces for the change in enthalpy due to the recombination of ions and other surface chemistry. In this case the temperature is held constant at the periphery of the mesh.

Eqs. 2.14-2.17 are implicitly solved using sparse matrix techniques in a similar manner as for the charged particle transport equations. For example, the solution method for the axial component of Eq. 2.16 will be discussed. With $\rho_t = N_t M_t \quad p_z = N_t M_t v_z$, $\Delta M = M(t+\Delta t) - M(t)$, M any quantity, and $\varepsilon = N_t c_v T$, we solve for component p_z at mesh point j having neighbor nodes m in the following equation,

$$
\begin{aligned}
p_{zj}(t+\Delta t) = p_{zj}(t) + [& -\frac{\partial}{\partial z}\left(P(t)\Delta t \cdot + \left(\frac{\partial P}{\partial \rho_t}(t)\right)\Delta\rho_t + \left(\frac{\partial P}{\partial T}(t)\right)\Delta T \right) + \\
& \sum_m \frac{A_{jm}}{V_j} \left(\begin{array}{l} -p_{zj}(t+\Delta t)\delta_{jm}\left(\left(\vec{v}_j(t)\Delta t + \left(\frac{\partial \vec{v}_j}{\partial \rho_t}(t)\right)\Delta\rho_{tj} + \left(\frac{\partial \vec{v}_j}{\partial T}(t)\right)\Delta T_j \right) \cdot \hat{n}_{jm} \right) \\ +p_{zm}(t+\Delta t)\delta_{mj}\left(\left(\vec{v}_m(t)\Delta t + \left(\frac{\partial \vec{v}_m}{\partial \rho_t}(t)\right)\Delta\rho_{tm} + \left(\frac{\partial \vec{v}_m}{\partial T}(t)\right)\Delta T_m \right) \cdot \hat{n}_{mj} \right) \end{array} \right) \\
& -\left(\nabla \cdot \left(\bar{\tau}\Delta t + \left(\frac{\partial \bar{\tau}}{\partial \rho_t}(t)\right)\Delta\rho_t + \left(\frac{\partial \bar{\tau}}{\partial T}(t)\right)\Delta T \right) \cdot \right)_z + \sum_i q_i N_i \left(\vec{E}(t)\cdot \hat{z}\right) + N_t M_t g\left(\hat{z}\cdot\hat{n}\right)
\end{aligned}
\qquad (2.18)
$$

where $\hat{n}_{jm}$ is the unit vector pointing along the chord from *j* to *m*. In the divergence operator having the sum over nearest neighbors, the donor cell method is used. The coefficient δ_{jm} is unity if $v_{\tilde{m}} \cdot \hat{n}_{jm}$ is positive and zero otherwise. As in the transport equations for charge, spatial gradients are performed by interpolating nearest neighbor values to the coordinate axis above and below the mesh point, and then differentiate the interpolated values.

Due to the unstructured nature of the mesh, densities, velocities (momenta) and temperatures are all directly computed at the mesh points. (In structured meshes, it is more common to compute momenta along the chord between mesh points.) The inlet boundary conditions on flow consist of specifying the fluxes perpendicular to the face of the gas nozzles and their average molecular weight is based on the mole fractions and molecular weights of the inlet gases. The outlet boundary condition is a specified pressure on the face of the pump ports and this pressure is directly incorporated into Eq. 2.16. A check is made on the normal velocity into the pump port and this velocity is required to be positive.

Modifications to the model (geometric and computational) will be introduced at the beginning of each subsequent chapter with the differences highlighted. All APPJ geometries were based primarily on the dimensions of the kINPen developed by the INP in Greifswald [9,10] and have helium seeded with 0.2% oxygen fraction into ambient conditions ($N_2/O_2/H_2O$ =79.5/20/0.5). The geometry used in this investigation for the plasma jet is a cylindrical tube with a diameter of 1.6 mm and walls that are 0.4 mm thick. The tip of the coaxial electrode, 0.25 mm in diameter, is 3.5 mm from the end of the tube, as shown in Fig. 2.1. In this configuration, there is an axial component of the electric field that better enables the plasma to intersect with the liquid.[11,12] This configuration differs from those that have an electric field that is dominantly perpendicular to the gas flow and which produces a plume that is dominated by neutral reactive species.[13]

2.3 Overview of chemistry input

The reaction mechanism used for the majority of the computational investigations conducted in this thesis includes over 50 species and more than 750 reactions and is shown in

Appendix I. The full reaction mechanism contains electron impact processes, ion-ion neutralization, ion-molecule reactions, Penning ionization, quenching, three-body neutral recombination, and neutral chemistry and was enhanced after reviewing several recent investigations.[14-20] In lieu of discussing each reaction, the reaction mechanism leading to a selected subsect of reactive oxygen and nitrogen species (RONS) will be emphasized. The primary paths to these RONS are highlighted in Table 2.1.

The first path is to ozone, O_3, and starts with the production of O atoms from electron dissociative excitation and dissociative attachment of O_2 (R1-R3) within the active plasma plume, with small contributions from dissociative ionization. Three body collisions of O and O_2 then produce O_3 (R8), which is slow in the active plasma inside the tube due to the low mole fraction of O_2. Other direct sources of O_3 in the active plasma include electron detachment reactions of O_2^- and O^- (R6-R7). In the effluent, the primary source of O atoms is the dissociative quenching of N_2^* by O_2 (R5) that forms two O atoms. The newly formed O atoms react with the increasing mole fraction of O_2 due to diffusion and mixing with the ambient. In the absence of organic molecules, O_3 is a fairly stable species. Ozone is primarily consumed by reactions with excited nitrogen, NO, and NO_2 (R24, R27, R29, R33, R39) to form NO and higher level N_xO_y.

Another important RONS formed by the plasma jet is hydrogen peroxide, H_2O_2. In the absence of hydrogen containing species in the gas feed, the path to H_2O_2 originates with the humidity in the air. The water vapor diffusing into the active plasma plume undergoes dissociative excitation and attachment to produce the hydroxyl radical, OH (R9, R10). Another source of OH is the ion-ion neutralization of O_2^- and H_2O^+ (R12) which occurs in the near effluent shortly after the ionization wave propagates. The three-body reaction of OH radicals

then forms H_2O_2 (R13). In the absence of organic molecules, H_2O_2 is also fairly stable. Most destruction mechanisms of H_2O_2 require higher temperatures than encountered in plasma jets.

The path to nitric oxide, NO, starts with electronic excitation of the N_2 to form N_2^* (the sum of $N_2(A^3\Sigma)$ and $N_2(B^3\Pi)$ in this mechanism) and N_2^{**} (the sum of $N_2(C^3\Pi)$ and higher states) (R14, R15). These excited states then react with O atoms and O_3 to form NO (R25-29). Additional routes to NO first include the dissociative excitation of N_2 (R16) or the rapid ion-ion neutralization of O_2^- and N_2^+ (R17) to form N atoms. Subsequent reactions with O, O_2, $O_2(^1\Delta)$, $O_2(^1\Sigma)$, O_3 and OH form NO (R18-23). Nitric oxide is the primary source for higher level oxides of nitrogen (N_xO_y) (R30-44). The nitric oxide acids, HNO_x, form primarily from the reaction of NO or N_xO_y with OH in a three-body collision (R49, R51, R53).

2.4 Overview of geometry input

The unstructured triangular mesh was created using the software Sky/Mesh2 developed by SkyBlue systems and is out of production. This is a mesh generator that initially creates the computational model geometry from three user-generated input files that define the overall geometric parameters, edge values, and connection of lines. Once the computational domain is formed, the software reads in a refinement file that creates the overall mesh as well as refinement zones that form finer regions for user-specified zones. These refinement zones are used to create more computational nodes in regions that require a finer mesh such as near the pin electrode in the region the plasma is formed. These zones are also used to buffer areas requiring fine mesh to those that can get by with coarse mesh without dramatic cell size changes. Additionally, this software packet allows for the definition of faces, edges, and vertices which are then translated into “materials” in the computation through the use of the namelist file. The resulting

specification of dielectrics, metals, nozzles, pumps, plasma (air) and set the boundary conditions at the interface of the various materials. An example of a computational domain is shown in Fig. 2.2.

In an effort to characterize the mesh dependence of the flow field, the global refinement spacing specified in the refinement input file was modified from the pre-determined "best" of 0.05 cm. This spacing was used as a default for the various regions specified throughout the computational model. Subsequent zone spacing was then based off of the default spacing (i.e. in the air zone the additional refinement used was "spacing*0.4" for a desired mesh size of 0.02 cm). Additional refinements, (i.e. near the pin electrode but within the plasma zone) were specified on top of those for the overall zone. In the pin electrode refinement example, the spacing was multiplied by 0.075 for a mesh size of 37.5 μm.

By only changing the default spacing from 0.05 cm, the effect of the mesh could be determined. The default spacing was compared to 0.045 cm, 0.0475 cm, 0.0525 cm, and 0.055 cm corresponding to a finer mesh by 10% and 5% and then a coarser mesh by 5% and 10%. Three geometries with meshes (-10%, base of 0.05 cm, and +10%) are shown in Fig. 2.4. The computational domain used in this analysis is shown in Fig. 2.2. Helium seeded with 0.2% O_2 flowed into humid air composed of 79.5% N_2, 20% O_2, and 0.5% H_2O at 4 slm. The humid air flowed at 4 slm through a much larger inlet area in order to encourage the development of the helium channel. The air diffused into the helium channel as both flowed for 5 ms to establish the steady state flow profile. The computational time required to complete 5 ms with the various meshes is shown in Table 2.2. The fine mesh (-10% from the base) took 29% longer to run and had 23% more plasma nodes than the base case of 0.05 cm mesh spacing. The coarse mesh was 18% faster and had 17% fewer plasma nodes than the base case. The meshes for -10%, the base

case, and +10% are shown in Fig. 2.3. The refinement zones highlighted in the base case apply to each case. The flow profiles corresponding to the helium and oxygen concentrations at 5 ms are shown in Fig. 2.4. The helium concentration, shown over one order of magnitude using a linear scale, highlights the effect of numerical diffusion at the pump. The fine mesh in the outer arcing refinement zone has too drastic an increase to the refinement used to buffer the pump. Because of the closer agreement in mesh sizing between the refinement zones, the profile at the pump of the coarse mesh does not have the circulation seen in the finer meshes. This effect would be corrected or compensated for in a computational investigation conducted for a publication or presentation through better matching of the pump refinement zone or by extending the computational domain. The oxygen concentration is shown using a three-decade log-scale to highlight the seed of 0.2% O_2 in the helium flow. Using the same scale for each allows us to recognize less diffusion of air into the helium channel in the fine mesh case as well as higher amounts of O_2 in the helium channel near the pump in the coarse mesh case. This is shown again in Fig. 2.5 in which a trace was taken along the centerline from the tip of the pin electrode to the pump. In each frame, the tube exit is at 0.5 cm on the horizontal axis. At 0.7 cm, or 2 mm from the exit of the dielectric tube, the molecular gases from the ambient have diffused to the centerline. This is shown best for N_2 in Fig. 2.5(c), and the densities grow quickly for both O_2 and N_2 down the centerline toward the pump. He shows the diffusion of air by decreasing in density along the centerline at 0.7 cm in Fig. 2.5(a). The coarser mesh shows the effects of diffusion earlier as a function of numerical diffusion and larger mesh spacing. The velocity for the -10%, base, +10%, +20%, and +100% cases is shown in Fig. 2.5(d). The increased coarse meshes were included after the initial mesh review yielded similar results. In effect, these coarser meshes pushed the extent of the mesh spacing to analyze the effect on the velocity. The

rise of velocity after the pin is identical for the -10%, base and +10% meshes, but the increased mesh spacing in the coarser +20% and +100% meshes delays the initial rise of velocity. The first mesh effect occurs between 0.3 and 0.4 cm centerline distance is the transition from the pin electrode refinement zone to a coarser plasma zone. The blending of these regions is poorest with the coarser mesh (+10 and +20%) and the larger variation in velocity supports that. The peak at 0.5 cm is the exit of the dielectric tube where the flow is discharged into the ambient and is again dependent on the mesh spacing at this important transition region. The base and the fine mesh case correspond well with the major discrepancy being the consistently higher velocity through the channel of the finer mesh. This again is due to the greater amount of numerical diffusion of the ambient air with the coarser meshes. The spread of the helium trace at the pump indicates a just over 2% range from the -10% to +10% mesh results at the pump. The +20% mesh showed more dramatic effect of the first (0.3 to 0.4 cm) refinement zone and increased to an artificially high velocity prior to the exit. The +100% mesh case reached a plateau within the tube with little variations, but the diffusion effects of the ambient into the helium channel decreased the velocity in the effluent (after 0.5 cm) to a decrease of 5 m/s at the pump.

At 5 ms, a radial trace was taken from the centerline to the dielectric wall at a position 5 mm from the exit of the dielectric tube. The radial trace results are shown in Fig. 2.6. The vertical axis is the concentration or velocity (Fig. 2.6(b)) and the horizontal axis shows the radial position. The width of the tube is indicated at 0.08 cm. Similar trends are seen again with the fine mesh having the lowest amount of the oxygen and nitrogen and the highest velocity at the centerline. Beyond the centerline differences, the meshes correspond well. The helium fills the channel and starts to drop rapidly at the air / helium interface. The nitrogen follows the opposite trend being higher in the ambient and approaching zero at the core of the helium channel. The

oxygen concentration does not drop as low in the center near the vertical axis because of the 0.2% seed of oxygen in the helium.

The mesh is optimized for the plasma calculations which occur within the tube and along the axis. Propagation of the guided ionization wave depends on many factors that will be discussed in later chapters, but in general, the IW propagates to an extent 1 cm from the tube exit. Within this region, the differences in species concentration for He, N2 and O2 are negligible. The largest variability is the velocity which fluctuates at the tube exit between 58 and 64 m/s. The effect of this variation in velocity on the plasma calculations, fed back to the plasma calculations through the neutral species update and the Navier-Stokes equations, is minimal.

Varying the mesh by 10% highlighted the effect of numerical diffusion through the coarser mesh and the direct impact on the predicted diffusion of the ambient air into the helium channel. The coarser mesh ran faster, but the variation in the centerline velocity profile was too drastic to use this as the "default" mesh size. The finer mesh took nearly 30% longer to complete the 5 ms than the base case. The variations in the resulting concentration profile and velocity were not great enough for the increase in computation time, however. This exercise showed the value in buffering the refinement zones and extending the boundary of refinement zones to less critically important positions in the computational domain. With subtle changes to the refinement zones, the base mesh proved it is suitable for these computations.

2.5 Tables

Table 2.1 Critical reaction pathways to form the near-terminal RONS

	Reaction[a]	Reaction Rate[b]	Ref.
	Path to O_3		
R1	$e + O_2 \rightarrow O + O + e$		[c], [21]
R2	$e + O_2 \rightarrow O^* + O + e$		[c], [21]
R3	$e + O_2 \rightarrow O^- + O$		[c], [21]
R4	$O_2^- + O_2^+ \rightarrow O_2 + O + O$	1×10^{-7}	[17]
R5	$N_2^* + O_2 \rightarrow O + O + N_2$	1.5×10^{-12}	[22]
R6	$O_2^- + O \rightarrow O_3 + e$	1.5×10^{-10}	[17]
R7	$O^- + O_2^* \rightarrow O_3 + e$	3×10^{-10}	[17]
R8	$O + O_2 + M \rightarrow O_3 + M$	$3.4 \times 10^{-34} (T_g/300)^{-1.2}$	[23]
	Path to H_2O_2		
R9	$e + H_2O \rightarrow H + OH + e$		[c], [24]
R10	$e + H_2O \rightarrow H^+ + OH + e + e$		[c], [24]
R11	$e + H_2O^+ \rightarrow OH + H$	$6.6 \times 10^{-6} T_e^{-0.5}$	[25]
R12	$O_2^- + H_2O^+ \rightarrow O_2 + OH + H$	1×10^{-7}	[17]
R13	$OH + OH + M \rightarrow H_2O_2 + M$	$6.9 \times 10^{-31} (T_g/300)^{-0.8}$	[23]
	Path to N_xO_y[a]		
R14	$e + N_2 \rightarrow N_2^* + e$		[c], [26]
R15	$e + N_2 \rightarrow N_2^{**} + e$		[c], [26]
R16	$e + N_2 \rightarrow N + N + e$		[c], [26]
R17	$O_2^- + N_2^+ \rightarrow O_2 + N + N$	1×10^{-7}	[17]
R18	$N + O + M \rightarrow NO + M$	$5.46 \times 10^{-33} \exp(155/T_g)$	[23]
R19	$N + O_2 \rightarrow NO + O$	$4.4 \times 10^{-12} (T_g/300) \exp(-3270/T_g)$	[23]
R20	$N + O_3 \rightarrow NO + O_2$	5×10^{-16}	[23]
R21	$N + OH \rightarrow NO + H$	4.7×10^{-11}	[23]
R22	$N + O_2^* \rightarrow NO + O$	$2 \times 10^{-14} \exp(-600/T_g)$	[18]
R23	$N + O_2 (^1S) \rightarrow NO + O$	2.5×10^{-10}	[27]
R24	$N^* + O_3 \rightarrow NO + O_2$	1×10^{-10}	[18]
R25	$N_2^* + O \rightarrow NO + N$	5×10^{-10}	[28]
R26	$N_2^* + O \rightarrow NO + N^*$	1×10^{-12}	[18]
R27	$N_2^* + O_3 \rightarrow NO + NO + O$	8.4×10^{-12}	[18]

R28	$N_2^{**} + O \rightarrow NO + N$	5×10^{-10}	[28]
R29	$N_2^{**} + O_3 \rightarrow NO + NO + O$	8.4×10^{-12}	[18]
R30	$O_2^- + N \rightarrow NO_2 + e$	5×10^{-10}	[17]
R31	$NO + O + M \rightarrow NO_2 + M$	$1\times 10^{-31} (T_g/300)^{-1.6}$	[23]
R32	$NO + O_2^* \rightarrow O + NO_2$	4.88×10^{-18}	[23]
R33	$NO + O_3 \rightarrow O_2 + NO_2$	$1.4 \times 10^{-12} \exp(-1310/T_g)$	[23]
R34	$NO + HO_2 \rightarrow NO_2 + OH$	8.8×10^{-12}	[23]
R35	$NO + NO + O_2 \rightarrow NO_2 + NO_2$	2×10^{-38}	[23]
R36	$NO_2 + O \rightarrow NO + O2$	$6.5 \times 10^{-12} \exp(120/T_g)$	[18]
R37	$NO_2 + H \rightarrow NO + OH$	1.28×10^{-10}	[23]
R38	$NO_2 + O + M \rightarrow NO_3 + M$	$9 \times 10^{-32} (T_g/300)^{-2}$	[23]
R39	$NO_2 + O_3 \rightarrow O_2 + NO_3$	$1.4 \times 10^{-13} \exp(-2470/T_g)$	[18]
R40	$NO + NO_3 \rightarrow NO_2 + NO_2$	$1.6 \times 10^{-11} \exp(150/T_g)$	[23]
R41	$NO_3 + NO_3 \rightarrow NO_2 + NO_2 + O_2$	1.2×10^{-15}	[29]
R42	$NO + NO_2 + M \rightarrow N_2O_3 + M$	3.1×10^{-34}	[23]
R43	$NO_2 + NO_2 + M \rightarrow N_2O_4 + M$	1.4×10^{-33}	[23]
R44	$NO_2 + NO_3 + M \rightarrow N_2O_5 + M$	3.6×10^{-30}	[23]
	Path to HNO_x[a]		
R45	$N_2O_3 + H_2O \rightarrow HNO_2 + HNO_2$	1.93×10^{-17}	[23]
R46	$N_2O_4 + H_2O \rightarrow HNO_2 + HNO_3$	1.33×10^{-18}	[23]
R47	$N_2O_5 + H_2O \rightarrow HNO_3 + HNO_3$	2×10^{-21}	[23]
R48	$NO + NO_2 + H_2O \rightarrow HNO_2 + HNO_2$	5.55×10^{-34}	[23]
R49	$NO + OH + M \rightarrow HNO_2 + M$	6×10^{-31}	[23]
R50	$NO + HO_2 + M \rightarrow HNO_3 + M$	2×10^{-30}	[23]
R51	$NO_2 + OH + M \rightarrow HNO_3 + M$	1.7×10^{-30}	[23]
R52	$HO_2 + NO_2 \rightarrow HNO_2 + O2$	1.2×10^{-13}	[23]
R53	$NO_2 + OH + M \rightarrow ONOOH + M$	3.37×10^{-30}	[23]
R54	$NO + HO_2 \rightarrow ONOOH$	6.09×10^{-11}	[23]

[a] O^* represents $O(^1D)$, O_2^* represents $O_2(a^1\Delta_g)$; N_2^* represents $N_2(A^3\Sigma, B^3\Pi)$; N_2^{**} represents $N_2(C^3\Pi$, and higher); M represents total gas density; N_xO_y represents NO_2, NO_3, N_2O_3, N_2O_4, and N_2O_5; HNO_x represents HNO_2, HNO_3, and ONOOH.

[b] Units are cm^3s^{-1} for two-body reactions and cm^6s^{-1} for three-body reactions

[c] Rate coefficient obtained from solution of Boltzmann's equation for the electron energy distribution. Cross section was obtained from cited reference.

Table 2.2 Comparison of mesh spacing with computational time

Mesh Spacing	Total Nodes	Plasma Nodes	Computation Time (min)
0.0450	14152	12749	622.47
0.0475	12708	11416	529.95
0.0500	11576	10352	480.70
0.0525	10387	9298	429.67
0.0550	9628	8618	391.98

2.6 Figures

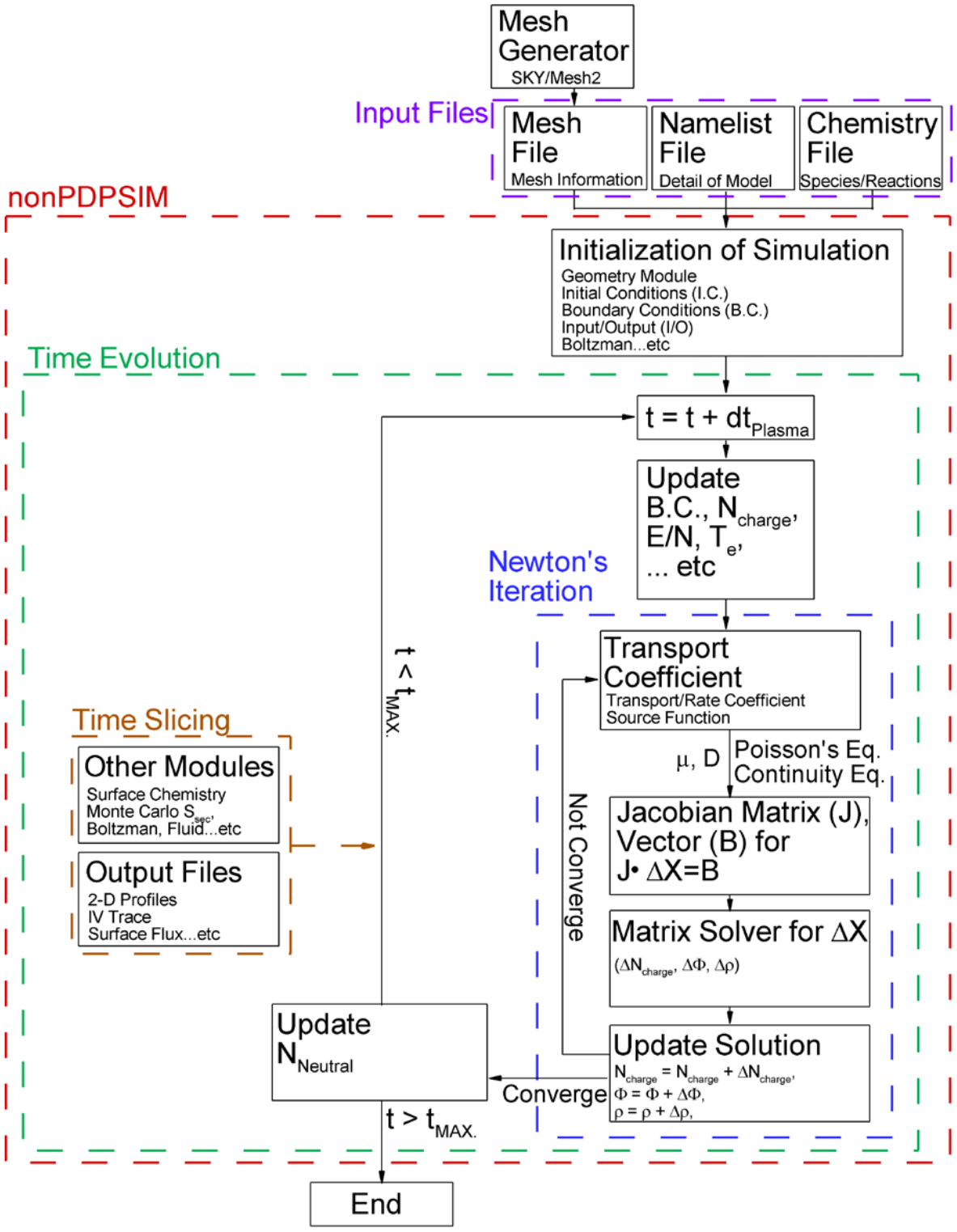

Figure 2.1 Block diagram of *nonPDPSIM*.[4]

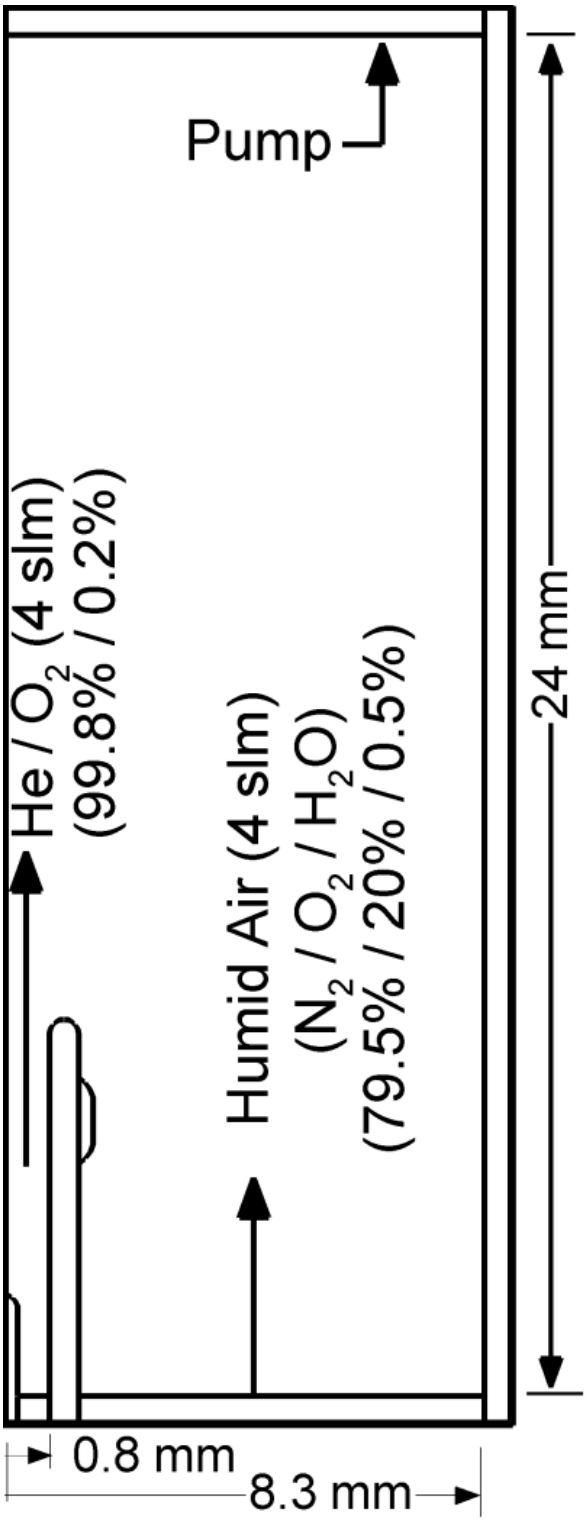

Figure 2.2 The computational domain of the helium atmospheric pressure plasma jet into humid air. The flow moves from the nozzle (inlet) at the base to the pump (outlet) at the top.

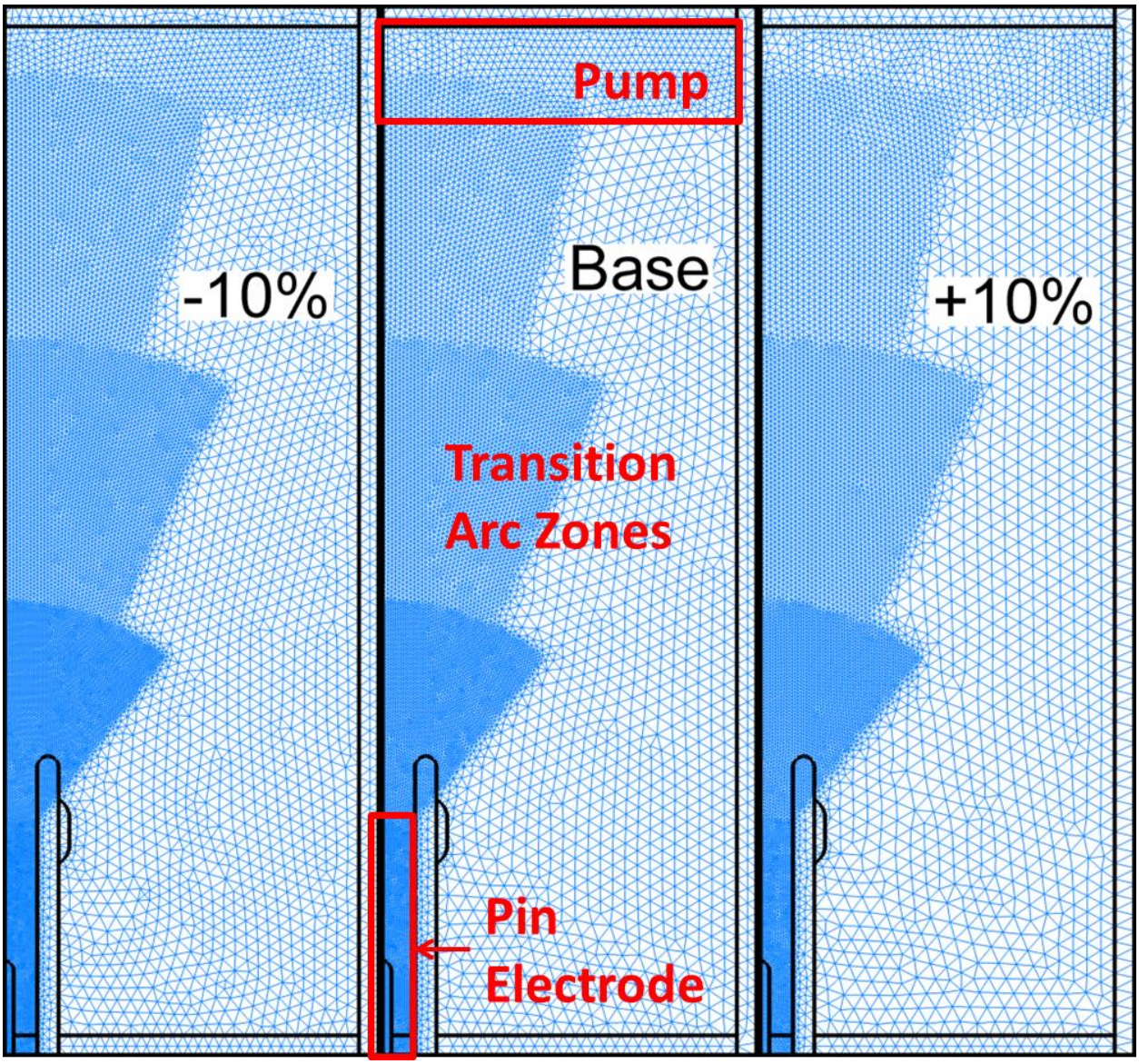

Figure 2.3 Comparison of mesh refinements with 10% finer mesh than the base shown in the left frame and 10% coarser shown in the right. The refinement zones highlighted in red in the base "default" mesh case are contained in each of the compared cases.

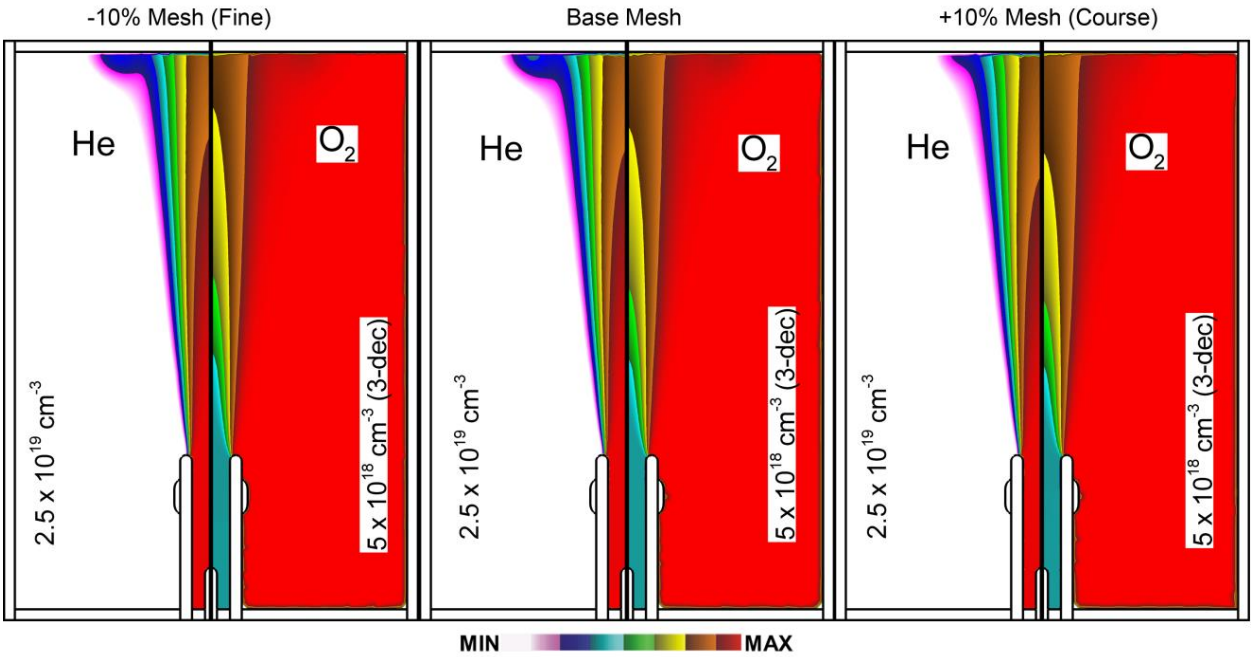

Figure 2.4 Comparison of concentration profile of helium and oxygen for the -10%, base and +10% mesh refinement cases. Helium is shown on a linear scale from the annotated maximum. Oxygen is shown on a log-scale over three-decades from the maximum annotated to highlight the seed of oxygen contained within the helium channel.

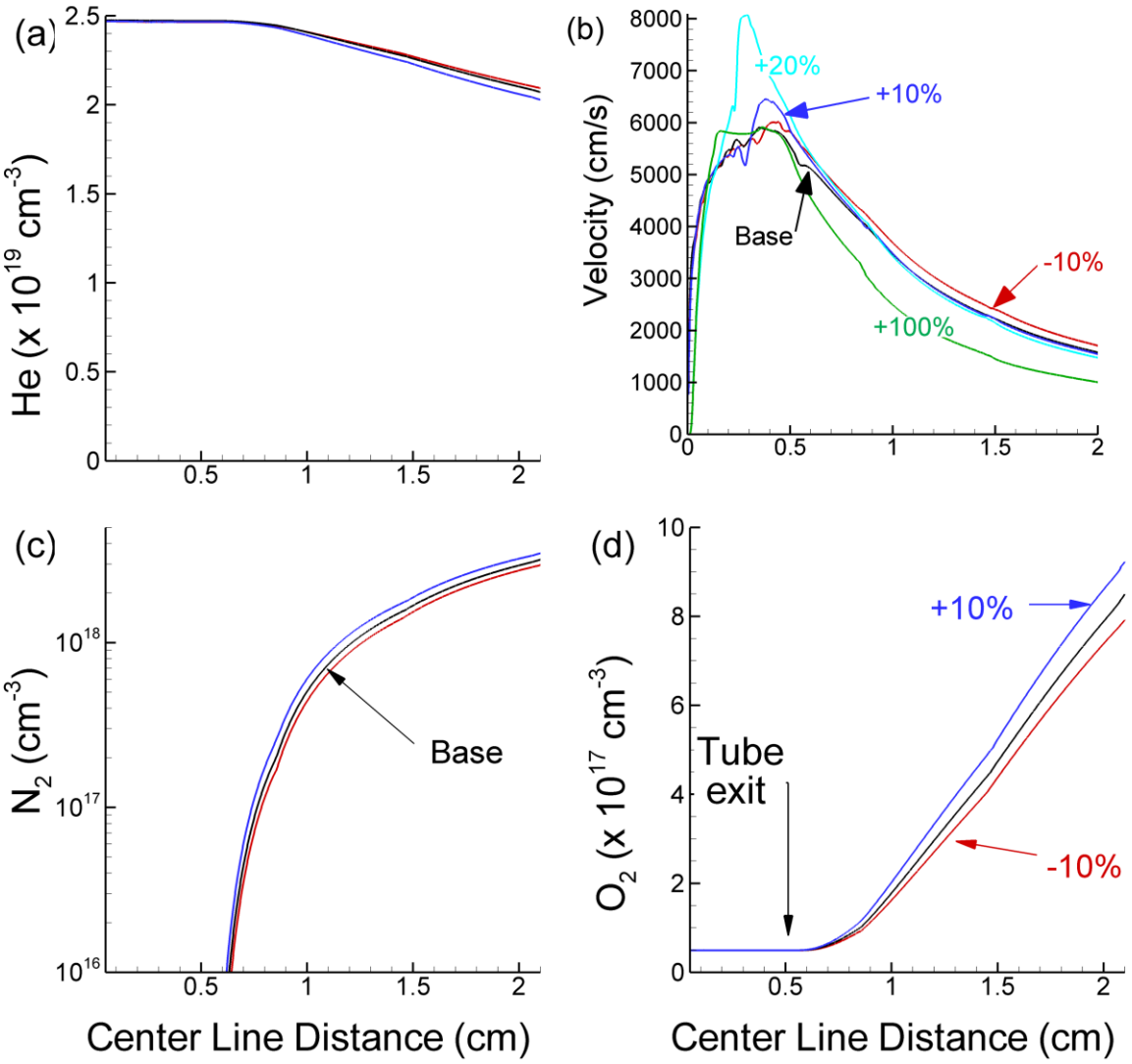

Figure 2.5 Centerline trace showing variations in concentration and velocity for the three mesh spacing cases. (a) Helium concentration profile. (b) Velocity profile with +20% and +100% meshes. (c) Nitrogen concentration profile. (d) Oxygen concentration profile with the tube exit annotated at 0.5 cm. The blue curve represents the coarser mesh, red represents the finer mesh, and black is the base "default" mesh for each frame.

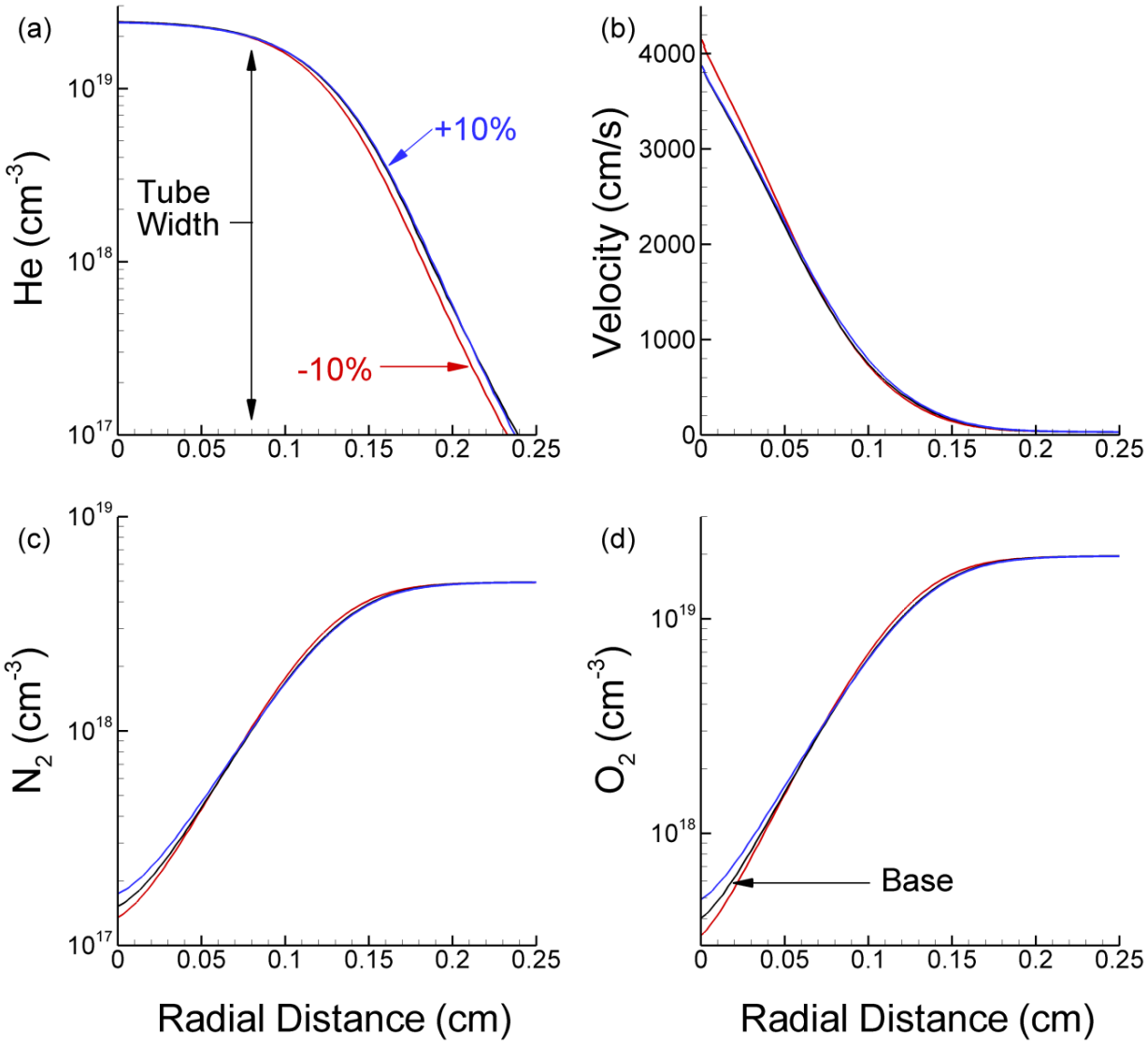

Figure 2.6 Comparison of radial trace taken 5 mm from the exit of the dielectric tube showing concentration and velocity changes from the centerline (y-axis) to a point of minimal change 2.5 mm away. (a) Helium concentration profile with tube width annotated at 0.08 cm. (b) Velocity profile. (c) Nitrogen concentration profile. (d) Oxygen concentration profile. The blue curve represents the coarser mesh, red represents the finer mesh, and black is the base "default" mesh for each frame.

2.7 References

[1] S. Rauf and M.J. Kushner, "Dynamics of a Coplanar-Electrode Plasma Display Panel Cell. I. Basic Operation", J. Appl. Phys. **85**, 3460 (1999).

[2] B. Lay, R. Moss, S. Rauf, and M. Kushner, "Breakdown Processes in Metal Halide Lamps", Plasma Sources Sci. Technol. **12**, 8 (2003).

[3] Z. Xiong and M. J. Kushner, "Surface corona-bar discharges for production of pre-ionizing UV light for pulsed high-pressure plasmas", J. Phys. D: Appl. Phys. **43**, 505204 (2010).

[4] J-C. Wang, Ph.D. Thesis, University of Michigan, 2014. (http://uigelz.eecs.umich.edu/theses.html)

[5] A. N. Bhoj and M. J. Kushner "Continuous Processing of Polymers in Repetitively Pulsed Atmospheric Pressure Discharges with Moving Surfaces and Gas Flow", J. Phys. D **40**, 6953 (2007).

[6] D. Scharfetter and H. Gummel, "Large-Signal Analysis of a Silicon Read Diode Oscillator", IEEE Trans. Electron Dev. **16**, 1 (1969).

[7] S. Nakamura, Applied Numerical Methods with Software, Prentice Hall, 1991.

[8] W. Tian, M. J. Kushner, "Atmospheric pressure dielectric barrier discharges interacting with liquid", J. Phys. D: Appl. Phys. **47**, 165201 (2014).

[9] S. Reuter, H. Tresp, K. Wende, M. Hammer, J. Winter, K. Masur, A. Schmidt-Bleker, and K-D. Weltmann, "From RONS to ROS: Tailoring Plasma Jet Treatment of Skin Cells", Trans. Plasma Sci., **40,** 2986 (2012).

[10] S. Reuter, J. Winter, A. Schmidt-Bleker, H. Tresp, M. Hammer, and K-D. Weltmann, "Controlling the Ambient Air Affected Reactive Species Composition in the Effluent of an Argon Plasma Jet", Trans. Plasma Sci., **40,** 2788 (2012).

[11] J. Walsh and M. Kong, "Contrasting characteristics of linear-field and cross-field atmospheric plasma jets", Appl. Phys. Lett. **93**, 111501 (2008).

[12] X. Lu, G. V. Naidis, M. Laroussi and K. Ostrikov, "Guided Ionization Waves: Theory and Experiments", Phys. Rep. **540**, 123 (2014).

[13] D. Maletic, N. Puac, S. Lazovic, G. Malovic, T. Gans, V. Schulz-von der Gathen and Z. Lj Petovic, "Detection of atomic oxygen and nitrogen created in a radio-frequency-driven micro-scale atmospheric pressure plasma jet using mass spectroscopy", Plasma Phys. Control. Fusion **54**, 124046 (2012).

[14] D. Liu, P. Bruggeman, F. Iza, M. Rong, and M. Kong, "Global model of low-temperature atmospheric-pressure He + H_2O plasmas", Plasma Sources Sci. Technol. **19**, 025018 (2010).

[15] T. Murakami, K. Niemi, T. Gans, D. O'Connell, and W. Graham, "Comparison of a global model to semi-kinetic fluid simulations for atmospheric pressure radio-frequency plasmas", Plasma Sources Sci. Technol. **22**, 032001 (2013).

[16] R. Dorai, PhD Thesis Department of Chemical Engineering, University of Illinois at Urbana-Champaign (2002).

[17] Y. Sakiyama, D.B. Graves, H-W. Chang, T. Shimizu, and G. Morfill, "Plasma chemistry model of surface microdischarge in humid air and dynamics of reactive neutral species", J. Phys. D: Appl. Phys. **45**, 425201 (2012).

[18] W. Van Gaens and A. Bogaerts, "Kinetic modelling for an atmospheric pressure argon plasma jet in humid air", J. Phys. D: Appl. Phys. **46**, 275201 (2013).

[19] D. Breden and L.L. Raja, "Computational study of the interaction of cold atmospheric helium plasma jets with surfaces", Plasma Sources Sci. Technol. **23,** 056020 (2014).
[20] K. Niemi, J. Waskoenig, N. Sadeghi, T. Gans, and D. O'Connell, "The role of helium metastable states in radio-frequency driven helium-oxygen atmospheric pressure plasma jets: measurement and numerical simulation", Plasma Sources Sci. Technol. **20**, 055005 (2011).
[21] A. V. Phelps, ""Tabulations of Collision Cross Sections and Calculated Transport and Reaction Coefficients for Electron Collisions with O2", JILA Information Center Report No. 28, 1985.
[22] N.A. Popov, "Fast gas heating in a nitrogen-oxygen discharge plasma: I. Kinetic mechanism", J. Phys. D: Appl. Phys. **44**, 285201 (2011).
[23] NIST Chemical Kinetics Database, Standard Reference Database 17, Version 7.0 (Web Version), Release 1.6.8 Data Version 2013.03, http://kinetics.nist.gov/kinetics/index.jsp
[24] Y. Itikawa, "Cross Sections for Electron Collisions with Water Molecules", J. Phys. Chem. Ref. Data **34**, 1 (2005).
[25] B.R. Rowe, F. Vallee, J.L. Queffelec, J.C. Gomet, and M. Morlais, "The yield of oxygen and hydrogen atoms through dissociative recombination of H_2O^+ ions with electrons", J. Phys. Chem. **88**, 845 (1988).
[26] Y. Itikawa, M. Hayashi, A. Ichimura, K. Onda, K. Sakimoto, K. Takayanagi, M. Nakamura, H. Nishimura, and T. Takayanagi, "Cross Sections for Collisions of Electrons and Photons with Nitrogen Molecules" J. Phys. Chem. Ref. Data **15,** 985 (1986).
[27] M. Uddi, N. Jiang, I. Adamovich, and W. Lempert, "Nitric oxide density measurements and air/fuel nanosecond pulse discharges by laser induced fluorescence", J. Phys. D: Appl. Phys. **42**, 075205 (2009).
[28] I. Shkurenkov, D. Burnette, W. Lempert, and I. Adamovich, "Kinetics of excited states and radicals in a nanosecond pulse discharge and afterglow in nitrogen and air", Plasma Sources Sci. Technol. **23**, 065003 (2014).
[29] J. C. Person and D. O. Ham, "Removal of SO_2 and NO_x from stack gases by electron beam irradiation", Radiat. Phys. Chem. **31**, 1 (1988).

Chapter 3 APPJ into Humid Air

3.1 Introduction

Non-equilibrium atmospheric pressure plasma jets (APPJs) provide therapeutic and sterilizing effects in the context of biomedical treatment of surfaces through delivery of fluxes of photons, charged and reactive species, and electric fields to tissue.[1-5] The complexity of APPJs has motivated significant research on the dynamics of these discharges.[6,7] The fluxes of ions and photons, and electric fields in APPJs that arrive at the surface being treated typically have lower intensities than in dielectric barrier discharges (DBDs).[8] However, with APPJs there may be more opportunity to controllably react plasma produced species with the ambient air to form reactive oxygen and nitrogen species (RONS) that are beneficial for surface treatment.

Typically, the plasma jet is a noble gas seeded with small amounts of O_2 or H_2O.[9] The noble gas flows through a capillary tube in which the discharge is formed and then flows into room air. In doing so, a rare-gas dominated channel in the air is hydrodynamically formed and through which the plasma produced reactive species flow. Mixing of the reactive species in the gas plume with the ambient air environment results in production of secondary species.[10,11] Due to the gas flow and repetitive pulsing, the temperature in the effluent of the plasma jet is near ambient.[12,13]

The *plasma bullet* that propagates through the plasma plume is also known as a *guided ionization wave* or *guided streamer*.[7] The structure of the guided streamer is similar to a conventional atmospheric pressure streamer where space charge produced electric field

enhancement in the head of the streamer generates an electron avalanche. The guided aspect of propagation results from the E/N (electric field/gas number density) required for avalanche is lower in the rare-gas dominated plume than in the surrounding air. The avalanche is then prevented from rapidly spreading laterally into the air.

There are a variety of geometries and discharge production techniques for APPJs.[9] The effects of admixtures to the noble gas [15], use of shielding gases [16,17], effects of positive and negative voltage pulses [18] and pulse repetition frequency [19] have been investigated in an effort to further understand and optimize the production of the RONS in APPJs.[20] Although the final desired outcome in the use of APPJs is typically to treat a surface, the first step in this process is to generate the reactive species in the gas phase through the repetitive sequence of electric discharge formation in the capillary, flow of primary reactive species into the rare-gas dominated plume, mixing with the ambient environment and transport to the surface.

In this chapter, a computational investigation of the production of reactive species in a repetitively pulsed APPJ sustained in He/O_2 mixtures is reported on. Many APPJs transition to turbulent flow due to the natural evolution of a jet flowing into stagnant air or through interaction with the plasma.[21] In this study, we have focused on purely laminar flows with the goal of providing further insights to the consequences of repetition rate, gas mixture, voltage, and flow rates. The simulations have also been performed for a jet into ambient air without intersecting a surface. Clearly the gas flow, mixing and subsequent reaction chemistry is affected by the perturbation of the flow by the surface. Our intent here is to investigate the process that delivers reactive species to the vicinity of the surface. In this regard, the flow distance modeled here is up to 8 cm with the rationale that the jet-to-surface distance is typically in the 1-10 cm range.

The model used in this investigation is briefly described in Sec. 3.2. Results from the investigation are discussed in Sec. 3.3 for a He/O_2 plasma jet flowing into room air produced a single and multiple discharge pulses (Sec. 3.3.1), with different voltages (Sec. 3.3.2), admixtures (Sec. 3.3.3), flow rates (Sec. 3.3.4), and pulse repetition rates (Sec. 3.3.5). The concluding remarks are in Sec. 3.4.

3.2 Description of the Model

The 2-D cylindrically symmetric model used in this investigation, *nonPDPSIM*, has been previously described in Chapter 2 and Refs. [22,23]. The model uses time-slicing techniques and an unstructured triangular mesh to bridge the sub-picosecond time steps necessary to resolve the discharge dynamics on micron spatial scales in the capillary tube during the discharge pulse, to the many microsecond timesteps over mm spatial scales up to many ms of elapsed time in the plume between and over many discharge pulses.

The process of simulating the discharge pulse and afterglow is as follows. The simulation begins by first computing the advective flow field solving only the continuity equations (Eqs. 2.14-2.17), using time steps of about 1 μs. These small time steps are required by the small dimensions of the mesh inside the tube. After the flow field is established, voltage is applied to the electrode and all modules of the model are then executed. The time steps for the plasma module, including solution of the electron energy equation and photon-transport are 0.1-5 ps. The table of electron transport coefficients is updated by re-solving Boltzmann's equation every 0.05 ns. The fluid module is executed every 0.05 ns. This process is continued for 80 ns (see below). At that point, the voltage pulse is terminated and Poisson's equation is no longer solved. A quasi-neutral assumption is then made which enables the time steps to greatly

increase. From the time that Poisson's equation is no longer solved to tens to hundreds of μs later, the timestep increases from < 1 ns to ≈ 1 μs, a value constrained by the small mesh inside the tube and the reaction rates of short lived species.

The primary modification to the base model in this Chapter is the inclusion of multiple discharge pulses. They are addressed in the following manner. Recomputing the discharge for every pulse is computationally intensive and would be prohibitive for the many tens of pulses and parametric study considered in Chapter 3. The length of time that species are produced by electron impact processes during the discharge pulse is tens of ns whereas the interpulse periods are hundreds of μs to ms, and gas residence times are many ms to tens of ms. On the timescale of the flow, the electron impact generated sources appear nearly instantaneously. During the first discharge pulse which is fully resolved in the manner described above, the source functions by electron impact, photoionization and fast neutral reactions are integrated in time. On the second and subsequent pulses we add in these source functions to the continuity equations as an impulsive source of species. The strength of this method is that many tens to hundreds of pulses can be addressed. The weakness of the method is that modifications to the source functions due to the changing composition of the gas on a pulse-by-pulse basis are not addressed. For high flow rates, short residence times of gas in the discharge tube and low repetition rates; this is not a particularly large effect. For these conditions, the gas is nearly refreshed inside the tube between pulses. For low flow rates, longer residence times and high repetition rates, the gas is not refreshed inside the tube and so some accuracy is lost.

The reaction mechanism used for the majority of the computational investigations conducted in this thesis includes over 50 species and more than 750 reactions and is shown in Appendix I. The reaction mechanism leading to a selected subsect of reactive oxygen and

nitrogen species (RONS) are emphasized in this chapter. The primary paths to these RONS are shown in Chapter 2, Table 2.1.

3.3 Dynamics of Plasma Jet

The experimental configuration modeled is a cylindrically symmetric tube with an inner pin electrode as shown in Fig. 3.1. Helium seeded with oxygen flows vertically through the tube into humid air. The inner diameter of the tube of 1.6 mm and length of 7 mm are roughly based on the dimensions of the kINPen plasma source.[16,17] The axial location of the powered electrode was based on various experiments of atmospheric pressure plasma jets.[13,40] The pin electrode has a radius of 0.25 mm. The entire computational domain shown in Fig. 3.1(a) is 2 cm by 10 cm and contains over 22,000 numerical mesh nodes with 20,000 being in the plasma or gas. (The plasma jet is shown in the lower right corner of Fig. 3.1(a)). The ring around the dielectric tube is treated as a dielectric as well. The minimum cell size inside the tube near the electrodes is 36 μm. The maximum cell size in the periphery of the mesh is 400 μm. The outer radial wall is dielectric and the top surface is a grounded metal mesh which also serves as the pump. The mesh is finest near the pin electrode and has a series of refinement zones that gradually increase the spacing of the mesh in the path of the ionization wave, shown in Fig. 3.1(b). The He/O_2 mixture is injected through the annular face between the pin electrode and the tube. Humid air is flowed into the volume through the annular face on the bottom boundary outside of the tube and inside of the outer wall. This slowly flowing shroud of ambient gas helps stabilize the jet and minimize the formation of vortices. The inlet and shroud gases are initially flowed for 50 – 80 ms to establish a steady state flow field prior to the discharge being ignited.

The base case has He/O_2 = 99.8/0.2 at atmospheric pressure flowing through the tube at 4 slm into the humid room air ($N_2/O_2/H_2O$ = 79.5/20/0.5). The flow of the humid air shroud is 4 slm. A single -15 kV pulse 80 ns long is applied (5 ns rise and 75 ns duration at the specified voltage with immediate drop to zero). Subsequent parameterizations from the base case will vary flow rate (2 - 7 slm), the admixture of O_2 (0.1 - 2%), applied voltage (-10 to -30 kV), and pulse repetition frequency- PRF (5 kHz – 500 kHz).

3.3.1 Base Case

The concentrations of He, N_2, O_2 and H_2O as the injected gases flow into the ambient are shown in Fig. 3.2 for the base case at the time that the discharge is initiated. (The O_2 concentration is shown over three orders of magnitude to capture the seed oxygen in the helium.) With flow distance from the end of the tube, air diffuses into the He plume as He diffuses into the ambient. The 4 slm flow rate for the base case and a tube radius of 1.6 mm produces an average speed of the helium mixture through the tube of 42 m/s. This speed corresponds to a Reynolds number for the helium gas of 630 indicating laminar flow. For pipe flow, the transition to turbulent flow occurs between 2300 and 4000. Once the jet leaves the tube the onset of turbulence will begin at about $50r_o$ from the outlet, where r_o is the jet radius.[41] This corresponds to about 4 cm for these conditions. The flow distances beyond the tube do not exceed 4 cm for the majority of the cases and not beyond 5-6 cm for a few select cases. For these select cases, the flow may be approaching turbulent conditions. For all cases, humid air flows outside the tube as a shroud at 4 slm with a corresponding speed of less than 1 m/s. This co-flow is intended to reduce instabilities at the helium / air interface and delay the onset of

turbulence. The room air is entrained into the jet of helium, thereby enabling reaction with the plasma excited species.

The electron temperature, T_e, ionization source, S_e, and electric potential contours for the base case, -15 kV, are shown in Fig. 3.3(a) for 20 (T_e only), 50 and 80 ns. Note that these figures show a small sub-region of the entire computational domain. Early during the discharge pulse at 20 ns, the plasma is still largely contained within the tube. At this time, a cathode-fall of 3 kV has already been established. As time increases, the guided ionization wave (represented by T_e and S_e) propagates out of the tube and into the previously established helium channel. The shape of T_e as well as the elongated ionization source for this negative streamer resembles those observed in experiments [18,42] and as predicted by Naidis for a negative streamer.[43] T_e is 5 eV near the front of the propagating ionization wave. At the termination of the pulse, T_e decreases to 3.3 eV, and into a range that agrees with those measured by experiments.[6,15] The velocity of the ionization wave is 1×10^7 cm/s which also agrees well with observed values.[5,18] The speed of the ionization front should not be considered a universal value but rather is a sensitive function of the proximity of ground planes.[44] In the conductive plasma channel behind the ionization wave, the normalized electric field drops to $E/N = 10^{-17}$ V-cm^2 (1 Td), resulting in T_e falling to < 0.5 eV. Without the close proximity of an electrically grounded surface, the intensity of the plasma in the effluent remains weak and the length of the plume shorter. The predicted shape and length of the guided streamer are similar to those observed for APPJs propagating into the atmosphere far from an electrical ground plane.[16] When the same device is moved near a grounded surface, the emission intensity of the guided streamer increases and a conduction channel appears to form.[45,46]

The electron density, n_e, during the discharge pulse and the total positive ion density at 80 ns are shown in Fig. 3.3(b). Ion and selected excited state and radical densities are shown in Fig. 3.4(a). At 50 ns, the electrons have separated from the cathode forming a cathode fall-like sheath of nearly 200 μm around the electrode. The highest electron density is at the edge of the cathode fall, up to 10^{14} cm^{-3}. The peak concentration in the tube outside the sheath and is $2 – 5 \times 10^{13}$ cm^{-3}. Within the effluent, the maximum is 3×10^{12} cm^{-3}. The majority of the electrons that have avalanched away from the cathode initially move toward and propagate along the wall of the tube, forming the annular appearing discharge observed and predicted by others.[42,43] At 80 ns, the ionization wave has propagated out of the tube and the electron density has transitioned onto the axis. This transition is in part due to the diffusion of air into the jet that reduces the mole fraction of helium at larger radii. The infusion of air increases electron losses due to attachment and electron energy losses due to excitation of low lying vibrational and electronic states in the molecular gases, both of which increases the T_e (or E/N) required to sustain the plasma above those values that are available. The end result is that the ionization wave is restricted to being on-axis. The on-axis electron density a few mm outside the tube is 10^{12} cm^{-3}.

The electrons do spread laterally at the exit of the tube leading to a halo of negative ions with peak value of 3×10^{10} cm^{-3}. These negative ions are in large part generated by diffusion of electrons at the periphery of the streamer and photoionization which produce electrons in a region of low E/N (and low T_e) which then quickly attach. This halo of low energy electrons having $T_e < 0.8$ eV are able to produce $O_2(^1\Delta)$ having a threshold energy of 1 eV but are less able to produce $N_2(A)$, having a threshold energy of 6 eV.

Ions produced by the ionization wave are shown at 80 ns in Fig. 3.4(a). The dominant cation is O_2^+ with a density of 3×10^{13} cm^{-3} at the edge of the sheath and 4×10^{12} cm^{-3} in the effluent. In spite of the mole fraction of O_2 in the tube being only 0.2%, the power flow favors formation of O_2^+. For example, for T_e = 5 eV (E/N = 25 Td) and an He/O_2 = 99.8/0.2 gas mixture, the fraction of power dissipation directly producing O_2^+ by electron impact is 1.5%. The fraction of power directly populating excited states of He is 72% and directly producing He^+ is 3.6%. (These values were obtained from stationary solutions of Boltzmann's equation for the electron energy distribution.) The lifetime for Penning ionization for the He excited states and charge exchange from He^+ and He_2^+ is 40-70 ns to form O_2^+, commensurate with the length of the discharge pulse.[26,29] So the majority of power dissipated into He is transferred to O_2 during the discharge pulse.

The N_2^+ density is maximum at 3×10^{11} cm^{-3}, extending from the edge of the tube to near the axis. This distribution of N_2^+ reflects the intersection of the N_2 diffusing into the plume from the humid air, the ionization wave propagating at this point along the axis and the He excited states and ions that form N_2^+ through Penning ionization and charge exchange, respectively. The lifetime for formation of N_2^+ by these processes at the location of the peak N_2^+ density is hundreds of ns. N_4^+ (not shown) follows the same trends as N_2^+ with a peak density of 3×10^{11} cm^{-3} at the end of the discharge pulse. The lifetime for formation of N_4^+ at the location of peak N_2^+ density is 100 ns. The density of He^+ in Fig. 3.4(a) decreases during the discharge pulse from 2×10^{11} cm^{-3} at 70 ns to 6×10^{10} cm^{-3} at 80 ns through recombination, formation of He_2^+ and charge exchange. The density of He_2^+ (not shown) remains relatively stable at 1 x 10^{11} cm^{-3}.

The neutral species that are the precursors to formation of RONS in the plume at the end of the discharge pulse (80 ns) are shown in Fig. 3.4(b). The He^* is the sum of all He excited

states [He(2^1S), He(2^1P), He(2^3S), He(2^3P), He(3S), He(3P)] and has a density of 4×10^{12} cm^{-3} in the effluent. These states are dominantly formed through electron impact of the ground state though there is a minor contribution from recombination of He^+ and He_2^+, no more than 1% of the total. Penning ionization from He^* dominantly forms O_2^+, N_2^+ and H_2O^+. The density of He_2^* (not shown) at this time at the same location as shown for He^* in Fig. 3.4(b) is 3×10^{10} cm^{-3}.

The RONS formed by this single pulse up to 80 ns can be placed into two categories – formation in the capillary tube dominantly by electron impact and formation by interaction of plasma activated species with the air diffusing into the plume. When the discharge is initiated, the O_2 in the feed gas undergoes electron impact dissociative excitation and attachment to form O in the tube. The highest density of O formed by this process, 1×10^{14} cm^{-3}, occurs near the tip of the pin electrode. The formation of O atoms by electron impact in the tube generally follows the electron density up the length of the tube and into the ambient producing an O atom density of 1×10^{13} cm^{-3} at the exit of the tube. Due to the low density of O_2 and lack of other species (such as H_2O) in the tube, the depletion of O by reactions in the tube is small. For example, the lifetime of O atoms for formation of O_3 in the tube is 1-2 ms. Meanwhile, other sources of O atoms, such as electron – ion recombination ($e + O_2^+ \rightarrow O + O$), continue to contribute to its density. This situation continues until diffusion of the humid air into the plume enables other reactions. As a result, the O atoms continue to accumulate from 80 ns to 1 μs. This accumulation of O atoms is aided by the quenching of N_2^* [which represents the sum of $N_2(A^3\Sigma, B^3\Pi, C^3\Pi)$ and higher states] by O_2 which produces O atoms.[32] The rate coefficient for dissociative quenching of N_2* by O_2 is 1.5×10^{-12} cm^3s^{-1} which accounts for the majority of production of O atoms where the ionization wave has produced significant densities of N_2^*.[32]

The distribution of $O_2(^1\Delta)$ also follows the path of the electrons as $O_2(^1\Delta)$ is formed initially from electron impact excitation of ground state O_2. Its density grows to a maximum of 2×10^{13} cm^{-3} in the effluent near the exit of the tube at the end of the discharge pulse. An additional source of $O_2(^1\Delta)$ is the three body recombination of O atoms, but this is a minor source due to the low density of O atoms. The radial spread of $O_2(^1\Delta)$ in the effluent above the tube results from the low energy electrons in the halo and the increasing O_2 density at increasing radius. Since the threshold energy for exciting $O_2(^1\Delta)$ is only 0.98 eV, even electrons having T_e of 0.5-0.6 eV are able to efficiently produce the state.[47] The rate coefficient for electron impact excitation $O_2(^1\Delta)$ in dry air for T_e = 0.6 eV (obtained from a stationary solution of Boltzmann' equation) is 1.5×10^{-11} cm^3s^{-1}. The post-pulse density of N_2^* more closely follows the path of the electron ionization wave as it intersects the N_2 diffusing from the ambient air into the He plume. The minimum threshold energy for creating N_2^* is 6.2 eV. The rate coefficient for electron impact excitation of N_2^* in dry air for T_e = 0.6 eV is 10^{-21} cm^3s^{-1}, and so there is essentially no direct production of N_2^* by electron impact in the halo. Some of higher excited states of N_2^* radiatively relax and others quench quickly with O_2 to produce O atoms, and with O atoms (when present) to form NO. The lifetime for quenching of N_2^* at the site of its highest density by collisions with O_2 is 1 μs.

The further development of the densities of O and O_3 up to 100 μs after the single discharge pulse is shown in Fig. 3.5(a). (This time was chosen as it is the inter-pulse period for a 10 kHz PRF.) Between 1 μs and 10 μs, the density of O atoms increases at the tip of the tube through ion – ion recombination between O_2^- and O_2^+. This process is aided by electrons from the plume diffusing radially outwards and intersecting the inwardly diffusing O_2 from the air. These low energy electrons then quickly attach to form additional O_2^-. (Although the dynamics

of this process likely occur in all plasma jets with a similar geometry, the details of where these additional O atoms are produced are device dependent.) The density of O atoms increases in the channel due to quenching of N_2^* by O_2. This locally high density of O atoms (up to 2×10^{14} cm^{-3} at 10 μs) react with O_2 diffusing from the ambient to form O_3 in nearly the same amount at 100 μs. Between at the end of the discharge pulse, the unreacted O atoms (and additional O atoms produced by quenching of N_2^*) move upwards with the flow. The maximum in the density of O atoms translates about 5 mm upwards while O atoms are depleted in the tube by this flow. (There are no additional sources of O atoms in the tube after the discharge pulse.) As the O atoms flow upwards, they continue to be depleted by formation of O_3.

The formation of NO and N_xO_y (sum of NO_2, NO_3, N_2O_3, N_2O_4, and N_2O_5) up to 100 μs for the first and thirtieth pulse is shown in Fig. 3.6. NO is dominantly formed through two, two-step mechanisms. The first is $e + N_2 \rightarrow N + N + e$, followed by $N + O_2 \rightarrow NO + O$. The second is $N_2^* + O \rightarrow NO + N$, which follows production of O atoms. Both of these processes involve reactants requiring high energy electrons in the ionization wave, either to produce N atoms by dissociative excitation of N_2 (threshold energy 11 eV) or to produce N_2^* (minimum threshold energy 6 eV). There is negligible production of N or N_2^* in the halo. Since the lifetime of N_2^* against quenching by O_2 is 1 μs, the second process contributes to NO production only during the first few μs after the discharge pulse. Subsequent production of NO is by the reactions of N atoms with O_2. The production of NO is relatively low (maximum density of 5×10^{10} cm^{-3}) following the single pulse. The low density results from the low production of N atoms (maximum density of 5×10^{11} cm^{-3}), small rate coefficient for the former reaction at the temperature in the effluent of 300 K (8.1×10^{-17} cm^3s^{-1}), and short lifetime for N_2^* for the second reaction. Overall, in the first 100 μs, 42% of NO is produced by the reaction of $N + O_2$ and 58%

is produced by the reaction of N_2^* with O. As the gas continues to flow upward, NO is slowly depleted by three-body reactions producing higher oxides. In the near field where O atoms have a higher density, these reactions are $NO + O + M \rightarrow NO_2 + M$ (R31) and $NO_2 + O + M \rightarrow NO_3 + M$ (R38). In the far field where the density of O_3 is higher, NO is depleted in the formation of NO_2 (R33) by reaction with O_3. Subsequent reactions of NO_x with O, O_3 and NO_x form higher oxides of nitrogen, N_xO_y (R39, R42-44).

From the development of the RONS over time shown in Figs. 3.5-3.7, we can envision the environment the next discharge pulse will see in a multiply pulsed system. The densities at 1 μs correspond to the initial conditions for a repetition rate of 1 MHz. For example, at 1 μs, there is still a significant density of O atoms within the tube and near the pin electrode, as shown in Fig. 3.5(a). At 10 μs, corresponding to a repetition rate of 100 kHz, the O atoms have moved away from the pin, but are still in the tube. At 100 μs (10 kHz), the O atoms have mostly cleared the tube and are dominantly in the plume. Continuing to lower the PRF will clear out the bulk of the reactive species in the tube and so provide a more pristine environment consisting of the injected gases for the next pulse. A high repetition rate results in the next pulse entering a more reactive environment.

Densities of O and O_3 are shown in Fig. 3.5(b) at different times after the 30^{th} discharge pulse for a 10 kHz PRF (100 μs interpulse period). By this pulse, a steady state O atom profile has emerged. Sufficient time has passed (3 ms) for the O atoms to be entrained in the flow extending to about 1.5 cm beyond the tube, and to be consumed by reactions. The dominant reactions which consume O atoms are with O_2 to form O_3, with N_2^* to form NO, and with NO to form NO_2. In the absence of organic compounds and with a low plume gas temperature that slows reactions of O_3 with NO and N_xO_y, O_3 is fairly stable in the plume. In this sense, O_3 is a

terminal species and so the density of O_3 accumulates in the effluent up to 4×10^{13} cm^{-3} over the 30 pulses. The major source of O_3 is at the intersection of the O_2 diffusing into the plume and the O atoms flowing up out of the tube in the plume.

The densities of NO and N_xO_y after the 30th discharge pulse are shown in Fig. 3.6(b). Since the conversion of NO to N_xO_y is relatively slow (longer than the interpulse period), pulses of NO of 2×10^{10} cm^{-3} convect with the flow. These pulses represent the NO produced in previous pulses as they move vertically upward with the flow. These pulses of NO are slowly depleted, reacting with O, O_3, and NO_x, to form N_xO_y which then accumulates in the plume. After the 30th discharge pulse, the density of N_xO_y accumulating from previous pulses reaches 1×10^{11} cm^{-3}.

The initial formation of the hydroxyl radical, OH, is through electron impact dissociative excitation and ionization of the water vapor diffusing into the plume from the ambient (R9,R10). Additional sources are dissociative recombination of H_2O^+ (R11) and ion neutralization of O_2^- and H_2O^+ (R12). The development of the OH density for the first and thirtieth pulses is shown in Fig. 3.7. The production of OH after the first discharge pulse when electron impact dissociation of H_2O terminates is by ion-ion neutralization of the superoxide anion, O_2^-, and H_2O^+ (R12), and electron-ion recombination of H_2O^+ (R11). (This is most clearly illustrated by the 10 and 100 μs frames in Fig. 3.7(a)) Hydrogen peroxide is formed by the three-body self-reaction of OH (R13) and grows appreciably over the 30 pulses. The spatial distribution of H_2O_2 follows that of OH as would be expected. The process of OH and H_2O_2 formation at the end of the dielectric tube is similar that of ozone – relying on diffusion of the ambient air into the active helium plume. The primary rate coefficient for the formation for H_2O_2 by two OH radicals (R13) is larger at ambient temperature than that for formation of ozone by reaction of O and O_2 (R8). However, the higher

reactant density favors the development of ozone. As the OH and H_2O_2 convect with and accumulate in the flow, the densities in the effluent are 7×10^{12} cm^{-3} and 1×10^{12} cm^{-3}, respectively, at the end of the 30^{th} pulse.

3.3.2 Voltage

Of the many system variables available to control the production of radicals in the flow, voltage is perhaps the least perturbing to other processes as, in principle; the major effect is the production rates of radicals. We do note that there have been observations of plasma-flow interactions related to voltage that either trigger or delay the onset of turbulence,[21] and so our comments here apply to laminar flow.

Densities of electrons, sum of all cations (N^+_{tot}), OH, He^*, N_2^*, $O_2(^1\Delta)$ and O are shown in Fig. 3.8 at the end of a single discharge pulse for -10, -15, -20 and -30 kV. All voltage pulses have the same rise time (5 ns) and duration (80 ns). These species were chosen as being representative of those produced by direct electron impact or one step removed, as would be the case of charge exchange or Penning reactions. The profiles of densities shown in Fig. 3.8 are along the axis. The end of the tube is at an axial location of 0.5 cm. Increasing the applied voltage increases energy deposition which then translates to higher electron densities, but also produces a higher speed of the ionization wave. The speed of the ionization wave increases from 1.2×10^7 cm-s^{-1} to 4.2×10^7 cm-s^{-1} from -15 kV to -30 kV. This higher speed extends the ionized region of the plume to 1.8 cm. The density of N^+_{tot} is predominantly produced from electron impact ionization or one step removed, such as Penning ionization. The densities of all species that are formed in the tube or directly from species formed in the tube first decrease along the axis and then, upon emerging from the tube, increase along the axis. These dynamics

result from the ionization wave being initiated on axis at the pin electrode (large density on axis), becoming annular along the wall moving up the tube (low density on axis) and then transitioning back to the axis when emerging from the tube (high density on axis). The densities of OH and N_2^* first emerge when the ionization wave intersects the ambient air diffusing into the plume beyond the end of the tube, and so these densities do not reflect the radial dynamics of the ionization wave inside the tube.

The densities of O and $O_2(^1\Delta)$ are dominated by electron impact excitation of the initial O_2 in the gas mixture and, upon leaving the tube, O_2 diffusing into the plume from the ambient. Their densities therefore increase and are maximum outside the tube. The production of He^* is dominated by direct electron impact of the ground state (a small contribution comes from dissociative recombination of He_2^+). Its dominant loss is by Penning reactions with the ambient gases. The density of He^* therefore sharply drops upon emerging from the tube when the ambient air begins diffusing into the plume.

The species perhaps most affected by voltage are OH and N_2^*. Without H_2O or N_2 in the initial mixture, OH (dissociative excitation of H_2O) or N_2^* (direct excitation of N_2) are dominantly produced by intersection of the ionization wave with H_2O and N_2 diffusing into the plume. The excitation energy for the lowest N_2 electronic state is 6.2 eV and so N_2^* will not be produced in large numbers in the halo. The higher speed and greater penetration distance of the ionization wave with the higher voltage enables the ionization wave to overlap with higher densities of H_2O and N_2 in the plume further from the tube. The fact that He^* does not also extend further into the plume with increasing voltage results from the rapid quenching of He^* by Penning collisions, and due to its lower rate of production by electron impact resulting from the lower electron temperature in the plume far from the end of the tube. For -30 kV, T_e falls to 2.6

eV a distance of 1 cm from the end of the tube. At this temperature, the electrons are still able to efficiently excite the N_2 (6.2 eV) but do not efficiently excite He^* (19.6 eV). At this point in the discharge, OH is produced from dissociation of the H_2O diffusing into the plume from the ambient.

The significant drop in the density of OH at -10 kV is a demonstration of the influence of the propagation distance of the ionization wave. Significant production of OH requires intersection of the ionization wave with water vapor diffusing into the plume from the ambient. With the lower voltage, the ionization wave simply does not propagate far enough into the plume to intersect with significant densities of H_2O. A similar trend occurs for $O_2(^1\Delta)$. With increasing voltage the ionization wave extends further into the plume where the density of O_2 diffusing from the ambient is larger. The extension of the density of O atoms with voltage is not as great since both its source (ionization wave intersecting with more O_2) and its sink (formation of O_3) increase further from the tube as the ambient O_2 diffuses into the plume.

The development of RONS (O, O_3, NO, N_xO_y, OH, and H_2O_2) after 30 pulses for a PRF of 10 kHz for voltages of -10 kV to -30 kV are shown in Fig. 3.9 to a distance of 4 cm. Densities along the axis are shown in Fig. 3.10 for OH, H_2O_2, HNO_x, O_3, NO and N_xO_y for different voltages to a distance of 6 cm. This distance is the extent of the flow after 30 pulses of reactive species that are initially formed in the tube. The increasing rate of formation of O with increasing voltage directly maps onto the increase in the density of O_3. The increasingly negative voltage also produces a larger halo which also produces more OH, NO, and O_3 at large radius. The nitric oxide acids, HNO_x, shown in Fig. 3.10(c) are formed predominantly from the three-body reactions of NO and NO_2 with OH (R49,R51,R53). Their axial profile is similar to

H_2O_2 indicating the influence of OH in their formation. The axial oscillations in HNO_x result from the axial oscillations in the density of the precursor NO from previous pulses.

Since the gas dynamics (in this model) are not terribly affected by the voltage, the major consequence of voltage on the densities NO and N_xO_y are the increasing densities of precursors. The higher voltages which extend the ionization wave deeper into the plume where N_2 densities are higher produce larger densities of N and N_2^*, the precursors for NO. The periodic maxima of NO densities resulting from prior pulses diminish as the voltage increases. This results from the ionization wave propagating further into the plume, overlapping the prior pulse of NO, and creating more O and OH, that deplete the density of NO.

OH is formed dominantly by electron impact dissociation in the ionization wave of H_2O diffusing into the plume. As the ionization wave penetrates deeper into the plume where the density of H_2O is higher, more OH is produced further from the end of the tube. The ionization wave penetrates to only 2 cm at -30 kV, however the greater extension is preserved by the flow. OH is produced in large numbers mostly by electron dissociative excitation of H_2O in the ionization wave. Reactions between OH to produce H_2O_2, and with NO and N_xO_y to form HNO_x (comprised of HNO_2, HNO_3, and ONOOH) deplete the density OH as the flow extends beyond 2 cm where the OH is dominantly produced. The density of N_xO_y is most sensitive to residence time since forming the higher N_xO_y requires multiple collisions. (To form N_2O_5, a minimum of 5 collisions are required.) The axial speed decreases with distance from the tube as the plume radially expands. This decrease in axial speed increases the residence time of reactants in the plume which in turn affords more collisions between species, to which N_xO_y is most sensitive. The end result is an increase in N_xO_y at the end of the plume.

3.3.3 O2 Fraction in Gas Feed

The production of specific ROS is sensitive to the fraction of O_2 in the He inlet gases. Experimentally, it was determined that the production of $O_2(^1\Delta)$ was maximum for an O_2 fraction of 0.5% [15] and computational investigations determined that an O_2 fraction of 0.5% maximized O atom production.[48] The densities of electron impact produced species (n_e, N^+_{tot}, $O_2(^1\Delta)$, He^*, N_2^* and O) at the end of the first discharge pulse are shown in Fig. 3.11 along the axis up to 1.5 cm for O_2 fractions of 0.1 to 1%. In all cases, the increased amount of O_2 in the mixture leads to an increase in the densities of O and $O_2(^1\Delta)$. In spite of O_2 diffusing into the plume, the majority of the oxygen based reactivity is produced by the O_2 flowing through the tube which directly overlaps the ionization wave where the electron density and temperature have their highest values. (Should the plume be turbulent, we expect more O_2 from the ambient would be intersected by the intense portion of the ionization wave.)

The axial electron density inside the tube decreases with increasing O_2 fraction, in large part due to increasing rates of dissociative and 3-body attachment to O_2. Outside the tube, the maximum electron density on axis occurs for an O_2 fraction of 0.5%. This result is a bit of an artifact of the dynamics of the ionization wave. Prior to the end of the tube the ionization wave is along the wall of the tube leaving the center of the tube with a lower T_e, which produces less ionization (and on a relative basis, more attachment). When the ionization wave leaves the tube, the maximum rate of ionization returns to the axis. This transition then favors production of ROS with for flows with higher O_2 fractions since the density O_2 on axis at this location is most influenced by the initial mole fraction of O_2 and not by diffusion from the ambient.

The density of He^* monotonically decreases with increasing O_2 fraction. A portion of this decrease results from the higher rate of quenching of He^* by the increasing fraction of O_2 in

the feed gas. However with increasing O_2, the electron temperature decreases. For these reasons, the sensitivity of the axial density of He^* to the fraction of O_2 is greater in the tube where the O_2 density on axis is determined by the feed gas than outside the tube where the O_2 density on axis has increasing contributions from the ambient. For example, 3 mm beyond the end of the tube, the maximum T_e decreases from 3.7 eV for an O_2 fraction of 0.1% to 2.3 eV for an O_2 fraction of 1%. This decrease in T_e results in a decrease in the rate coefficient for electron impact excitation of He^* from 9×10^{-15} cm^3s^{-1} for an O_2 fraction of 0.1% to 5×10^{-21} cm^3s^{-1} for an O_2 fraction of 1%. However, reactions that have lower threshold energies, such as direct electron impact production of N_2^+, O_2^+, and H_2O^+, are less sensitive to the decrease in T_e.

The ionization wave speeds up with increasing O_2 fraction. The speed of the ionization wave is 1×10^7 cm-s^{-1} for an O_2 fraction of 0.1% and 1.8×10^7 cm-s^{-1} for 1%. This higher speed and greater extension of the ionization wave enables the wave to intersect with higher densities of air diffusing into the plume that produces more N_2^*. Despite the lower value of T_e, the extent of the ionization wave at the end of the pulse for an O_2 fraction of 1% is 3 mm longer than that of the O_2 fraction of 0.1%.

The densities of RONS (O, O_3, NO, N_xO_y) after 30 pulses are shown Fig. 3.12 in the tube and plume for different O_2 fractions. Densities of RONS (OH, H_2O_2, HNO_x, O_3, NO and N_xO_y) along the axis are shown in Fig. 3.13. With increasing O_2 fraction, the speed-up and further extension of the ionization wave increases the axial extent of O atom production. When combined with the increase in density of O_2 further from the tube due to diffusion from the ambient, the extended production of O atoms increases the production of ozone, O_3. The higher density and larger spread of O atoms is not only a source of O_3, but also a source of NO. The larger density of O atoms surviving from previous pulses results in N_2^*, and N produced by

following pulses to more readily creating NO. This accumulation of NO does not directly produce higher densities of N_xO_y. NO accumulates dominantly downstream of the highest concentration of O atoms which are progressively depleted in the plume by formation of O_3 by reactions with the increasing density of O_2. The end result is a decrease in production of NO_2, the dominant N_xO_y species after NO, and precursor for higher N_xO_y.

The axial density of OH is significantly higher for O_2 mole fractions of 0.1% and 0.2%, as shown in Fig. 3.13(a), These trends result, in part, from higher rates of production of H_2O^+ produced by Penning ionization facilitated the larger densities of He^*. The larger density of H_2O^+ produces OH by dissociative electron – ion recombination and by ion-ion neutralization with O_2^- (R11, R12). The higher densities of OH then react with other hydroxyl radicals in three-body collisions to form H_2O_2 and with NO_x to form HNO_x.

After 30 pulses at a PRF of 10 kHz, the inventories of selected terminal or near-terminal species (O_3, NO, N_xO_y, OH, H_2O_2, and HNO_x) are shown in Fig. 3.14. The inventory is the spatial integral of the species over the entire computational domain. The inventories are perhaps a better indication of total reactivity produced by the plume than the density at selected locations. The integrated inventory of ozone is not a very sensitive function of O_2 mole fraction with only a reduction of 50% from the mole fraction with the highest inventory (0.1%) and to smallest inventory least (0.5%). The higher inventories of N_xO_y produced for the 0.1% and 0.2% O_2 fractions indicate that the NO is produced in the proper spatial location to react with O atoms and ozone to form NO_2, (R31,R33) which then leads to N_xO_y (R38,R39,R42-R44). The higher spatial concentration of O_3 near the axis and the higher concentrations of N_xO_y are also shown for 0.1 and 0.2% fractions of O_2 in Fig. 3.12. The trends of higher densities of OH and H_2O_2 on the axis produced with small fractions of O_2 (0.1 and 0.2%) extend to the total inventory as well.

An order of magnitude higher inventory of OH is produced with 0.1 and 0.2% fractions of O_2 (3-4 × 10^{12}) compared to 0.3% (3 × 10^{11}). This higher inventory of OH at relevant spatial locations to react with NO and N_xO_y produces the significantly higher inventory HNO_x (R49, R51, and R53). Increasing O_2 mole (1-2%) can significantly decrease RONS species with the exception of O_3 and $O_2(^1\Delta)$. Although more O atoms are produced at the end of the discharge pulse, the higher mole fraction of O_2 quickly scavenges the O in the formation of O_3, and so fewer O atoms remain for other reactions. Depending on the desired treatment outcome, the fraction of oxygen can be used to vary the relative fractions of RONS. For example, small mole fractions of O_2 produce larger densities of OH, H_2O_2 and HNOx relative to O_3 than obtained at large mole fractions of O_2. Intermediate fractions of O_2 increase the ratio of NO/O_3.

3.3.4 Flow

Changing the flow rate has direct consequences on the flow dynamics. The flow speed increases which, for a constant PRF, decreases the residence time of species in the tube and extends the plume where the He mole fraction is large. As the flow rate of the He/O_2 mixture increases the diffusion of humid air into the helium jet begins further from the exit of the tube. In spite of these changes in flow dynamics, at the end of the first pulse, there is little change in the discharge for flow rates of 2 – 7 slm since the speed of the ionization wave is much higher than that of the gas. However, when varying flow rate, significant differences occur in the densities of RONS at 100 μs after the pulse. (Recall that 100 μs is the interpulse period for a 10 kHz pulse PRF.) Densities of RONS on the axis for flow rates of 2, 3, 5 and 7 slm are shown in Fig. 3.15 at 100 μs after the pulse. For a flow rate of 2 slm, the ROS formed in the tube (O, $O_2(^1\Delta)$, and O_3) have not flowed out of the tube by the time of the next discharge pulse. For

these ROS there are two maxima – in the tube resulting from in-tube production of ROS that has not yet flowed out of the tube, and outside the tube where the ionization wave has intersected O_2 diffusing into the plume. At the higher flowrates of 4, 5 and 7 slm, the higher flow speed carries the ROS out of the tube and into the effluent prior to the next pulse.

The integral rate of production of RONS by electron impact processes (on the first pulse) is not a sensitive function of flow rate while the speed of the flow increases. So in the absence of other processes a pulse of reactants would flow downstream with increasing speeds into increasing densities of diffusing air. For terminal species such as $O_2(^1\Delta)$, its *plug* of density largely translates further downstream with increasing flow rate with a peak axial density of 2.3×10^{13} cm^{-3} that changes by less than 30% with flow rate. O_3 and OH, which benefit from the greater mixing with the ambient humid air that occurs with the longer plume, have densities that increase with flow rate. The minor decrease in the maximum axial densities of N and NO with increasing flowrate after 100 μs is a bit deceiving as the total inventory of N and NO is approximately the same. The N and NO are initially produced over a larger spatial extent because the ionization wave penetrates further from the tube through the extended portion of the plume having a large He mole fraction.

The PRF and flow rate collectively determine the environment that a successive discharge pulse encounters. For a PRF of 10 kHz and a flow of 7 slm, the next pulse will enter a pristine environment since the RONS formed on the previous pulse have largely flowed out of the tube. For a flow rate of 2 slm, the discharge will encounter the RONS still in the tube formed during the previous pulse. The densities of O, O_3, NO, N_xO_y, OH and H_2O_2 after 30 pulses are shown in Fig. 3.16 for flow rates of 2 – 7 slm. Densities of RONS (OH, H_2O_2, HNO_x, O_3, NO, and N_xO_y) along the axis for these conditions are shown in Fig. 3.17. The density of O_3 in the

effluent 3 cm from the inlet is maximum with the 2 slm flow rate (4.3×10^{13} cm^{-3}) and a minimum with the 7 slm flow rate (2.3×10^{13} cm^{-3}). The spatial integral (inventory) O_3 produced over 30 pulses increases from 1.9×10^{13} molecules for a flowrate of 2 slm case to 3.9×10^{13} molecules for a flowrate of 7 slm. This increase in the inventory of O_3 is enabled by the higher flowrate carrying O atoms further into the plume where they intersect with a higher density of O_2 entering the plume from the ambient. The axial extent of the O_3, a terminal species, increases with flow rate, as observed by Xian *et al*.[49] For a flowrate of 2 slm, the presence of the O atoms in the proximity of the N_2^* produced by the next pulse allows for a large production and accumulation of NO and N_xO_y in the effluent. The higher flow rates transport O atoms further into the effluent away from where N and N_2^* are produced by the ionization wave and so reduces the NO initially formed by subsequent pulses. However, some downstream accumulation of N_xO_y occurs for 7 slm after 3 cm.

The production of O_3 depends nearly linearly on the density of its precursor, O atoms. As a result, its inventory, all other conditions being equal, should not depend strongly on the pulse-to-pulse accumulation of its precursor. Species such as H_2O_2 whose production depends on collisions between a pair of its precursor OH (and so depends on the square of its density) have densities and inventories that are much more sensitive to flow rates. Low flow rates produce more accumulation of OH which translates to a higher inventory of H_2O_2. For example, the inventory of H_2O_2 decreases an order of magnitude from 1.3×10^{12} molecules at 2 slm to 1.3×10^{11} molecules at 7 slm. A similar scaling occurs with production of HNO_x whose density and inventory benefits from the accumulation of its precursors, NO and OH, which occurs at low flow rates.

3.3.5 Pulse Repetition Frequency (PRF)

PRF is another method of controlling the residence time and accumulation of species between pulses. The length of the inter-pulse period has significant effects on the density and distribution of the RONS in the effluent of the plasma jet. At high PRFs which produce inter-pulse periods shorter than the gas clearing time, there is an accumulation of RONS in the plume on a pulse-to-pulse basis, enabling further reactions between these species. At lower PRFs where the inter-pulse periods are commensurate or longer than the clearing time of the gas through the device, the ionization wave enters a more pristine and controllable environment in which there are fewer radicals remaining from the prior pulse.

PRF has little effect on the production of primary species during the first pulse, and so our prior discussion on the discharge characteristics of the first pulse for the base case (He/O_2 = 99.8/0.2, -15 kV, 4 slm) in large part applies to all PRF. The PRFs investigated here are 500 kHz, 100 kHz, 50 kHz, 10 kHz and 5 kHz, having interpulse periods of 2 μs, 10 μs, 20 μs, 100μs, and 200 μs. The densities of O and O_3 for a high PRF (100 kHz, 10 μs period) and a low PRF (10 kHz, 100 μs) are shown in Fig. 3.18(a) at the end of the 5^{th} and 10^{th} pulses. This corresponds to a total time of 50 μs at the high PRF and 500 μs at the low PRF. The density of O atoms at 100 kHz is nearly an order of magnitude higher than for 10 kHz, a consequence of there being more accumulation between pulses as the O atoms have flowed a shorter distance. In contrast, the inventory of O_3 is significantly higher for the 10 kHz case. The elapsed time for 10 kHz is ten times that for 100 kHz. The longer elapsed time for 10 kHz has enabled flow to extend the plume of O atoms further downstream and to achieve a near steady state profile for O atom density from the 5^{th} to the 10^{th} pulse. The flow of O atoms further downstream intersect

with more O_2 diffusing into the plume in addition to the longer time that allows more O atoms to react to form O_3.

Densities of O and O_3 are shown in Fig. 3.18(b) at the end of the 30th pulse for PRFs of 500 kHz, 100 kHz, 50 kHz, and 10 kHz (corresponding to elapsed times of 60 μs, 0.3 ms, 0.6 ms, and 3 ms). Since energy deposition per pulse is essentially the same, examining densities after the same number of pulses compares results after the same energy deposition. After 30 pulses at the highest PRF of 500 kHz, O atoms have accumulated in the tube and in the effluent with a maximum density of 5×10^{14} cm^{-3} as the interpulse period is shorter than the gas clearing time. The O atoms have not yet been converted to O_3 due to both the shorter elapsed time and since the plume of O atoms has not yet encountered the high density of O_2 that occurs further downstream where diffusion of ambient air into the jet occurs. As the PRF decreases for the same number of pulses (and essentially the same production of O atoms), the O atom density first increases and then reduces its extent and value. At 100 kHz the plume of O atoms is 2 cm long and the density is above 10^{14} cm^{-3}. At 10 kHz the O atom density is 10^{12} cm^{-3} the plume is only 1 cm at the onset of the next pulse. The plume of the ozone extends beyond that for the O atom at 100 kHz and the length of the O_3 plume continues to increase with lower PRF (longer elapsed time). The diminishing density of O atoms in the plume at low PRF (long elapsed time) compared to high PRF is due, in part to the reaction of O atoms with NO, N_xO_y and H_2O formed during the longer elapsed time.

The densities of NO and N_xO_y for a high PRF (100 kHz, 10 μs period) and a low PRF (10 kHz, 100 μs) are shown in Fig. 3.19(a) at the end of the 5th and 10th pulses. Densities are shown in Fig. 3.19(b) at the end of the 30th pulse for PRFs of 500 kHz, 100 kHz, 50 kHz, and 10 kHz. Operating at the higher PRF enables more accumulation of NO on a pulse to pulse basis prior to

the gas flowing downstream. The density of NO is 10^{12} cm^{-3} after 10 pulses at 100 kHz and 10^{13} cm^{-3} after 30 pulses at 500 kHz. As O atoms enter this environment and react with NO, N_xO_y increases to 2×10^{11} cm^{-3} after only 10 pulses. At the other extreme, lower PRFs allow for the NO created during the pulse to move with the flow further from the active plasma, a location where there would be opportunity for reacting with O to form N_xO_y. The longer interpulse periods also tend to preserve the pulses of NO and N_xO_y formed from the previous pulses, visible in the plumes for 10 kHz. At 5 kHz (not shown), the pulses begin to merge as there is sufficient time for diffusion and mixing with the ambient gases to blur the boundaries

The NO is highly concentrated at high PRF (500 kHz) with densities exceeding 10^{13} cm^{-3} and corresponding densities of N_xO_y of 5×10^{11} cm^{-3}. As the PRF decreases to 100 kHz, the plume spreads while densities drop to 10^{12} cm^{-3} and 10^{11} cm^{-3} for NO and N_xO_y. As the PRF decreases, the peaks of density from previous pulses have flowed downstream and the accumulation of RNS tends to occur more downstream where the axial speed decreases.

The densities of OH and H_2O_2 for a high PRF (100 kHz, 10 μs period) and a low PRF (10 kHz, 100 μs period) are shown in Fig. 3.20(a) at the end of the 5^{th} and 10^{th} pulses. Densities at the end of the 30^{th} pulse are shown in Fig. 3.20(b) for all PRFs. The growth in the density of OH begins at the edge of the dielectric tube at the boundary between the inflowing ambient air and the ionization wave. The maximum density of OH is 2×10^{13} cm^{-3} at this boundary and grows toward the axis (100 kHz PRF) or onto the axis (10 kHz) with subsequent pulses.

The densities on the axis up to 8 cm after 30 pulses for OH, H_2O_2, HNO_x, O_3, NO and N_xO_y are shown in Fig. 3.21 for PRFs of 5 kHz to 500 kHz. The accumulation of the terminal species O_3, H_2O_2 and HNO_x extends along the axis for the low PRF cases due to the longer residence times. Maximum densities of OH and H_2O_2 in the effluent occurs at 10 kHz with peak

values of 7×10^{12} cm^{-3} and 2×10^{12} cm^{-3}, respectively. The limited axial extent of the radicals after 30 pulses at 500 kHz (short residence time) leads to lower concentrations of OH and H_2O_2. The higher PRFs produce locally high densities of O and NO that then facilitate locally higher densities of HNO_x and N_xO_y. At these flow rates and for this geometry, the long interpulse period at the lower PRFs allows RONS formed in the tube to flow out into the plume.

The discussion of densities as a function of PRF for the same number of pulses (and same energy deposition) is complicated by the different elapsed times. To minimize the consequences of elapsed time, densities along the axis are shown in Fig. 3.22 for different PRFs for a total elapsed time of 6 ms. This elapsed time coincides with the completion of the 30^{th} pulse at 5 kHz. For higher PRFs, 30 pulsed discharge periods were simulated followed additional time for flow and chemistry until a total elapsed time of 6 ms. For example, this additional flow time is 5.7 ms for the 100 kHz case. The additional flow time after 30 pulses for all PRFs other than 5 kHz results in a *plug* of reactants flowing downstream. After 30 pulses (shown in Fig. 3.21), the higher PRFs, 500 and 100 kHz, produce the highest densities of NO and the lowest densities of OH and H_2O_2. All PRFs produce similar densities of O_3 with a reduction in the peak density from 3×10^{13} cm^{-3} at 50 kHz to $1 \times 10^{13} cm^{-3}$ at 500 kHz. The higher density of ozone in the 5 kHz case spread over six cm in the effluent and its proximity to the large spatial extent of NO and NO_2 lead to the greater production of N_xO_y.

The total inventories of O_3, NO, N_xO_y, OH, H_2O_2, and HNO_x at the end of the 30^{th} pulse are shown in Fig. 3.23(a) for different PRF. Inventories at the end of 30 pulses with additional flow to 6 ms are shown in Fig. 3.23(b). High repetition rates result in the next pulse entering a more reactive environment. The subsequent discharge pulses will increase the possibility of quenching, recombination or reaction of RONS directly produced by the ionization wave (or

once removed such as Penning reactions) with the reactants from the prior pulse. This phenomenon assists the production of N_xO_y and hinders the production of OH, H_2O_2 and HNO_x. Terminal RONS which depend linearly on their precursors, such as O_3, have lower inventories at higher PRF after a fixed number of pulses due to the shorter elapsed time. These inventories rebound to be commensurate with lower PRF after flowing for the same total time. RONS that depend on multiple collisions, such as N_xO_y have inventories that decrease with increasing PRF for a fixed number of pulses due to the shorter reaction time. The inventories increase with increasing PRF after the same flow time. This reversal in the magnitude of the inventory, favoring high PRF, results from the greater spatial overlap between the precursors at high PRF compared to low PRF. (Recall that for high PRF, the plug of overlapping precursors propagates downstream together.) The increase in the inventory for HNO_x with increasing PRF results from the same spatial overlap in precursor densities. The high inventory of NO for the 5 kHz case appears to be an artifact of having the elapsed time coincide with the end of its 30^{th} pulse.

3.4 Concluding Remarks

In this computational investigation, production of RONS in an oxygen seeded He plasma jet flowing into atmospheric pressure humid air as discussed for different voltage, flow rate, repetition rate and O_2 admixture. Several trends emerged in the analysis of the development of RONS over 30 discharge pulses. The first is the importance of residence time on the reaction hierarchy. Low flow rate and high PRF results in RONS produced on a previous pulse remaining in the discharge tube and near the exit of the tube. (High flow rates and low PRF result in short residence times and the RONS flowing out of the tube.) RONS produced by a subsequent pulse then accumulates, which enables more reactions that produce higher order

RONS that require multiple reactions, such as N_xO_y and HNO_x. A second trend is that over a range of mole fractions, less oxygen in the initial mixture increases the inventory of RONS produced over 30 discharge pulses. This is in part due to a more intense ionization wave that propagates deeper into the plume into which ambient air is diffusing, A third trend is that although higher voltages do deposit more energy, a significant effect of increasing voltage is that the faster, more intense ionization wave penetrates further into the plume. This creates more reactive species in the near field of a longer effluent that react to form the quasi-terminal species, O_3, H_2O_2, N_xO_y, and HNO_x in greater quantities in the far-field. Lastly, the total elapsed time is important. A comparison of the inventories of RONS for different PRFs at the end of the 30^{th} pulse and after the same elapsed time shows that the additional time allows for reactions between species that are in spatial proximity. The higher densities of reactants that accumulate at high PRF flows downstream together and mutually react. The additional flow time increased the overall inventory of RONS requiring multiple reactions for the high PRF cases, such as HNO_x and N_xO_y.

3.5 Figures

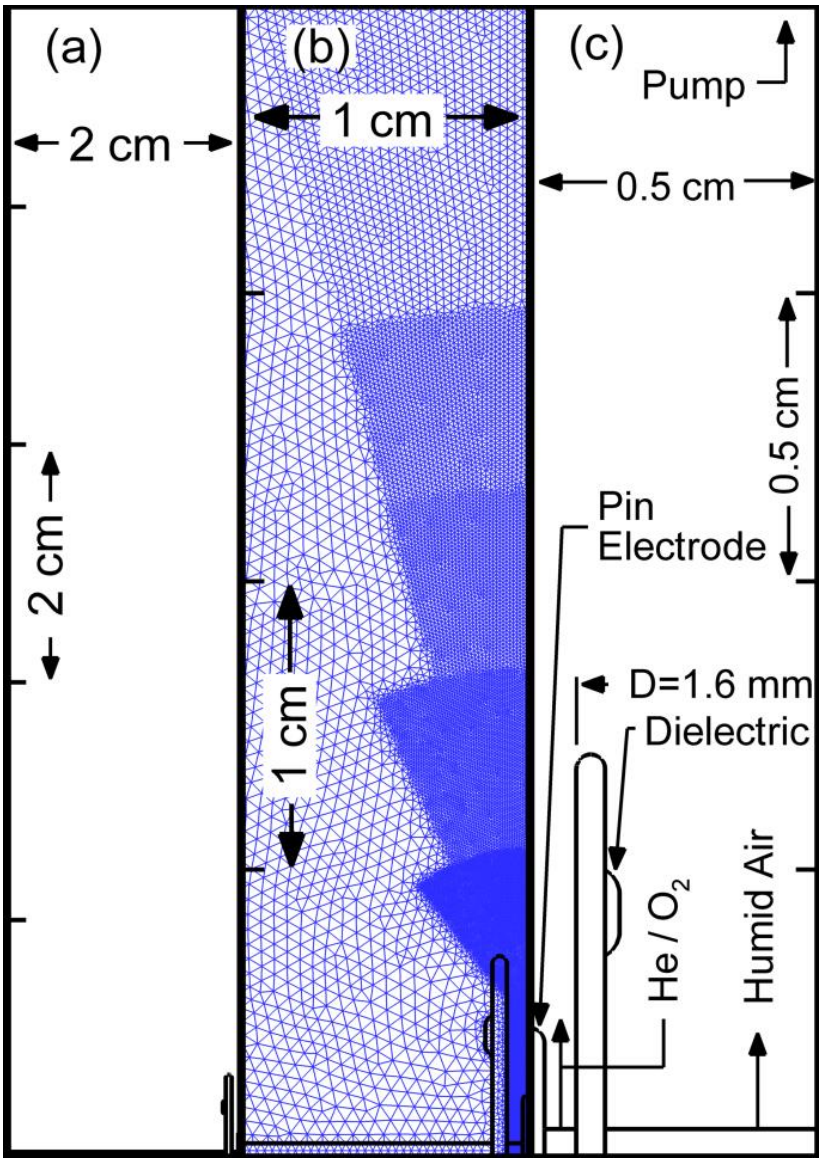

Figure 3.1 Schematic of the cylindrically symmetric plasma jet. (a) The full computational domain is 10 cm by 2 cm. (b) The numerical mesh with refinement zones. (c) Enlargement of the discharge tube.

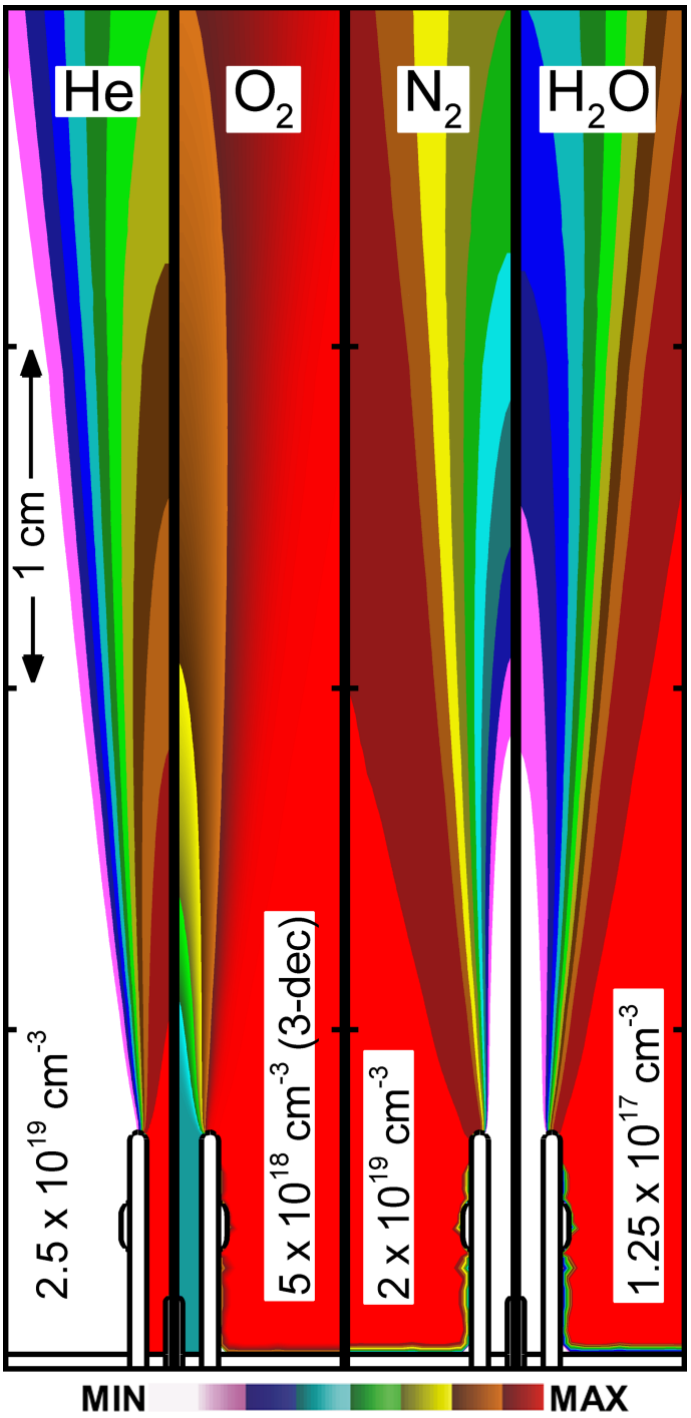

Figure 3.2 He, O_2, N_2 and H_2O concentrations for a flow rate of 4 slm (base case) through the tube and 4 slm in the shroud prior to discharge ignition. The O_2 concentration is over 3 decades from the maximum of 5×10^{18} cm^{-3} to highlight the seeded O_2 flowing with the He.

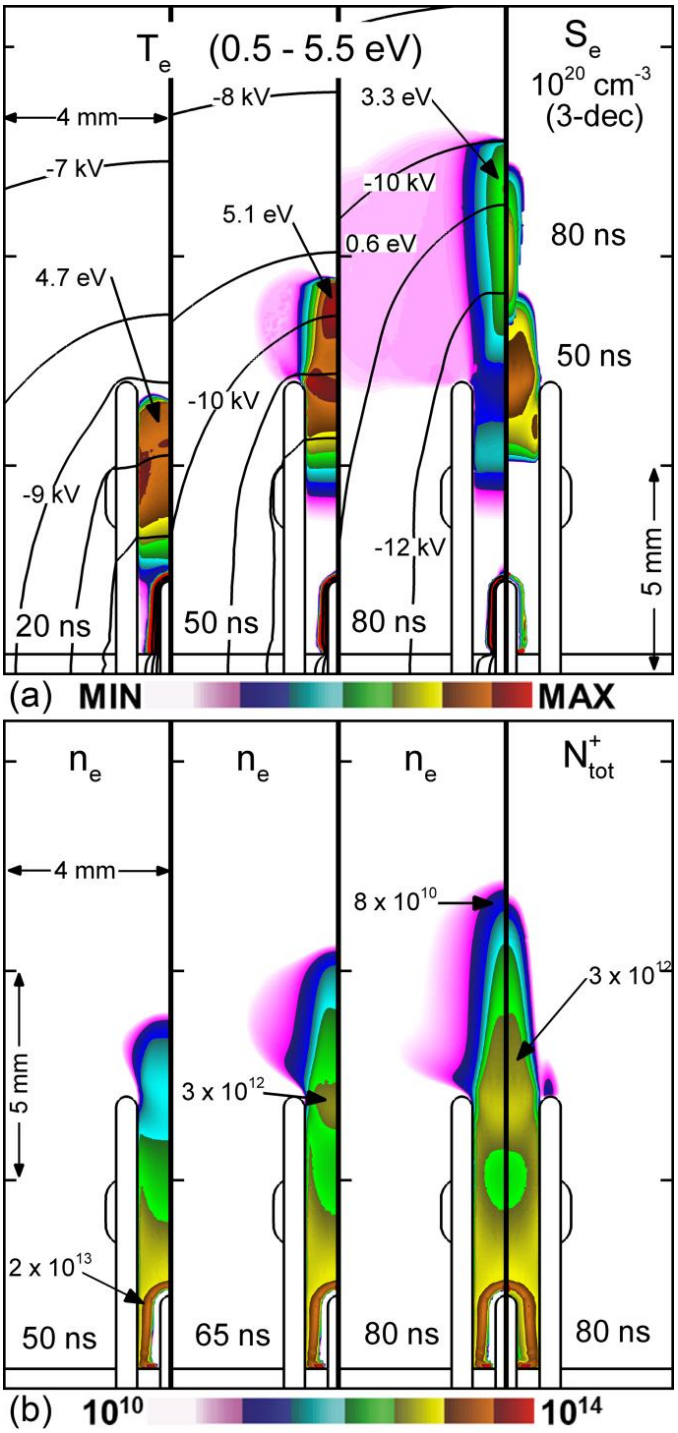

Figure 3.3 Plasma dynamics for the base case of He/O_2 = 99.8/0.2 at 4 slm with -15 kV applied for 80 ns. a) Electron temperature T_e from left to right at 20, 50 and 80 ns on a linear scale between 0.5 – 5.5 eV. Potential contours are at 1 kV intervals. The electron impact ionization source S_e, is shown in the right frame at 50 and 80 ns using a log scale. (b) Electron density showing the propagation of the ionization wave into the effluent at 50, 65 and 80 ns. The cation density at 80 ns is the right image. Contours are on a four decade log-scale.

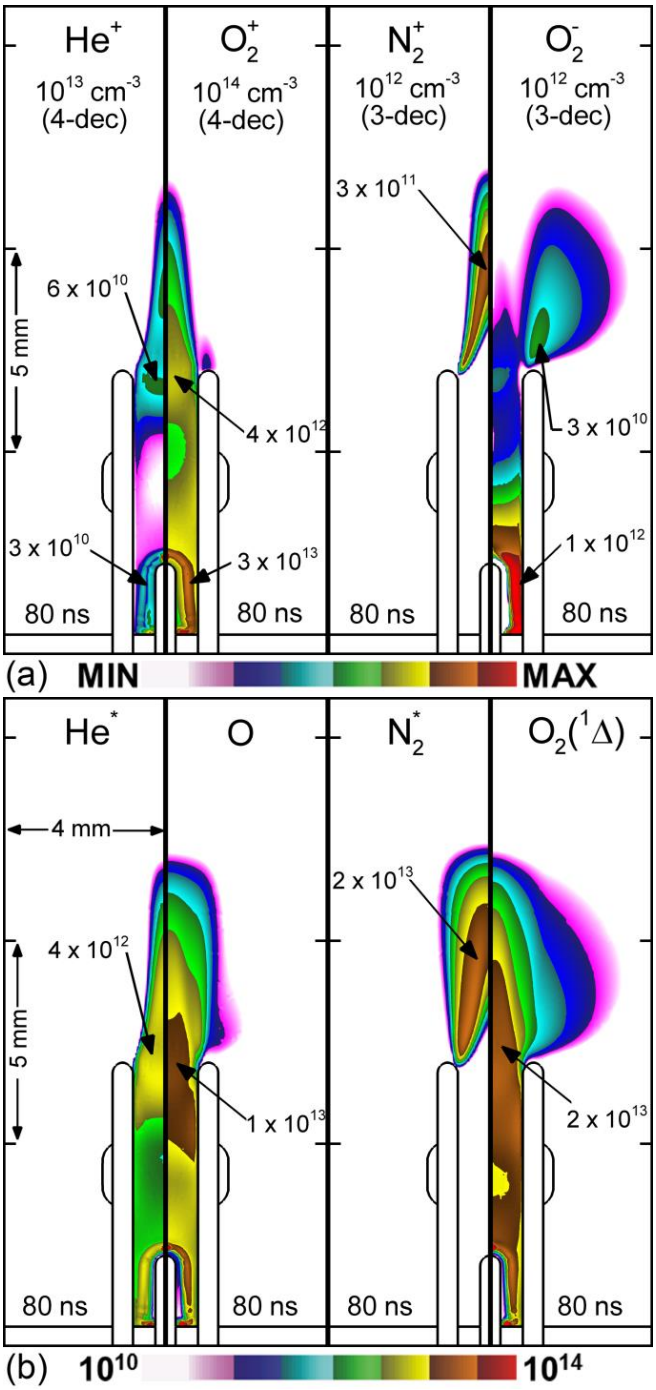

Figure 3.4 Reactant densities for the base case at 80 ns for the first discharge pulse. (a) Cation and anion densities. (b) Densities of primary excited states and radicals. Excited helium density, He^*, is the sum of $He(2^1S)$, $He(2^1P)$, $He(2^3S)$, $He(2^3P)$, He(3S), and He(3P) states. The excited molecular nitrogen, N_2^*, represents $N_2(A^3\Sigma, B^3\Pi, C^3\Pi$, and higher) and follows from the ionization wave intersecting the N_2 from the ambient diffusing into the plume. The lateral spread of $O_2(^1\Delta)$, indicates that the laterally spreading of low energy electrons. Contours are on a four decade log-scale.

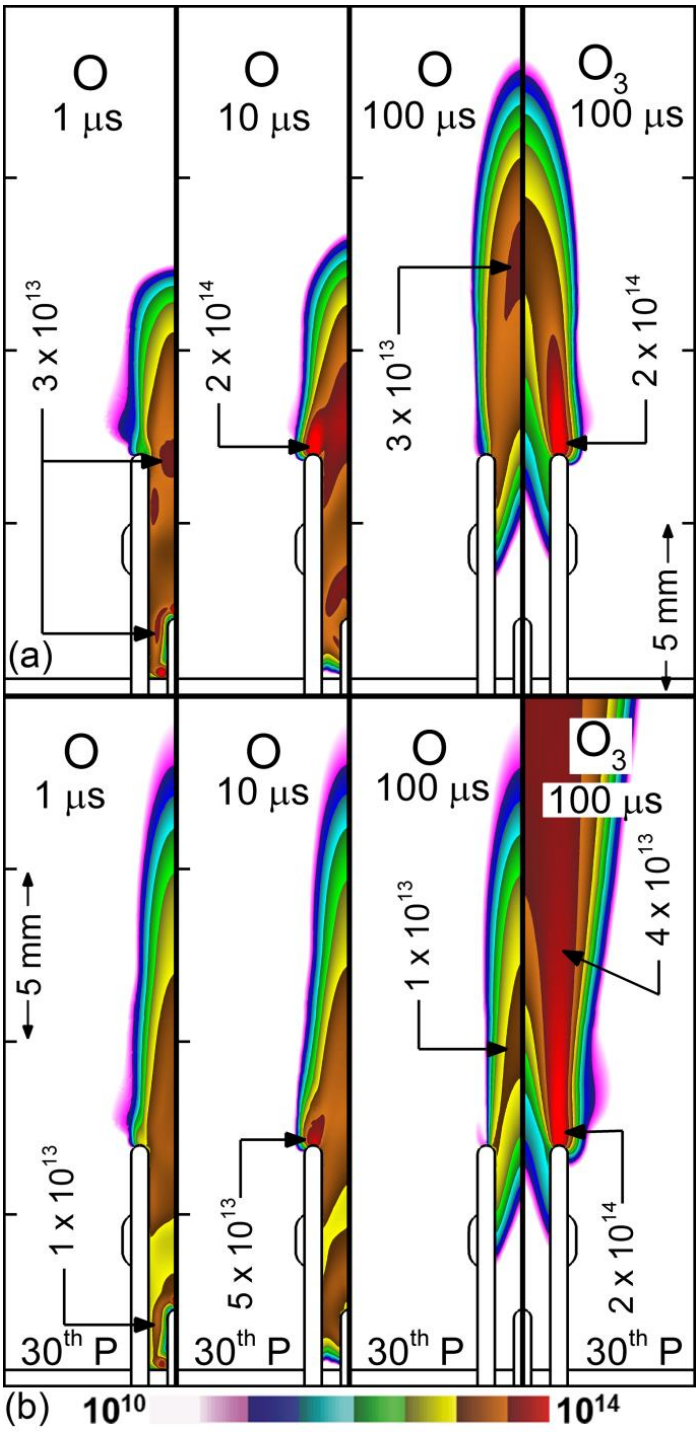

Figure 3.5 Densities of O and O_3 at different times following the (a) first and (b) 30th discharge pulse at a PRF of 10 kHz. The times selected show the environment that the next pulse would encounter at a 1 MHz, 100 kHz, and 10 kHz PRF (left to right). Contours are on a four decade log-scale. At 100 μs, the O atoms produced by the 30th pulse have spread and reacted with O_2 from the ambient to form O_3. The ozone accumulates in the plume.

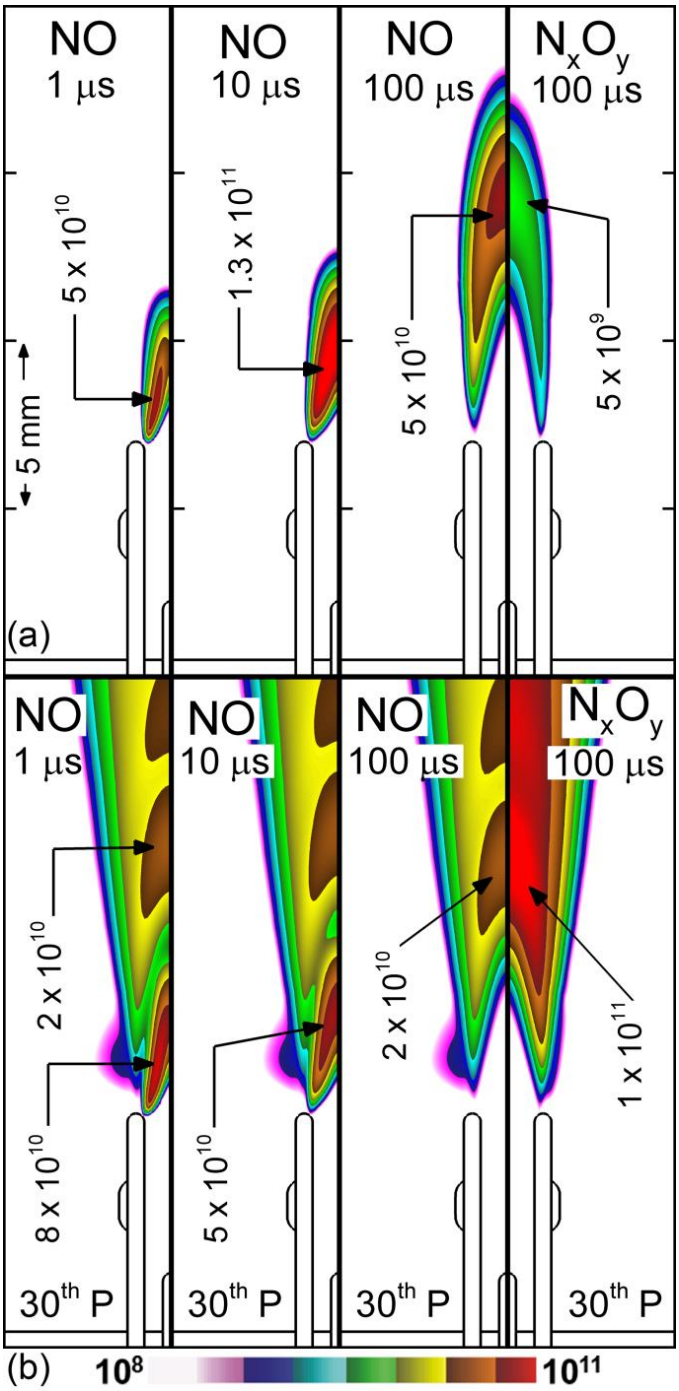

Figure 3.6 Densities of NO and N_xO_y at different times following the (a) first and (b) 30th discharge pulse at a PRF of 10 kHz. The times selected show the environment that the next pulse would encounter at a 1 MHz, 100 kHz, and 10 kHz PRF (left to right). At a PRF of 10 kHz, the NO produced by the previous pulse(s) moves downstream at lower, but significant, densities. N_xO_y has accumulated to 1 x 10^{11} cm^{-3} over the 30 pulses in the effluent. Contours are on a three decade log-scale.

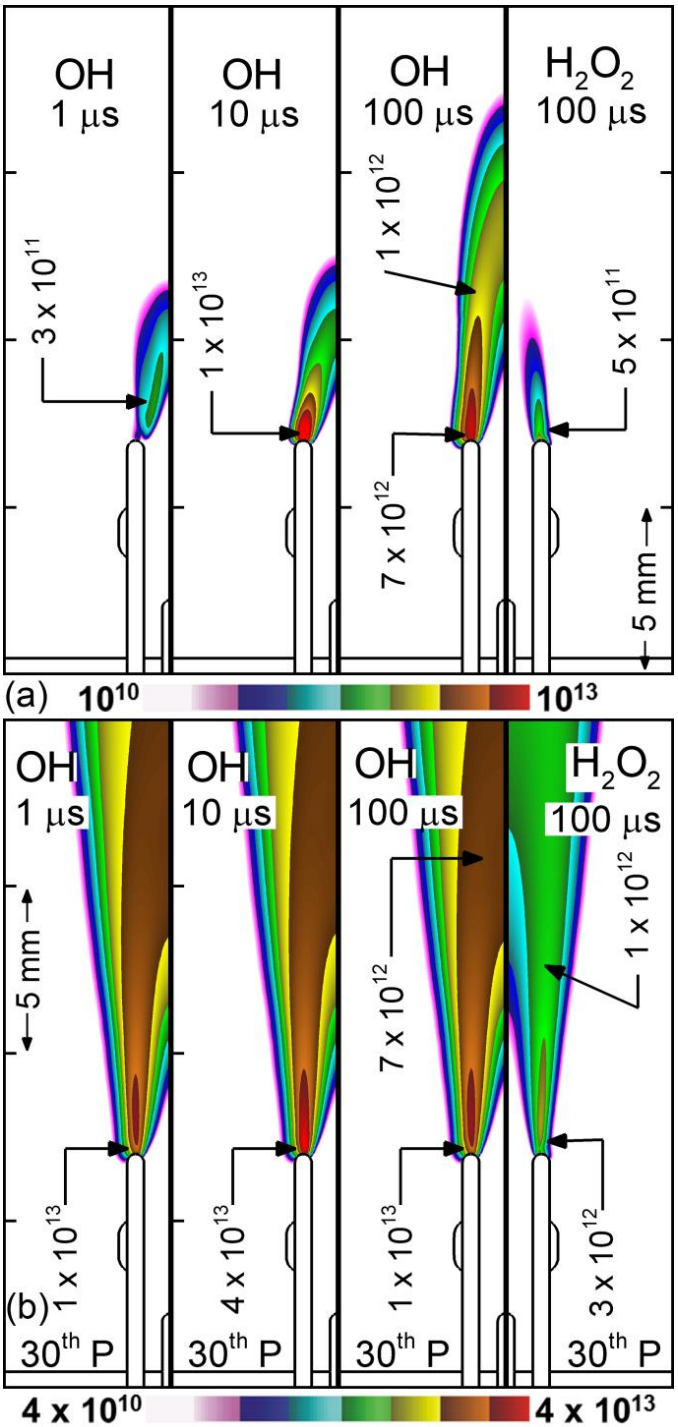

Figure 3.7 Densities of OH and H_2O_2 at different times following the (a) first and (b) 30th discharge pulse at a PRF of 10 kHz. The times selected show the environment that the next pulse would encounter at a 1 MHz, 100 kHz, and 10 kHz PRF (left to right). The OH density is at its maximum at the tip of the dielectric tube at 10 μs, which transitions towards the axis as the humid air diffuses into the helium jet. H_2O_2, primarily created by the reaction of two OH radicals, increases to 1 x 10^{12} cm^{-3} over the 30 pulses in the effluent following the similar spatial trend of OH. Contours are on a three decade log-scale.

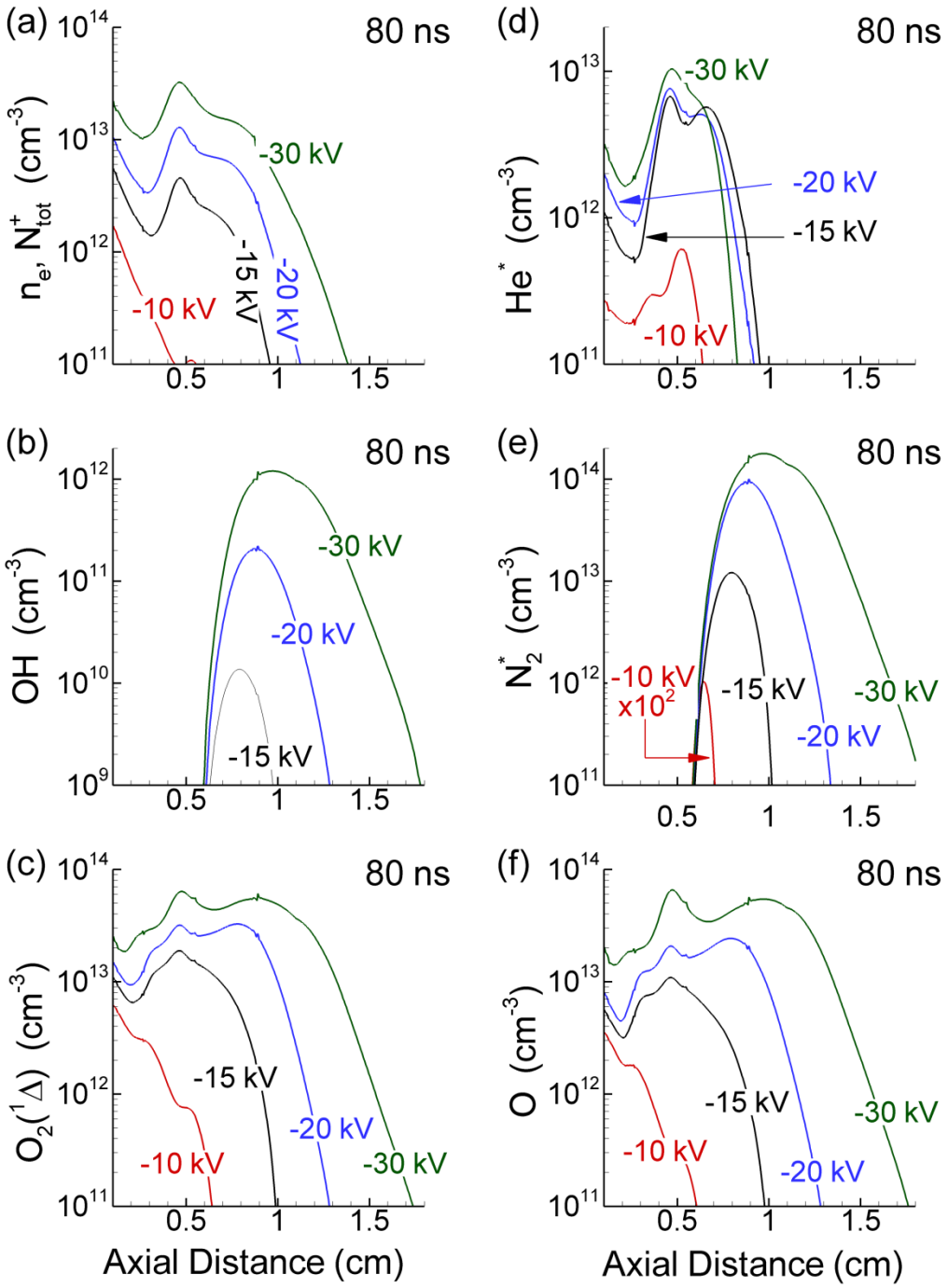

Figure 3.8 Densities on the axis at the end of the first discharge pulse (80 ns) for voltages of -10 kV, -15 kV (base case), -20 kV, and -30 kV. (a) electrons and total cations, (b) OH, (c) $O_2(^1\Delta)$, (d) total He excited states, (e) total N_2 excited states, and (f) O atoms. The end of the tube corresponds to 0.5 cm.

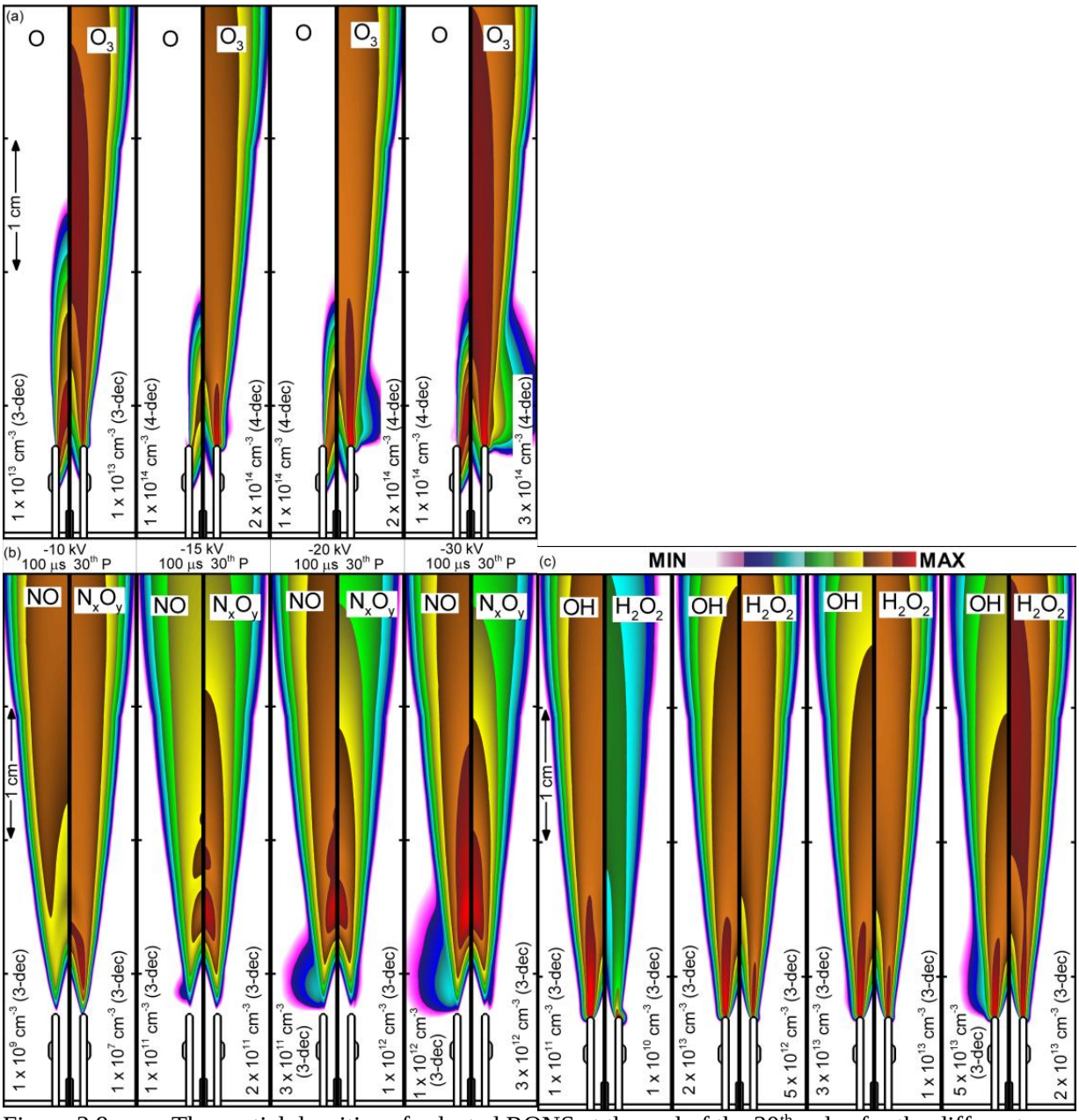

Figure 3.9 The spatial densities of selected RONS at the end of the 30th pulse for the different voltages (-10 kV, -15 kV, -20 kV, -30 kV). The mixture is $He/O_2 = 99.8/0.2$ flowing at 4 slm with a 10 kHz PRF. (a) O atoms and O_3. (b) NO and N_xO_y. (c) OH and H_2O_2. Contours are on a log-scale with the number of decades shown in the frame.

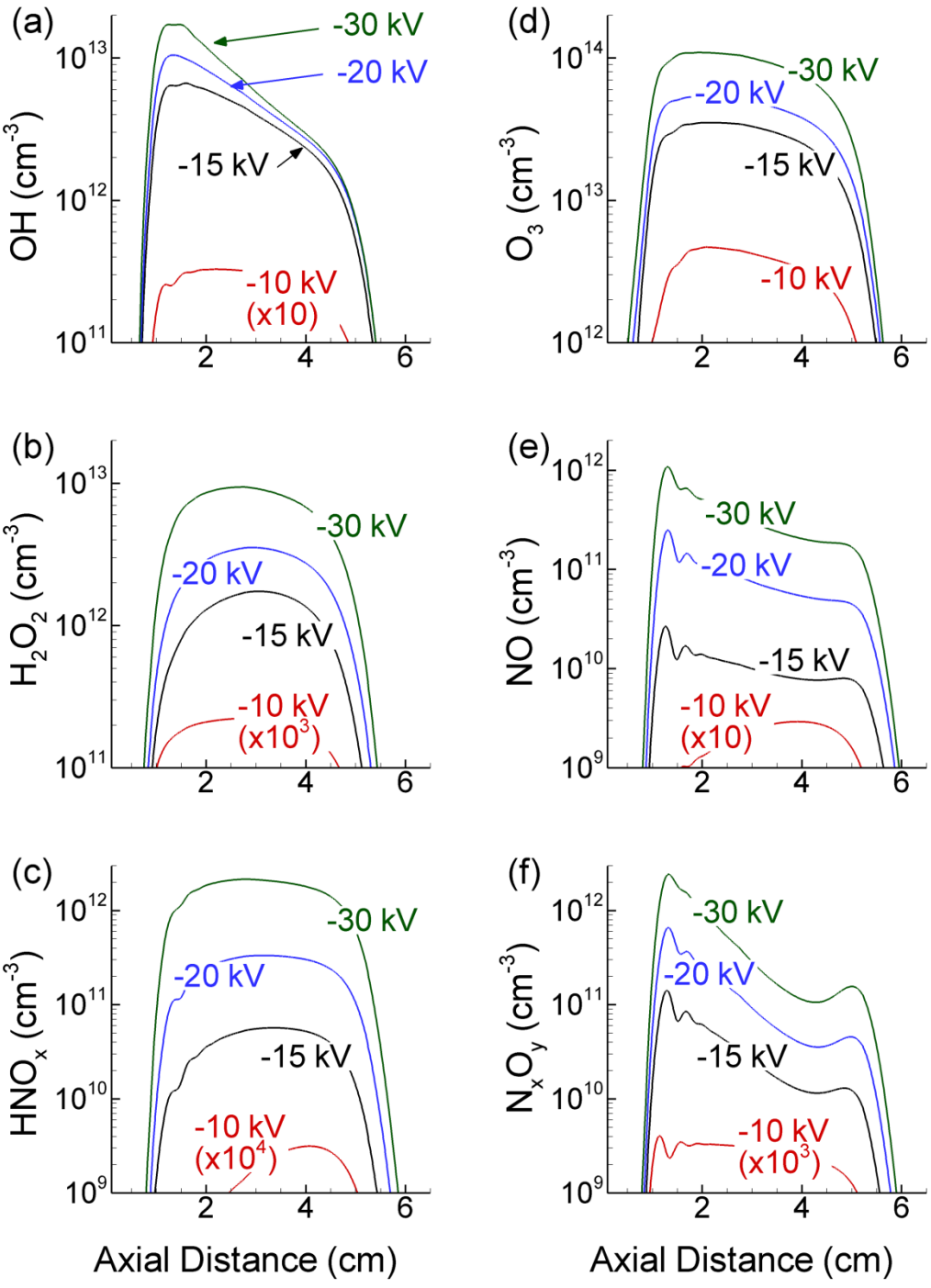

Figure 3.10 Densities on the axis at the end of 30 pulse for a flow rate of 4 slm for voltages from -10 kV to -30 kV. (a) OH, (b) H_2O_2, (c) HNO_x, (d) O_3, (e) NO , and (f) N_xO_y. The end of the tube is at 0.5 cm. At this flow rate and elapsed time, the reactive species in the effluent reach nearly 5.5 cm from the exit of the tube.

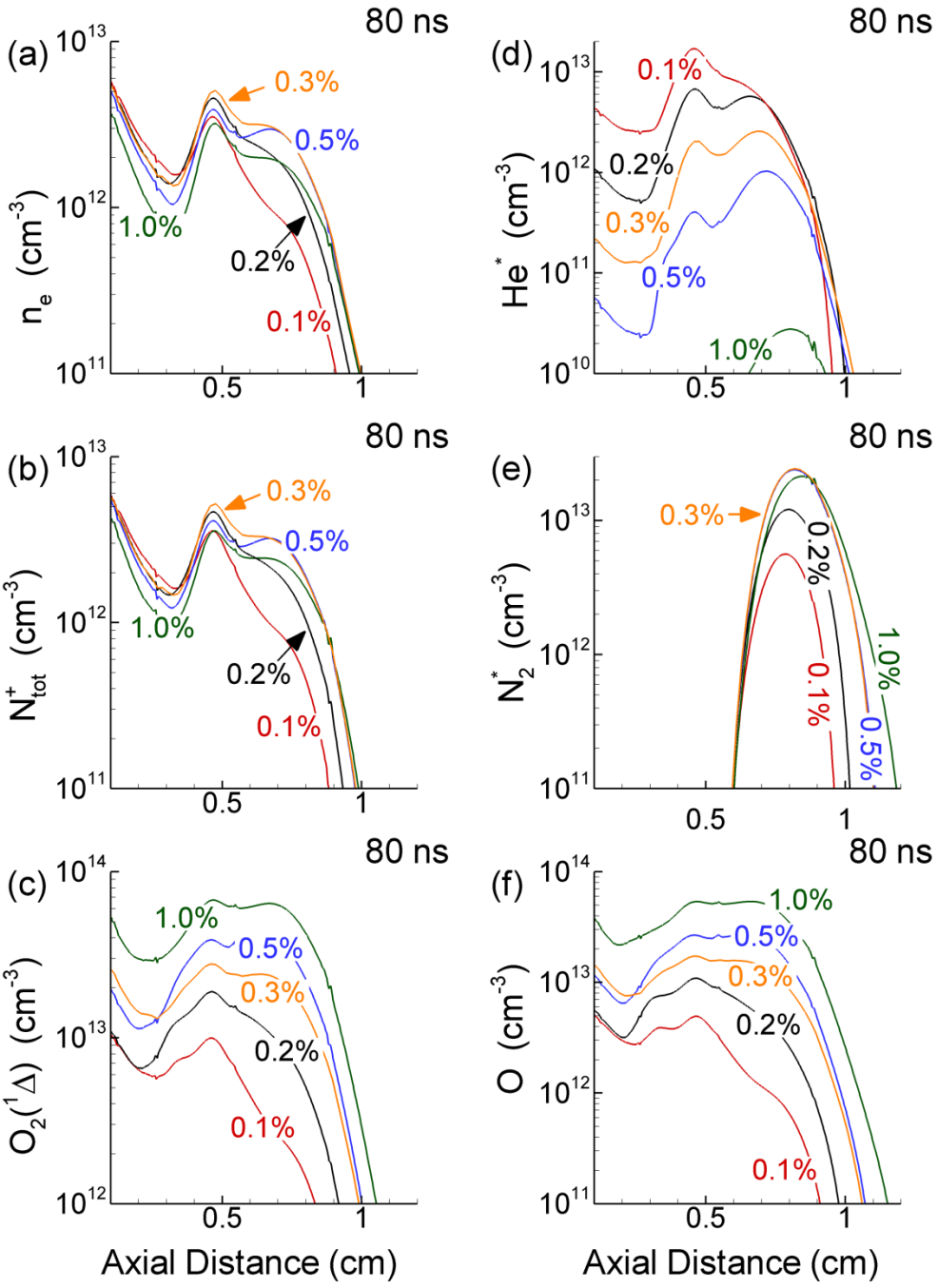

Figure 3.11 Densities on the axis at the end of the first discharge pulse (80 ns) for O_2 concentrations in He of 0.1%, 0.2% (base case), 0.5%, and 1.0%. (a) electrons, (b) total cation, (c) $O_2(^1\Delta)$, (d) total He excited states, (e) total N_2 excited states, and (f) O atoms. The end of the tube is at 0.5 cm.

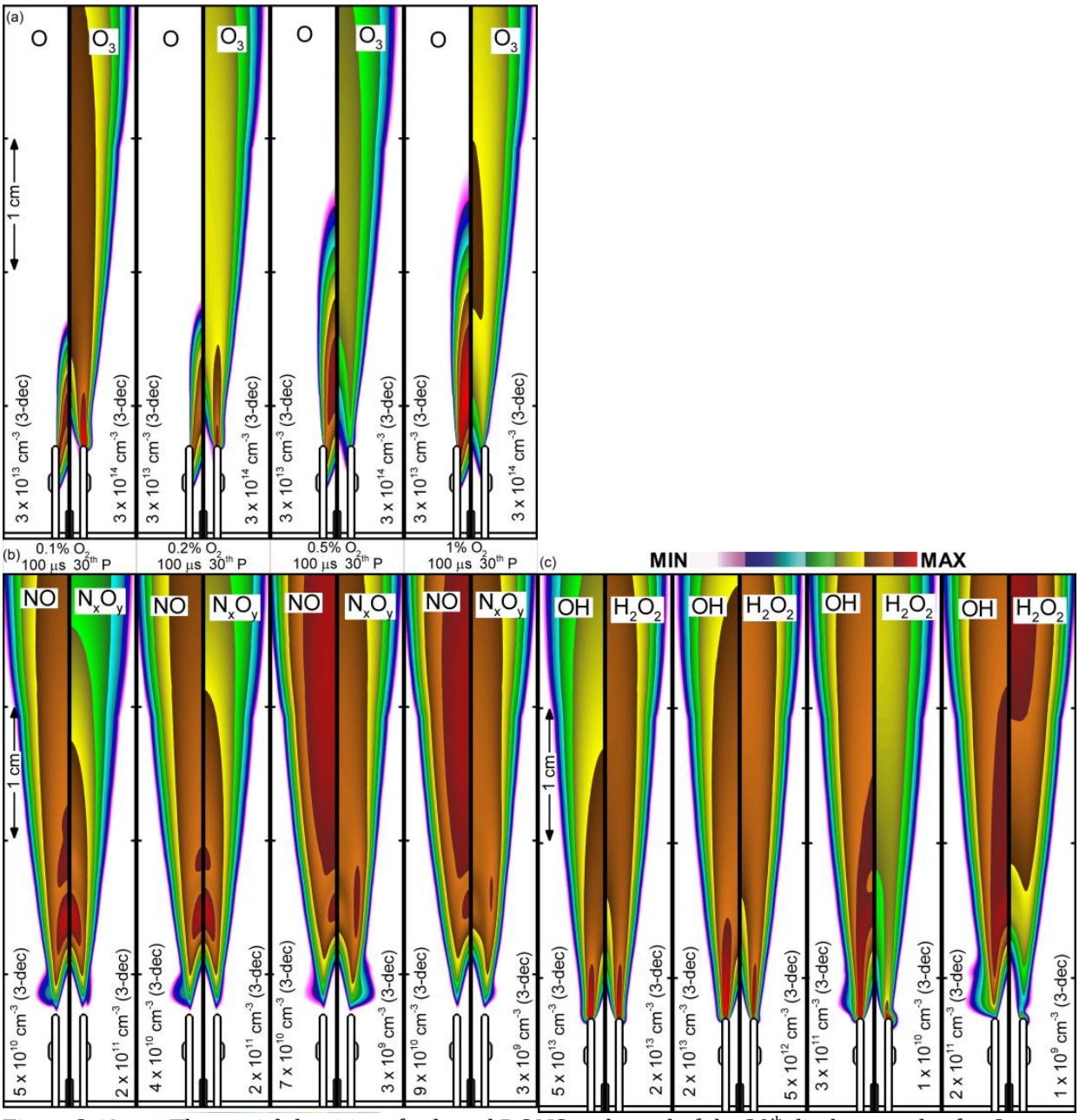

Figure 3.12 The spatial densities of selected RONS at the end of the 30th discharge pulse for O_2 concentration in He of 0.1%, 0.2%, 0.5%, and 1.0% O_2. (a) O atoms and O_3. (b) NO and N_xO_y. (c) OH and H_2O_2. Contours are on a three decade log-scale.

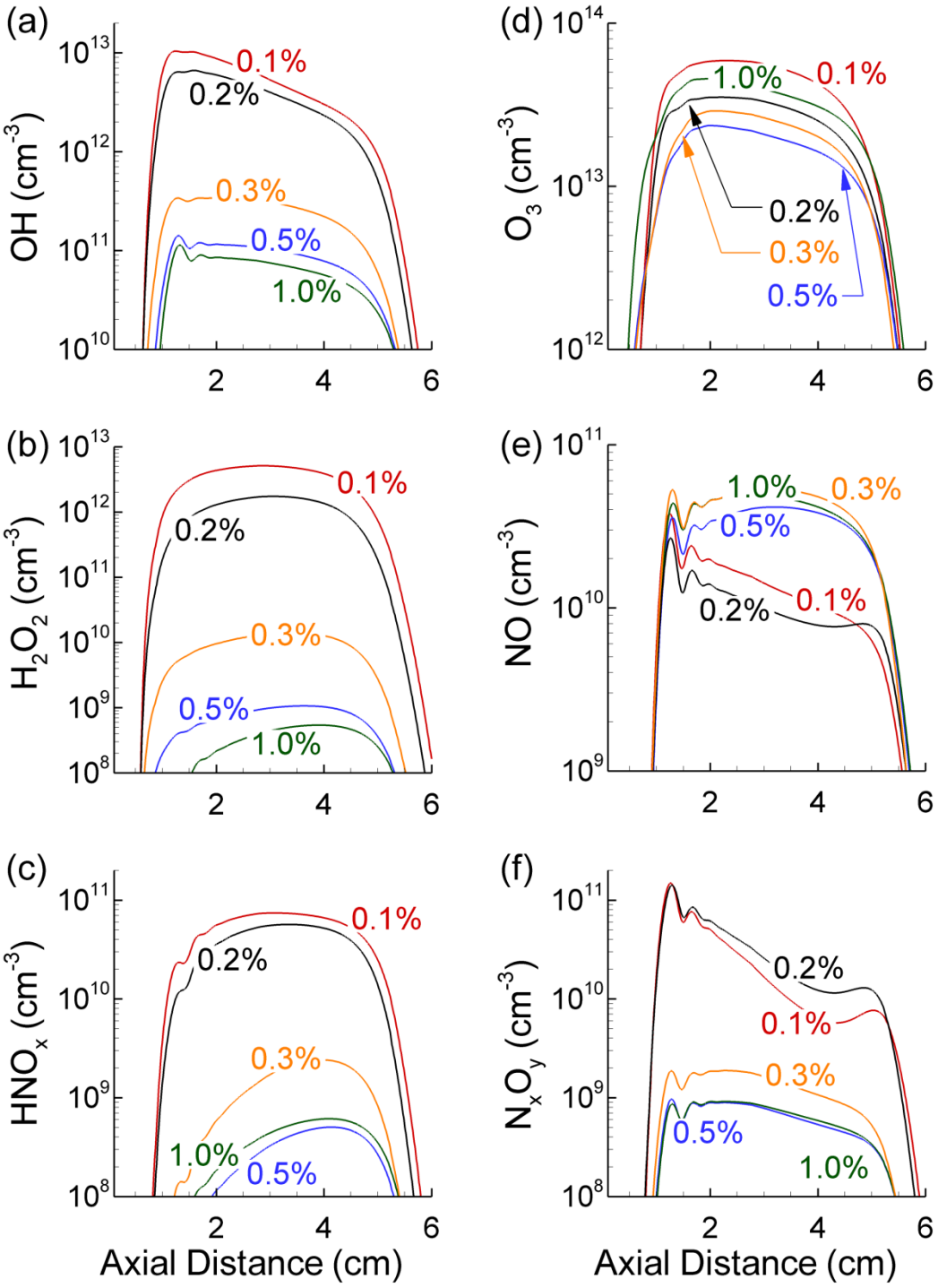

Figure 3.13 Densities on the axis at the end of the 30th discharge pulse for O_2 concentrations in He of 0.1%, 0.2% (base case), 0.3%, 0.5%, and 1.0%. (a) OH, (b) H_2O_2, (c) HNO_x, (d) O_3, (e) NO, and (f) N_xO_y.

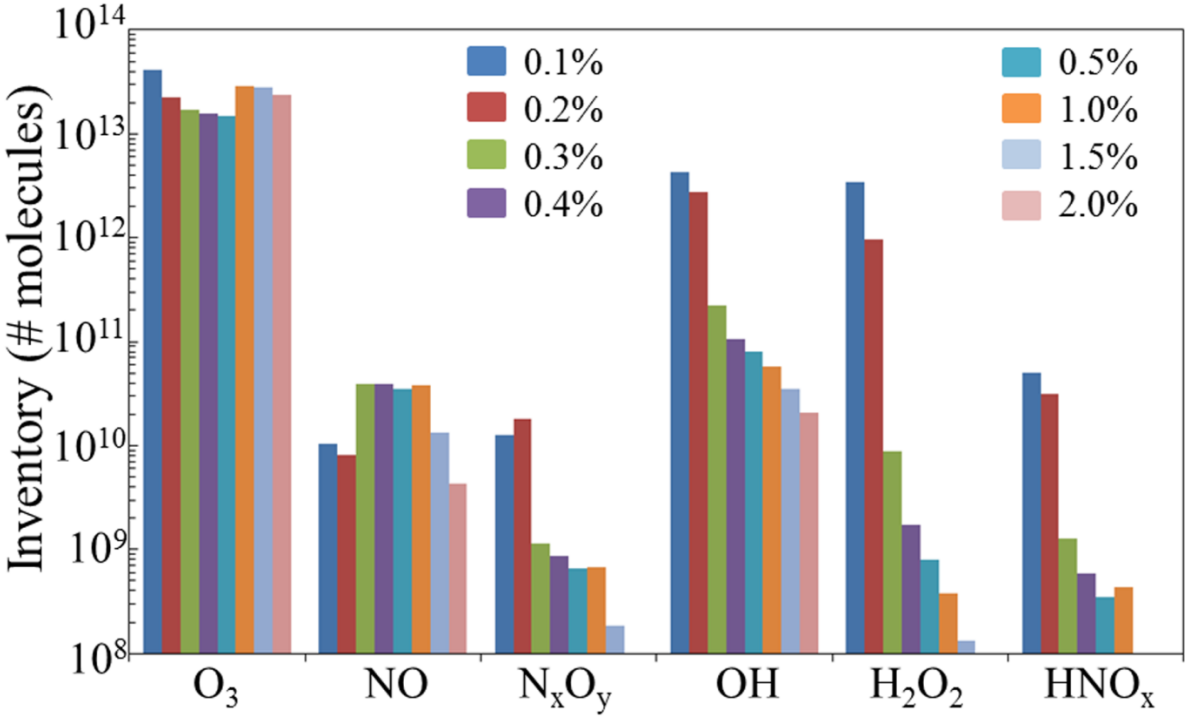

Figure 3.14 The inventory (spatial integral) of selected species at the end of the 30th discharge pulse for O_2 concentrations from 0.1% to 2%. The O_3 inventory is relatively constant. The lower inventory of NO for 0.1 and 0.2% can be attributed to the higher amount of N_xO_y at the end of the 30th pulse. The NO is depleted by reactions with O to form NO_2.

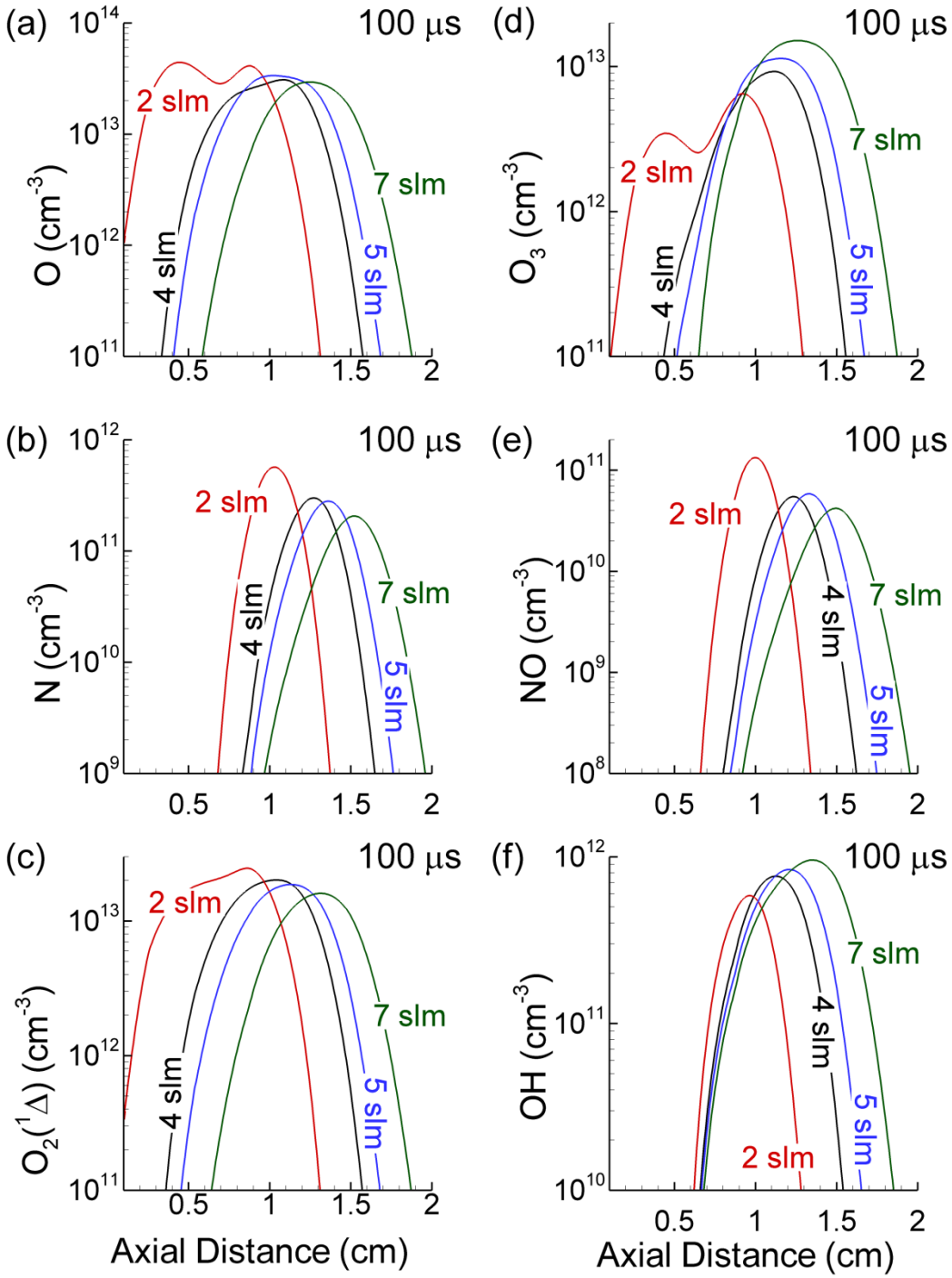

Figure 3.15 Axial densities for flow rates of 2 slm, 4 slm (base case), 5 slm, and 7 slm 100 μs after the of the discharge pulse. (a) O, (b) N, (c) $O_2(^1\Delta)$, (d) O_3, (e) NO, and (f) OH. The end of the tube is at 0.5 cm.

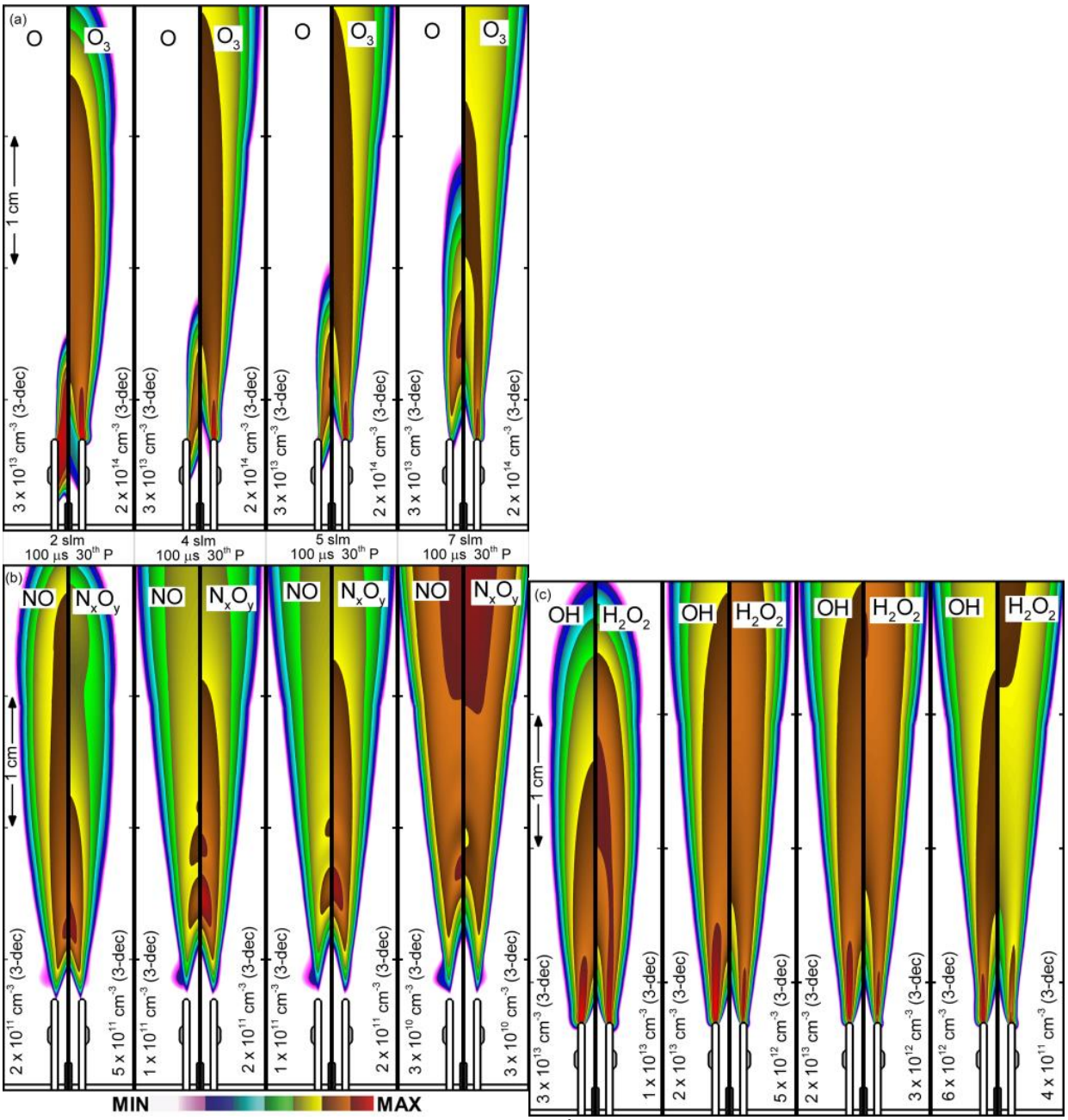

Figure 3.16 Densities of RONS at the end of the 30th discharge pulse for flow rates of 2-7 slm with -15 kV pulses at 10 kHz and He/O_2=99.8/0.2 (a) O and O_3, (b) NO and N_xO_y, (c) OH and H_2O_2. At 2 slm, the primary reactants do not flow out of the tube before the next pulse which allows for accumulation of reactants in the tube. At 7 slm, the primary reactants flow out of the tube and the species formed by the next pulse enter a pristine environment. Contours are on a three decade log-scale from the maximum value listed in the frame.

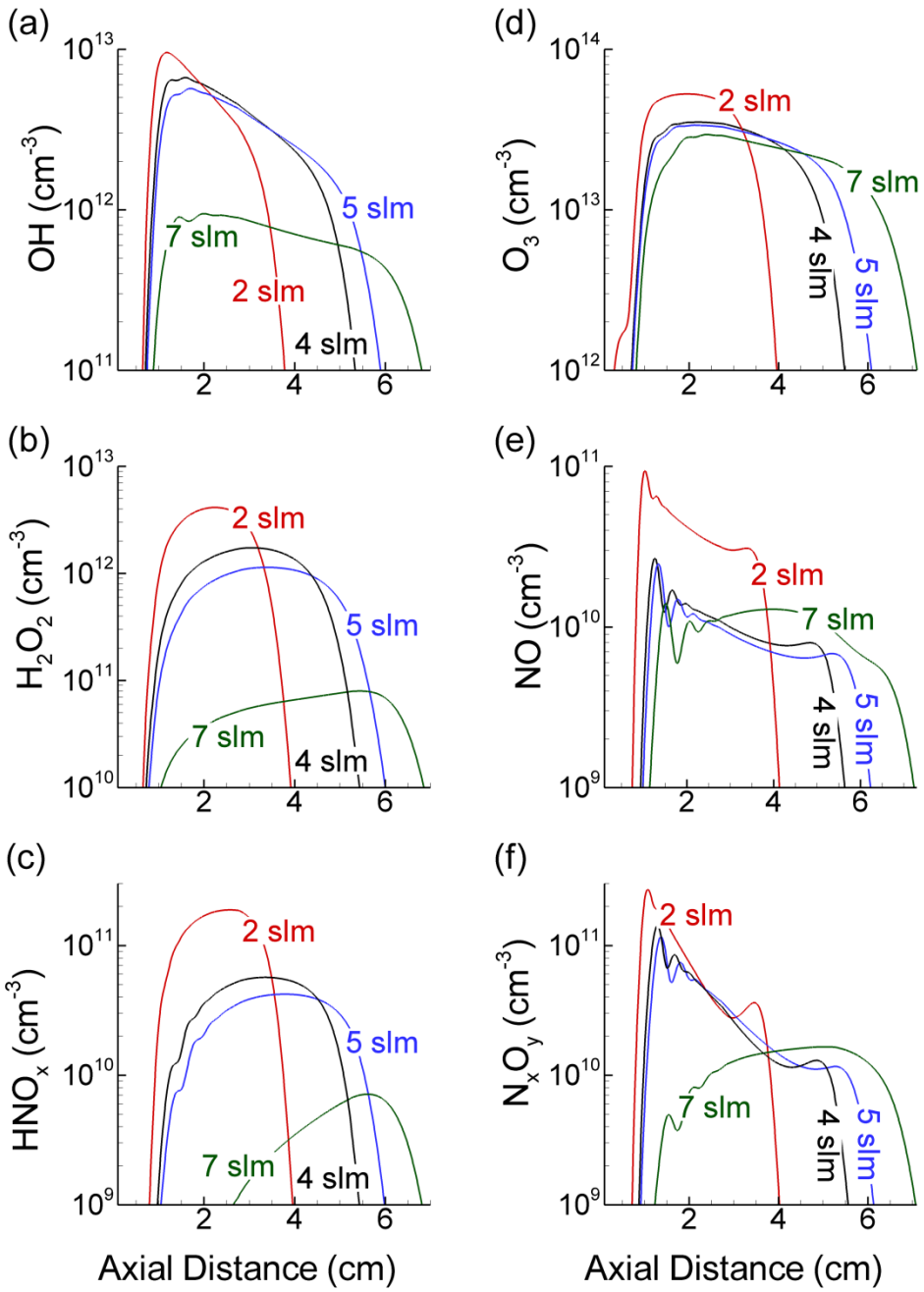

Figure 3.17 Axial densities for flow rates of 2 slm, 4 slm (base case), 5 slm, and 7 slm at the end of the 30th discharge pulse. (a) OH, (b) H_2O_2, (c) HNO_x, (d) O_3, (e) NO, and (f) N_xO_y. The exit of the tube exit is at 0.5 cm.

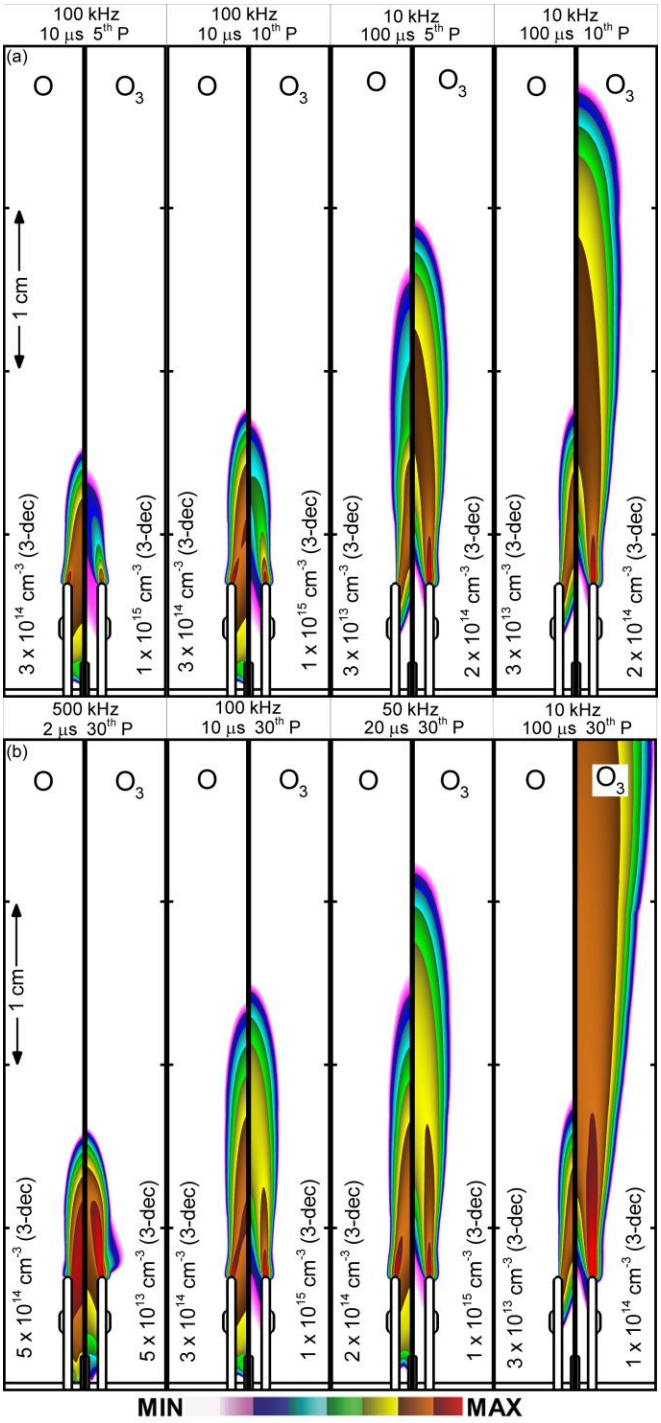

Figure 3.18 O atom and O_3 densities for -15 kV, 4 slm and He/O_2=99.9/0.2. (a) Densities at the end of 5th and 10th discharge pulses for 100 kHz (left) and 10 kHz (right) PRF. The higher PRF allows O atoms to accumulate in the tube. (b) Densities at the end of the 30th discharge pulse for PRFs of 500 kHz to 10 kHz. Note the accumulation of O atoms in the tube in the high PRF cases. The O_3 plume is longer, though less dense for the low PRF cases. Contours are on a three decade log-scale from the maximum value listed on the frame.

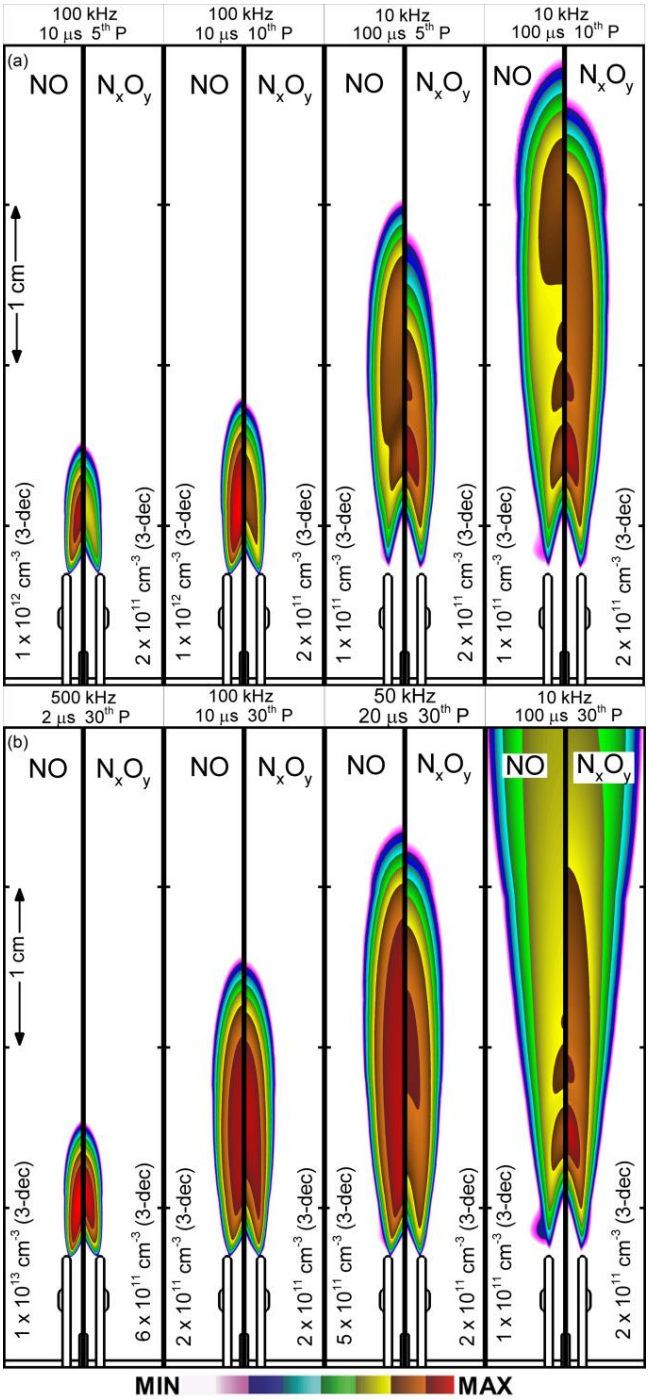

Figure 3.19 NO atom and N_xO_y densities for -15 kV, 4 slm and He/O_2=99.9/0.2. (a) Densities at the end of 5th and 10th pulses for 100 kHz (left) and 10 kHz (right) PRF. (b) Densities at the end of the 30th discharge pulse for PRFs of 500 kHz to 10 kHz. The higher PRF allows NO to accumulate in the tube. For the lower PRFs, NO accumulates at lower densities further downstream. The NO accumulation is significant in the high PRF cases. Contours are on a three decade log-scale with the maximum value noted in each frame.

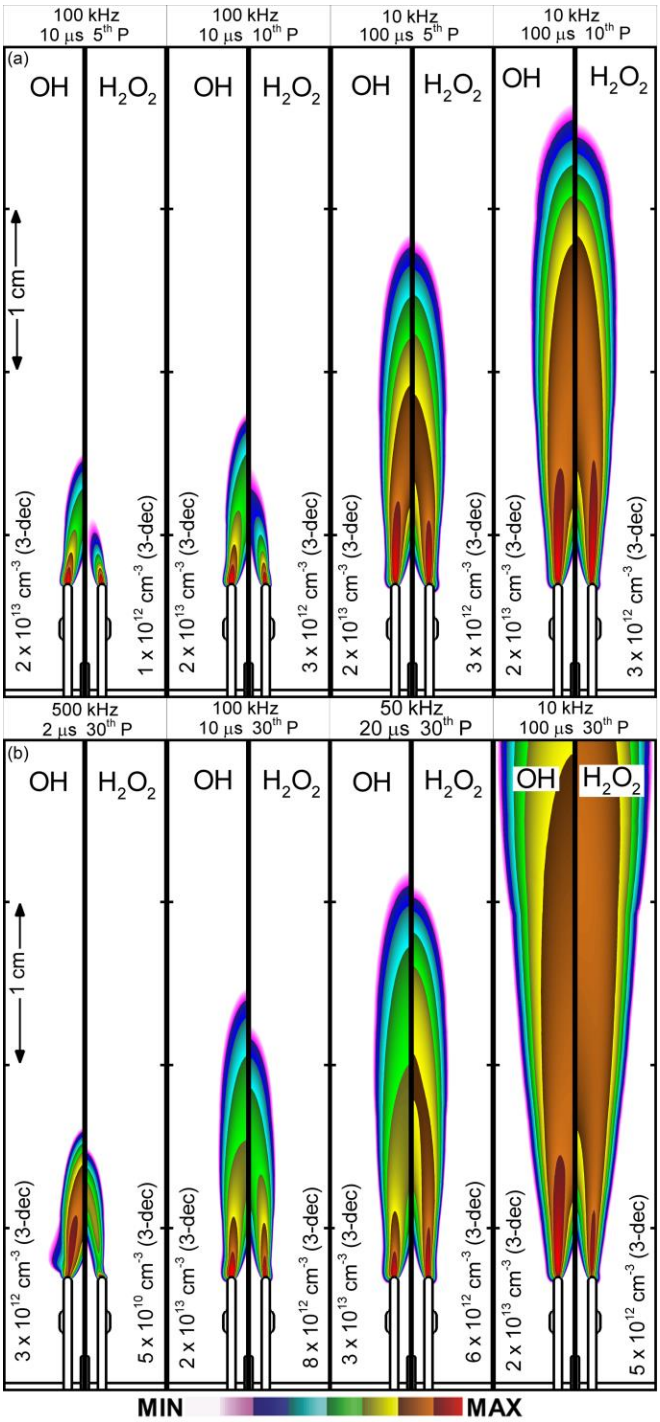

Figure 3.20 OH and H_2O_2 densities for -15 kV, 4 slm and He/O_2=99.9/0.2. (a) Densities at the end of the 5th and 10th pulses for 100 kHz (left) and 10 kHz (right) PRF. (b) Densities at the end of the 30th discharge pulse for PRFs of 500 kHz to 10 kHz. Contours are on a three decade log-scale with the maximum value noted in each frame.

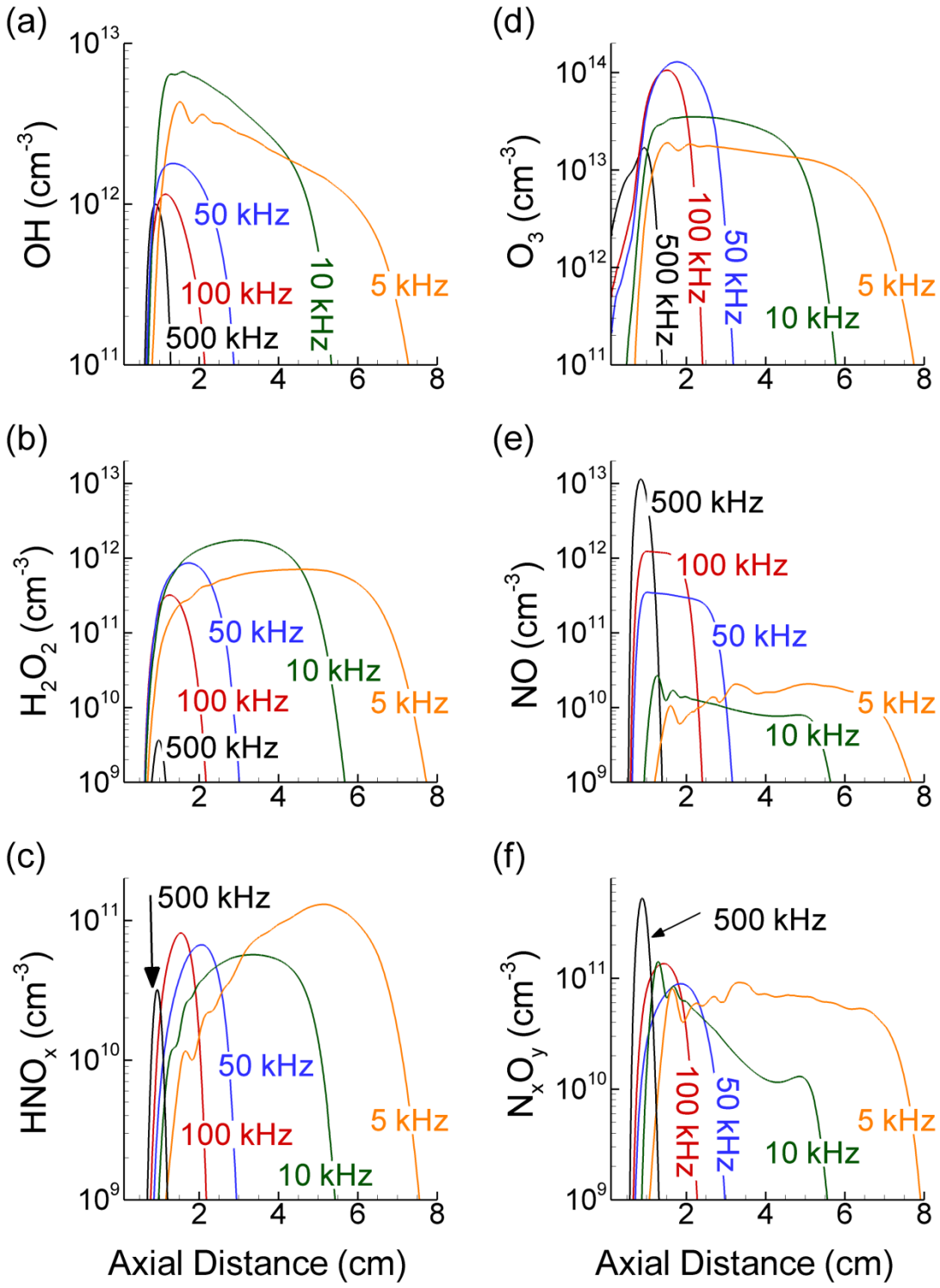

Figure 3.21 Axial densities for PRFs of 500 kHz, 100 kHz, 50 kHz, 10 kHz, and 5 kHz at the end of their 30th discharge pulse. (a) OH, (b) H_2O_2, (c) HNO_x, (d) O_3, (e) NO, and (f) N_xO_y. The end of the tube is at 0.5 cm. The length of the effluent is proportional to the total elapsed time after the 30 pulses at the different PRFs.

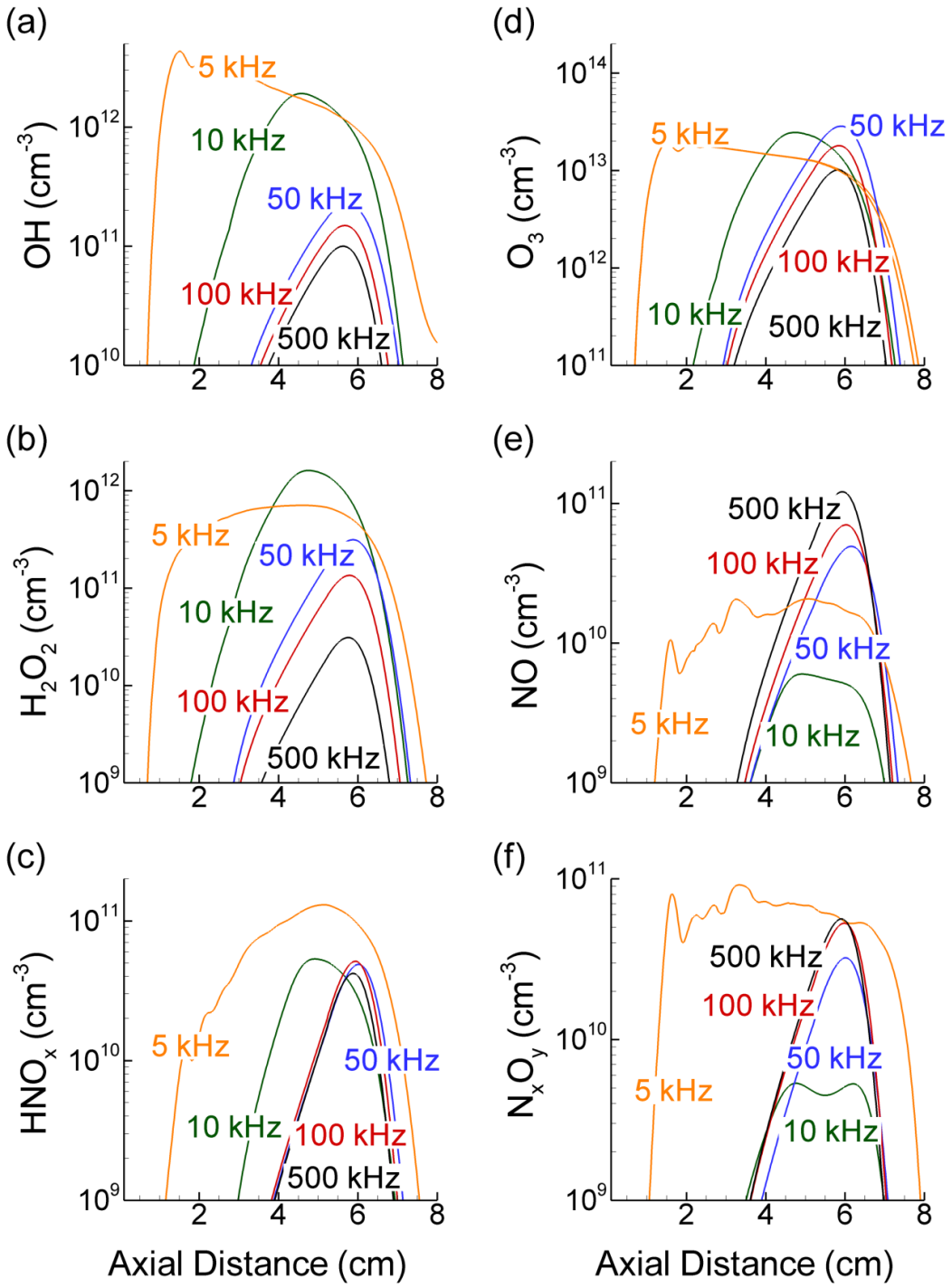

Figure 3.22 Axial densities for PRFs of 500 kHz, 100 kHz, 50 kHz, 10 kHz, and 5 kHz after a total elapsed time of 6 ms (corresponding to the end of the 30th pulse at 5 kHz PRF case. In each case 30 pulses were computed, followed by flow without additional pulsing until a total time of 6 ms. (a) OH, (b) H_2O_2, (c) HNO_x, (d) O_3, (e) NO, and (f) N_xO_y. The end of the tube corresponds to 0.5 cm.

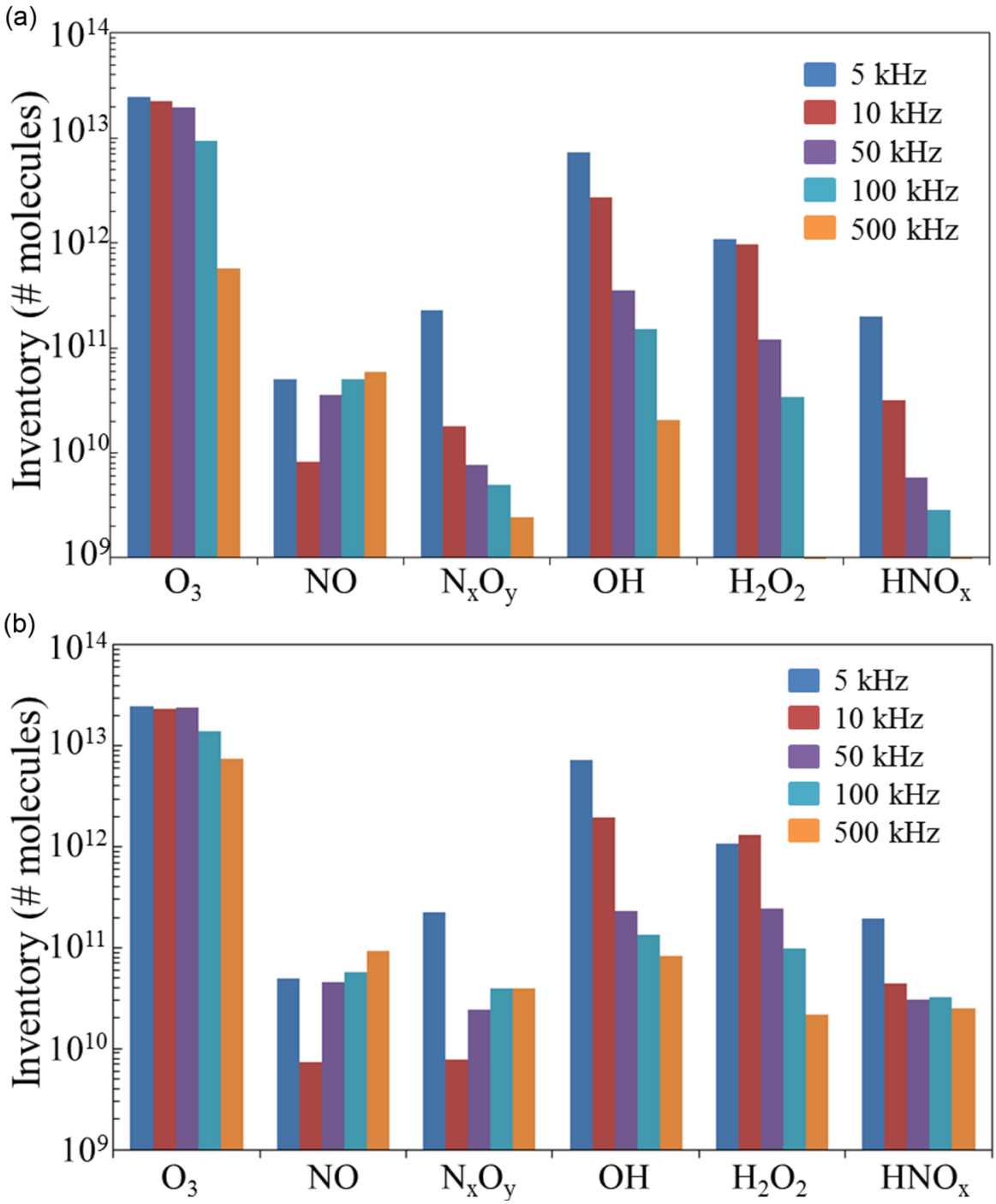

Figure 3.23 Total inventory (integral of the density over the entire volume) for different PRF. (a) Inventory immediately after the completion of the 30th pulse. (b) Inventory after 30 pulses followed by additional flow for the same elapsed time of 6 ms. The additional flow time allows for the creation of O_3, H_2O_2, N_xO_y and HNO_x in the 50, 100, and 500 kHz cases.

3.6 References

[1] A. Schutze, J. Jeong, S. Babayan, J. Park, G. Selwyn and R. Hicks, "The Atmospheric-Pressure Plasma Jet: A Review and Comparison to Other Plasma Sources", Trans. Plasma Sci., **26**, 1685 (1998).

[2] M.G. Kong, G. Kroesen, G. Morfill, T. Nosenko, T. Shimizu, J. van Dijk, and J.L. Zimmerman, "Plasma medicine: an introductory review", New J. Phys. **11**, 115012 (2009).

[3] M. Laroussi, "Low-Temperature Plasmas for Medicine?", Trans. Plasma Sci., **37**, 714 (2009).

[4] M. Laroussi, M. Kong, G. Morfill, and W. Stolz *Plasma Medicine: Applications of Low-Temperature Gas Plasmas in Medicine and Biology*, (Cambridge, Cambridge University Press, 2012), pp. 1-6.

[5] M. Keidar, A. Shashurin, O. Volotskova, M. Stepp, P. Srinivasan, A. Sandler, B. Trink, "Cold atmospheric plasma in cancer therapy", Phys. Plasmas **20**, 057101 (2013).

[6] M. Teschke, J. Kedzierski, E.G. Finantu-Dinu, D. Korzec, and J. Engemann, "High-Speed Photographs of a Dielectric Barrier Atmospheric Pressure Plasma Jet", Trans. Plasma Sci. **33**, 310 (2005).

[7] M. G. Kong, B. N. Ganguly, and R. F. Hicks, "Plasma jets and plasma bullets", Plasma Sources Sci. Technol. **21**, 030201 (2012).

[8] W. Tian and M. Kushner, "Atmospheric Pressure Dielectric Barrier Discharges Interacting with Liquid Covered Tissue", J. Phys. D: Appl. Phys. **47**, 165201 (2014).

[9] X. Lu, M. Laroussi, V. Puech, "On atmospheric-pressure non-equilibrium plasma jets and plasma bullets", Plasma Sources Sci. Technol. **21**, 034005 (2012).

[10] U. Kogelshatz, "Dielectric-barrier Discharges: Their History, Discharge Physics, and Industrial Applications", Plasma Chem. Plasma Proc. **23**, 1 (2013).

[11] I. Kossyi, A. Kostinsky, A. Matveyev, and V. Silakov, "Kinetic scheme of non-equilibrium discharge in nitrogen-oxygen mixtures", Plasma Sources Sci. Technol. **1**, 207 (1992).

[12] A. Fridman, A. Chirokov, and A. Gutsol, "Non-thermal atmospheric pressure discharges", J. Phys. D: Appl. Phys. **38**, R1 (2005).

[13] X. Lu, Z. Jiang, Q. Xiong, Z. Tang, X. Hu, Y. Pan, "An 11 cm long atmospheric pressure cold plasma plume for applications of plasma medicine", Appl. Phys. Lett. **92**, 081502 (2008).

[14] D.B. Graves, "The emerging role of reactive oxygen and nitrogen species in redox biology and some implications for plasma applications to medicine and biology", J. Phys. D: Appl. Phys. **45**, 263001 (2012).

[15] J.S. Sousa, K. Niemi, L.J. Cox, Q. Th. Algwari, T. Gans, and D. O'Connell, "Cold atmospheric pressure plasma jets as sources of singlet delta oxygen for biomedical applications", J. Appl. Phys. **109**, 123302 (2011).

[16] S. Reuter, H. Tresp, K. Wende, M. Hammer, J. Winter, K. Masur, A. Schmidt-Bleker, and K-D. Weltmann, "From RONS to ROS: Tailoring Plasma Jet Treatment of Skin Cells", Trans. Plasma Sci. **40**, 2986 (2012).

[17] S. Reuter, J. Winter, A. Schmidt-Bleker, H. Tresp, M. Hammer, and K-D. Weltmann, "Controlling the Ambient Air Affected Reactive Species Composition in the Effluent of an Argon Plasma Jet", Trans. Plasma Sci. **40**, 2788 (2012).

[18] E. Karakas, M. Akman and M. Laroussi, "The evolution of atmospheric-pressure low-temperature plasma jets: jet current measurements", Plasma Sources Sci. Technol. **21**, 034016 (2012).
[19] J. L. Walsh and M. G. Kong, "Frequency Effects of Plasma Bullets in Atmospheric Glow Discharges", Trans. Plasma Sci. **36**, 954 (2008).
[20] X. Lu, G.V. Naidis, M. Laroussi, and K. Ostrikov, "Guided ionization waves: Theory and experiments", Phys. Rept. **540**, 123 (2014).
[21] E. Robert, V. Sarron, T. Darny, D. Ries, S. Dozias, J. Fontane, L. Joly, and J-M Pouvesle, "Rare gas flow structuration in plasma jet experiments", Plasma Sources Sci. Technol. **23**, 012003 (2014).
[22] B. Lay, R. Moss, S. Rauf, and M. Kushner, "Breakdown Processes in Metal Halide Lamps", Plasma Sources Sci. Technol. **12**, 8 (2003).
[23] Z. Xiong and M. J. Kushner, "Surface corona-bar discharges for production of pre-ionizing UV light for pulsed high-pressure plasmas", J. Phys. D: Appl. Phys. **43**, 505204 (2010).
[24] D. Scharfetter and H. Gummel, "Large-Signal Analysis of a Silicon Read Diode Oscillator", IEEE Trans. Electron Dev. **16**, 1 (1969).
[25] D. Liu, P. Bruggeman, F. Iza, M. Rong, and M. Kong, "Global model of low-temperature atmospheric-pressure He + H_2O plasmas", Plasma Sources Sci. Technol. **19**, 025018 (2010).
[26] T. Murakami, K. Niemi, T. Gans, D. O'Connell, and W. Graham, "Comparison of a global model to semi-kinetic fluid simulations for atmospheric pressure radio-frequency plasmas", Plasma Sources Sci. Technol. **22**, 032001 (2013).
[27] R. Dorai, PhD Thesis Department of Chemical Engineering, University of Illinois at Urbana-Champaign (2002).
[28] Y. Sakiyama, D.B. Graves, H-W. Chang, T. Shimizu, and G. Morfill, "Plasma chemistry model of surface microdischarge in humid air and dynamics of reactive neutral species", J. Phys. D: Appl. Phys. **45**, 425201 (2012).
[29] W. Van Gaens and A. Bogaerts, "Kinetic modelling for an atmospheric pressure argon plasma jet in humid air", J. Phys. D: Appl. Phys. **46**, 275201 (2013).
[30] K. Niemi, J. Waskoenig, N. Sadeghi, T. Gans, and D. O'Connell, "The role of helium metastable states in radio-frequency driven helium-oxygen atmospheric pressure plasma jets: measurement and numerical simulation", Plasma Sources Sci. Technol. **20**, 055005 (2011).
[31] A. V. Phelps, ""Tabulations of Collision Cross Sections and Calculated Transport and Reaction Coefficients for Electron Collisions with O2",JILA Information Center Report No. 28, 1985.
[32] N.A. Popov, "Fast gas heating in a nitrogen-oxygen discharge plasma: I. Kinetic mechanism", J. Phys. D: Appl. Phys. **44**, 285201 (2011).
[33] NIST Chemical Kinetics Database, Standard Reference Database 17, Version 7.0 (Web Version), Release 1.6.8 Data Version 2013.03, http://kinetics.nist.gov/kinetics/index.jsp
[34] Y. Itikawa, "Cross Sections for Electron Collisions with Water Molecules", J. Phys. Chem. Ref. Data **34**, 1 (2005).
[35] B.R. Rowe, F. Vallee, J.L. Queffelec, J.C. Gomet, and M. Morlais, "The yield of oxygen and hydrogen atoms through dissociative recombination of H_2O^+ ions with electrons", J. Phys. Chem. **88**, 845 (1988).

[36] Y. Itikawa, M. Hayashi, A. Ichimura, K. Onda, K. Sakimoto, K. Takayanagi, M. Nakamura, H. Nishimura, and T. Takayanagi, "Cross Sections for Collisions of Electrons and Photons with Nitrogen Molecules" J. Phys. Chem. Ref. Data **15,** 985 (1986).
[37] M. Uddi, N. Jiang, I. Adamovich, and W. Lempert, "Nitric oxide density measurements and air/fuel nanosecond pulse discharges by laser induced fluorescence", J. Phys. D: Appl. Phys. **42**, 075205 (2009).
[38] I. Shkurenkov, D. Burnette, W. Lempert, and I. Adamovich, "Kinetics of excited states and radicals in a nanosecond pulse discharge and afterglow in nitrogen and air", Plasma Sources Sci. Technol. **23**, 065003 (2014).
[39] J. C. Person and D. O. Ham, "Removal of SO_2 and NO_x from stack gases by electron beam irradiation", Radiat. Phys. Chem. **31**, 1 (1988).
[40] J. Walsh and M. Kong, "Contrasting characteristics of linear-field and cross-field atmospheric plasma jets", Appl. Phys. Lett. **93**, 111501 (2008).
[41] C. Bogey and C. Bailly, in V. Armenio, B. Geurts and B. Frohlich (eds.), *Direct and Large-Eddy Simulation VII: Proceedings of the Seventh International ERCOFTAC Workshop on Direct and Large Scale Eddy Simulation VII*, (Springer Science, 2010).
[42] C. Jiang, M. T. Chen, and M. A. Gundersen, "Polarity-induced asymmetric effects of nanosecond pulsed plasma jets", J. Phys. D: Appl. Phys. **42**, 232002 (2009).
[43] G. V. Naidis, "Simulation of streamers propagating along helium jets in ambient air: Polarity-induced effects", Appl. Phys. Lett. **98**, 141501 (2011).
[44] N.Y. Babaeva and M. J. Kushner, "Interaction of multiple atmospheric-pressure micro-plasma jets in small arrays: He/O_2 into humid air", Plasma Sources Sci. Technol. **23**, 015007 (2014).
[45] M. Hoentsch, T. von Woedtke, K-D Weltmann, and J. B. Nebe, "Time-dependent effects of low-temperature atmospheric-pressure argon plasma on epithelial cell attachment, viability and tight junction formation *in vitro*", J. Phys. D: Appl. Phys. **45**, 025206 (2012).
[46] D. Breden and L.L. Raja, "Computational study of the interaction of cold atmospheric helium plasma jets with surfaces", Plasma Sources Sci. Technol. **23**, 065020 (2014).
[47] J. Hon, G. Hager, C. Helms, and K. Truesdell, "Heuristic Method for Evaluating COIL Performance", AIAA J. **34**, 1595 (1996).
[48] H.W. Lee, G.Y. Park, Y.S. Seo, Y.H. Im, S.B. Shim, and H.J. Lee, "Modelling of atmospheric pressure plasmas for biomedical applications", J. Phys. D: Appl. Phys. 44, 053001 (2011).
[49] Y. Xian, X. Lu, S. Wu, P. Chu, and Y. Pan, "Are all atmospheric pressure cold plasma jets electrically driven?", Appl. Phys. Lett. **100**, 123702 (2012).

Chapter 4 APPJ onto Dielectric and Metal Surfaces

4.1 Introduction

Atmospheric pressure plasma jets (APPJs) leverage a channel of noble gas created in air as a guide for an ionization wave, the guided streamer, to deliver plasma produced activation energy to surfaces.[1] The resulting production of UV/VUV radiation, charged and reactive oxygen and nitrogen species (RONS) have motivated the use of APPJs for medical applications, from deactivation of bacteria to cancer treatment.[2-7] Recent investigations of APPJ have addressed surface functionalization [8] of various plastics, interaction with liquids [9,10], and etching.[11,12] The parameters in these studies include the distance between the plasma jet and the surface (touching or not-touching), the adjacency of the electrical ground and the electrical properties of the surface being treating. These parameters, in turn, modify the characteristics of the APPJ, in some cases significantly affecting the plasma properties. For example, in recent experiments the material of the target being treated by an APPJ was varied, with the result being a significantly different response of the plasma.[13,14] Recent computational investigations have also been conducted into the behavior of APPJs interacting with surfaces.[15]

The source of this sensitivity of APPJs to the electrical composition of the surface results, to first order, from the surface being an element in the electrical circuit of the APPJ. Power is applied to the electrodes of the APPJ through which current is delivered to the plasma. The current, in the form of conduction and/or displacement current, must return to electrical ground while conserving the total current through the circuit. Some of this current returns to ground

through displacement current terminating on grounded surfaces surrounding the APPJ, and some of this current returns to ground through the surface being treated. If that surface is a dielectric, the current returning to ground through the surface charges its capacitance, which in turn reduces the voltage drop across the APPJ. This effect is the basis of the dielectric barrier discharge (DBD) in which virtually all the current returns to ground through a dielectric.

In some applications of the APPJ treating a surface, the composition of the surface does not significantly vary from case to case. For example, the APPJ treatment of plastics for surface functionalization to modify the hydrophobic nature of the surface has a negligible effect on the bulk electrical properties of the material.[16] In other applications, the electrical properties of the surface may significantly vary from case to case. For example, in plasma medical applications, the permittivity of a wound can differ depending on the state of the wound during the healing process, and whether the wound is wet or dry.[17,18]

In this paper, we report on results of a computational investigation of an APPJ sustained in He/O_2 flowing into air which is incident onto a surface whose electrical properties are varied. The surface is a thin dielectric whose relative permittivity is varied from 2 to 80, or is a metal. To simplify the investigation, we have assumed that the dielectric materials are ideal and so have zero conductivity. The study is limited to a single discharge pulse onto each surface. The consequences of the electrical properties of the treated material on the properties of the APPJ are discussed. Through the high voltage portion of the pulse, high relative permittivity promotes a faster, more intense, ionization wave that leads to the formation of a conductive channel between the pin electrode and the treated surface. The higher capacity resulting from the higher ε_r leads to more charging at the surface which results in a higher electric field at the surface of the material. The lower permittivity has a weaker ionization wave with less production of charged species and

key neutrals within the conductive channel. However, the lower permittivity promotes penetration of the electric field into the material as well as the creation of a surface ionization wave.

Following a brief description of the model in Sec. 4.2, characteristics of the APPJ onto surfaces having different electrical properties during and after a single discharge pulse are discussed in in Sec. 4.3. Concluding remarks are provided in Sec. 4.4.

4.2 Description of the Model

The 2-dimensional cylindrically symmetric model used for this computational investigation is *nonPDPSIM,* whose algorithms are discussed in Ref. [19]. Briefly, *nonPDPSIM* is plasma hydrodynamics model that solves Poisson's equation simultaneously with charged species transport using fully implicit techniques. Using time-slicing techniques, the electron energy equation with transport coefficients provided by solutions of Boltzmann equation, neutral species transport equations, radiation transport and Navier-Stokes equations for bulk fluid transport are sequentially integrated. During the discharge pulses, time steps for modules vary from picoseconds for charged particle transport to hundreds of ps for fluid transport. The reaction mechanism discussed in Ref. [20], includes 51 neutral and charged species and 441 reactions.

The computational configuration uses an unstructured mesh and addresses a downward pointing plasma jet incident onto a surface of varying electrical composition. The computational domain is 19.5 mm by 8.8 mm, and has 7,200 nodes of which 5,400 are plasma nodes with various refinement zones as shown in Fig. 1. The unstructured, triangular mesh had spacing of 50 μm at the tip of the electrode, 100 μm at the surface of the dielectric and 300 μm in the

periphery of the mesh. A He/O_2 = 99.8/0.2 gas mixture at atmospheric pressure is flowed through the inner tube at 4 slm, conditions inspired by several experiments.[21-24] Humid air ($N_2/O_2/H_2O$ = 79.5/20/0.5) flows coaxially to the tube from the top surface at 4 slm to reduce the propensity for shear instabilities. All injected gases exit through a side port which is grounded. The material surface is 7.5 mm from the exit of the tube. The ring electrode has been treated as a dielectric for these simulations.

The electrical properties of the materials of the surface upon which the jet is incident were selected based on possible applications of APPJs. The relative permittivity ($\varepsilon_r = \varepsilon/\varepsilon_o$) of the material has values of ε_r = 2, 5, 10 and 80, and metal. The low value of ε_r = 2 represents organic polymers such as polyethylene (ε_r = 2.25) and fluorocarbon polymers such as Teflon (ε_r = 2.1) [25]. An intermediate value of ε_r = 5 was chosen to represent biological tissue [26]. An additional intermediate value of ε_r = 10 was chosen to represent materials such as glass (ε_r = 5-10), graphite (ε_r = 10-15), and silicon (ε_r = 11.7).[25,27] Liquid water surfaces are represented by ε_r = 80. The metal surface provides a reference. All non-metal materials had zero conductivity. The thickness of the material was 5 mm in order to allow propagation of the electric field into the dielectric material prior to reaching the ground plate beneath the material.

4.3 APPJ Properties Dependent on Surface Properties

In each case, the He/O_2 mixture was first flowed through the tube and into humid air to establish the flow field, typically for 8 ms. The steady state flow field is shown in Fig. 2 for He, O_2, N_2 and H_2O. The average speed of the flow in the dielectric tube is 42 m/s corresponding to a Reynolds number of 630 indicating laminar flow.[28] After the profile was established, one -15 kV pulse was applied to the pin electrode creating the discharge and launching an ionization

wave. The voltage pulse has a 5 ns rise time, 75 ns duration at -15 kV and a 20 ns fall time to zero for a total duration of 100 ns. There is no ballast resistance in series with the discharge. In each case, an ionization wave is launched at the pin electrode and propagates through the helium channel inside the tube, out of the tube into the ambient air and strikes the surface. The properties of the APPJ will be discussed for early during the pulse when the ionization wave touches the surface, 10 ns after touching the surface, at 80 ns which is the end of the high voltage portion of the pulse, and for 100 ns which is the time the voltage is terminated. In summary, the electron avalanche quickly moves from the tip of the pin electrode to the wall, charges the wall until the exit, and then moves on axis upon exiting the tube. The effluent is near room temperature; however, the *plasma bullet* is typically 2-3 eV in the head of the ionization wave [29,30] with an electron density ranging from 1-2 × 10^{13} cm^{-3}.[7] The structure of the guided streamer is similar to a conventional atmospheric pressure streamer where space charge produced electric field enhancement in the head of the streamer generates an electron avalanche. The guided aspect of propagation results from the *E/N* (electric field/gas number density) required for avalanche is lower in the rare-gas dominated plume than in the surrounding air. The avalanche is then prevented from spreading laterally into the air.

4.3.1 Touching the Surface

As the guided ionization wave exits the dielectric tube, the spatial distribution of the electric field is determined by many factors. The space charge in the head of the ionization wave (IW) produces the electric field that avalanches the streamer and sustains the IW. The axial electric field in the plasma column behind the IW is determined by the conductivity of the column. The radial electric field is determined by the effective ambipolar forces that confine the

IW and, inside the tube, the charging of and dielectric properties of the tube itself. All of these properties are in turn sensitive to the proximity of the electrical ground and the capacitance (or dielectric properties) of solid materials between the IW and ground. The IW is a transient phenomenon and so the current from the metal of the powered electrode to the metal of the ground contains both conduction and displacement currents. The conduction current in large part resides from the electrode through the plasma column to the head of the IW. The current transitions from conduction to displacement current in the head of IW and continues as displacement current to the ground plane.

The dielectric properties of the materials between the IW and ground affect the propagation of the IW in at least two ways. First, the continuity of the electric displacement vector, $\vec{D} = \varepsilon\vec{E}$ reapportions electric field magnitude from regions of larger ε (here, solid material) into regions of smaller ε (the gas and plasma). Second, when the conduction current of the IW and plasma column intersect with the solid dielectric, the solid electrically charges which in turn produces electric fields.

The electron temperature, T_e, electron impact ionization source, S_e, magnitude of the electric field, E, and electric potential contours are shown in Fig. 3 for ground-covering-dielectrics with relative permittivities of ε_r = 2 to 80 and for a metal substrate. The times of the images are when the IW touches the material. The speed of the ionization wave is indicated by the time of impact time shown in the figure. In general, the speed of the IW, the magnitude of the ionization source and the peak electric field all increase with increasing ε_r (and to the metal). The speed of the ionization waves increases from 5.2 × 10^7 cm-s^{-1} to 6.8 × 10^7 cm-s^{-1}, S_e increases from 5.2 × 10^{20} $cm^{-3}s^{-1}$ to 2.5 × 10^{21} $cm^{-3}s^{-1}$, T_e increases from 5.3 eV to 6.3 eV and the electric field increases from 22 to 28 kV/cm (85 Td to 110 Td, 1 Td = 10^{-17} V-cm^2) as ε_r

increases from 2 to 80. Prior to striking the surface, the increase in these quantities saturates by ε_r = 80, with there being little difference in peak magnitudes and spatial distribution between ε_r = 80 and the metal surface. The high permittivity materials create a large capacitance with no change to the surface area or distance to the electrode. Impedance, being inversely proportional to capacitance, decreases with increasing ε_r. The lower impedance consumes a smaller fraction of the applied voltage, thereby increasing the voltage across the electrode-to-dielectric gap relative to small ε_r. From another perspective, high permittivity materials exclude electric fields, thereby displacing voltage into the gap. For ε_r = 2, this effect is small, thereby enabling voltage contours to penetrate into the dielectric. The resulting smaller voltage across the gap produces an ionization wave that is 5.5 ns slower to the surface with an electron temperature 1 eV lower than for the high permittivity material. Increasing ε_r to 5 produces an ionization wave that strikes the surface 3.5 ns earlier than for ε_r = 2 with a higher electron temperature, ionization source, and magnitude of electric field in the streamer head. At the time of impact, only for the ε_r = 2 case is there significant penetration of the electric field into the dielectric. The electric potential drop across the dielectric is > 2 kV. For ε_r = 10, the penetration of potential into the material is less than 600 V.

4.3.2 Touch + 10 ns

At the point at which the ionization wave just impacts the dielectric, only a small fluence of electrons has reached the surface and there is little charging. At 10 ns after the ionization wave strikes the dielectric, charging of the capacitance of the surface has occurred and continues to occur. This charging has significant feedback to the properties of the plasma plume. The ionization source term (S_e), electron density (n_e), total positive ion density (N^+_{tot}) and total

negative ion density (N^-_{tot}) are shown in Fig. 4 for a time 10 ns after the IW strikes the surface. (Note that the absolute time is different for each material due to the difference in the speed of the IW.) The S_e responds in three distinctly different ways depending on the ε_r of the dielectric. The first response is highlighted by the lower permittivity cases a few ns after impact. Here the IW spreads across the surface and eventually splits from the vertical IW, forming a surface ionization wave (SIW). The SIW is sustained by horizontal components of the electric field at the surface of the dielectric. The S_e in the vertical column decreases and eventually terminates due to the charging of the surface which removes voltage from the gap. This is in some ways reminiscent of a DBD. The spreading phenomenon in DBDs lead to self-organization of the plasma filaments.[31,32] The SIW increases in intensity for small increases in ε_r. For example, the S_e in the SIW for ε_r =5, 3×10^{20} $cm^{-3}s^{-1}$ is commensurate with that in the plasma column, 8×10^{20} $cm^{-3}s^{-1}$. The second response of S_e for larger ε_r, is a restrike in which a vertical IW travels back up the conductive channel away from the surface. The intensity of the restrike depends on the effective capacitance of the material and increases with increasing ε_r. With the increase in S_e in the restrike, the SIW decreases in intensity relative to the plasma column. The third response of S_e is the establishment of a conduction channel between the surface and the electrode at ε_r =80 and for the metal substrate. This conduction channel coincides with the termination of the SIW. For example, S_e in the SIW for ε_r =80, 5×10^{20} $cm^{-3}s^{-1}$, is small compared that in the plasma column, 6×10^{21} $cm^{-3}s^{-1}$. For the metal surface, S_e in the plasma column is 9×10^{21} $cm^{-3}s^{-1}$ with there being essentially no SIW due to the lack of a horizontal component of the electric field at the surface of the metal.

The dominance of the restrike or the SIW is largely a function of the charging of the dielectric. The SIW is sustained by horizontal components of the electric field produced by

surface charging of the dielectric. This surface charging is at the expense of the vertical electric field and is the basis of operation of DBDs where voltage is removed from the gap prior to arcing. The smaller ε_r and so smaller capacitance results in a smaller RC time constant for charging the surface, more rapid production of the horizontal component of the electric field that sustains the SIW and more rapid depletion of the vertical electric field. At the other extreme, with a metal substrate there is no charging of the surface and a horizontal component of the electric field cannot be supported, at least at the surface. As a result, the SIW fails to significantly form. In this case, in the absence of a ballast resistor, the full voltage remains across the gap. With increasing ε_r a transition occurs between two states. The first is surface charging, production of lateral electric fields and an SIW; the second is a fully sustained conduction channel and a restrike that eventually returns into the tube to connect with the electrode. At touch + 10 ns, the $\varepsilon_r = 80$ case combines the characteristics of the grounded case in which a fully developed plasma column connects the surface and the electrode, with the beginning of the formation of an SIW. As long as there is a finite capacitance, given a long enough pulse, the surface will eventually charge, an SIW will eventually be formed and the S_e in the vertical column will diminish. For example, for $\varepsilon_r = 80$, the SIW separates from the vertical plasma column 17.5 ns after the impact of the ionization wave onto the dielectric.

At touch + 10 ns, n_e for $\varepsilon_r = 2$ is 2×10^{13} cm^{-3}, and is nearly an order of magnitude lower than that for $\varepsilon_r = 80$ and for the metal substrate, 1.5×10^{14} cm^{-3}. As ε_r increases, n_e in the conductive channel increases. This increase in n_e is facilitated by the larger capacitance of the surface with increasing ε_r that enables more conduction current to flow through the channel, and displacement current through the dielectric, prior to charging of the capacitance. The lower n_e in the plasma columns with lower ε_r is partially compensated by greater spread of the plasma on the

dielectric facilitated by the SIW. However the electron density in the SIW is 10-100 times smaller than that in the vertical plasma column. The grounded plate enables formation of a conduction channel unimpeded by charging of the surface, albeit at the loss of spreading of the discharge on the surface.

The density of cations (positive ions) follows that of the electrons with nearly identical values at this time in the discharge. That is, the anion (negative ion) density is small. At touch + 10 ns, the electrons and cations start to spread across the surface of the dielectric material, most clearly shown for ε_r = 2, 5, and 10, following the propagation of the SIW. The spread is most rapid in the ε_r =10 case. At a distance of 3 mm from the exit of the dielectric tube, the cation having the highest density is O_2^+, comprising 54%, 49%, 48%, 43%, and 42% of the total cation density for ε_r = 2, 5, 10, 80, and metal surfaces. O_2^+ is dominantly formed through direct electron impact ionization of O_2 in the admixture or ambient or by the multistep ionization of $O_2(^1\Delta)$ or $O_2(^1\Sigma)$. For example, near the He – air interface ionization of the ground state of O_2 accounts for 67% of the formation of O_2^+ by electron impact, and multistep ionization of $O_2(^1\Delta)$ or $O_2(^1\Sigma)$ accounts for roughly a third. The next most prevalent cation is N_4^+ formed from N_2^+ in a three-body collision with N_2 and another neutral. N_4^+ comprises 40%, 37%, 36%, 36%, and 35% of the cations for ε_r = 2, 5, 10 and 80, and metal surfaces. Along the surface, at the farthest extent of the spread of the SIW for ε_r = 2, 5 and 10, N_4^+ slightly exceeds O_2^+ as the dominant cation. This reversal of the dominant cation results from the greater amount of mixing of ambient air with the He/O_2 mixture flowing radially outward from the stagnation point. This mixing increases the N_2 density.

The density of cations generally decreases from the plasma column in the tube to the surface and into the SIW. However, the density of anions increase as the surface is approached

and increases with increasing permittivity. At 2 mm above the surface,, the anion density increases from 6×10^{11} cm^{-3} for $\varepsilon_r = 2$ to 2×10^{12} cm^{-3} for the metal substrate. At this point in the development of the discharge (touch + 10 ns) and same location (2 mm above the surface), the dominant anion is O^- formed by dissociative attachment of O_2, and comprises 88%, 86%, 84%, 82%, and 82% of the anions for $\varepsilon_r = 2$, 5, 10 and 80, and metal. O_2^- comprises the majority of the remaining anions formed through three-body electron impact attachment. The O^- anion also dominates in the spread of the discharge along the surface with similar proportions.

Several key reactive species have been formed by electron impact excitation at this point in the discharge. The densities of He^*, O, N_2^* and OH at touch + 10 ns are shown in Fig. 5. He^*, represents the sum of the excited states of He included in the model. [He(2^1S), He(2^1P), He(2^3S), He(2^3P), He(3S), and He(3P).] At touch + 10 ns, the dominant excited state is the metastable He(2^3S), comprising between 50% and 33% of the He^* density from low to high permittivity. The production of He^* by electron impact with the helium feed gas has a minimum threshold energy of 19.8 eV for He(2^3S). As a result, He^* is dominantly formed in the high density, more energetic stream of electrons ($T_e = 3 - 4$ eV) that occurs along the wall of the discharge tube, and transitioning back to the axis of the plasma column near the exit of the tube. These excited states are important for subsequent Penning ionization and helium dimer formation.

The density of O atoms significantly increases with the increase in electron density in the conductive channel rising from 1×10^{14} to 7×10^{14} cm^{-3} as the relative permittivity increases from 2 to 80 (and metal). The O atoms are formed from electron impact dissociation of O_2 and react with O_2 and another neutral in a three-body collision in the ambient or admixture to form O_3. The density of O atoms should increase with extension of the ionization wave further from the end of the tube into the plume where the density of O_2 from the ambient is larger. This

increase in O is somewhat tempered by the loss of O atoms in forming ozone, which also increases with O_2 diffusing into the plume from the ambient. Also in the far-field, the O atoms collide with N atoms and another neutral to be a secondary source of NO, an important molecule for cell signaling.

The electronically excited N_2^*, representing the sum of the metastable $N_2(A^3\Sigma)$ and $N_2(B^3\Pi)$ states, is formed from electron impact with N_2 (minimum threshold energy 6 eV) that has diffused into the helium channel. The density of N_2^* increases from 9×10^{14} cm^{-3} to $4 - 5 \times 10^{15}$ cm^{-3} from $\varepsilon_r = 2$ to 80 (and metal). The density of N_2^* is maximum on axis in spite of the N_2 diffusing into the plume from larger radius because the ionization wave propagates on axis outside the tube where N_2 is found. N_2^* provides another source of O atoms through dissociative excitation transfer collisions with O_2. The N_2^* also provides another source of NO through its reaction with O or O_3.

Similar to N_2^*, the hydroxyl radical, OH, is also formed from the interaction of the electrons on axis in the plume with H_2O diffusing into the plume. As a result, the spatial profiles of N_2^* and OH are similar. As OH accumulates, it combines with itself in a three-body reaction to form H_2O_2. The lateral spread of the key neutrals along the material surface is best shown in $\varepsilon_r = 10$ frame of Fig. 5. The density accumulating on the surface is lower than that in the channel at this point and follows the spread of the surface ionization wave and the electrons.

4.3.3 End of Maximum Applied Voltage 80 ns

Plasma properties [T_e, n_e, N^+_{tot} (cation density) and N^-_{tot} (anion density)] are shown in Fig. 6 at the end of the maximum applied voltage of the pulse (80 ns). At this time, the low permittivity materials have nearly fully charged and removed voltage from the gap, resulting in

the electric field in the gap being low. For example, at mid gap, *E/N* increases from 5 Td for ε_r = 2 to 18 Td for ε_r = 80 (metal). As a result, at mid gap T_e increases from 1 eV for ε_r = 2 to 2.8 eV for ε_r = 80 (metal). In spite of the large range of T_e in the gap, the temperature is 3 eV throughout the extent of spread of the SIW. The spread of the SIW requires a minimum value of T_e regardless of the value of ε_r. The ε_r = 80 case combines the two trends of increasing T_e in the plasma column and having a finite SIW. The maximum value of T_e in the conduction channel is 2.9 eV and in the SIW along the surface is 3 eV. Although the spatial distribution of n_e is less sensitive to ε_r, the spatial distribution of T_e depends on ε_r. Subsequently, the rates of formation and accumulation of the charged species on the different surfaces and in the conduction channel are largely influenced by T_e.

For all values of ε_r, the electron density increases during the voltage pulse and is maximum at the end of the high voltage portion of the pulse at 80 ns. In the channel, 2 mm from the end of the dielectric tube, the electron density increases from 4×10^{13} cm^{-3} for ε_r = 2 to 7×10^{14} cm^{-3} for the metal substrate. The conductivity of the channel increases proportionally to the permittivity. The maximum density in the spread of electrons along the surface increases with permittivity as well from 1.5×10^{12} cm^{-3} for ε_r = 2 to 3×10^{13} cm^{-3} for ε_r = 80 while the spatial extent decreases with increasing ε_r

The density of cations, N^+_{tot}, follows that of the electron density in the conductive channel increasing with increasing permittivity by an order of magnitude from ε_r = 2 (4×10^{13} cm^{-3}) to ε_r = 80 (7×10^{14} cm^{-3}). Similarly along the surface of the material, the maximum N_{tot}^+ increases from 2×10^{12} cm^{-3} to 2×10^{13} cm^{-3} for ε_r = 2 to ε_r = 80 while again the spatial extent decreases with increasing ε_r. In the channel, O_2^+ is the dominant anion comprising 60 – 80% of the total cation density (higher percentage at lower ε_r) with He^+ accounting for up to 20% of the

cation density for ε_r = 80 and the metal substrate. In the lower permittivity cases (ε_r = 2, 5, and 10), N_4^+ is the second most prevalent cation contributing between 10 and 20% to the total. At the surface of the dielectric material, the cations are dominated by O_2^+ with one to two orders of magnitude drop for the next most prevalent cation (N_4^+). Over the length of the pulse, the higher rate coefficient for electron-ion recombination for N_4^+ (1.4×10^{-7} $cm^{-3}s^{-1}$ at 2 eV)[33,34] compared to 7.3×10^{-9} $cm^{-3}s^{-1}$[35,36] for O_2^+ at 2 eV caused the sharp drop in N_4^+ on the surface.

At the end of the high voltage portion of the discharge pulse, anions accumulate near the surface of the dielectric material and spreading across the dielectric as they are formed by electron impact. This distribution of anions reflects the greater degree of mixing of the ambient air into the plasma column and SIW the further from the exit of the discharge tube. Unlike electrons and cations, the maximum density of anions occurs near the tip of the dielectric tube where less energetic electrons attach to O_2 forming O_2^- at the interface of the He plume with the ambient humid air. Following the production of electrons, but with less dramatic increases, the range of cation density increases from 1.5×10^{12} cm^{-3} for ε_r = 2 to 4×10^{12} cm^{-3} for ε_r = 80. Along the surface, O^- is the dominant anion comprising 6×10^{11} cm^{-3} of the total anion density of 9×10^{11} cm^{-3} for ε_r = 2, or 2/3 of the total. For ε_r = 80 the density of O^- is 2×10^{12} cm^{-3} of the total anion density of 3×10^{12} cm^{-3}, also 2/3 of the total due to the values of T_e being similar. The remainder of the anions is dominantly O_2^-. The neutral species that will contribute to the production of the near-terminal reactive species (i.e., O_3, N_xO_y, H_2O_2) are shown in Fig. 7 at the end of the 80 ns high voltage portion of the discharge pulse. The lifetime of He^* against quenching by Penning ionization at mid-gap is 35 ns for ε_r = 2. So in the absence of continuous production, He^* can be depleted during the discharge pulse. As the *E/N* decreases in the plasma channel with decreasing ε_r, the rate of production of He^* decreases and so the He^* is increasingly

quenched in the absence of production. With increasing ε_r, and increasing *E/N*, the rate of production of He^* is maintained and so is competitive with quenching. The density of He^* at 80 ns increases from 1.3×10^{10} cm^{-3} for $\varepsilon_r = 2$ to 1×10^{14} cm^{-3} for $\varepsilon_r = 80$.

Over the 50 ns from the ionization wave touching the dielectric to the end of the high voltage discharge pulse, the densities of the remaining key neutrals, O, N_2^* and OH, increase both in the channel and along the surface. In spite of initially being produced in the tube, the density of O increases in the conduction channel as the electrons and N_2^* accumulate, both dissociating O_2 by either direct electron impact or excitation transfer. The highest density of O atoms, 2×10^{16} cm^{-3}, is again with the metal substrate and increases by an order of magnitude from 5×10^{14} cm^{-3} for $\varepsilon_r = 2$ to 8×10^{15} cm^{-3} for $\varepsilon_r = 80$. The spread of O atoms along the surface is greater for $\varepsilon_r = 2$, 5 and 10 compared to 80 due to the reduction in the SIW, but the largest density at the surface, 2×10^{15} cm^{-3}, occurs for $\varepsilon_r = 80$.

The density of N_2^* increases by an order of magnitude from 5×10^{15} cm^{-3} to 5×10^{16} cm^{-3} for the metal substrate between touching + 10 ns to the end of the high voltage portion of the pulse at 80 ns. The density of N_2^* increases by a lesser degree with lower permittivity. The charging of the dielectric and reduction in *E/N* (and T_e) in the plasma column with lower ε_r essentially terminates production of high threshold energy species such as N_2^*. For the higher ε_r and metal substrates, the continuing conduction current (and restrike) maintains production of high threshold energy species for the duration of the discharge pulse. As in the distribution of ions, the tradeoff is in the spatial distribution of excited states. The conversion of conduction current in the plasma column into current in the SIW for low ε_r results in a greater spatial extent of N_2^* along the surface, here maximizing for $\varepsilon_r = 10$ to a distance of 3.9 mm. Although the spread of N_2^* is spatially more pronounced with lower permittivity, its density is higher at the

surface (6×10^{15} cm^{-3}) for $\varepsilon_r = 80$. Following the trends of N_2^*, the production of OH increased for all cases over the duration of the pulse (touching to 80 ns), nearly doubling to 1×10^{12} cm^{-3} with $\varepsilon_r = 2$ to increasing by a factor of 20 (8×10^{13} cm^{-3}) for the metal substrate.

The charging of the dielectric removes voltage from the gap, thereby reducing Joule heating, electron density and radical production in the plasma column. This voltage ultimately appears in the dielectric. The absence of a significant electric field in the conduction channel for $\varepsilon_r = 2$, 5 and 10 not only decreases the current density, it also limits the Joule heating produced by these discharges. For example, the electric fields at the end of the high voltage discharge pulse are shown in the conduction channel and dielectric in Fig. 8. Increasing ε_r decreases the voltage and the subsequent electric field propagation into material from 36 kV/cm for $\varepsilon_r = 2$ to 23 kV/cm for $\varepsilon_r = 80$. At a depth of 1 mm into the surface, or the bottom edge of Fig. 8(b), the magnitude of the electric field ranges from 28 kV/cm for $\varepsilon_r = 2$ to 13 kV/cm for $\varepsilon_r = 80$. Following the trend at touch + 10 ns, the potential drop across the dielectric is greatest for $\varepsilon_r = 2$ at 10 kV decreasing to a penetration of potential of 3 kV for $\varepsilon_r = 80$.

The extent of the spread of the surface ionization wave and region of high electron temperature follows from the region of high electric field in the plasma above the material surface. In order to conserve current, the low dielectric constant material requires a larger time rate of change of the electric field leading to the higher electric fields in the material. This maintains the displacement current at the interface to be similar to the conduction currents through the plasma region. The metal target provides a direct path to ground for the conduction current without electric field enhancement at the surface.

4.3.4 End of Pulse (100 ns)

The formation of the plasma column in the atmospheric pressure guided streamer follows the same conceptual precepts as in a conventional low pressure glow discharge sustained in a dielectric tube. An ambipolar electric field is produced in the radial direction to confine the more mobile electrons and accelerate the less mobile positive ions to have equal fluxes. The end result is an electropositive plasma – a small net positive charge density in the plasma column. The majority of the positive charge resides at the edge of the plasma column where the ambipolar electric field is the largest. In a low pressure, glow discharge, the negative charge that balances the electropositive charge in the plasma column resides on the surface of the discharge tube. This negative charge results from the more mobile electrons that initially leave the plasma and so create the positive space charge. A similar process occurs in the atmospheric pressure guided streamer. However, since there is no tube on which the diffusing negative charge resides, the negative charge takes the form of a negative space charge layer bounding the positive space charge layer. Due to the streamer being bounded by the ambient air, the negative space charge layer is eventually dominated by negative ions as the low energy electrons attach to O_2. The negative ions are dominantly O_2^- near the exit of the tube where T_e is smaller, and transitioning at the midgap to O^- formed by dissociative attachment to O_2 and attachment of low energy electrons to previously formed O atoms.

These trends are shown in Fig. 9 where the positive space charge, negative space charge, magnitude of the electric field and electric potentials are shown at 100 ns, the termination of the voltage pulse, for ε_r = 5 and 80, and metal substrate. The electric fields and potentials, with enlargement of the plasma-dielectric interface, are shown in Fig. 10 for all cases. The boundary of the plasma column is defined by the positive space charge layer which itself is bounded by the

balancing negative space charge layer. In between is the ambipolar electric field. For that portion of the plasma column that is inside the tube, the positive space charge bounds the tube and the negative charge is largely on the tube.

As the voltage pulse falls from -15 kV to 0 kV from 80 ns to 100 ns, most electrons in the boundary layer attach to form negative ions. The heavier cations remain in place and form an ion matrix. The resulting radial electric field is then largely sustained between the positive and negative ion matrices. As ε_r increases, the magnitude of the ion matrix sustained electric field decreases from 34 kV/cm (132 Td) for ε_r = 2 to 19 kV/cm (73 Td) for ε_r = 80. These trends in electric field are produced by a decreasing charge density bounding the plasma column. The maximum total positive charge is 2×10^{12} cm^{-3} for $\varepsilon_r = 5$ compared to 1×10^{12} cm^{-3} for ε_r = 80. The balancing negative ion matrix has a lower peak density (for example, 2×10^{11} cm^{-3} for ε_r = 5) due to its larger volume.

The charge balance and resulting electric fields are in some cases dominated by the surface charging. With the pin electrode inside the tube now at ground potential, the charge on the surface represents a negative voltage source producing a -4 to -5 kV potential drop. The resulting electric fields are shown in Fig. 10(b). Here the maximum magnitude of the electric field at the surface has the opposite trend of the electric field produced by the ion matrices in the gas phase. The local electric fields at the surface increase with increasing permittivity, these maxima have smaller spatial extent. A larger charge accumulates on the higher capacitance, higher permittivity materials as shown in Fig. 6. When the applied voltage is removed, this larger accumulated charge produces a larger surface electric field. As shown in Fig. 10(b), increasing permittivity increases the magnitude of the surface electric field from 40 kV/cm (170 Td) for ε_r = 2 to 108 kV/cm (400 Td) for ε_r = 80.

The distribution of charge in the vicinity of the surface has two components, as shown in Fig. 11 for ε_r = 5 and 80, and for the metal. There is negative charge deposited on the surface of the material and positive space charge density in the plasma above the surface. The positive space charge results from a positive-ion matrix sheath – the more mobile electrons flowed from this region into the surface leaving behind the ion matrix sheath. For the low permittivity case (ε_r = 5), the smaller RC time constant for charging the surface and the more rapid spread of negative charge produces comparable charge densities on the surface (negative) and in the sheath (positive). The end result is a lower intensity electric field 75 kV/cm (286 Td). The high permittivity case (ε_r = 80) has nearly an order of magnitude lower positive charge density (2×10^{13} cm^{-3}) compared to the negative charge (1×10^{14} cm^{-3}). This situation results from electron current flowing through the ion matrix sheath to the surface to charge the larger capacitance. This large imbalance produces an electric field of 108 kV/cm. The positive charge density does increase with ε_r = 80 compared to ε_r = 5 due to the larger electron current density producing more ionization in the sheath. However, the negative charge density on the surface increases by an order of magnitude from 1×10^{13} cm^{-3} for ε_r = 5 to 1×10^{14} cm^{-3} for ε_r = 80 due to the flow of electron current through the sheath to charge the capacitance. The negative charge extends further along the surface than does the positive change, a consequence of the negative SIW that is sustained by negative space charge at its leading edge

These trends apply to non-conducting material which translates to an infinite dielectric relaxation time, ε/σ. Materials with finite conductivities and a finite dielectric relaxation time will dissipate the surface charge. At one extreme, the metal does not accumulate surface charge because that charge is virtually instantly dissipated. The electric field produced at the surface of the metal substrate is due to an anode sheath created by the accumulation of positively charged species

near the surface as the electrons flow into the metal. The negative charge that extends from above into the frame of Fig. 11(c) for the metal surface is from the lower extent of the anions that forms the ion-matrix, ambipolar, electric field that confines the plasma column. It is not due to surface charging.

4.4 Concluding Remarks

By changing only the relative permittivity of the material upon which an APPJ is directed, significant effects on the dynamics of the discharge, production of charged and reactive species and the behavior of the electric field are realized. Increasing the permittivity increases the speed of the ionization wave to the surface, increases the electron density and subsequent ion density. The larger electron density and higher electron temperature in the conduction channel and along the surface of the high permittivity materials over the pulse duration increase the production of key neutrals of interest to biological applications created by the discharge. A lower permittivity allows more penetration of the electric field into the material.

The dynamics of the fall of the voltage pulse revealed that the development of an ion matrix electric field at the edge of the conductive channel and the electric field at the surface were influenced by the permittivity of the material as well. The ion matrix produced ambipolar electric field is larger for lower permittivity materials and is produced from the greater number of negatively charged species remaining in the plasma region. However, this increase in negative charged species that reached the surface at the end of the pulse fall increased the magnitude of the surface electric field for higher permittivity materials.

4.5 Figures

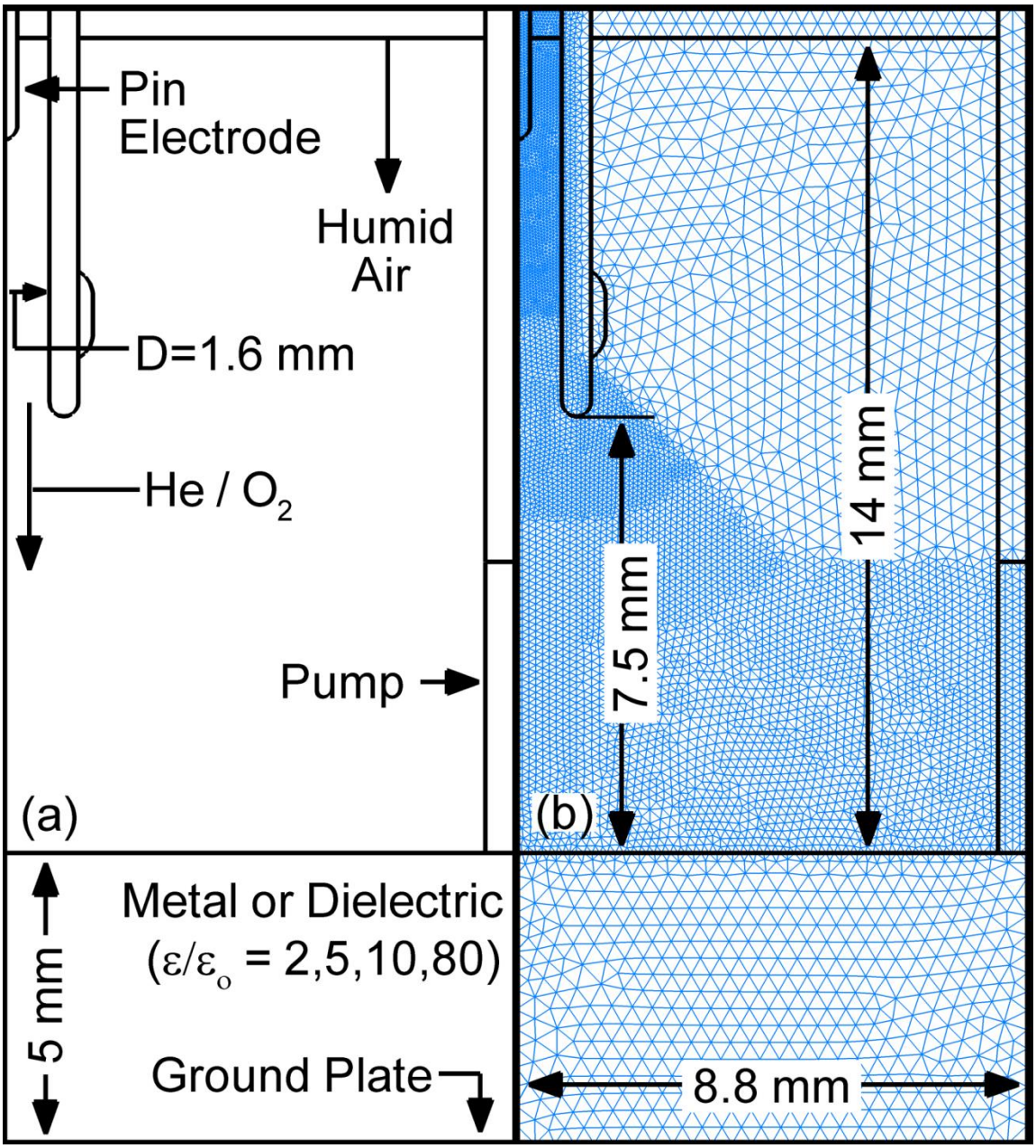

Figure 4.1 The cylindrically symmetric model geometry. (a) The full computational domain is 1.95 cm by 0.88 cm. (b) The numerical mesh with refinement zones.

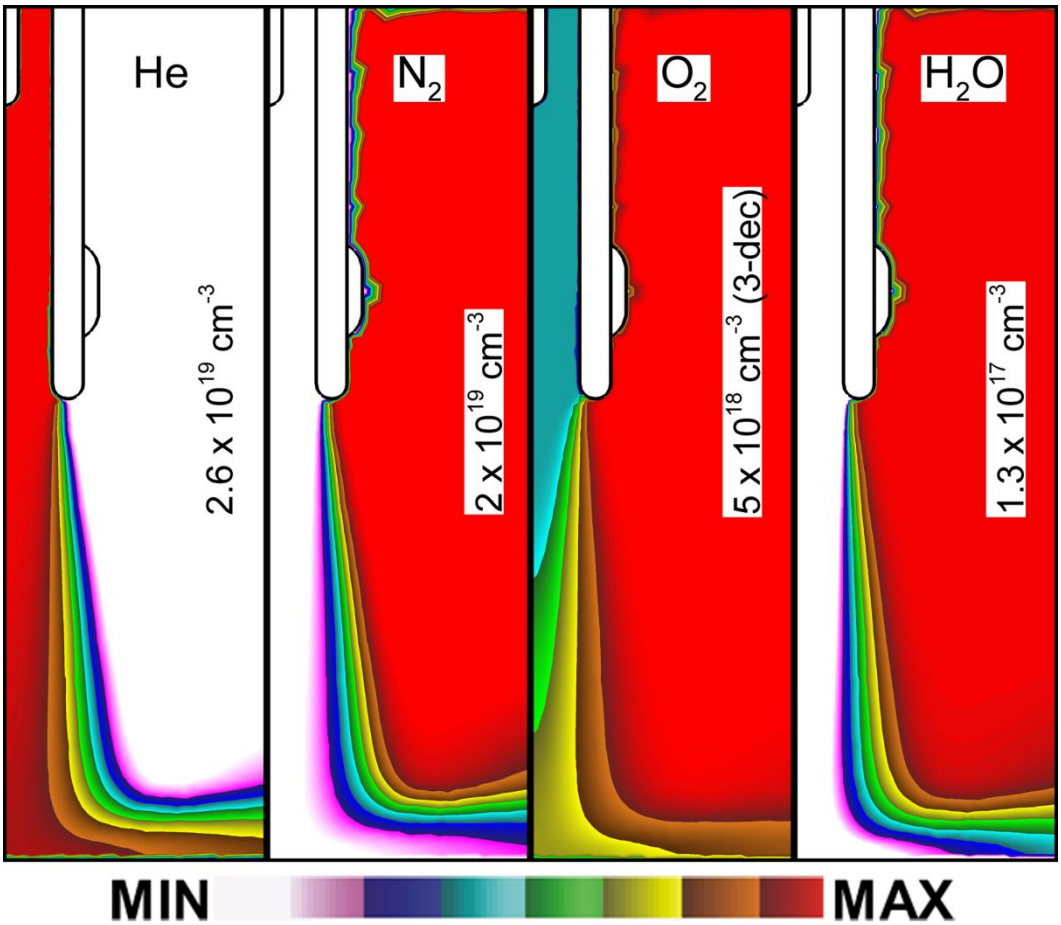

Figure 4.2 He, N_2, O_2, and H_2O concentrations for a flow rate of 4 slm He/O_2=99.8/0.2 through the tube prior to discharge ignition and humid air flowed as a shroud. Maximum values are shown in each frame (1 decade log scale). The O_2 concentration is plotted over 3 decades to highlight the 0.2% O_2 seeded in the He.

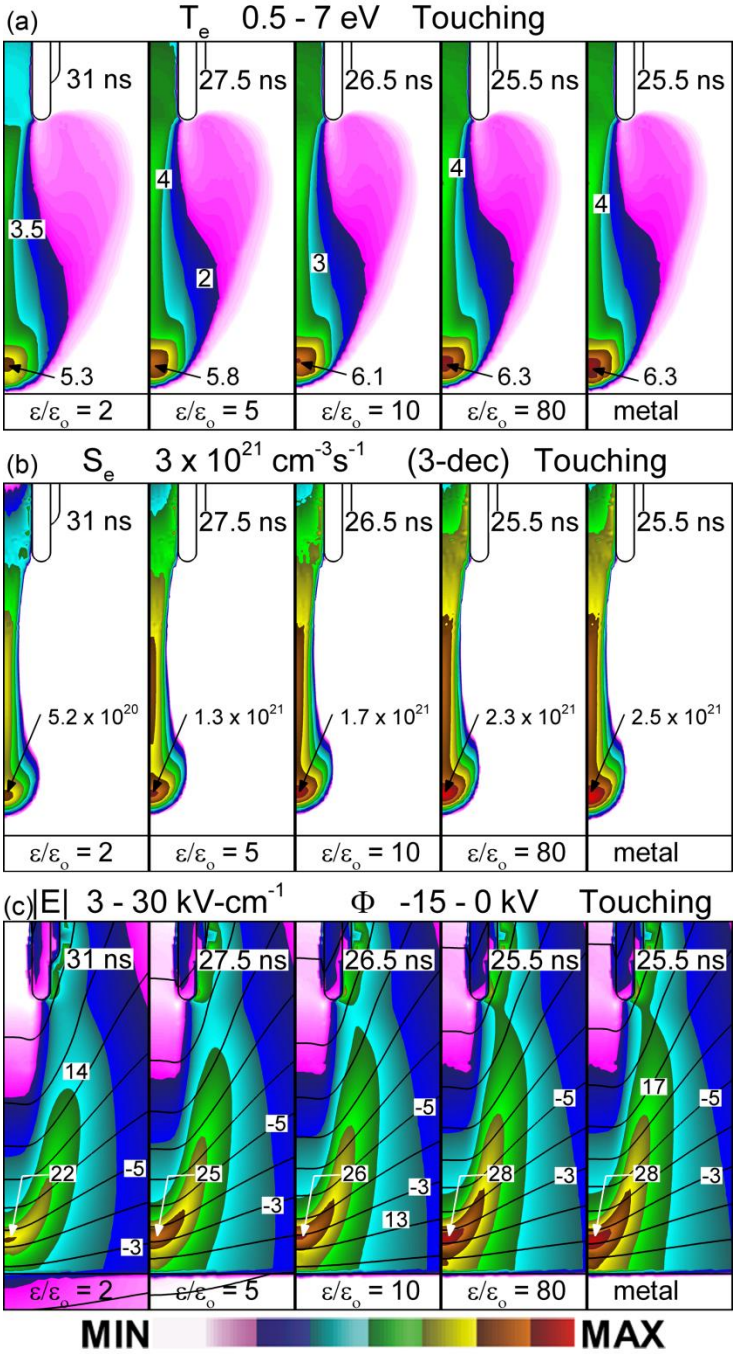

Figure 4.3 Plasma dynamics at the time the ionization wave arrives at the material surface. Each case has He/O_2 = 99.8/0.2 flowing at 4 slm into humid air and a -15 kV applied voltage. From left to right, the frames correspond to relative permittivities of 2, 5, 10 and 80, and metal. The time from beginning of the pulse to impact are listed for each permittivity. (a) Electron temperature T_e, (b) electron impact ionization source S_e, and (c) magnitude of the electric field with potential contours at -1 kV intervals. The maximum value or range of values are noted in each figure.

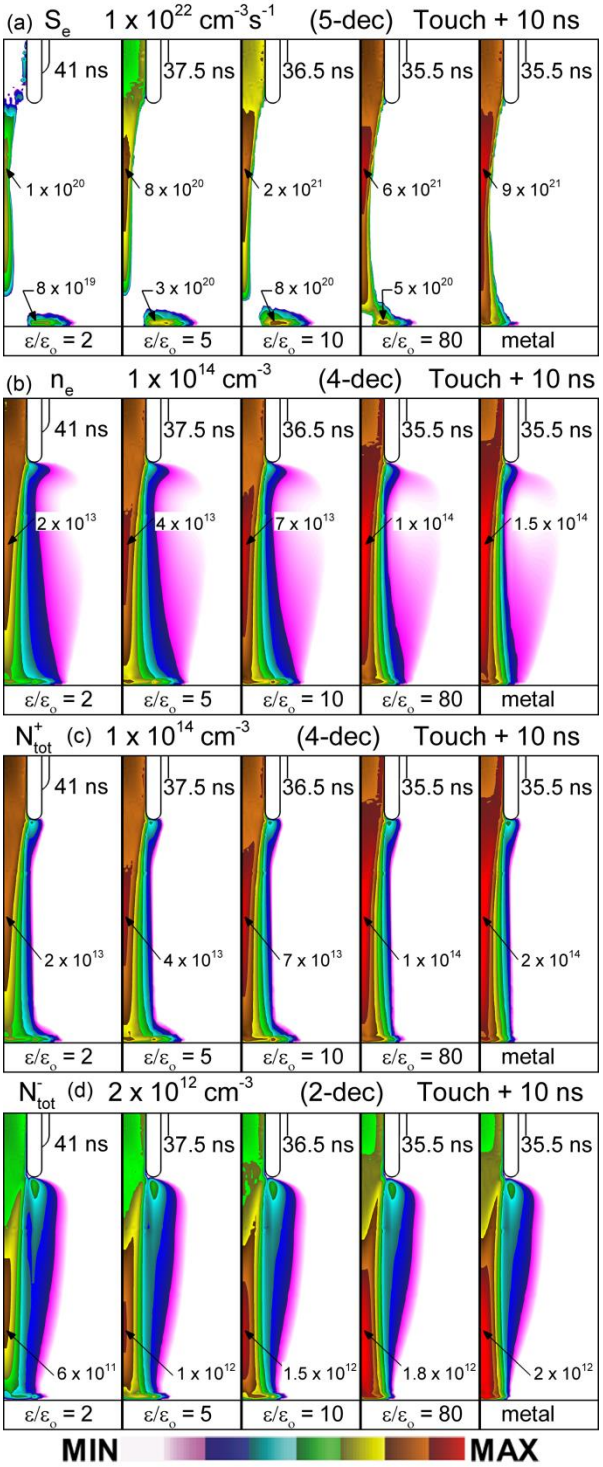

Figure 4.4 Plasma dynamics at 10 ns after the ionization wave touches the material surface. From left to right, the frames correspond to relative permittivities of 2, 5, 10 and 80, and metal. The *touch + 10 ns* time is listed in each frame. (a) Electron impact ionization source S_e, (b) electron density, (c) total cation density, and (d) total anion density. Contours are on a log-scale with the maximum value and number of decades listed in the frame.

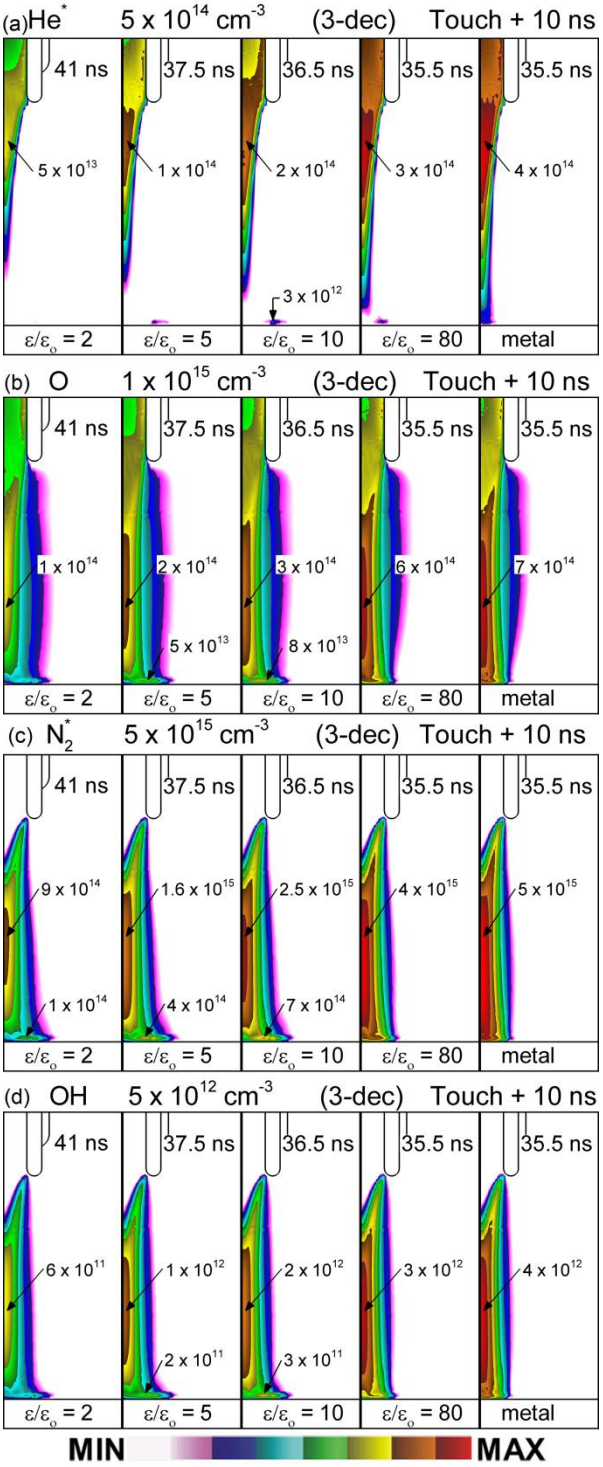

Figure 4.5 Production of key neutrals at 10 ns after the ionization wave touches the material surface (*touch + 10 ns*). From left to right, the frames correspond to relative permittivities of 2, 5, 10 and 80, and metal. The times listed correspond to *touch + 10 ns*. (a) He^*, (b) O atoms, (c) N_2^* and. (d) OH. Contours are on a three decade log-scale from the maximum value listed in the frame.

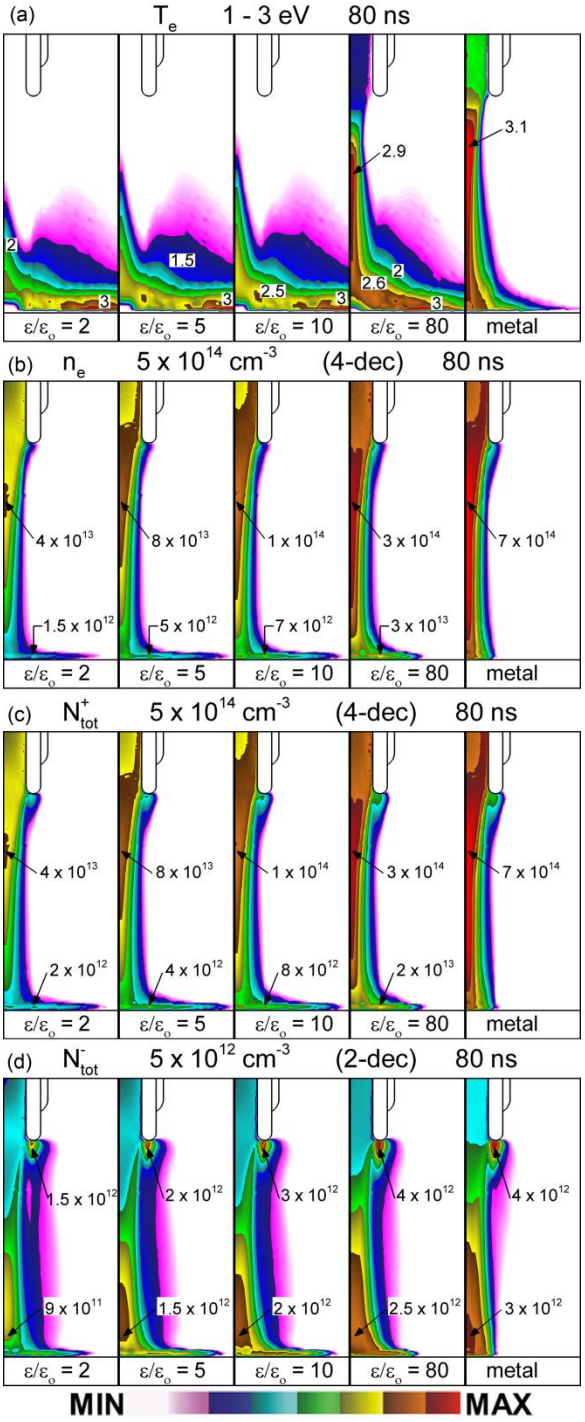

Figure 4.6 Plasma dynamics at the end of the maximum applied voltage (80 ns). From left to right, the frames correspond to relative permittivities of 2, 5, 10 and 80, and metal. (a) Electron temperature T_e (linear scale from 1 – 3 eV), (b) electron density, (c) total cation density and (d) total anion density. Contours are on a log-scale with the maximum value and number of decades listed on the frame.

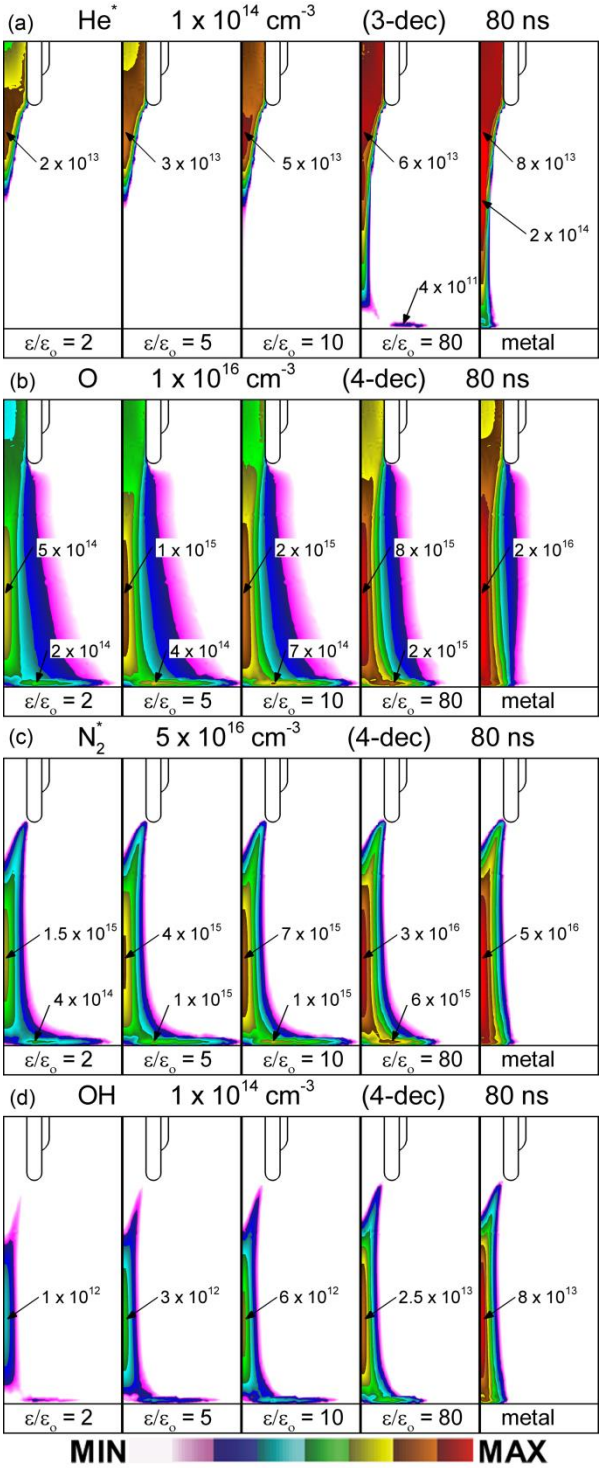

Figure 4.7 Production of key neutrals at the end of the maximum applied voltage (80 ns). From left to right, the frames correspond to relative permittivities of 2, 5, 10 and 80, and metal. (a) He^* decreases in density compared to *touch + 10 ns*, (b) O atoms accumulate in the channel and on the surface, (c) N_2^* also accumulates in the channel and along the surface and (d) OH. Contours are on a log-scale with the maximum value and number of decades listed on the frame.

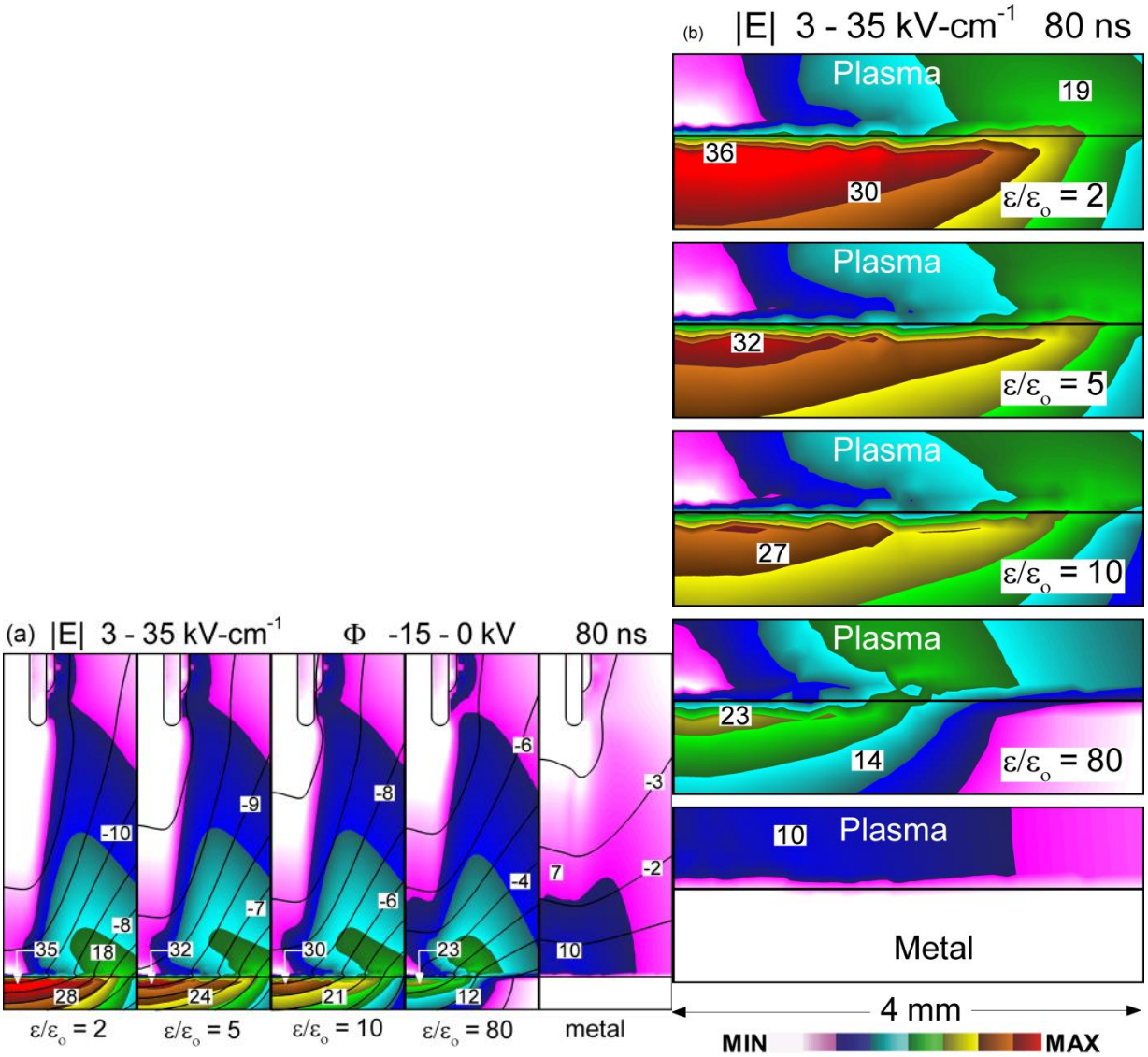

Figure 4.8 Magnitude of the electric field at the end of the maximum applied voltage (80 ns). From left to right or top to bottom, the frames correspond to relative permittivities of 2, 5, 10 and 80, and metal. (a) The maximum extent of the penetration of the electric field into the dielectric from and electric potential contours at -1 kV intervals. (b) Close up of the material surface showing the penetration of the electric field. Contours for the electric field are on a linear scale from 3 – 35 kV/cm.

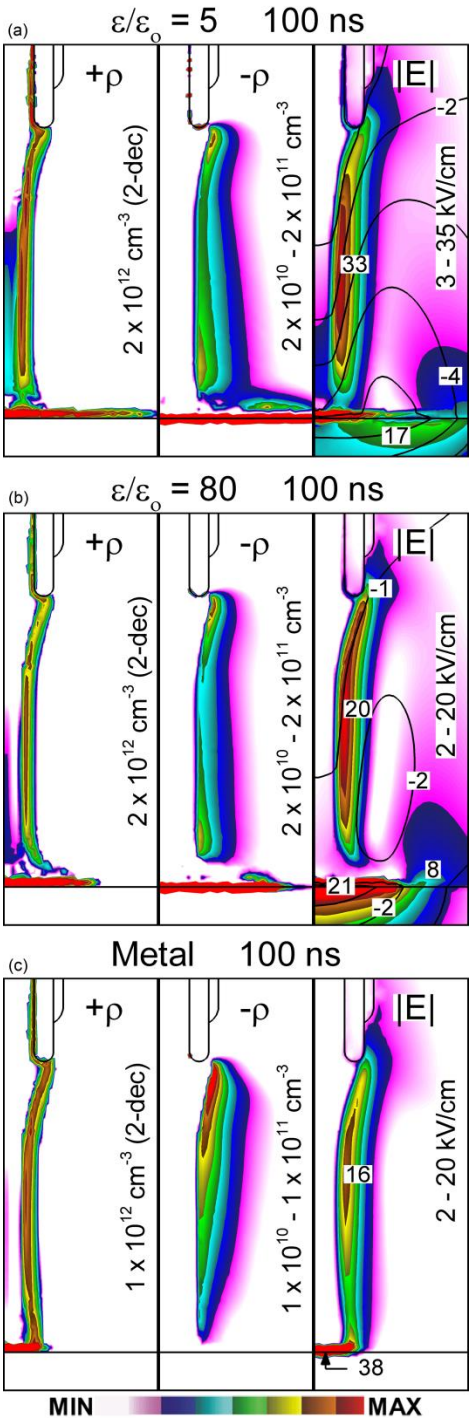

Figure 4.9 Total positive and negative charge density, and resulting electric field (with voltage contours) when the applied voltage pulse returns to 0 at 100 ns. (a) ε_r = 5 (tissue-like), (b) ε_r = 80 (water-like) and (c) metal. For positive charge density, contours are on a log-scale with the maximum value and number of decades listed on the frame. For negative charge density and magnitude of the electric field, the contours are on a linear scale from the range of values listed.

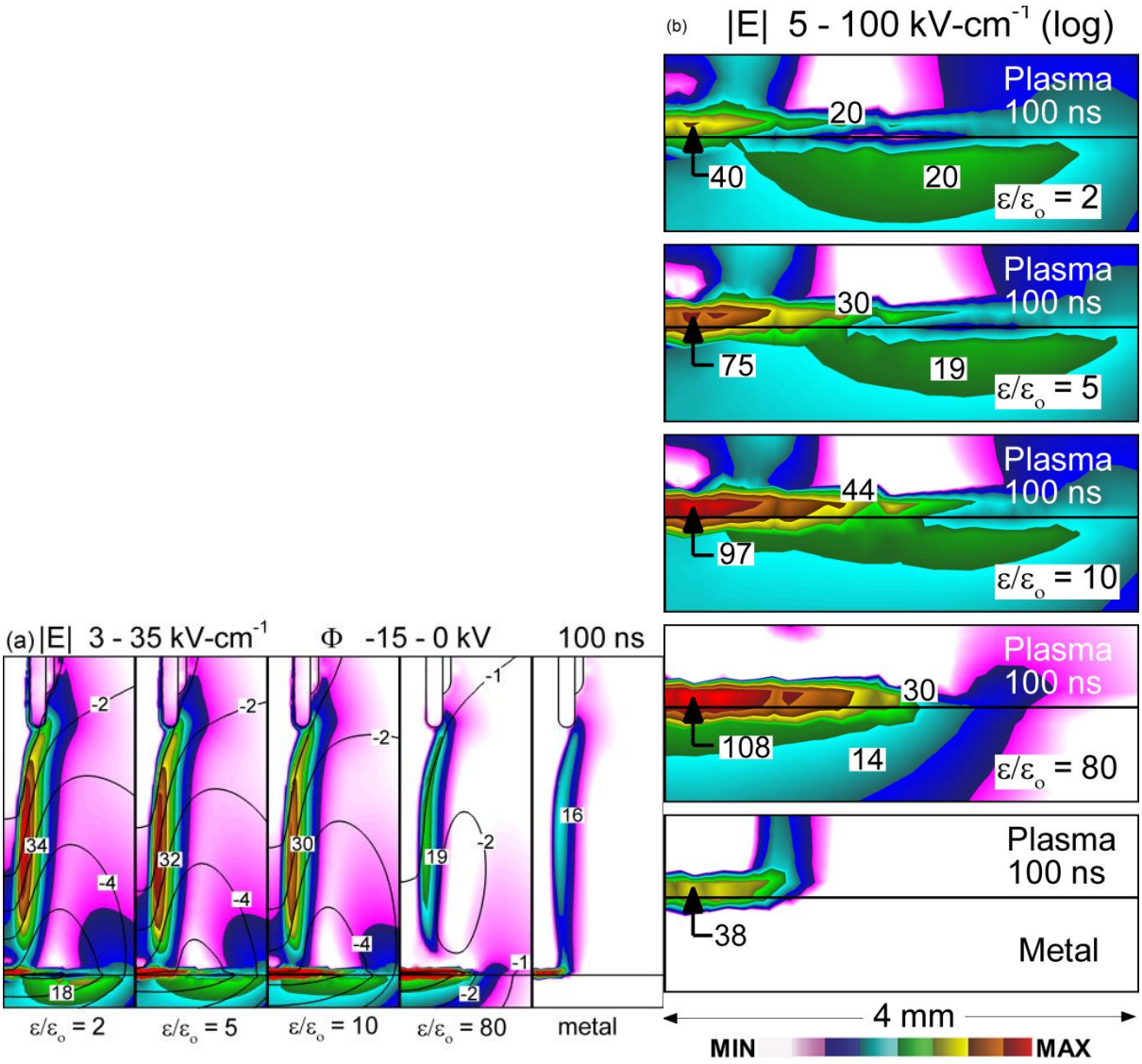

Figure 4.10 Magnitude of the electric field at the end of the applied voltage (100 ns). From left to right or top to bottom, the frames correspond to relative permittivities of 2, 5, 10 and 80, and metal. (a) The resulting ion matrix and surface electric fields resulting from the charge separation when the applied voltage returns to 0. Contours are on a linear scale from 3 – 35 kV/cm. The potential contours at -1 kV intervals. (b) Close up of the electric field at the material surface. Contours are on a log-scale from 5 – 100 kV/cm.

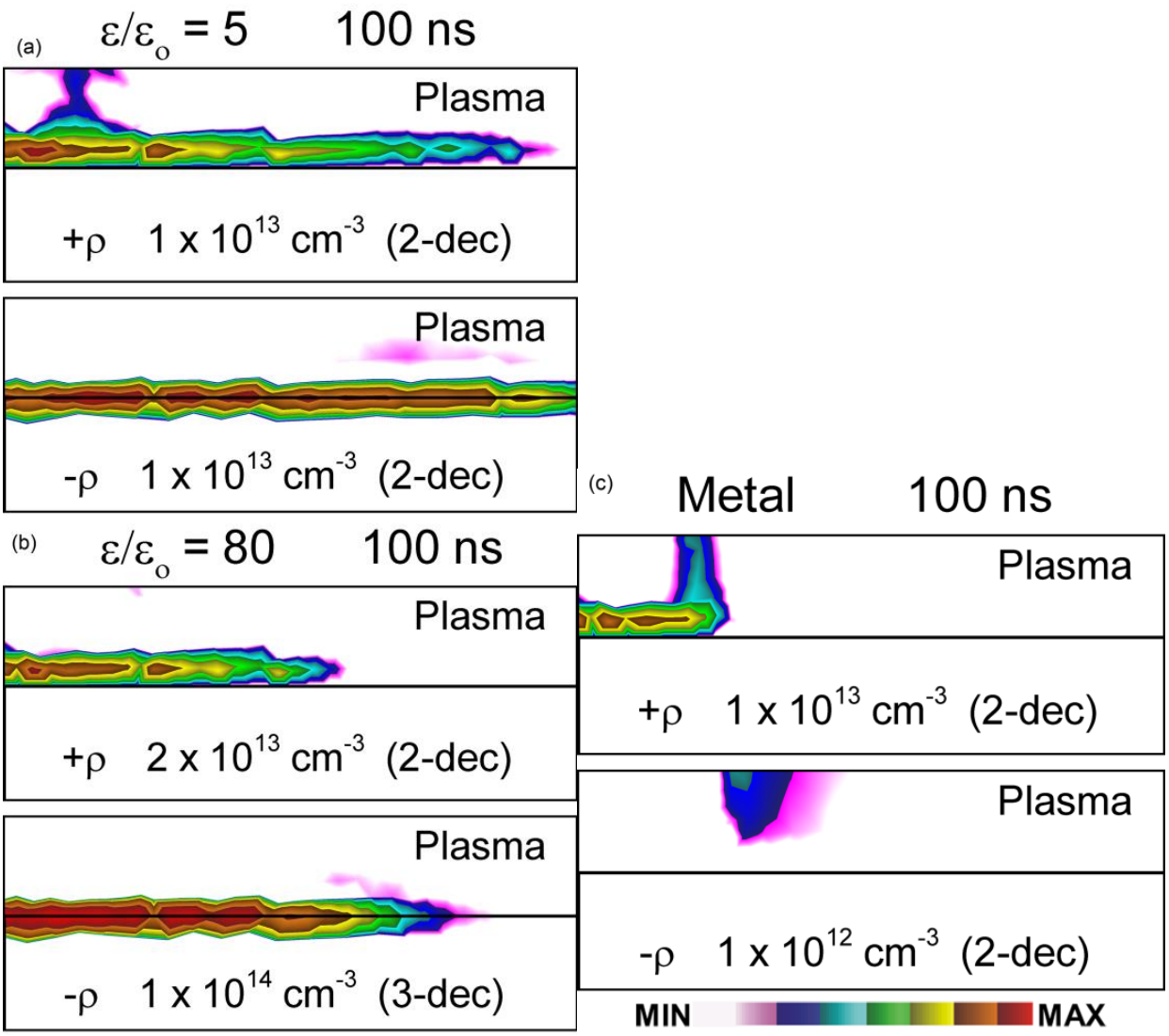

Figure 4.11 An enlarged view of the material surface showing total positive (top frame) and negative charge density (bottom frame) that result in a surface electric field. The time is 100 ns when the applied voltage pulse returns to 0. (a) ε_r = 5 (tissue-like), (b) ε_r = 80 (water-like) and (c) metal. Contours are on a log-scale with the maximum value and number of decades listed on the frame.

4.6 References

[1] A. Schutze, J. Jeong, S. Babayan, J. Park, G. Selwyn, and R. Hicks, "The Atmospheric-Pressure Plasma Jet: A Review and Comparison to Other Plasma Sources", Trans. Plasma Sci. **26**, 1685 (1998).

[2] M. G. Kong, G. Kroesen, G. Morfill, T. Nosenko, T. Shimizu, J. van Dijk, and J. L. Zimmerman, "Plasma medicine: an introductory review", New J. Phys. **11**, 115012 (2009).

[3] M. Laroussi, "Low-Temperature Plasmas for Medicine?", Trans. Plasma Sci. **37**, 714 (2009).

[4] M. Laroussi, I. Alexeff, and W. Kang, "Biological Decontamination by Non-thermal Plasmas", IEEE Trans. Plasma Sci. **28**, 184 (2000).

[5] M. Laroussi, M. Kong, G. Morfill, and W. Stolz, *Plasma Medicine: Applications of Low-Temperature Gas Plasmas in Medicine and Biology*, (Cambridge, Cambridge University Press, 2012), pp. 156-174.

[6] G. Fridman, G. Friedman, A. Gutsol, A.B. Shekter, V.N. Vasilets, and A. Fridman, "Applied Plasma Medicine", Plasma Process. Polym. **5**, 503 (2008).

[7] M. Keidar, A. Shashurin, O. Volotskova, M. Stepp, P. Srinivasan, A. Sandler, B. Trink, "Cold atmospheric plasma in cancer therapy", Physics of Plasmas, **20**, 057101 (2013).

[8] K. Fricke, H. Steffen, T. von Woedtke, K. Schroder, K-D. Weltman, "High Rate Etching of Polymers by Means of an Atmospheric Pressure Plasma Jet", Plasma Process. Polym. **8**, 51 (2011).

[9] C. van Gils, S. Hofmann, B. Boekema, R. Brandenburg, and P. Bruggeman, "Mechanisms of bacterial inactivation in the liquid phase induced by a remote RF cold atmospheric pressure plasma jet", J. Phys. D: Appl. Phys. **46,** 175203 (2013).

[10] P. Bruggeman and C. Leys, "Non-thermal plasmas in and in contact with liquids", J. Phys. D: Appl. Phys., 42, 053001 (2009).

[11] J.Y. Jeong, S.E. Babayan, V.J. Tu, J. Park, I. Henins, R.F. Hicks, and G.S. Selwyn, "Etching materials with an atmospheric pressure plasma jet", Plasma Sources Sci. Technol. **7**, 282 (1998).

[12] H. Paetzelt, G. Bohm, and T. Arnold, "Etching of silicon surfaces using atmospheric plasma jets", Plasma Sources Sci. Technol. **24**, 025002 (2015).

[13] E. Robert, T. Darny, D. Ries, S. Dozias, and J-M. Pouvesle, "Non thermal plasma jets interacting with targets and gas flows", 67th Gaseous Electronics Conference (GEC), BAPS.2014.GEC.ET1.6, November 2-7, 2014, Raleigh, NC.

[14] E. Robert, V. Sarron, T. Darny, D. Ries, S. Dozias, J. Fontane, L. Joly, J-M Pouvesle, "Rare gas flow structuration in plasma jet experiments", Plasma Sources Sci. Technol. **23**, 012003 (2014).

[15] D. Breden and L.L. Raja, "Computational study of the interaction of cold atmospheric helium plasma jets with surfaces", Plasma Sources Sci. Technol. **23**, 065020 (2014).

[16] J.M. Strobel, M. Strobel, C.S. Lyons, C. Dunatov, and S.J. Perron, "Aging of air-corona-treated polypropylene film", J. Adhesion Sci. Technol. **5**, 119 (1991).

[17] I. Ermolina, Y. Polevaya, Y. Feldman, B. Ginzburg, and M. Schlesinger, "Study of normal and malignant white blood cells by time domain dielectric spectroscopy", IEEE Trans. Dielectr. Electr. Insul. **8**, 253 (2001).

[18] Y. Feldman, I. Ermolina, and Y. Hayashi, "Time domain dielectric spectroscopy study of biological systems", IEEE Trans. Dielectr. Electr. Insul. **10**, 728 (2003).
[19] S. Norberg, E. Johnsen, and M.J. Kushner, "Formation of reactive oxygen and nitrogen species by repetitive negatively pulsed helium atmospheric pressure plasma jets propagating into humid air" Plasma Sources Sci. Technol. (accepted 2015).
[20] S. Norberg, PhD Thesis Department of Mechanical Engineering, University of Michigan at Ann Arbor (2015).
[21] X. Lu, M. Laroussi, V. Puech, "On atmospheric-pressure non-equilibrium plasma jets and plasma bullets", Plasma Sources Sci. Technol. **21**, 034005 (2012).
[22] X. Lu, Z. Jiang, Q. Xiong, Z. Tang, X. Hu, Y. Pan, "An 11 cm long atmospheric pressure cold plasma plume for applications of plasma medicine", Appl. Phys. Lett. **92**, 081502 (2008).
[23] E. Karakas, M. Akman and M. Laroussi, "The evolution of atmospheric-pressure low-temperature plasma jets: jet current measurements", Plasma Sources Sci. Technol. **21**, 034016 (2012).
[24] S. Reuter, J. Winter, A. Schmidt-Bleker, H. Tresp, M. Hammer, and K-D. Weltmann, "Controlling the Ambient Air Affected Reactive Species Composition in the Effluent of an Argon Plasma Jet", Trans. Plasma Sci. **40**, 2788 (2012).
[25] H.D. Young and R.A. Freedman, *Sears and Zemansky's University Physics with Modern Physics 13th Edition*, (San Francisco, Addison-Wesley, 2012), p. 801.
[26] S. Gabriel, R.W. Lau, and C. Gabriel, "The dielectric properties of biological tissues: III. Parametric models for the dielectric spectrum of tissues", Phys. Med. Biol. **41**, 2271 (1996).
[27] A. Laughton and D.F. Warne, *Electrical Engineer's Reference Book, 16th Edition*, (London, Butterworth & Co, 2002), p. 6/4.
[28] C. Bogey and C. Bailly, in V. Armenio, B. Geurts and B. Frohlich (eds.), *Direct and Large-Eddy Simulation VII: Proceedings of the Seventh International ERCOFTAC Workshop on Direct and Large Scale Eddy Simulation VII*, (Springer Science, 2010).
[29] M. Teschke, J. Kedzierski, E.G. Finantu-Dinu, D. Korzec, and J. Engemann, "High-Speed Photographs of a Dielectric Barrier Atmospheric Pressure Plasma Jet", Trans. Plasma Sci. **33**, 310 (2005).
[30] J. S. Sousa, K. Niemi, L. J. Cox, Q. Th. Algwari, T. Gans, and D. O'Connell, "Cold atmospheric pressure plasma jets as sources of singlet delta oxygen for biomedical applications", J. Appl. Phys. **109**, 123302 (2011).
[31] S. Cellestin, G. Canes-Boussard, O. Guaitella, A. Bourdon, and A. Rousseau, "Influence of the charges deposition on the spatio-temporal self-organization of streamers in a DBD", J. Phys. D: Appl. Phys. 41, 205214 (2008).
[32] S. Cellestin, Z. Bonaventura, O. Guaitella, A. Rousseau, and A. Bourdon, "Influence of surface charges on the structure of a dielectric barrier discharge in air at atmospheric pressure: experiment and modeling", Eur. Phys. J. Appl. Phys. 47, 22810 (2009).
[33] R. Dorai, PhD Thesis Department of Chemical Engineering, University of Illinois at Urbana-Champaign (2002).
[34] J. B. A. Mitchell, Phys. Rpts. **186**, 215 (1990).
[35] D.S. Stafford and M.J. Kushner, J. Appl. Phys. **96,** 2451 (2004).
[36] B. F. Gordiets, C. Ferreira, V. Guerra, J. Loureiro, J. Nahorny, D.Pagnon, M. Touzeau, and M. Vialle, IEEE Trans. Plasma Sci. **23**, 750 (1995).

Chapter 5 APPJ onto Water Layer

5.1 Introduction

The use of atmospheric pressure plasma jets in the context of plasma medicine for wound healing, sterilization of surfaces and cancer treatment is an increasingly important area of research.[1-3] Often the surface being treated is cellular tissue, which is covered by a thin liquid layer of a blood serum-like liquid a few hundred microns thick.[4] Instead of directly interacting with the tissue, the plasma-produced neutral reactive species, ions and photons first react with the liquid layer. Gas phase species solvate into the liquid and undergo additional reactions before the plasma produced activation energy reaches the underlying tissue. Photolysis and photoionization from plasma-produced ultraviolet and vacuum-ultraviolet (UV/VUV) photons may directly produce active species (neutral reactive species and ions) in the top layer of the liquid that subsequently react to form other aqueous ions and neutral reactive species.

Many recent investigations have addressed the manner in which plasma jets produce reactivity in liquids, starting with water.[5-7] The majority of these studies have used a rare-gas seeded with a small amount (usually < 1%) of a reactive gas (e.g., O_2, N_2, H_2O) as the media flowing through the plasma tube, which is then exhausted into room air. RONS (reactive oxygen and nitrogen species) are directly produced in the plasma jet and by mixing with the ambient air.[8] Configurations using gas shrouds around the jet have been investigated to control the mixing of the ambient air with the jet to then control reactive species production.[9,10]

A parameter in these investigations is whether the plasma plume emanating from the jet contacts the liquid layer (touching) or is not in direct contact with the liquid layer (not-touching). Experimentally, this distinction is usually made on whether the luminous visible plume from the jet extends to the surface of the liquid. Significantly different results for the reactive species composition in the liquid have been reported based on whether the plasma jet is touching or not-touching the liquid.[11] The delivery of electric fields to the underlying tissue is also expected to be sensitive to the touching or not-touching conditions. In this paper, we discuss results from a computational investigation of plasma jets incident onto a thin water layer over a tissue-like dielectric. Different applied voltages are used which result in touching and not-touching configurations. The proportion and magnitude of aqueous charged and neutral species that diffuse to the underlying tissue depends on the touch or no-touch conditions. Aqueous ions diffusing through the liquid to the underlying tissue are significantly greater for touching conditions due to the rapid solvation of gas phase ions afforded by the contact. Neutral aqueous species produced by the jet are less sensitive to the touch or no-touch conditions, and scale more proportionately with the energy deposition per pulse in the jet.

The model used in this investigation is described in Sec. 5.2. A comparison of touching and not-touching plasma jets onto thin liquid layers is discussed in Sec. 5.3. The concluding remarks are in Sec. 5.4.

5.2 Description of the Model

The 2-D cylindrically symmetric, plasma hydrodynamics model utilized in this investigation is *nonPDPSIM* which is executed on an unstructured mesh as described in detail in Refs. [12,13]. For the purpose of this study, *nonPDPSIM* consists of three major modules – the

plasma transport module, the radiation transport module and the fluid transport module. In the plasma transport module, Poisson's equation and continuity equations for all charged species (in the volume and on surfaces) are integrated in time using a fully implicit Newton-iteration technique.[13] Spatial derivatives and divergence operators are expressed in fully conservative finite-volume form. Each time step is then followed by an implicit update of the electron energy equation for electron temperature, neutral species continuity equations and radiation transport. Transport coefficients and rate coefficients for electrons as a function of electron temperature are obtained from solutions of the stationary Boltzmann's for the electron energy distribution. These tabulated coefficients which are interpolated during execution of the model are updated on sub-nanosecond time scales to reflect changing species and mole fractions. Radiation transport addresses photoionization of O_2 and H_2O in the gas phase, and photoionization and photo-dissociation of H_2O_{aq} in the liquid phase. (The subscript $_{aq}$ denotes aqueous or in liquid species.) This portion of the model is discussed in detail in Chapter 2 and Refs. [13,14].

In the fluid module, a modified form of the Navier-Stokes equations (continuity, momentum, energy) are solved to produce the advective flow field while including body forces (e.g., momentum transfer from charged particles) and heat sources (e.g., Joule heating and change in enthalpy due to reactions) produced in the plasma transport module.[15] Since the gas constituents have large differences in atomic or molecular mass, the mass continuity equation is replaced by a number-density continuity equation and a fourth equation for the average molecular weight. These equations are simultaneously and implicitly solved using numerically derived Jacobian elements on the same unstructured mesh as the plasma calculation. The individual continuity equations for all species are simultaneously integrated using the advective flow field as a check for the average molecular weight.

The key modification to the model discussed in Chapter 2 is the incorporation of a liquid layer above the tissue. The initial liquid layer in this investigation is pure water with 8 ppm dissolved O_2. The water layer is included in the model using the same algorithms as in the gas phase. In principle, the water layer is just another region of the plasma – albeit with a higher density and different reaction mechanism. Surface tension is not explicitly calculated in the model – the boundary between the liquid and gas phase is specified. However, evaporation of the water layer into the gas phase is included. The methods used to couple the gas phase plasma and the liquid phase calculations, the reaction mechanism, and method for representing water vapor evaporating from the reactive and dielectric water layers (see below) are discussed in Ref. [14].

The fluid module is first executed without the plasma to establish the advective flow field. For the geometry and flow rates of interest, the flow field is established in tens of ms of integration time using timesteps that are typically many times the Courant limit for the smallest cells in the mesh. The plasma is then initiated as described below, and the fluid and plasma modules are simultaneously integrated until the voltage pulse is terminated and space charge is allowed to dissipate. At that point, we stop solving Poisson's equation and assume local charge neutrality. The fluid module and continuity equations of individual species continue to be integrated with ns timesteps to account for rapid reactions that initially take place. As the reactivity diminishes, the timesteps grow to 1 μs over 50 ms of flow during which the majority of reactive gaseous species are blown out of the computational domain. At this point, the fluid module is terminated and the reactions of the aqueous species are continued to be solved with a time step of 10 – 100 μs until the computation is terminated at one second.

Based primarily on the dimensions of the kINPen developed by the INP Greifswald, [9-10] the geometry used in this investigation for the plasma jet is a cylindrical tube with a diameter of 1.6 mm and walls that are 0.4 mm thick. The tip of the coaxial electrode, 0.25 mm in diameter, is 3.5 mm from the end of the tube, as shown in Fig. 5.1. In this configuration, there is an axial component of the electric field that better enables the plasma to intersect with the liquid.[16,17] This configuration differs from those that have an electric field that is dominantly perpendicular to the gas flow and which produces a plume that is dominated by neutral reactive species.[18] The end of the tube is 7.5 mm above a 200 μm thick water layer covering the tissue-like dielectric. The portion of the water treated as plasma extends to a radius of 2.75 mm. For larger radii, the water is not treated as a reactive zone but rather is represented simply as a dielectric material. These separate water zones were implemented to lower the computational cost. Water evaporates from both water zones. The numerical mesh, also shown in Fig. 5.1, consists of 12,700 nodes with several refinement zones having spatial resolution varying from 24 μm near the tip of the electrode and within the water layer to 300 μm in the periphery of the domain.

Helium seeded with O_2 (He/O_2 = 99.8/0.2, 5 slm) is flowed through the tube. Humid air ($N_2/O_2/H_2O$ =79.5/20/0.5) flows at a lower rate outside the tube (4 slm) to entrain the helium and guide the helium flow over the surface. The resulting mixture flows out of the computational domain through a pump port on the side boundary. The material for the tube has a dielectric constant $\varepsilon_r = \varepsilon/\varepsilon_o = 4$, the tissue underlying the liquid has $\varepsilon_r = 5$ and the non-reactive water layer has $\varepsilon_r = 80$. At the beginning of the plasma period, the voltage pulse is applied for 50 ns (5 ns rise time).

A single discharge pulse of a plasma jet, its afterglow and activation of a thin water layer are discussed here. Actual systems are operated with a pulse-repetition frequency (PRF). Plasma jet treatment of tissue differs significantly from DBD treatment in many ways – one being that the gas in a plasma jet has a finite residence time in the vicinity of the tissue. Depending on flow rates, jet diameter and situational factors (e.g., turbulence, eddies produced by local structures) [19], the gas and plasma may smoothly blow out of the vicinity of the tissue in a laminar manner with air diffusing into the jet or there may be significant recirculation. All of these effects are important to the final fluence of reactants to the tissue underlying the liquid. The results of this study are therefore applicable to conditions of laminar flow with a PRF of less than a few kHz where the plasma activated gas flows out of the volume between pulses.

5.3 Touching and not-Touching Plasma Jets onto a Liquid Layer

5.3.1 Transport of gas phase RONS

The pre-pulse steady-state densities of He, O_2, N_2 and H_2O in the fluid flow-field are shown in Fig. 5.2 from the exit nozzle of the jet. Helium flows down from the tube into the ambient air where the helium is largely confined to the center of the jet by air diffusing into the core. The He then flows radially outward from the stagnation point on axis. The axial speed of the flow field inside the tube is 42 m/s. The corresponding Reynolds number is Re = 630, which is less than the value for onset of turbulence for pipe flow, Re = 2300. So the flow should be laminar leaving the tube. Once the jet leaves the tube, for Re = 630 the onset of turbulence will occur at about $50r_0$ from the outlet, where r_0 is the jet radius.[20] For our conditions, the onset of turbulence would be expected at about 4 cm from the tube outlet, which is larger than our outlet-surface distance. The increase in the He concentration at the right of the panel is a vortex at

larger radii. The density of O_2 is shown over three decades to highlight the small amount, 5.9×10^{16} cm^{-3}, contained in the input He gas flow. The diffusion of air into the He jet increases the O_2 concentration to 3.9×10^{17} cm^{-3}, on axis 1 mm above the water. N_2 from the ambient is absent from the interior of the tube and becomes entrained in the He jet further from the exit as air diffuses into the jet stream. The density of N_2 is 1.3×10^{18} cm^{-3} on axis 1 mm above the water. The water vapor that evaporates from the water layer is displaced by the helium jet and flows to the pump. The density of H_2O in the ambient air is 1.2×10^{17} cm^{-3}. Directly above the liquid water on the axis, the density of H_2O is low, $\approx 10^{16}$ cm^{-3}, due to the inability for the ambient water vapor to diffuse into the core of the helium jet. The flow of the jet displaces the evaporating water vapor directly above the liquid layer at small radii and compresses the water vapor at larger radii. The reactive species delivered to the surface of the liquid are determined by the species initially produced by electron impact excitation, dissociation and ionization in the plasma plume, their subsequent reactions, convection in the fluid flow field and density gradient driven diffusion.

Plasma jets for three voltages were investigated – -10 kV, -15 kV and -20 kV. The voltage pulses have a 5 ns rise time and 45 ns duration. A cloud of plasma with density of 10^{11} cm^{-3} and radius 0.7 mm is seeded at the tip of the powered electrode for ignition. The electron densities, n_e, at the end of the discharge pulse for each voltage are shown in Fig. 5.3. The electron avalanche begins as an ionization wave at the tip of the pin electrode, and quickly assumes an annular, wall hugging mode [21,22], which charges the inside surface of the glass tube. As the ionization wave exits the tube, the avalanche returns to the axis. This is the same behavior for all voltages – n_e is annular and surface-hugging inside the tube and transitions to on-axis within a few mm of exiting the tube. The n_e on axis 1 mm from the end of the tube is $6.7 \times$

10^{12} cm^{-3}, 2.7×10^{13} cm^{-3}, and 6.9×10^{13} cm^{-3} for -10 kV, -15 kV and -20 kV. In the -10 kV case, the plasma plume, represented by the electron density, does not reach the surface of the water with a significant density and this is considered the indirect, or not-touching, case. The plasma plumes for the -15 kV and -20 kV cases both reach the water and are the direct, or touching cases. The electron density 1 mm above the water layer on axis is 4.2×10^{12} cm^{-3} and 6.7×10^{12} cm^{-3} for the -15 kV and -20 kV cases.

The electron density, electron temperature (T_e) and electron impact ionization source (S_e) are shown in Fig. 5.4 for the -15 kV case. The speed of the ionization wave depends on the applied voltage. For the -15 kV case, the electron plume touches the surface of the water at 26 ns. A conducting channel of increasing electron density is produced on axis as the capacitance of the water layer is charged until the voltage is terminated. T_e, and S_e trace the trajectory of the head of the ionization wave (the *plasma bullet*) or guided streamer.[8] T_e and S_e in the head of the plasma bullet midway through the gap are 5 eV and 1×10^{21} $cm^{-3}s^{-1}$. The mushroom shaped luminous plasma bullet from the simulation before striking the surface of the water layer is similar to those shapes experimentally observed for plasma bullets.[23] Upon striking the water layer, a restrike, positive ionization wave propagates back up the plasma column.

The ionization wave generated in the plasma tube propagates through the helium dominated channel and, if sufficient duration or length, intersects with the liquid layer. Since the liquid layer has largely dielectric properties, the discharge at this point behaves similarly to a dielectric barrier discharge (DBD) – the plasma spreads on the surface of the liquid as the surface charges. This spreading results from many causes. The large dielectric constant of the liquid excludes electric fields, on a relative basis, out of the liquid in favor of the air. The lower electric field and higher neutral density in the water produces a low E/N [electric field/(gas or

liquid number density)] that will not self-sustain the plasma. For example, at the instant the ionization wave reaches the surface of the water at 26 ns, the E/N = 60 Td (1 Td = 10^{-17} V-cm^2) 25 μm above the surface of the water while the E/N = 0.0025 Td 25 μm below the surface of the water. These latter values of E/N are well below that required to self-sustain a plasma. The charged particle inventory in the water is therefore a result of electrons and ions solvating into the liquid, photoionization and water chemistry, and not direct electron impact dissociation and ionization.

There is also *de facto* charging of the surface layer of the liquid due to the long dielectric relaxation time of the low-conductivity water. The solvation of electrons into the water, and charge exchange from positive ions with water molecules, occurs on a ps to ns timescale, transferring charge to the water. The low mobility of these charged species in the water confines the transferred charge to the surface of the water for the duration of the discharge. The charge injection into the water is augmented by photoionization of the water by UV/VUV photons produced by the plasma adjacent to the water. For these conditions, the charge at the surface of the water at the end of the discharge pulse is due 90% from solvation of gas phase charged particles into the liquid and 10% from photoionization.

Plasma plumes that do not touch the water layer lack the nearly immediate electron solvation, charge exchange and photoionization (and photolysis) reactions at the surface of the liquid that result from plasma contact. The spreading of the plasma on the surface of the water is important to the production of charged aqueous species. The solvation of charged species is distributed over a larger radius, and the close contact enables UV/VUV radiation, that has a short mean-free-path, about 12 μm, to penetrate into the water. The electron density in the not-touching plasma plume largely decays due to recombination with molecular ions, dominantly

N_4^+ and O_2^+, and electron attachment to O_2 in many to tens of microseconds. This time is short compared to the time for the convective gas flow to reach the liquid, about 0.34 ms. So the vast majority of electrons will have recombined or attached prior to reaching the liquid. The end result is that the effluent of the plume consists of a low density ion-ion plasma. Since the time scale for ion-ion recombination can be commensurate with the time for the convective gas flow to reach the liquid, a low density of ions does reach the water even in the not-touching case. For example, for the -10 kV not-touching case, the maximum gas phase negative ion density adjacent to the water is 10^{10} cm^{-3} at tens of μs after the discharge pulse. Note that this long time scale ion-ion plume occurs for the higher voltages as well. As discussed below, its influence is simply smaller in the touching cases.

The gas dynamics play an important role in distributing gas phase reactive species to the liquid. For example, the density of O_3 is shown in Fig. 5.5 for the –15 kV case. The O atoms that produce O_3 by a 3-body reaction with O_2 are formed dominantly inside the tube by electron impact dissociation of the O_2 additive. Since the density of O_2 is low in the tube, the formation of O_3 is low. The formation of O_3 is dominantly outside the tube where the O_2 in the air diffuses into the plasma plume and reacts with the O atoms formed in the tube. Once formed, O_3 is relatively unreactive in the absence of organic impurities in the air, and so flows with the plume to the surface of the liquid. As the plume spreads along the surface of the water, the O_3 solvates to form the terminal species O_{3aq}. The solvation of O_3 is therefore fairly uniform over a large radius. The majority of O_3 flows out of the computational domain. Here is where the details of the local flow dynamics are important. Vortices, turbulence or stagnation-point flow that are produced by, for example, non-vertical jets or the structure of sample-wells will recirculate species such as O_3 back to the water layer instead of directly flowing out of the region of interest.

O_{3aq} largely results from solvation of gas phase O_3 and the production of O_3 depends largely on the inventory of O atoms produced by the discharge. The formation of O_3 is therefore only weakly dependent on whether the plasma touches or does not tough the liquid, other than plasma touching plumes are typically of longer duration and so produce more O atoms in the vicinity of the liquid. The maximum O_3 density 1 mm above the liquid layer at 100 μs is 1.1×10^{13} cm^{-3}, 4.6×10^{13} cm^{-3}, and 1.4×10^{14} cm^{-3} for -10 kV, -15 kV and -20 kV. The end result is that O_{3aq} is produced in large amounts in both the touching and not-touching cases.

The production of the hydroxyl radical, OH, in the gas phase significantly differs from that of O_3. OH is initially formed by electron impact dissociation of H_2O during the interaction of the plasma and the humidity in the air and, more importantly, the evaporated water vapor above the water layer. The density of OH is shown in Fig. 5.6 at 1 μs and 200 μs after the discharge pulse for the –15 kV case. OH is largely produced in the plasma column by electron impact dissociation of water diffusing into the jet, generating a maximum density of 2.2×10^{12} cm^{-3} at mid-gap at the end of the pulse. A larger density is produced adjacent to the water by the spreading plasma over the liquid intersecting with the evaporating water vapor. The maximum OH density adjacent to the water is 7.2×10^{14} cm^{-3} at the end of the discharge pulse. Although the production of OH does not significantly change in mid-gap for the touching and not-touching cases beyond the change in energy deposition (8.0×10^{11} cm^{-3}, 2.2×10^{12} cm^{-3}, and 8.5×10^{12} cm^{-3} for -10 kV, -15 kV and -20 kV), the absence of spreading of the plasma on the liquid in the not-touching case significantly reduces the inventory of OH available. The OH mutually reacts to form H_2O_2, reacts with nitrogen atoms to form NO, solvates into the water to form OH_{aq}, or blows away within a few ms with the flow.

Photolysis of the water also produces OH_{aq}. The production of OH_{aq} by photolysis is less than 1% in the not-touching case and 10% in the touching case. The reason for more photolysis producing OH_{aq} in the touching case is that electron impact excitation produces N_2^{**} in the immediate vicinity of the surface of the water by the surface hugging plasma. VUV photons emitted by N_2^{**} are then able to reach the water prior to being absorbed in the humid air. By mutual reaction of OH_{aq}, H_2O_{2aq} is produced which is also largely a terminal species in the absence of organic matter in the liquid. As shown in Fig. 5.6, the high concentrations of OH at 1 μs resulting from spreading of the plasma through the evaporating water vapor produces a distribution of OH_{aq} having a maximum density of 2.2×10^{14} cm^{-3} or (3.7×10^{-7} M) at a radius of 1 mm. The primary loss mechanism for OH_{aq} is the reaction forming H_2O_{2aq}, $OH_{aq} + OH_{aq} \rightarrow H_2O_{2aq}$. The lifetime of OH_{aq} based on this maximum density and rate coefficient of 5.5×10^9 $M^{-1}s^{-1}$ [14,24] is about 0.25 ms. The resulting H_2O_{2aq} then diffuses through the water layer to the underlying tissue.

Reactive nitrogen species (RNS), N_xO_y, consist of the sum of NO, NO_2, NO_3, N_2O_3, N_2O_4 and N_2O_5. RNS are formed as the plasma plume reacts with the ambient air as shown in Fig. 5.7. Nitrogen oxide (NO) is initially formed primarily by reaction of N atoms with O_2. The N atoms are formed dominantly by the electron impact dissociation of N_2 resulting from air diffusing into the plume. Since the He flow from the jet displaces air at the surface of the water and there is no N_2 injected through the tube, the RNS are primarily produced at the edge of the plasma jet where air diffuses into the plume. The precursor species to N_xO_y, NO, is largely formed at the boundary of the plasma where the density of the N_2 is largest and secondarily in the core of the plasma plume where the O atom density is the highest. The N_xO_y that are formed from the plasma discharge reacting with the ambient air react further react with OH and HO_2 in the

ambient to form HNO_2, HNO_3 and HOONO. The large densities of N_xO_y produced in, for example, DBDs accumulates over thousands of pulses and can reach 3×10^{17} cm^{-3} in DBDs sustained in non-flowing air.[25] In the absence of vortices or other forms of recirculation in the gas phase, the NO and NO_2 that would normally be the starting point for forming higher N_xO_y in stagnant systems are blown out of the volume in plasma jets. The density of higher N_xO_y and acids HNO_x are therefore small compared to DBDs, reaching a maximum density 1 mm above the liquid of only 2×10^{11} cm^{-3} during the single pulse.

5.3.2 Evolution of Aqueous Reactivity

The gas phase species in contact with the water then solvate to form aqueous species. The densities of aqueous ions averaged over the water layer as a function of time are shown in Fig. 5.8 for the -10 kV, -15 kV and -20 kV cases. Positive water ions are produced by charge exchange from gas phase positive ions striking the water and by photoionization. The $H_2O^+_{aq}$ then quickly charge exchange with water to produce hydronium, $H_3O^+_{aq}$ and hydroxyl radicals, OH_{aq}. $H_3O^+_{aq}$ is a terminal species that dominates the positive ions and whose density is largely established by 1 ms after the discharge pulse. The average density of $H_3O^+_{aq}$ in the water layer is 2×10^{14} cm^{-3} and 3×10^{13} cm^{-3} for the -20 and -15 kV cases, respectively. The aqueous anions are initially formed by solvated electrons dissociatively attaching with H_2O_{aq} to form OH^-_{aq} or by attaching to the dissolved O_{2aq} to form $O_2^-{}_{aq}$. The OH^-_{aq} then combines with $H_3O^+_{aq}$ or OH_{aq} to form OH_{aq} and O^-_{aq} respectively. The O^-_{aq} then combines with O_{2aq} to form the terminal negative ion $O_3^-{}_{aq}$. In the absence of significant densities of N_xO_{yaq}, the long lived $O_2^-{}_{aq}$ and $O_3^-{}_{aq}$ dominate the negative ions.

As shown in Fig. 5.8 for -20 kV, $O_2^-{}_{aq}$ is quickly formed during the discharge pulse by attachment of solvated electrons to dissolved O_2 as the plasma touches and spreads on the surface of the water. The time for electron solvation is only tens of ps and the density of solvated electrons reaches its maximum value of 2.1×10^{14} cm^{-3} within 200 ns. The density of $H_3O^+{}_{aq}$ develops over a few μs since up to two charge exchange reactions are required for its formation – solvating ions reacting with water to form $H_2O^+{}_{aq}$, and then a second reaction with water to form $H_3O^+{}_{aq}$. There is also a contribution to $H_3O^+{}_{aq}$ by hydrolysis of HNO_{xaq}, however since the density of the acids is low, this is a minor contribution. The densities of $O_2^-{}_{aq}$ and $H_3O^+{}_{aq}$ for -15 kV show the same trends as for -20 kV. The initial rise in densities for -15 kV are delayed in time by about 20 ns compared to -20 kV, which is the difference in arrival times of the electron plumes at the surface of the water. The densities are also decreased by a factor of 5-6, a consequence of the shorter length of time that the surface ionization wave spreads on the water at the lower voltage.

The electron plume does not reach the water layer with a significant density for the -10 kV case and so there is no prompt formation of aqueous ions. As noted above, the electron-ion plume transitions to an ion-ion plume as recombination and attachment reduce the electron density. This recombining ion-ion plume then intersects with the water layer on up to a ms timescale, which is the time required for the plume containing the ion-ion plasma to cross the gap. Upon intersection with the water, the low density of gas phase ions (10^{10} at 10 μs) solvate into the water over several ms, producing average aqueous densities of $>10^9$ cm^{-3}. $O_2^-{}_{aq}$ and $H_3O^+{}_{aq}$ are produced in a similar manner as described above for the higher voltages, evolving over 10s to 100s ms to produce an aqueous density of nearly 10^{10} cm^{-3}, a factor of 10^4 smaller than for the touching cases. This same, longer time solvation of the ion-ion plume also occurs

for the higher voltages. However, the contribution of the ion-ion plasma plume to aqueous ion formation is simply smaller than the direct solvation of the electron-ion plasma in contact with the water.

The N_xO_y that reaches the water also solvates into the liquid, where N_xO_{yaq} eventually forms HNO_{2aq}, HNO_{3aq} and $HOONO_{aq}$.[14] HNO_{2aq} is a weak acid so only about 1% of its concentration hydrolyzes to $H_3O^+_{aq}$ and $NO_2^-_{aq}$. HNO_{3aq} and $HOONO_{aq}$ are strong acids and nearly completely hydrolyze to form $H_3O^+_{aq}$, $NO_3^-_{aq}$ and $ONOO^-_{aq}$. The terminal anions for N_xO_{yaq} species are $NO_3^-_{aq}$ and $ONOO^-_{aq}$. Since the majority of N_xO_y that solvates in the water is not formed in the spreading plasma on the surface, these molecules must convect and diffuse from more remote locations. This convection requires about 1 ms for the touching cases, resulting in the $NO_3^-_{aq}$ and $ONOO^-_{aq}$ reaching a maximum density of 10^{11} cm^{-3} for -20 kV and 10^{10} cm^{-3} for -15 kV. The same process requires tens of ms in the not-touching cases producing a density of 10^8 cm^{-3}. The dynamics of N_xO_y for DBDs in stagnant gases and in jets do significantly differ. In stagnant DBDs, N_xO_y accumulates in the gas phase, diffuses into the water and hydrolyzes. In jets, there are shorter residence times for the N_xO_y in the gas phase due to the convective flow and so less opportunity to accumulate to large densities. The result is less hydrolysis in the water and low densities of nitrates and nitrites in the liquid. For both types of plasmas sources, N_xO_{yaq} will accumulate in the liquid phase over successive discharge pulses.

The densities of neutral aqueous species averaged over the water layer as a function of time are shown in Fig. 5.9 for the -10 kV, -15 kV and -20 kV cases. In the touching cases (-15 kV, -20 kV), the OH_{aq} has a rapid rise during the discharge pulse (tens of ns) due to photolysis, augmented on the hundreds ns time scale by charge exchange reactions forming $H_3O^+_{aq}$ and OHaq. The maximum densities for OH_{aq} are 5.8×10^{14} cm^{-3} for -20 kV and 7.4×10^{13} cm^{-3} for -

15 kV. The majority of OH_{aq} is expended in forming H_2O_{2aq}, whose maximum densities of 2.7×10^{14} cm^{-3} for -20 kV and 4.4×10^{13} cm^{-3} for -15 kV are reached in about 1 ms. The H_{aq} that is produced by photolysis of H_2O_{aq} reacts with the dissolved O_{2aq} to form HO_{2aq}, which is also formed by O_{aq} reacting with OH_{aq}. As the OH_{aq} converts to H_2O_{2aq} over time in the water layer, the primary loss mechanisms for HO_{2aq} become reactions with NO_{aq} to form HNO_{3aq} or hydrolysis to form $H_3O^+_{aq}$ and $O_2^-{}_{aq}$. The density of HO_{2aq} rises during the discharge pulse due primarily to the source of H_{aq} in photolysis reactions (6×10^{14} cm^{-3} for -20 kV and 7×10^{13} cm^{-3} for -15 kV) and slowly declines on ms timescales as NO solvates to form NO_{aq}. Since the source of O_{3aq} is dominated by diffusion of O_3 from the gas phase, its density increases over many ms with maximum values of 2.1×10^{14} cm^{-3} for -20 kV and 5.6×10^{13} cm^{-3} for -15 kV.

The time evolution of OH_{aq} for the not-touching case (-10 kV) significantly differs from the touching cases. Lacking the photolysis and charge exchange reactions which produce OH_{aq} on ns timescales as for touching cases, diffusion of OH into the water and dissociative excitation transfer to water molecules by $N_2(A)$ produce OH_{aq} over hundreds of μs. Note that the rise of O_{3aq} shadows that of OH_{aq} as both require diffusion of neutral species from the gas phase for their formation in the liquid. The maximum densities of O_{3aq} and OH_{aq} are 6.4×10^{12} cm^{-3} and 2.8×10^{12} cm^{-3}, respectively. The OH_{aq} converts to H_2O_{2aq} whereas O_{3aq} is a terminal species. The density of OH_{aq} falls below that of H_2O_{2aq} within 1 μs, in agreement with Tresp *et al.*[7] The formation of the other major neutral aqueous species is less dependent on the plasma striking the surface than for ion species. An exception is HO_{2aq} whose formation benefits from the production of H_{aq} during photolysis reactions which have at best a minor role in the not-touching case. As a result, HO_{2aq} is disproportionately smaller for the -10 kV case.

5.3.3 Fluences to the Tissue

The treatment of the underlying tissue ultimately depends on the fluence of reactive species that transport through the liquid layer. These fluences are shown in Fig. 5.10 after 10 s following a single discharge pulse. The maximum fluences for $H_3O^+_{aq}$ and $O_2^-{}_{aq}$ for -20 kV are 10^{10} cm^{-2}. For the -15 kV touching case, the fluences are reduced by a factor of 10. This reduction is largely a consequence of the shorter time the plasma spreads on the liquid for -15 kV. The small production of aqueous ions by the ion-ion plume for -10 kV does not register a fluence on this scale. The low rate of solvation of N_xO_y to form aqueous RNS is reflected in the small fluences of $NO_3^-{}_{aq}$ and $ONOO^-_{aq}$ to the tissue, and which is only significant in the high voltage case. The neutral species are less affected by the touching or not-touch conditions. For example, the formation of O_{3aq} results from the advective flux of O_3 from above the water layer, a process which is not particularly sensitive to touching or not-touching conditions. So the fluence of O_{3aq} is largely a function of energy deposition and decreases in proportion to the applied voltage (4 times more energy per pulse for -20 kV compared to -10 kV). The fluence of H_2O_{2aq} to the tissue has a larger decrease with decreasing voltage than O_{3aq} due to the contribution of photolysis and charge exchange to formation of its precursor OH_{aq}. However this decrease in H_2O_{2aq} is small compared to the ions – a consequence of a large fraction of OH_{aq} originating from diffusion of neutral species into the water. The fluence of HO_{2aq} for the not-touching case is not appreciable, as its formation depends on the production of H atoms by photolysis which is only significant for touching cases.

5.3.4 Electric Fields

Another factor which is sensitive to the plasma jet touching or not-touching the liquid is the delivery of electric fields to the tissue underlying the liquid. The maximum electric field at the surface of the tissue occurs at the end of the discharge pulse for the -10 kV, not-touching, case and is 1 kV-cm^{-1}. For the touching cases, the maximum electric field at the surface of the tissue occurs within 5 – 10 ns of the ionization wave striking the water layer and reaches a value of 14 kV-cm^{-1} for the -15 kV case and 17 kV-cm^{-1} for the -20 kV case. From shortly after impact of the ionization wave until the pulse terminates, the magnitude of the electric field decreases by only a few kV-cm^{-1}. Once the voltage is removed, the field quickly dissipates as the charge density on the surface of the water decreases. These values of electric field for a single pulse, up to 20 kV-cm^{-1} for tens of ns, are near the threshold for producing electroporation.[26] The threshold electric field for electroporation decreases with increasing number of pulses, and so the potential for producing electroporation with touching plumes may be significant at high PRF.

5.4 Concluding Remarks

One of the major distinctions in producing active aqueous species in water layers over tissues by plasma jets is whether the visible electron-ion plasma plume touches the surface of the water. There are at least two major modes for delivery of active species to the water layer. The first can dominate in touching cases – the spreading of plasma over the liquid surface. This immediate proximity of the plasma to the liquid enables photolysis, direct charge exchange reactions with H_2O_{aq}, and direct solvation of electrons. The longer the dwell time of the plasma on the surface of the liquid, the more aqueous ions and photolysis products are formed over a

larger area. Species such as HO_{2aq} that trace their origins to these reactions are also produced in larger numbers. Not-touching plasmas do receive fluxes of gas phase ions in the form of an ion-ion plume, however these fluxes can be orders of magnitude smaller than in the touching cases.

The second mode of delivery is convection and diffusion of neutral species to the liquid which are formed remotely from the surface. The formation of aqueous reactivity by neutral species is much less sensitive to touching or not-touching conditions, as demonstrated by the commensurate, voltage scaled fluences of O_{3aq} to the tissue discussed here. The delivery of these neutral species to the water is more sensitive to fluid dynamics than for the ions. Vortices, turbulence and other forms of recirculation that extend the residence time of neutral species at the surface of the water increases the likelihood of their solvation. This is particularly the case for N_xO_y species that typically accumulate over many discharge pulses in DBDs sustained in non-flowing gas. For strictly laminar, non-vortexed flows, N_xO_y must diffuse through the He core of the jet to reach the surface, and is more likely to be blown away before solvating in significant amounts.

5.5 Figures

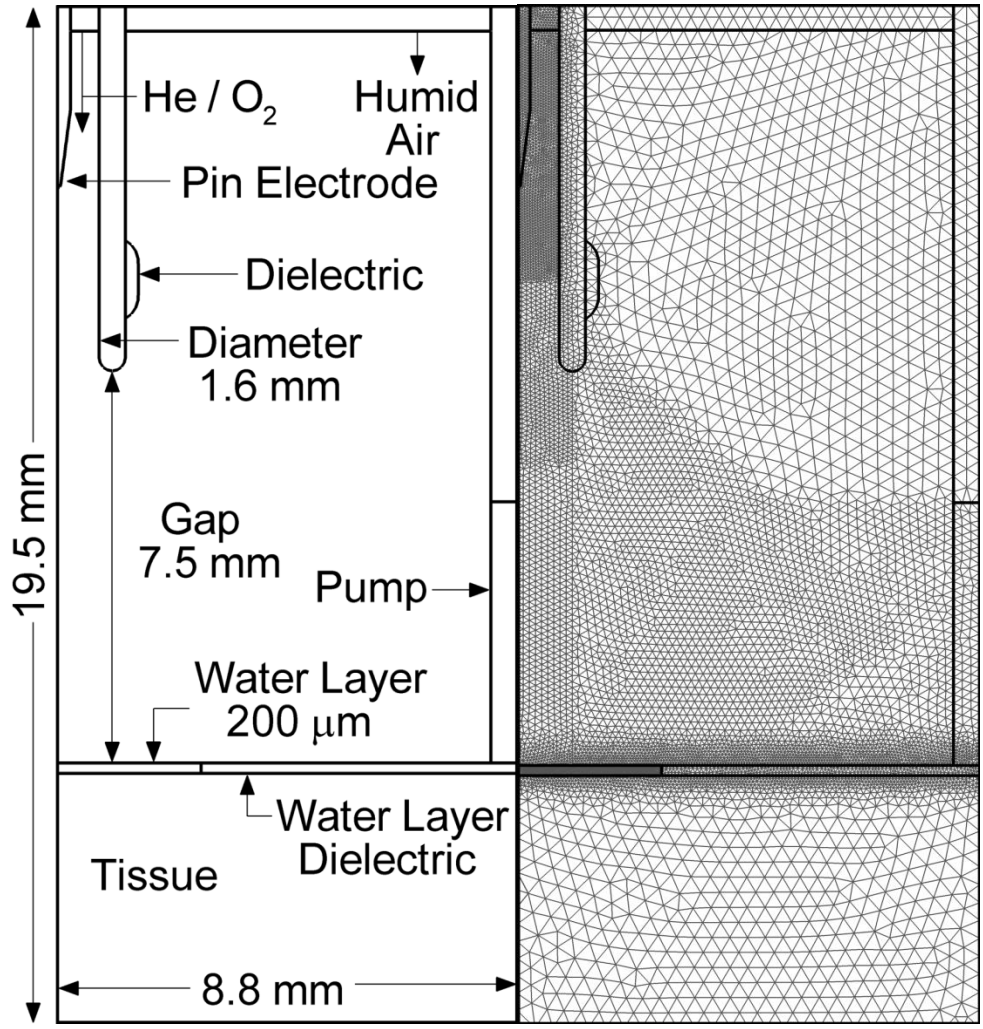

Figure 5.1 Schematic of the cylindrically symmetric model geometry. (a) The total computational domain is 1.95 cm in height and 0.88 cm in radius. (b) Numerical mesh showing different refinement zones.

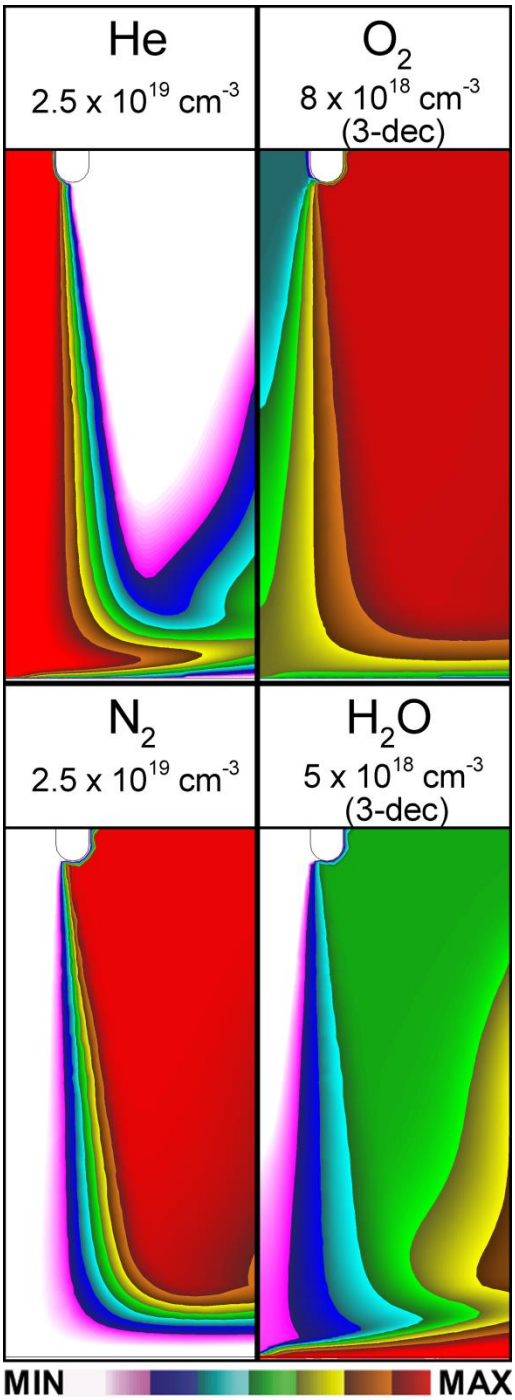

Figure 5.2 Flow profiles at 8 ms prior to initiating the discharge for (a) He, (b) O_2, (c) N_2 and (d) H_2O. The water vapor is blown from the surface of the water layer by the jet. The maximum value is noted in each frame. Contours are on a linear scale unless the number of decades for a log scale is noted.

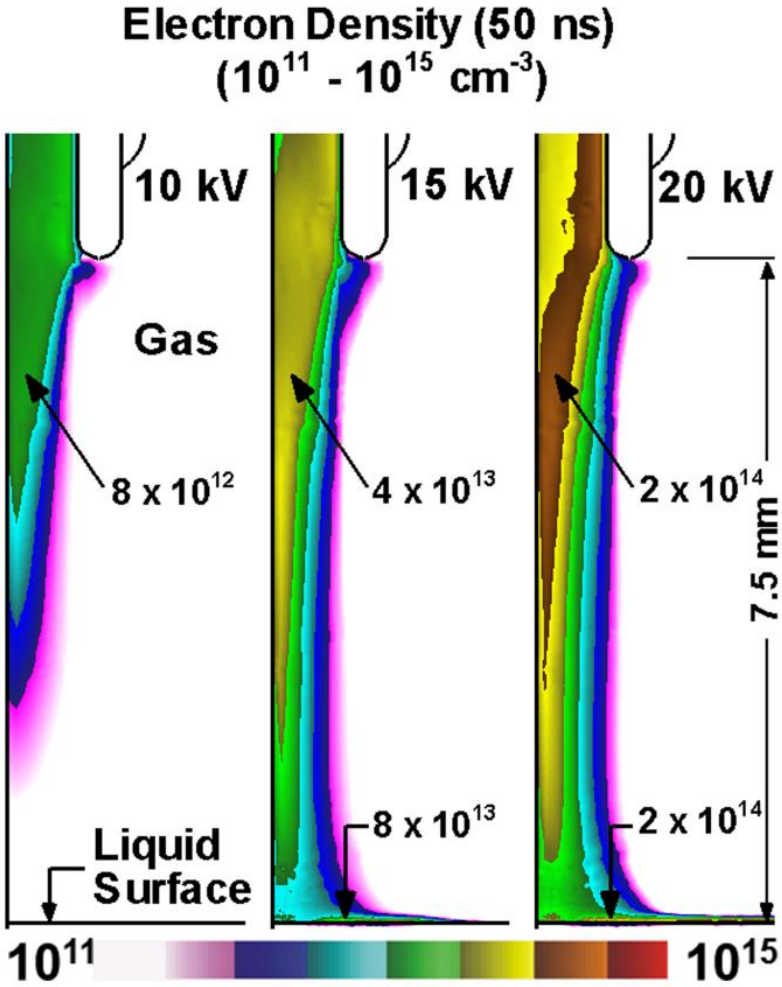

Figure 5.3 Electron density for applied potentials of -10 kV, -15 kV and -20 kV at 50 ns prior to pulse termination. The electron plume for -10 kV does not touch the liquid surface and is not-touching. The electron plume for -15 kV touches at 35 ns (in contact with water and spreading for 15 ns) and the plume for -20 kV touches at 20 ns (in contact for 30 ns). Contours are on a log-scale over 4 decades.

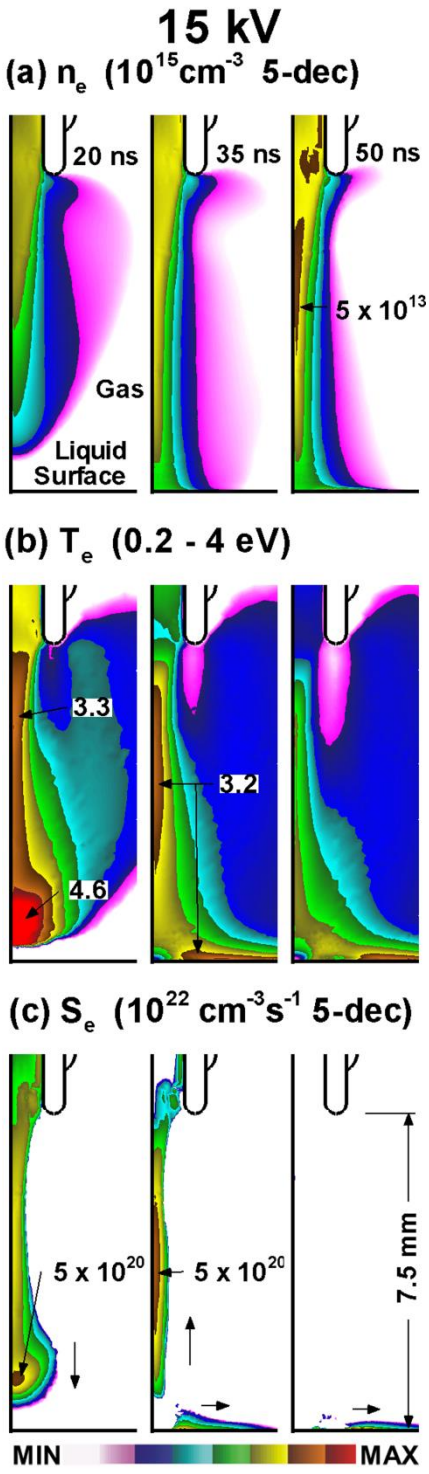

Figure 5.4 Plasma dynamics -15 kV. (a) electron density, (b) electron temperature and (c) electron impact ionization source at 20, 35 and 50 ns after start of the pulse. At 20 ns the ionization wave has not touched the surface. The spread of the ionization as a surface ionization wave continues after touching. Contours are on a linear scale unless the number of decades for a log scale is noted.

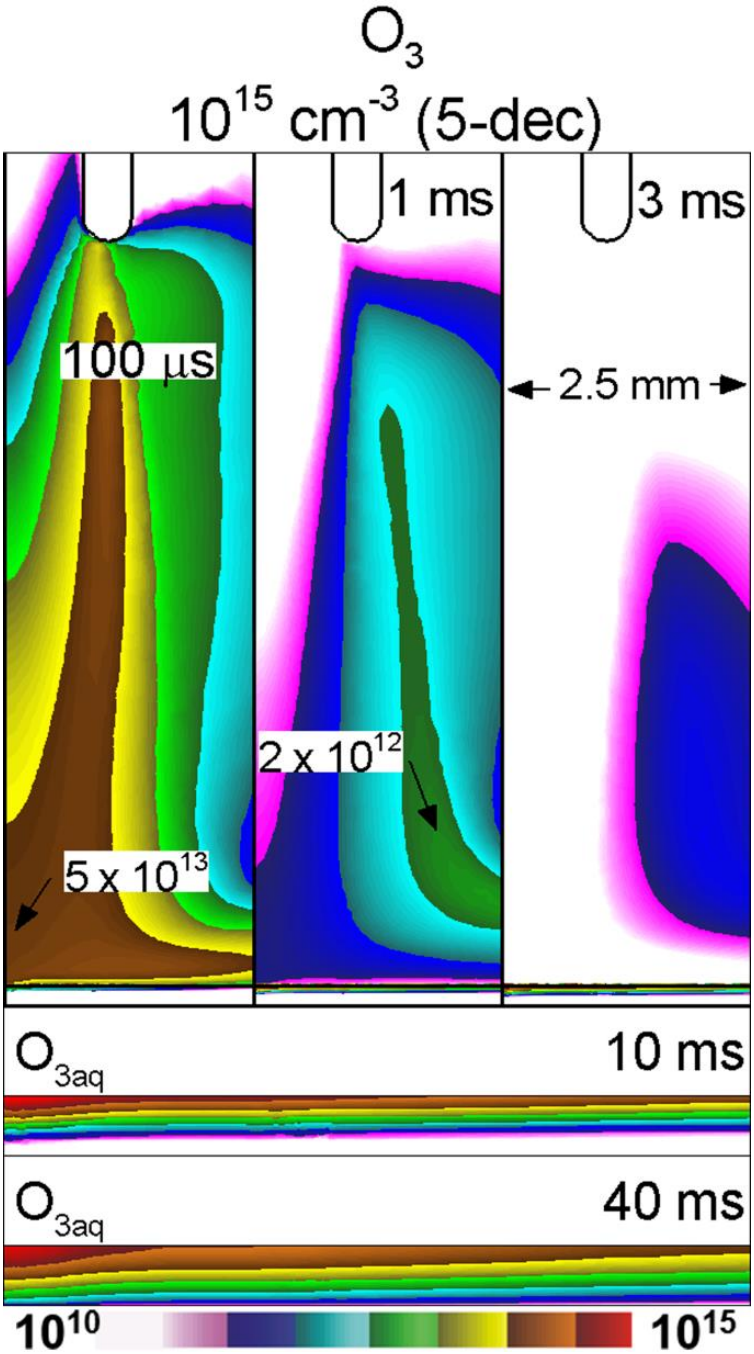

Figure 5.5 Ozone density in the gas phase and in the liquid for -15 kV at varying times after the discharge pulse. Ozone is relatively non-reactive in both phases. . Contours are on a 5-decade log-scale.

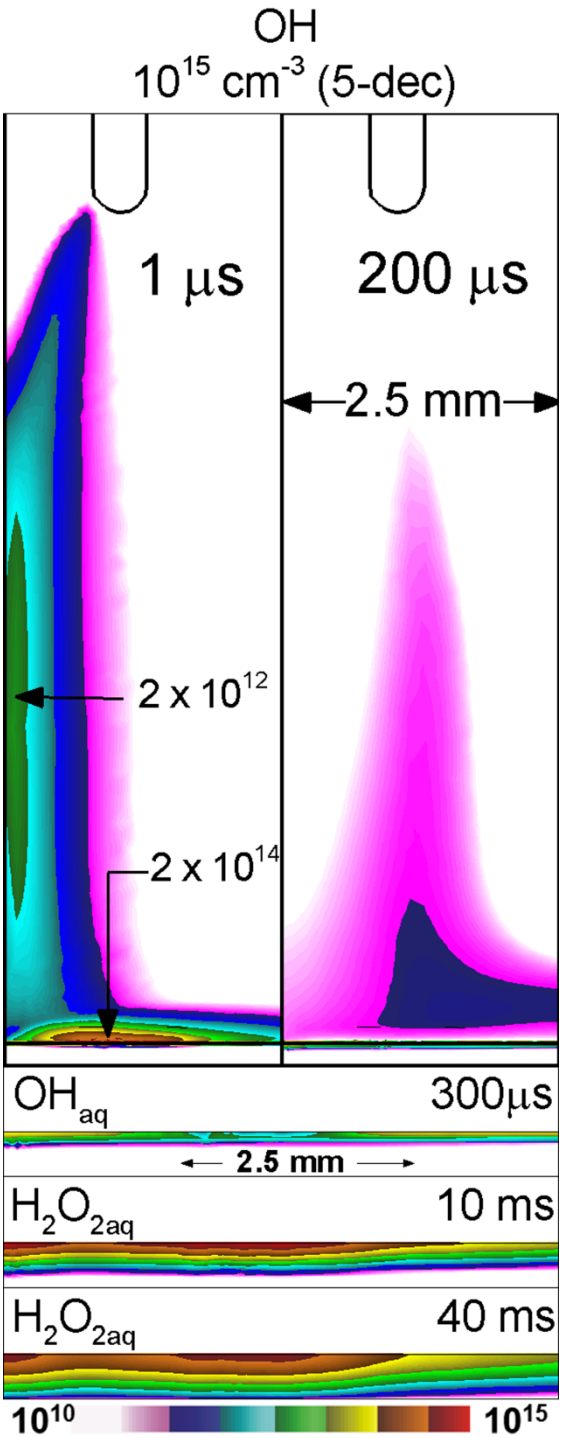

Figure 5.6 OH in the gas phase and water, and H_2O_2 in the water for the -15 kV at varying times after the discharge pulse. At 1 μs, the highest OH concentration is adjacent to the water layer where the electron plume intersects the evaporating water. Over the next 200 μs the OH reacts or blows away. The evolution of OH_{aq} into H_2O_{2aq} is shown in the lower panels. Notice that the location of the high concentration of OH at 1 μs becomes the location of the highest concentration of H_2O_{2aq}. Contours are on a 5-decade log-scale.

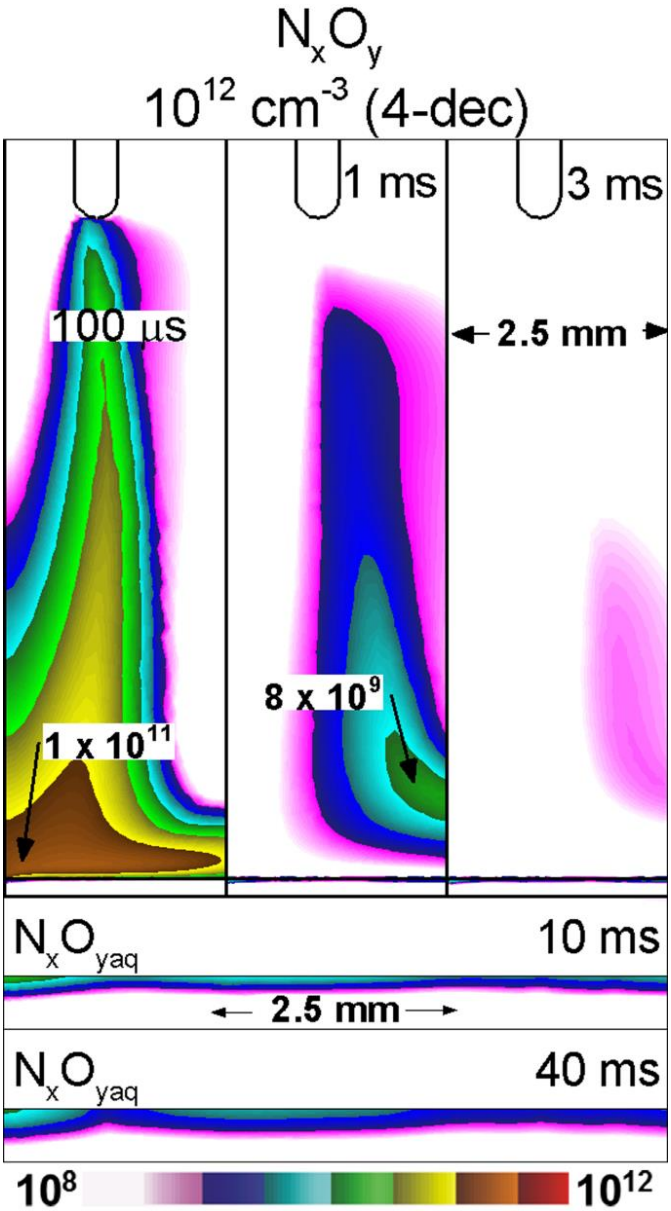

Figure 5.7 N_xO_y density for -15 kV case shown at varying times after the discharge pulse in the gas and water layer. NO is the initiating molecule for N_xO_y. The comparatively low density of N_xO_y results from the effectiveness of the helium jet blocking access of NO to the water layer and the laminar flow that blows NO away. Contours are on a 4-decade log-scale.

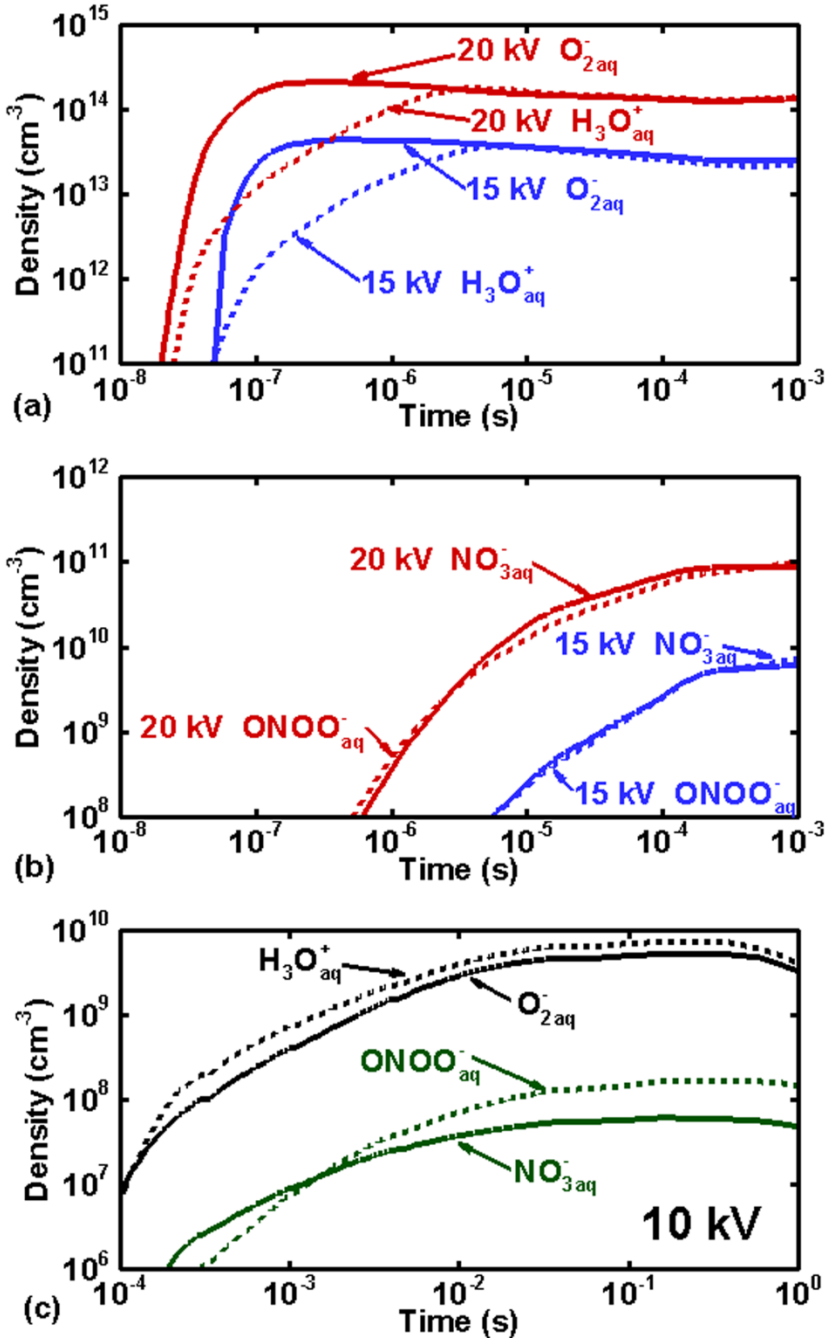

Figure 5.8 The time evolution of the liquid volume average densities of aqueous ions. (a) $O_2^-{}_{aq}$ and $H_3O^+{}_{aq}$; and (b) $NO_3^-{}_{aq}$ and $ONOO^-{}_{aq}$ for the touching -15 kV and -20 kV cases. (c) Densities for the -10 kV (no-touch) case.

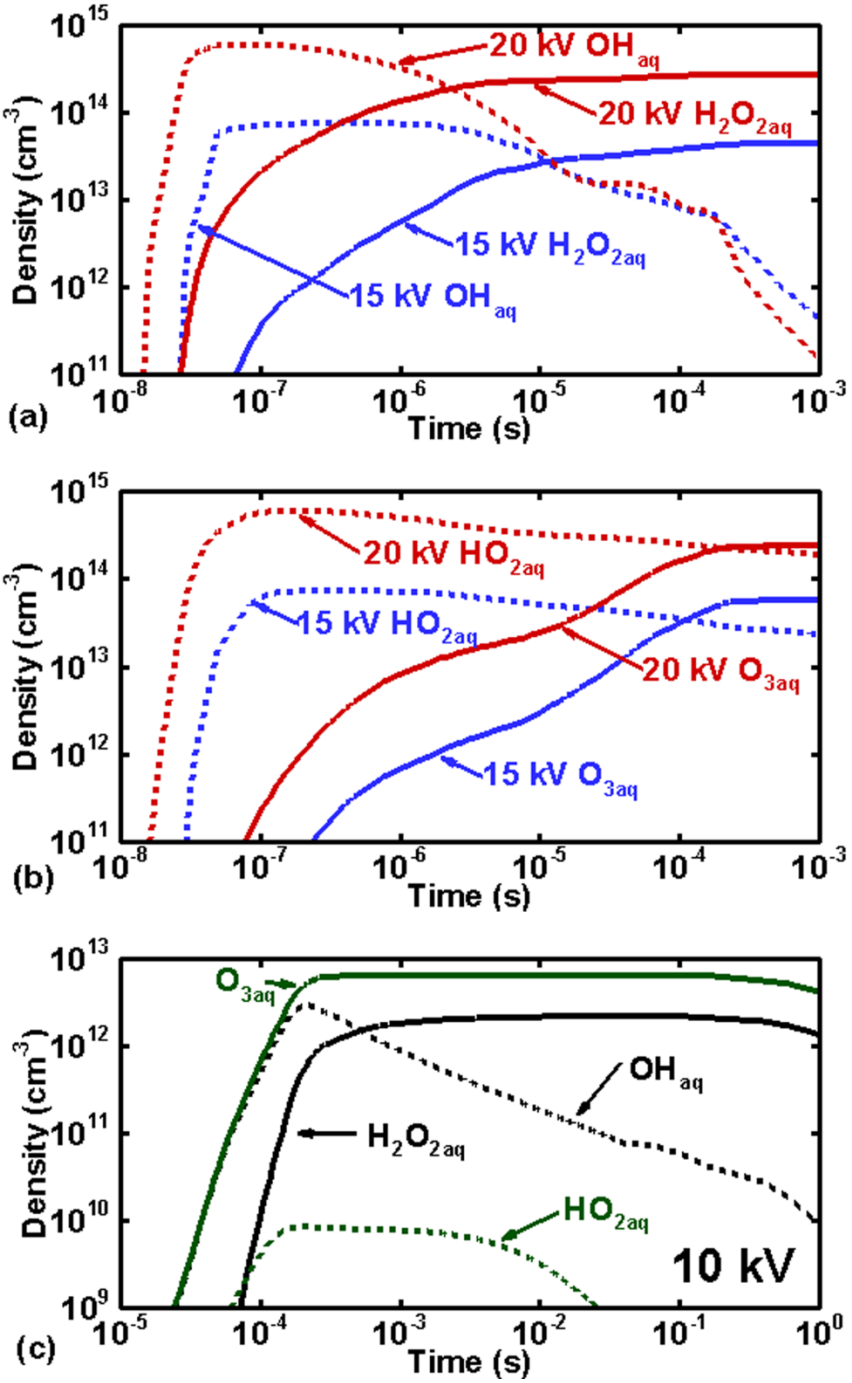

Figure 5.9 The time evolution of the liquid volume average densities of neutral aqueous species (a) H2O2aq and OH_{aq}; and (b) O3aq and HO_{2aq} for the touching -15 kV and -20 kV cases. (c) Densities for the -10 kV (no-touch) case.

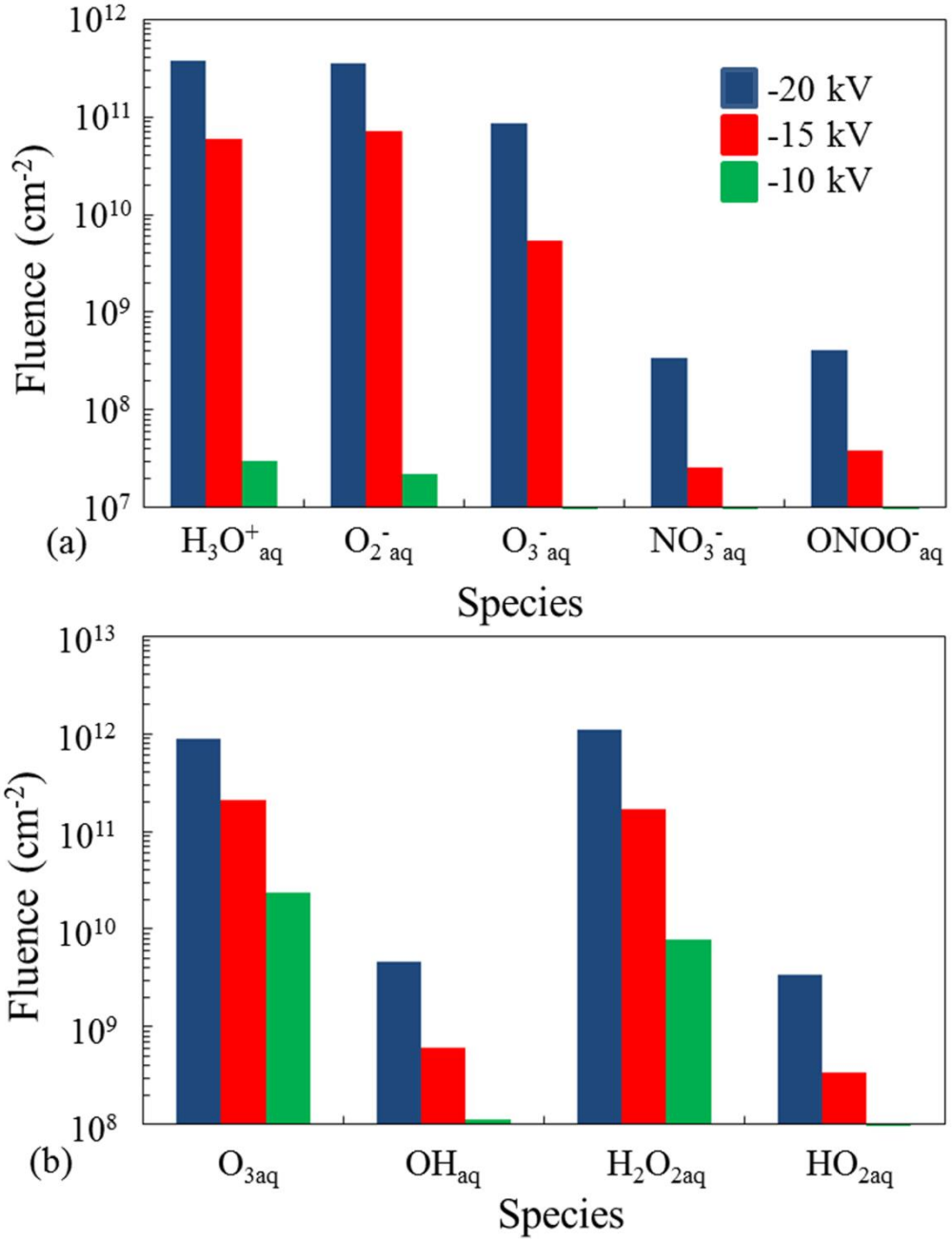

Figure 5.10 Fluences to the tissue beneath the water over one second for not-touching (-10 kV) and touching (-15 kV, -20 kV) cases. a) ions and b) neutral species.

5.6 References

[1] M. Laroussi, M. Kong, G. Morfill, and W. Stolz *Plasma Medicine: Applications of Low-Temperature Gas Plasmas in Medicine and Biology*, (Cambridge, Cambridge University Press, 2012), pp. 239-260.

[2] M. G. Kong, G. Kroesen, G. Morfill, T. Nosenko, T. Shimizu, J. van Dijk, and J. L. Zimmerman, "Plasma medicine: an introductory review", New J. Phys. **11**, 115012 (2009).

[3] M. Laroussi, "Low-Temperature Plasmas for Medicine?", Trans. Plasma Sci. **37**, 714 (2009).

[4] R.A. Rhoades, D.R. Bell, *Medical Physiology: Principles for Clinical Medicine* 4th ed. (Baltimore, Williams & Wilkins, 2012), pp. 167-177.

[5] C. A. J. van Gils, S. Hofmann, B. K. H. L Boekema, R. Brandenburg, and P. J. Bruggeman, "Mechanisms of bacterial inactivation in the liquid phase induced by a remote RF cold atmospheric pressure plasma jet", J. Phys. D: Appl. Phys. **46,** 175203 (2013).

[6] P. Lukes, E. Dolezalova, I. Sisrova, M. Clupek, "Aqueous-Phase Chemistry and Bactericidal Effects from an Air Discharge Plasma in Contact with Water: Evidence for the Formation of Peroxynitrite through a Pseudo-Second-Order Post-Discharge Reaction of H_2O_2 and HNO_2", Plasma Sources Sci. Technol. **23**, 015019 (2014).

[7] H. Tresp, M. U. Hammer, J. Winter, K-D. Weltmann, and S. Reuter, "Quantitative detection of plasma-generated radicals in liquids by electron paramagnetic resonance spectroscopy", J. Phys. D: Appl. Phys. **46,** 435401 (2013).

[8] X. Lu, G.V. Naidis, M. Laroussi, K. Ostrikov, "Guided ionization waves: Theory and experiments", Physics Reports **540**, 123 (2014).

[9] S. Reuter, H. Tresp, K. Wende, M. Hammer, J. Winter, K. Masur, A. Schmidt-Bleker, and K-D. Weltmann, "From RONS to ROS: Tailoring Plasma Jet Treatment of Skin Cells", Trans. Plasma Sci., **40,** 2986 (2012).

[10] S. Reuter, J. Winter, A. Schmidt-Bleker, H. Tresp, M. Hammer, and K-D. Weltmann, "Controlling the Ambient Air Affected Reactive Species Composition in the Effluent of an Argon Plasma Jet", Trans. Plasma Sci., **40,** 2788 (2012).

[11] P. Bruggeman, private communication, 2014.

[12] B. Lay, R. Moss, S. Rauf, and M. Kushner, "Breakdown Processes in Metal Halide Lamps", Plasma Sources Sci. Technol., **12**, 8 (2003).

[13] Z. Xiong and M. J. Kushner, "Surface corona-bar discharges for production of pre-ionizing UV light for pulsed high-pressure plasmas", J. Phys. D: Appl. Phys. **43**, 505204 (2010).

[14] W. Tian and M. J. Kushner, "Atmospheric pressure dielectric barrier discharges interacting with liquid", J. Phys. D: Appl. Phys. **47**, 165201 (2014).

[15] A. N. Bhoj and M. J. Kushner "Continuous Processing of Polymers in Repetitively Pulsed Atmospheric Pressure Discharges with Moving Surfaces and Gas Flow", J. Phys. D **40**, 6953 (2007).

[16] J. Walsh and M. Kong, "Contrasting characteristics of linear-field and cross-field atmospheric plasma jets", Appl. Phys. Lett. **93**, 111501 (2008).

[17] X. Lu, Z. Jiang, Q. Xiong, Z. Tang, X. Hu, and Y. Pan, "An 11 cm long atmospheric pressure cold plasma plume for applications of plasma medicine", Appl. Phys. Lett. **92**, 081502 (2008).

[18] D. Maletic, N. Puac, S. Lazovic, G. Malovic, T. Gans, V. Schulz-von der Gathen and Z. Lj Petovic, "Detection of atomic oxygen and nitrogen created in a radio-frequency-driven micro-scale atmospheric pressure plasma jet using mass spectroscopy", Plasma Phys. Control. Fusion **54**, 124046 (2012).

[19] E. Robert, V. Sarron, T. Darny, D. Ries, S. Dozias, J. Fontane, L. Joly, J-M Pouvesle, "Rare gas flow structuration in plasma jet experiments", Plasma Sources Sci. Technol. **23**, 012003 (2014).

[20] C. Bogey and C. Bailly, in V. Armenio, B. Geurts and B Frohlich (eds.), *Direct and Large-Eddy Simulation VII: Proceedings of the Seventh International ERCOFTAC Workshop on Direct and Large Scale Eddy Simulation VII*, (Springer Science, 2010).

[21] E. Karakas, M. A. Akman, and M. Laroussi, "The evolution of atmospheric-pressure low-temperature plasma jets: jet current measurements", Plasma Sources Sci. Technol. **21**, 034016 (2012).

[22] N. Jiang, A. Ji, and Z. Cao, "Atmospheric pressure plasma jets beyond ground electrode as charge overflow in a dielectric barrier discharge setup", J. Appl. Phys. **108**, 033302 (2010).

[23] S. Hubner, S. Hofmann, E.M. van Veldhuizen, and P.J. Bruggeman, "Electron densities and energies of a guided argon streamer in argon and air environments", Plasma Sources Sci. Technol. **22,** 065011 (2013).

[24] K. P. Madden and Stephen P. Mezyk, "A critical review of aqueous solution reaction rate constants for hydrogen atoms", J. Phys. Chem. Ref. Data **40**, 023103 (2011).

[25] Y. Sakiyama, D. Graves, H-W. Change, T. Shimizu, G. E. Morfill, "Plasma Chemistry Model of Surface Micro-discharge in Humid Air and Dynamics of Reactive Neutral Species", J. Phys. D **45**, 425201 (2012).

[26] S. J. Beebe, P. F. Blackmore, J. White, R. P. Joshi and K. H. Schoenbach, "Nanosecond pulsed electric fields modulate cell function through intracellular signal transduction mechanisms", Physiol. Meas. **25,** 1077 (2004).

Chapter 6 APPJ onto Wet Cells

6.1 Introduction

As discussed in Chapter 1, atmospheric pressure plasma jets (APPJ) have been the subject of much interest in the biomedical field in the last decade. They have been shown to deactivate bacteria [1], sterilize surfaces [2], heal wounds [3] and kill cancer cells.[4] Despite these experimental successes, there is still much to be learned about the mechanisms responsible for success. One path to success is the reactive oxygen and nitrogen species (RONS) produced by the APPJ contributing to the treatment of the biological surface through signaling mechanisms, oxygenation, and providing activation energy by the delivery of charged species and photons to the surface as well as the electric field produced by the discharge.[5] In this chapter, the penetration of the electric field in the plasma region, into the water layer, and cells under the water layer will be analyzed.

For understanding the effects of the electric field of the discharge as well as the local electric field produced by charging of surfaces, we turn to the field of bioelectronics. Much effort and interest has been shown in the study of the effects of electrical fields on and interacting on cellular structures.[6-8] In this area of study, the amplitude and duration of the voltage pulse applied to the cell cause significantly different effects on cells (see Fig. 6.1). At low electric fields (few kV/cm), but long pulse widths (0.1 – 10 ms), electroporation occurs. Electroporation is the formation of pores in the membrane as a result of an accumulation of charge at the surface cell membrane. This phenomenon then allows the delivery of genes or

drugs to the interior of the cell. The voltage drop across the membrane needs to be between 0.1 and 1 V for electroporation.[8]

If the electric field in the interior of the cell within the cytoplasm is on the order of 10s kV/cm and short enough duration (10 – 100 ns) [9], the charging time required for electroporation is not reached. The predicted requirements are shown in Fig. 6.1 and indicated by the dielectric relaxation time shown in Table 6.1 for membrane. However, the intracellular substructure can be influenced with these electric field conditions through a process known as intracellular electromanipulation.[9-12] Experiments have shown that micro-pores form from the short intense fields that are large enough to allow transfer of molecules and ions into and out of the cell [13], but too small for drug or gene delivery. The membrane remains intact after the pulse. The primary effect is influencing the interaction of the proteins within the cytoplasm and the nucleus in eukaryote cells and certainly influencing the protein function within the cytoplasm of prokaryotic cells. The short intense fields cause the mitochondria membrane to become permeable [14] and activate mitogen-activated protein kinases (MAPKs) pathways [15] which influence the intercellular communication. These nanosecond pulsed electric fields (nsPEF) have been shown to induce apoptosis in T cells.[16]

Escherichia coli (E. coli) bacteria and other prokaryotic cells are typically on the order of 1 μm in diameter. Eukaryotic cells are typically 10 – 100 μm in diameter. The membrane surrounding the cell is a lipid bilayer with a thickness of 3 – 10 nm. Some bacteria have double membranes with a total thickness of 25 nm. E. coli are Gram-negative bacteria since the presence of a double membrane does not allow the bacteria to respond to Gram staining.[17] Gram-positive bacteria have a single membrane. Using the thickness of the membrane, the voltages are determined using the predicted electric field and compared to threshold voltages.

An early relationship between electric field and pulse width was proposed by Schoenbach *et al.* in [10] and is shown in Fig. 6.1 with appropriate biomedical applications. At high electric fields and short pulse durations, intracellular electromanipulation occurs. Over longer durations at lower electric fields, the effect of charge accumulation causes the eventual formation of pores in the membrane through a process termed electroporation. Once these pores are formed, drugs or genes can be delivered to the interior of the cell. An additional application shown is bacterial decontamination which has also been shown using APPJs.[18] These ranges of electrical fields and the duration of the pulses are similar to those used in plasma medicine.

Additional voltage regulated methods exist for external ions to enter the cells. Voltage-gated cation channels exist in membranes of nerve, muscle and other electrically excitable cells and typically require a transmembrane voltage of up to 100 mV [8], an effect governed by the Nernst equation. In the body, these are calcium and potassium cations that are key signals to contract a muscle or propagate a nerve signal along an axon or to reset the cell back to equilibrium. Electric fields from APPJs could potentially affect these processes.

The intent of this computational investigation is to determine if APPJs can create the conditions required for electroporation, voltage-gated channels, or intracellular manipulation of cells. The discharge characteristics and geometries analyzed were meant to approximate extreme, yet realistic, discharge conditions that could plausibly create these responses.

6.2 Description of the model

Beyond the description of the *nonPDPSIM* model provided in Chapter 2, modifications include the reactive water layer described in Chapter 5 and the use of a 2-D Cartesian symmetric coordinate system instead of the cylindrical coordinates used in the other chapters. This change

in coordinate system enables addressing the cell structure beneath the water layer. The computational domain shown in Fig. 6.2 is 19 mm by 9 mm and has 26,600 nodes of which 17,000 were plasma nodes. The unstructured, triangular mesh had spacing of 36 μm at the tip of the electrode, 20 μm in the water layer, and smaller than 1 μm in the cells. Helium with 0.2% oxygen flowed through the inner tube at 4 slm and was shrouded by humid air (79.5/20/0.5 – $N_2/O_2/H_2O$) flowing at 1 slm simulating a shielding gas. These gases flowed into humid air (same composition) and exited at the side port labeled pump. The humid air shielding gas is included to provide a baseline for future studies on the effect using oxygen, nitrogen or dry air as a shielding gas. This is not included in this chapter. The water layer was 7.5 mm from the exit of the helium tube and was 200 μm thick. Water vapor was included in the model above the water layer. The thickness of the water layer remains the same as that studied in Chapter 5 in order to allow for easy comparisons as well as representing the typical thickness of biofilm that would be present in applications.[19] The cells were placed on the axis and were comprised of a nucleus, cytoplasm, and membrane. Each component of the cell and the tissue beneath were modeled as lossy dielectrics with values for relative permittivity and conductivity shown in Table 6.1. Expanding on a previous study on the effect of dielectric barrier discharges on skin and the underlying cells by Babaeva and Kushner [20], the values of the permittivity and conductivity were based on those used in their model which were from an electroporation model [21] and dielectric spectroscopy.[22,23]

In this model, an atmospheric pressure plasma jet will deliver the discharge effects to the cell structure through a thin layer of water containing 8 ppm dissolved oxygen. The cell structure shown in Fig. 6.2(b) consists of three layers of cells for a total thickness of 40 um and width of 100 um. This small size was selected to reduce the computational burden as this block

of cells consisted of over 6000 mesh points. The three layers are intended to show the effect of the propagation of the electric field through the cell layers. The dielectric relaxation time is the dielectric constant divided by the conductivity (ε/σ). The dielectric relaxation time of the cytoplasm of less than 10 ns supports the theory of intracellular electromanipulation and the cell response to ultrashort pulsed electric fields.

The conditions analyzed will build upon those discussed in Chapter 5 [24] with voltage regulating the touching of the ionization wave and the water layer. Three voltages were analyzed (-10 kV, -15 kV, and -20 kV) and their interaction with cells lying beneath a 200 μm water layer. The ionization wave touched the water layer for the -15 and -20 kV cases. In addition to the use of a Cartesian coordinate system, another difference from the analysis conducted in Chapter 5 is that in this study the pulse began its fall at 50 ns to zero applied potential at 60 ns. In Chapter 5, the pulse was truncated at 50 ns. This fall encouraged accumulation of surfaces charges on the water layer and subsequent creation of a surface electric field as discussed in Chapter 4 and is another attempt to create extreme electric fields to influence cell response. The 2-D Cartesian symmetric geometry also affects the tip of the electrode. The rounded tip of the powered electrode in the 2-D cylindrical geometry becomes a plane in the Cartesian geometry. The resulting electric field and electron avalanche produced by the applied voltage are different. The effect of a second pulse 50 ms after the first pulse will also be analyzed. The intention of the long delay between the first and second pulses is to allow the aqueous reactive species and ions formed by the first pulse to solvate into and continue to react within the water layer. The effect of the more conductive water layer will then be analyzed.

Lastly, the water layer thickness was analyzed using the -15 kV case as a baseline and modifying the thickness of the water layer from 200 μm to 50 μm and 1 mm. In each of these

cases, the duration of the pulse is on the order of that required for intracellular electromanipulation [8,14-15] and the direct comparisons will be made with those thresholds. Electroporation effects caused from accumulation of charge on cells are discussed using the predicted voltages and charging effects on the cell membrane. In these cases, the pulse will be allowed to return to zero applied voltage creating a surface electric field as discussed in Chapter 4. Additional speculations will be made based on these larger magnitude electric fields.

6.3 Results and Discussion

With the inclusion of cells into the geometry, the model must use a 2-D Cartesian coordinate system. The flow is run for 13 ms to establish the flow field prior to pulsing. As shown in Fig. 6.3, the thickness of the helium profile in the jet and at the surface of the water layer is thicker than in the 2-D cylindrical cases with the same volumetric flow rate. As in the cases analyzed in Chapter 5, the flow is laminar. The concentration profiles of oxygen, nitrogen and water vapor are also shown in Fig. 6.3. The water vapor is allowed to evaporate from the surface of the water layer, has some compression at the water layer as the jet impinges, but mostly flows away with the jet flow out the pump on the right side.

Once the flow stabilizes, one (-10, -15 or -20 kV) pulse is applied to the pin electrode to create the discharge. Each pulse has a 5 ns pulse rise to the final voltage, a duration of 45 ns, and then a fall of 10 ns to zero for a total pulse duration of 60 ns. In each case, a guided ionization wave is formed from the applied voltage and propagates through the helium channel into the ambient air. With the exception of the -10 kV pulse, the ionization wave strikes the surface of the water layer. The electron avalanche quickly moves from the tip of the pin electrode to the

wall, charges the wall, and then moves on axis upon exiting the tube. The ionization wave then interacts with the molecules in the ambient air and charged and reactive species are formed.

6.3.1 Not-touching case

In the -10 kV case, the propagation of the guided ionization wave as represented by the front in the electron temperature Fig. 6.4(a) as well as the source ionization term in Fig. 6.4(b) moves at a speed of 2×10^7 cm/s. After the voltage begins to fall at 50 ns, the electron temperature drops from 5.5 eV in the head and 7-8 eV at the ionization front to 3.3 and 5 eV at 60 ns (the end of the pulse). The ionization source term drops from a peak of 5×10^{19} $cm^{-3}s^{-1}$ at 50 ns to nearly two orders of magnitude lower at 60 ns. The electron density increases through the duration of the pulse and reaches a maximum of 8×10^{11} cm^{-3} at 60 ns as shown in Fig. 6.4(c). The electric field shown in the air (Fig. 6.5(a)), at the air – water – tissue interface (Fig. 6.5(b)) and at the water – cell interface (Fig. 6.5(c)) show that the electric field does not exceed 13 kV/cm in the gaseous region and is much lower (2 kV/cm) at the cell membrane and tissue. In the middle frame (50 ns) of Fig. 6.5(a), the high electric field, 13 kV/cm, corresponds to the position of the ionization wave front. The pulse is terminated before the ionization wave can touch the water layer. At the air / water interface, the water layer acts as a large capacitor and blocks the tissue beneath from the electric field. The maximum magnitude of the electric field reaches 13 kV/cm at 50 ns near the axis and coincides with the location of the ionization wave. The electric field quickly dissipates with the fall of the applied voltage as shown at 60 ns. The low electric field behind the ionization wave at 60 ns indicates a nearly constant voltage at that point.

The close up of the wet cells in Fig. 6.5(c) shows the accumulation of charge at the less conductive membrane from 40 to 50 ns and the decrease in electric field as the applied voltage goes to zero from 50 to 60 ns. The voltage drop across the membrane needs to be between 0.1 and 1 V for electroporation – at 50 ns the voltage drop is 0.0014 V, well below the level for electroporation. The predicted threshold for intracellular electromanipulation on these length scales is in the 10's kV/cm within the cytoplasm – nowhere near what we are predicting.

If we imagine that there is no water layer and the electric field touched the tissue, the maximum electric field the membrane sees would be 10 kV/cm at 50 ns which is still below the threshold for intracellular electromanipulation and does not have the charging time required for electroporation. Since this electric field quickly dissipates as the pulse falls and the absence of charged species on the surface of the water layer removes the possibility of surface charging. With a not-touch APPJ onto wet cells, electric fields appear to be too small to have significant effects on the cells.

6.3.2 Touching Cases (-15 kV, -20 kV, and second pulse of -15 kV)

In the next case a higher voltage (-15 kV or -20 kV) pulse was applied to the same geometry. In each of the higher voltage cases, the guided ionization wave produced by the discharge touched the water layer, split into two sections with one portion spreading across the surface of the water layer, a surface ionization wave (SIW), and the other portion acting as a restrike travelling back up the helium channel toward the electrode. The intensity of these varied with the voltage, however. For the -15 kV case, a detailed look at the discharge dynamics and magnitude of the electric field in the plasma portion, in or on the water layer, and the region around the cellular structure will be conducted at 3 ns prior to, at, and 3 ns after the ionization

wave touches the surface as well as at the end of the maximum applied voltage (50 ns), at the end of the applied voltage (60 ns) and after 10 ns of afterglow (70 ns). Subsequent cases will highlight changes in magnitude and trends from the base case of -15 kV. For the base case, the electron temperature is 9 eV at the front of the ionization wave and the wave travels at a speed of 8×10^7 cm/s. Electron temperature, ionization source term and electron density are shown in Fig. 6.6, as the ionization wave propagates down the helium channel, 3 ns before touching, at the moment of touching, and 3 ns after the ionization wave touches the water layer. The electrons form a conducting channel upon touching and grow in density to 1×10^{13} cm^{-3}. The electrons and ions accumulate on the surface of the water and create a surface electric field as they solvate or charge exchange into the water layer. The maximum electron density occurs on the water layer surface near the axis at 1×10^{13} cm^{-3} at 35.5 ns in Fig. 6.6(c).

The spatial location of the plasma bullet corresponds to the area of high electric field (24 kV/cm) that is noticeable on axis in the left (29.5 ns) frame of Fig. 6.7(a). The corresponding potential contours are not compressed at this time in front of the ionization wave. As the ionization wave strikes the surface at 32.5 ns, the electric field increases at the head of the streamer to 44 kV/cm and the potential lines compress against the high capacitance water layer surface as shown in Fig. 6.7(a). At 35.5 ns, the electric field has also propagated through the water layer into the tissue beneath to a magnitude of 12 kV/cm. The potential has propagated into the tissue beneath the cells as indicated by the contours in the right frame of Fig. 6.7(a). The low magnitude electric field at 35.5 ns behind the ionization wave reflects the spatially homogenous voltage profile due to the conductivity of the plasma channel at the time of the high intensity electric field penetrating into the tissue. The formation of the conduction channel

behind the head of the ionization wave is indicated by the concentration profile of the electrons at 35.5 ns in Fig. 6.6(c).

When the ionization wave hits the surface of the water layer, charging is fast and the electric field penetrates through the water layer and into the tissue to a maximum magnitude of 14 kV/cm at 35.5 ns. The air / water layer interface above the cells (to a width of 2.75 mm) is shown at 3 ns before, at, and 3 ns after touching in Fig. 6.7(b). Prior to the ionization wave touching the water layer (29.5 ns, top frame), the electric field is 17 kV/cm corresponding to a fully realized -15 kV potential over a distance from electrode to water layer of nearly 1 cm. There is little effect of the discharge on or in the water layer at this point. At touching, 32.5 ns (middle frame), the electric field at the surface of the water layer grows to 44 kV/cm and there is a rise in the magnitudes in both the water layer and tissue beneath to 1 and 5 kV/cm, respectively. At 3 ns after touching, the intense electric field at the surface of the water layer at touching has propagated through the water layer and into the tissue beneath. At this point, the magnitude of the electric field is 14 kV/cm in the tissue and 5 kV/cm in the water layer. The intense electric field (12 kV/cm) along the water layer surface about 1.5 mm from the axis in the lower frame at 35.5 ns indicates the position of the propagating surface ionization wave.

The cells are too small to be seen individually in Fig. 6.7(a) and 6.7(b) and are shown in Fig. 6.7(c). As the ionization wave closes prior to touching, the cells are buffered by the high capacitance of the water layer. At the moment of touching, the electric field has increased by 2-3 times in magnitude. Three nanoseconds after touching, the electric field in the membrane is between 10 and 14 kV/cm. The cytoplasm has a higher conductivity and higher dielectric constant than the membrane and experiences a lower electric field of 3.5 kV/cm at 35.5 ns. At this time, the nucleus with a dielectric constant and conductivity between the membrane and

cytoplasm experiences an electric field of 5.5 kV/cm in the third row of cells. Beneath the cells, the electric field in the tissue is 14 kV/cm. At this point, within the first 3 ns of ionization wave striking the surface and the most intense electric field experienced by the cells, the electric field is too low to promote intracellular electromanipulation (3.5 kV/cm) and electroporation (short charging period and 0.01 V both below threshold).

As the applied voltage is removed, several interesting phenomenon occur. First, at the extent of the maximum voltage in the pulse at 50 ns, the electron density is shown in the left frame of Fig. 6.8(a). The electron density in the conduction channel is 1.3×10^{13} cm^{-3} and in the spread of the electrons across the water layer surface is 2×10^{13} cm^{-3}. The connection of the electrons from the pin to the surface has created a conduction channel that increases the conductivity of the plasma and, consequently, decreases the electric field. The electric field in the plasma region is also shown in Fig. 6.8(a), from the maximum voltage at 50 ns, to the end of the fall at 60 ns and 10 ns into the afterglow at 70 ns. At 50 ns, the magnitude of the electric field in the tissue beneath the water layer is 22 kV/cm. The electric field considerably decreases in the plasma region and in the tissue at the end of the applied voltage at 60 ns. At this time, the development of an ion-matrix electric field at the edge of the conduction channel occurs with a magnitude of 5.5 kV/cm. This electric field is shown more clearly at 70 ns as is the development of a surface electric field on the water layer. The spread of the ionization wave across the water layer and the electric field due to surface charge (60 – 100 kV/cm along the surface) are shown at the air / water / tissue interface in Fig. 6.8(b). The extent of the local electric field due to surface charge corresponds to the spread of the ionization wave and subsequent spread of charged species across the water surface.

Beneath the water layer, the cell structure is shown in Fig. 6.8(c). The cell membrane and tissue experience an electric field ranging from 15 – 26 kV/cm at the extent of the high voltage pulse and drops rapidly once the pulse goes to zero. At 60 ns, the electric fields in the cytoplasm and nucleus are 6 kV/cm and 11 kV/cm, respectively. At 70 ns, or 10 ns post pulse, the electric field in the water layer and the cell are below 1 kV/cm, but the local electric field at the water surface is still quite large showing the longer effects of the surface charging. The electric field and voltage across a 10 nm membrane dissipate quickly in the 10 ns afterglow and would not allow sufficient charging to promote electroporation. The predicted electric field in the cytoplasm is still below the intracellular electromanipulation threshold. In a hypothetical dry cell case in which we speculate on the absence of the water layer and subsequent charging on the cell surface, the electric fields resulting from surface charging would be at the level for intracellular electromanipulation and seem to fade quickly as required.

Increasing the applied voltage to -20 kV directly corresponds to a faster and stronger ionization wave touching the water layer at 20 ns, 13 ns earlier than the -15 kV case with a propagation speed of 1.3×10^8 cm/s. The electron temperature in the head of the guided streamer is 2 eV higher than the -15 kV case as shown in the left frame of Fig. 6.9. The touching of the electrons to the water layer creates a conducting channel in which the electrons increase to 3×10^{13} cm^{-3} at the surface and doubling the density of electrons in the channel from the -15 kV case to 1×10^{13} cm^{-3} at 3 ns after the ionization wave strikes the surface as shown in the right frame of Fig. 6.9. The ionization wave that propagates along the surface of the water layer has an electron temperature 1 eV higher and the ionization source term (1×10^{21} $cm^{-3}s^{-1}$) is an order of magnitude higher than the -15 kV case as shown in the center frame of Fig. 6.9.

The electric field formed by the applied potential follows the trends of the -15 kV case and, as with the other pulse profiles considered, the pulse stays at its maximum (-20 kV) until 50 ns and drops to zero over the next 10 ns. The electron density grows to 2×10^{13} cm^{-3} in the conductive channel and to 8×10^{13} cm^{-3} along the surface of the water layer as shown in Fig. 6.10(a). At 50 ns, the electric field is absent from the plasma region and has penetrated entirely into the tissue (32 kV/cm). The plasma region has only the ion-matrix electric field as the voltage no longer changes at this point in the pulse. The rapid fall over the next 10 ns to 60 ns creates dynamics in the electric field as the charge separation creates local regions of higher electric fields.

Looking more closely at the water layer shown in Fig. 6.10(b) at 60 ns, the charge on the surface of the water layer produce an electric field with a maximum magnitude of 100 kV/cm at the point the ionization wave touches. At the extent of the spread of the electrons the electric field is 30 kV/cm. The electric field produced by the surface charging has a small effect on the cells as shown in Fig. 6.10(c). The electric field in the membrane is 25 – 35 kV/cm, 9 kV/cm in the cytoplasm, and 13 kV/cm in the nucleus at the extent of the high voltage pulse (50 ns).

The increased voltage has increased the predicted electric field within the cytoplasm to nearly the threshold for intracellular electromanipulation of 10 kV/cm. A number of system variables, could push the interior electric field above the low end of the intracellular electromanipulation threshold, such as a slight increase in voltage or pulse duration, or the cumulative effects of pulse repetition on the aqueous species in the water layer or charge accumulation on the cells. The voltage across a 10 nm membrane is still below the critical voltage for electroporation at 0.035 V. The hypothetical dry cell is exposed to an electric field of

100 kV/cm for nearly 10 ns which is lower than the -15 kV case, but still possibly produces intracellular electromanipulation.

The effect of a more conductive water layer was studied by allowing the aqueous reactions resulting from the first -15 kV pulse onto the 200 μm water layer to continue for 50 ms and then applying a second (-15 kV) pulse. This technique is similar to the nanosecond pulsed electric field (nsPEF) cases investigated by [15] in which 20 individual 80 ns pulses occurred at a frequency of 1 Hz. The amount of charged species that remained in the water layer ranged from nearly 1×10^{14} cm^{-3} at the surface of the water layer to nearly 1×10^{10} cm^{-3} at the tissue as shown in Fig. 6.11. Using a value of 10^{13} cm^{-3}, the conductivity of the resulting liquid is 3×10^{-5} $\Omega^{-1}cm^{-1}$. The accumulation of charge on the surface (density of 10^{14} cm^{-3}) produces a higher conductivity (3×10^{-4} $\Omega^{-1}cm^{-1}$). This is an increase of nearly two orders of magnitude in conductivity from the pure water subjected to the first pulse. Over the interpulse period of 50 ms, the gaseous reactive species have moved out with the flowing helium and the second pulse enters a pristine environment in the gaseous region.

The discharge dynamics, shown in Fig. 6.12, are interesting as with all else the same, the ionization wave strikes the more conductive water layer nearly 3 ns later than the first pulse. This phenomenon was discussed in Chapter 4, whereby reducing the dielectric constant of the material; the speed of the ionization wave slowed and the intensity decreased. The increase of charged species residing in the water layer increases the conductivity and effectively decreases the capacitance of the water layer. The electron impact ionization source term, S_e, decreases along the surface from 2×10^{20} $cm^{-3}s^{-1}$ at 3 ns after the first pulse to 9×10^{19} $cm^{-3}s^{-1}$ at 3 ns after the second as shown in the center frame of Fig. 6.12. A lower electron density follows the touching of the ionization wave resulting in a lower density in the conducting channel as shown

in the right frame of Fig. 6.12. The electric field follows similar trends as the first pulse, but is slightly lower in all regions at the times framing the ionization wave impact than the first pulse.

At the end of the pulse and into the afterglow, some differences appear. The electron density at the extent of the maximum applied voltage (50 ns) is lower in both the conductive channel (4×10^{12} cm^{-3} to 1.3×10^{13} cm^{-3}) and on the water layer surface (8×10^{12} cm^{-3} to 2×10^{13} cm^{-3}) compared to the first pulse as shown in Fig. 6.13(a). The spread of the electrons on the water layer is also reduced. The electric field is also slightly lower at 50 ns in the tissue dropping from 24 kV/cm after the first pulse to 20 kV/cm after the second as shown in the right frame of Fig. 6.13(a). The spatial spread of the electric field on the surface of the water layer has decreased from the first pulse (Fig. 6.8(a)) to the second pulse (Fig. 6.13(a)). The magnitude of the electric field at the surface of the water layer remains at 130 kV but the extent of high magnitude region decreased from 2.5 mm to 1.5 mm from the axis at 60 ns as shown in Fig. 6.13(b).

Within the cells as shown in Fig. 6.13(c), the electric field magnitudes at 50 ns are close to those produced by the first pulse but slightly lower in the cytoplasm (7 kV/cm in the first and 6.1 kV/cm in the second) and nucleus (9.5 to 8.5 kV/cm). At the end of the second pulse, the conclusions drawn must remain the same as after the first pulse, little chance for electroporation and still a low possibility of intracellular electromanipulation.

The time evolution of the electric field at the surface of the water layer, within the cell membrane, cell cytoplasm and cell nucleus are shown in Fig. 6.14(a) – (d). At the surface of the water layer, 10 μm from the centerline, the intense electric field created by the compression of the potential contours (as shown in Fig. 6.7(a) for the -15 kV case) and the time of the ionization wave touching the water layer surface are shown in Fig. 6.14(a). The development of the surface

electric field beginning at the termination of the high applied voltage to the maximum at 60 ns as the pulse reaches 0 kV is shown between 50 and 70 ns for the touching cases. At the end of the pulse fall (60 ns), the charge separation discussed in Chapter 4 creates a significant surface electric field. The charge separation in this simulation is enhanced by the immediate solvation of negative ions and a two-step process required for the charge exchange reactions to create aqueous cations from gaseous positive ions. Into the afterglow from 60 ns to 70 ns, the magnitude of the surface electric field has reduced by over 20 kV/cm for the -15 kV case and by 30 kV/cm for the -20 kV case. Interestingly, the second -15 kV pulse does not drop as sharply due to the presence of existing aqueous charged species and reasonably reflects the effects of charge accumulation and increases the potential for electroporation. Unfortunately, no cases that extend beyond 10 ns of afterglow have been attempted.

Within the cellular structure shown in Fig. 6.14(b) – (d), taken at points indicated in Fig. 6.2(b), the electric field is routinely higher for the -20 kV pulse case. Despite the 3 ns delay in the touching of the ionization wave, the -15 kV first and second pulse follow similar trends to similar magnitudes in each component of the cell structure. Looking first at the -20 kV case, there is a dramatic initial rise to 24 kV/cm in the membrane and similarly to lower magnitudes in the cytoplasm and nucleus. The second rise in the magnitude that begins at 30 ns results from the connection of the propagating electric field through the tissue to the ground plate beneath. This displacement current through the tissue continues to increase the electric field within the cell. At the end of the maximum applied voltage, the electric field in each region falls by up to an order of magnitude. One interesting phenomenon occurs during the pulse fall, the electric field in the membrane, cytoplasm and nucleus after the second pulse have increased to levels above those from the first pulse. Again, the charge accumulation and the presence of charged

species in the water layer does have an effect that may serve to increase the voltage seen on the cells and electric field within the cytoplasm to make this plausible with subsequent pulsing. The best case for intracellular electromanipulation is from the -20 kV pulse, but interesting possibilities are shown resulting from the more conductive water layer.

6.3.3 Water layer thickness (50 and 1000 μm)

Using the same voltage (-15 kV) and pulse profile, the thickness of the water layer was decreased and increased from 200 μm to 50 μm and 1 mm, respectively. In order to save computation time, the reactive portion of the water layer was reduced to 2.75 mm (corresponding to the radius of the tube for the shielding gas) with the remainder of the water layer treated as a dielectric ($\varepsilon/\varepsilon_o = 80$). In order to accurately compare the results, a new 200 μm case with the same geometric modifications was modeled as well. No major changes were seen between the new 200 μm case and the complete reactive water layer 200 μm case discussed in the earlier sections.

Some of the key differences in the dynamics of the discharge between the 1 mm and 200 μm water layers include a faster ionization wave resulting from the same applied voltage for the 1 mm case, earlier touching of the water layer with a more intense restrike and a lower intensity surface ionization wave, as shown in Fig. 6.15. In the left frame, the electron temperature at the time of impact with the surface of the water layer is shown. The maximum value of T_e is higher (9.4 eV compared to 9 eV with the 200 μm case) and the time of impact is 3 ns earlier. The restrike of the thicker water layer reflects from the surface of the water layer at 5×10^{20} $cm^{-3}s^{-1}$ compared to 2×10^{20} $cm^{-3}s^{-1}$ for the 200 μm case, as shown at 32 ns in the center frame of Fig. 6.15. The thicker water layer slows propagation of the potential and electric field into the water

layer and cells / tissue beneath. At 3 ns after touching, the electron density, shown in the right frame, is similar to the 200 μm case with a slightly higher density at the surface of the water layer.

At the end of the high voltage portion of the pulse at 50 ns, the electrons have formed a conducting channel and spread across the surface of the 1 mm water layer at higher levels than the 200 μm layer as shown in Fig. 6.16(a). The electron density is double in the channel and nearly doubled in the lateral spread compared to those in the 200 μm case. The electric field on the surface of the water layer is shown at 60 ns in Fig. 6.16(b). The low capacitance of the thicker water layer produces more surface charging resulting in an electric field with a maximum of 153 kV/cm compared to the 130 kV/cm for the 200 μm case (Fig. 6.8(b)). However, there is less lateral spread in the electric field than the 200 μm case. The electric field was 50 kV/cm at 2 mm along the surface laterally from the centerline for 200 μm compared with less than 5 kV/cm in the thicker case. The highest electric fields within the cells occur at the end of the high voltage part of the pulse at 50 ns. As the trends are the same, only the electric field magnitude at 50 ns is shown in Fig. 6.16(c). The electric field in the membrane and tissue ranges from 19 – 34 kV/cm, within the cytoplasm is 9 kV/cm and the within the nucleus is 12 kV/cm, each of which are higher than those occurring in the 200 μm case.

The thinner water layer produces several key differences in the discharge dynamics from the 200 μm case. One difference is that the ionization wave touches the surface of the water layer 4 ns earlier, as indicated by electron temperature, T_e, at 28.5 ns in the left frame of Fig. 6.17. Another is a stronger surface ionization wave for the thinner layer, as indicated by the nearly one order of magnitude higher S_e (2×10^{20} $cm^{-3}s^{-1}$ compared to 1×10^{21} $cm^{-3}s^{-1}$). Otherwise, the dynamics of the discharge shown in Fig. 6.17 show similar trends when the

ionization wave touches the surface of the water layer and spreads. The electron density at 3 ns after touching changes little from the 200 μm. However, at 50 ns, at the end of the maximum applied voltage, the lateral spread of electrons along the surface of the water layer, shown in Fig. 6.18(a), is greater with similar density values compared to the 200 μm case. As the applied voltage returns to zero at 60 ns, the spread of the electric field on the surface of the water layer is the greatest. However, as shown in Fig. 6.18(b), the magnitude of the electric field at 60 ns at the surface is lower than the 1 mm and 200 μm thick cases. The maximum electric field in the cellular structure is shown in Fig. 6.18(c). The membrane and tissue have values from 17 – 25 kV/cm and the cytoplasm and nucleus are 6 and 9 kV/cm, respectively. These are similar values to those occurring for the 200 μm case, and the same observations about the possibility of electroporation (low) and intracellular electromanipulation (plausible) apply.

The electric fields within the cell structure vary with time as shown in Fig. 6.19. The thin water layer enables the voltage and electric field to propagate to the cells earlier, with the thicker water layers initially buffering the cells. The electric field development at the selected positions at the surface of the water layer and within the membrane, cytoplasm, and nucleus (annotated in Fig. 6.2(b)) are shown in Fig. 6.19. The electric field at the surface of the water layer 10 μm from the axis is shown in Fig. 6.19(a) as it varies with time from 3 ns before impact of the ionization wave to 10 ns into the afterglow. The earlier impact of the 50 and 1000 μm thick layer and the increase in the magnitude of the surface electric field from 50 to 60 ns as the applied voltage goes from a maximum of -15 kV to 0 kV are shown in Fig. 6.19(a).

The cellular response to the electric field is shown in Fig. 6.19(b) – (d). One noticeable trend in each is the delay of the 200 μm cell response. This delay is from the lag in the impact of the ionization wave onto the surface of the water layer. The 1 mm thick water layer is expected

to have the lowest capacitance. From the analysis conducted in Chapter 4, the thinner water layer with highest capacitance results in a faster ionization wave. The ionization wave in the 200 μm case strikes the water layer a few ns later. The electric field in both the 50 and 200 μm cases rises quickly in the 3 ns after impact for each component of the cell structure. The 50 μm case then has a slow rise to a maximum at 50 ns which is the extent of the maximum applied voltage of -15 kV. The 200 μm case has a less significant initial rise, but climbs steadily and passes the electric field magnitude produced by the 50 μm case at 44 ns to a higher maximum at 50 ns. This is also shown for the entire cell structure in Fig. 6.8(c) for the 200 μm case and Fig. 6.18(c) for the 50 μm case.

The electric field for the 1000 μm (or 1 mm) thick water layer has a slower initial response, but increases to a higher maximum within each component of the cell compared to 50 and 200 μm. At 40 ns, the rising electric field for the 1 mm case for each of the cell components (Fig. 6.19(b)-(d)) surpasses the electric field of the 50 μm case. The electric field for the 1 mm case continues to increase to maximum values that are 7 kV/cm higher for the membrane and nearly 3 kV/cm higher for the cytoplasm and nucleus when compared to the next highest 200 μm case. This higher growth is counterintuitive as a thicker water layer of the same conductivity would be expected to decrease the magnitude of the electric field in the tissue beneath and within the cells. However, the cause of this response may be shown in Fig. 6.16(a) and (b) at the surface of the water layer. A spatially smaller lateral spread of electrons across the water layer and a more intensely concentrated electric field at the surface of the water layer may indicate that the electric field penetrates deeper into the tissue rather than propagating along the surface.

Further investigation compares results for two times analyzed for the 50 μm and 1 mm cases, 40 ns, corresponding to the crossing of the electric fields shown in Fig. 6.19(b) – (d), and

at 50 ns, at the end of the maximum applied voltage. These cases are shown in Fig. 6.20(a) – (d). Selecting a range of values that highlights the electric field within the tissue beneath the water layer and showing the entire computational domain, the 50 μm thick water layer case is shown in Fig. 6.20(a) at 40 ns and in Fig. 6.20(b) at 50 ns. The corresponding 1 mm thick water layer results are shown in Fig. 6.20(c) at 40 ns and Fig. 6.20(d) at 50 ns. Due to surface charging the electric field in the 50 μm case hugs the water layer and propagates through the tissue beneath the water layer remaining connected to the surface ionization wave moving laterally away from the centerline toward the grounded pump. The charging pulls the electric field from the cells at the centerline. Conversely, the electric field produced for the 1 mm thick water layer case remains more focused and penetrates through the tissue to the grounded plate beneath at 40 ns. At this point, a displacement current is formed through the tissue to the ground and begins to spread laterally through the tissue as shown at 50 ns to much higher values than the 50 μm case. This displacement current promotes the penetration of the electric field through the tissue (and cells) efficiently and increases the magnitude of the electric field in each component of the cell interior.

As the voltage pulse falls over 10 ns, the electric field drops nearly an order of magnitude. In the 1 mm case, the development of a displacement current through the tissue to the ground plate influenced the response of the electric field in the cells. The electric fields in the cells for the thicker water layer grew to values that are on the cusp of intracellular electromanipulation. These results also show the impact of the experimental set up. Cells suspended in a medium or fixed to the bottom of a petri dish can be expected to respond similarly to the formation of a displacement current. A plastic petri dish resting on a metal surface could have significantly different results that glass on a ceramic surface.

6.4 Concluding Remarks

In this chapter, the electric fields produced by the atmospheric pressure plasma jet modeled by a single pulse onto a 200 μm thick water layer were analyzed and compared while varying the applied voltage, thickness of the water layer, and a second pulse onto a more conductive water layer. Certain results are clear, if the ionization wave does not touch the surface of the water layer, there is little chance of any significant electrical effect on the cell. Another clear result is the variability of the experimental conditions. If a displacement current is formed through the tissue to ground beneath the tissue the electric fields within the cells grow considerably. Additionally, the 60 ns pulse duration does not promote either electroporation or stimulating voltage-gated channels in the membrane in any of the scenarios modeled.

On the other hand, with the short duration and relatively high electric field produced, intracellular electromanipulation is possible. With an increase in the number of pulses, increase in conductivity in the solution through pulsing or the presence of additional species, application to dry cells, and/or increase in voltage, intracellular electromanipulation is definitely plausible based on the predicted thresholds.

6.5 Table

Table 6.1 Selected constants of the cell components

	Permittivity ($\varepsilon/\varepsilon_o$)	Conductivity (Ω^{-1} cm^{-1})	Dielectric Relaxation Time (s)
Membrane	5.8	8.7×10^{-8}	5.9×10^{-6}
Cytoplasm	30	4.8×10^{-3}	5.5×10^{-10}
Nucleus	20	3.0×10^{-5}	5.9×10^{-8}
Tissue	5	1.0×10^{-6}	4.4×10^{-7}

6.6 Figures

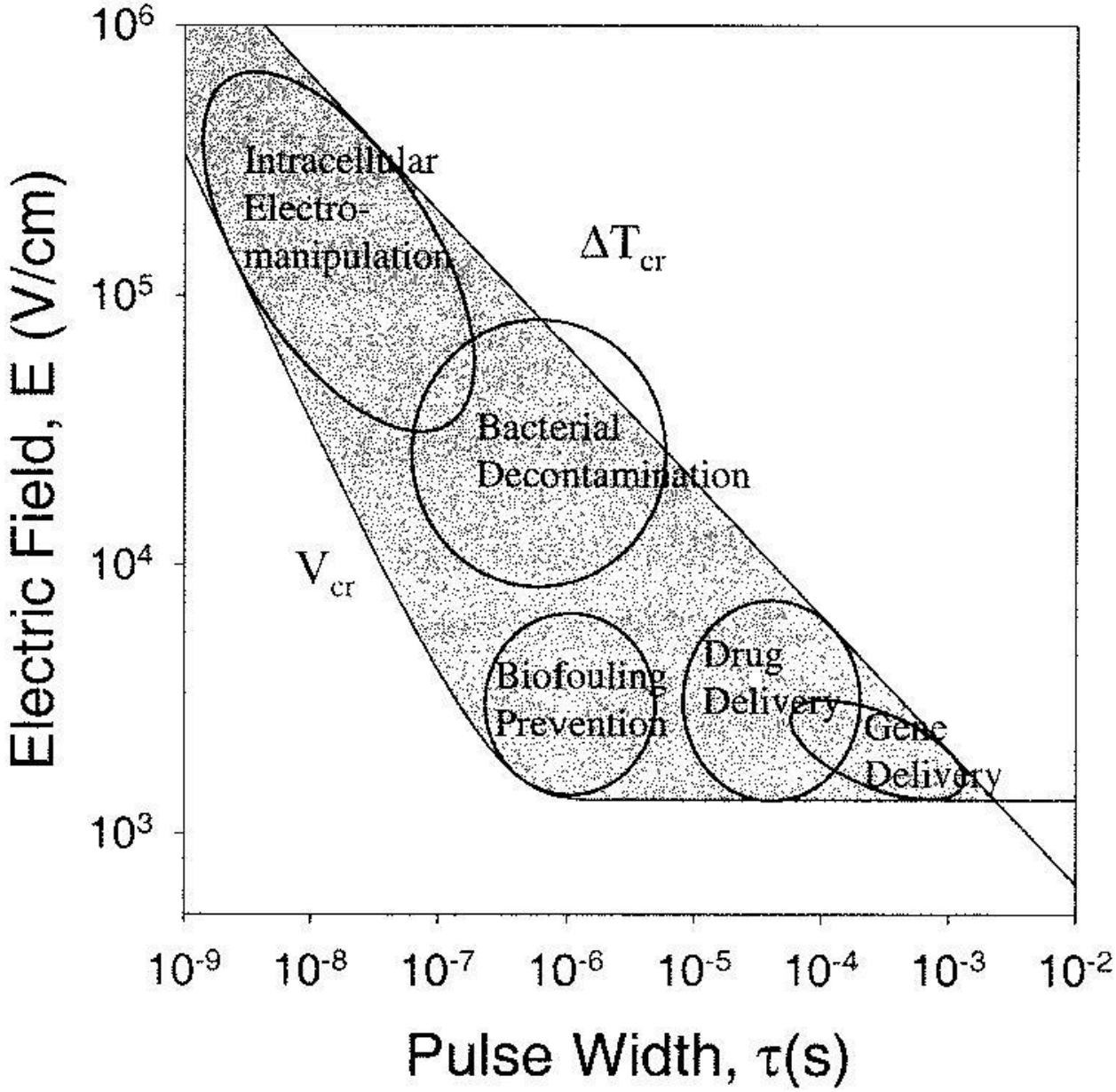

Figure 6.1 Range of electrical field effects based on pulse duration and the resulting application.[10]

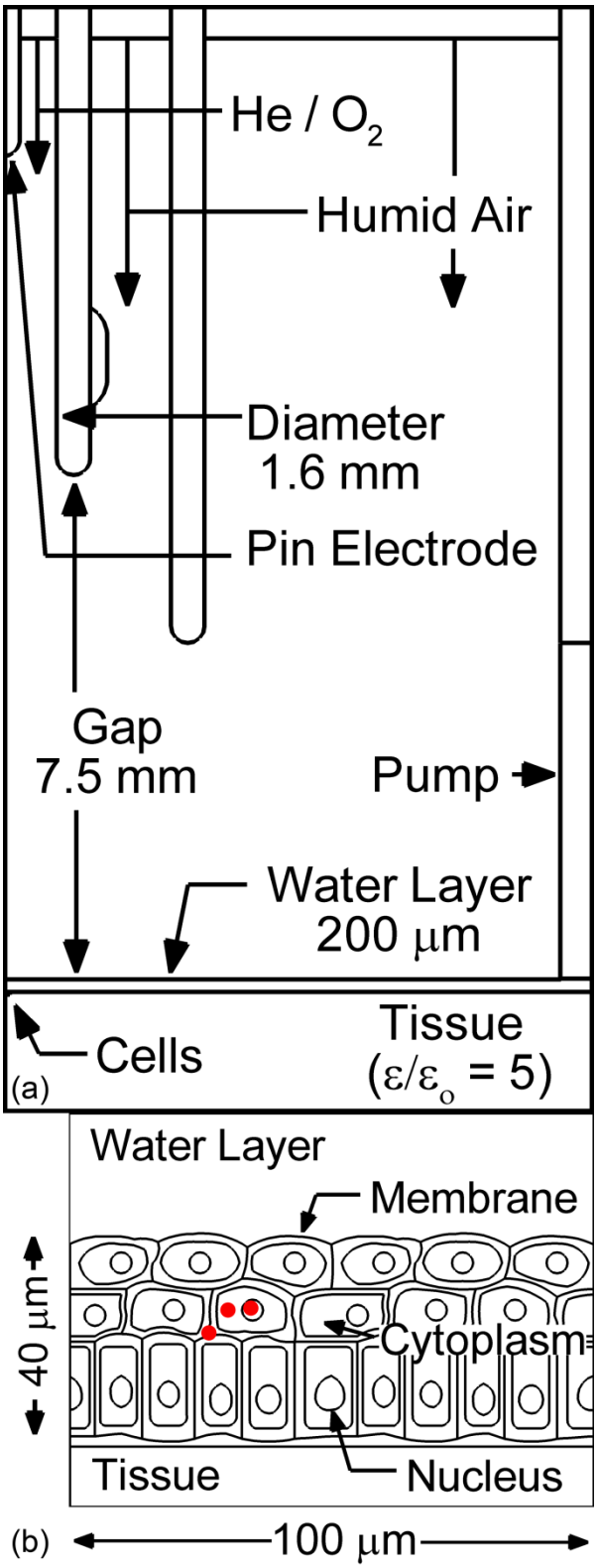

Figure 6.2 Schematic of the 2-D Cartesian symmetric model geometry. (a) The full computational domain is 19 mm by 9 m. (b) A closer look at the cells beneath the water layer with locations for further investigation annotated by the red dots.

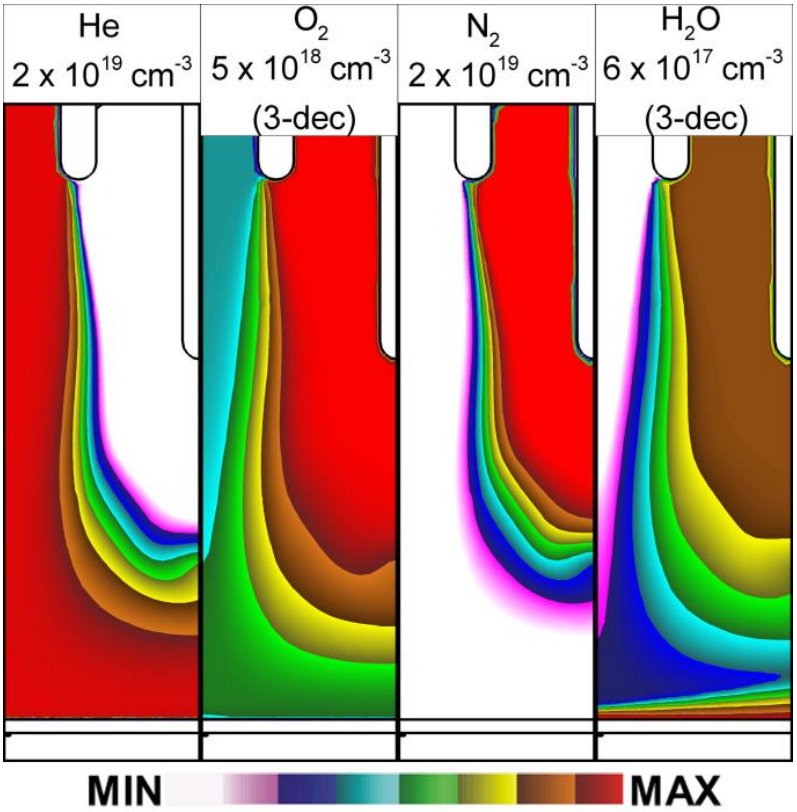

Figure 6.3 Helium, oxygen, nitrogen and H_2O concentrations of the He/O_2 = 99.8/0.2 flow at 4 slm and 1 slm of humid air from shroud into the ambient prior to discharge ignition. The color contours on the helium and nitrogen images represent 10% decreases from the maximum listed value. The oxygen and H_2O concentrations are over 3 decades from the maximum listed to highlight the seeded oxygen within the helium and the movement of the water vapor from the surface of the water layer.

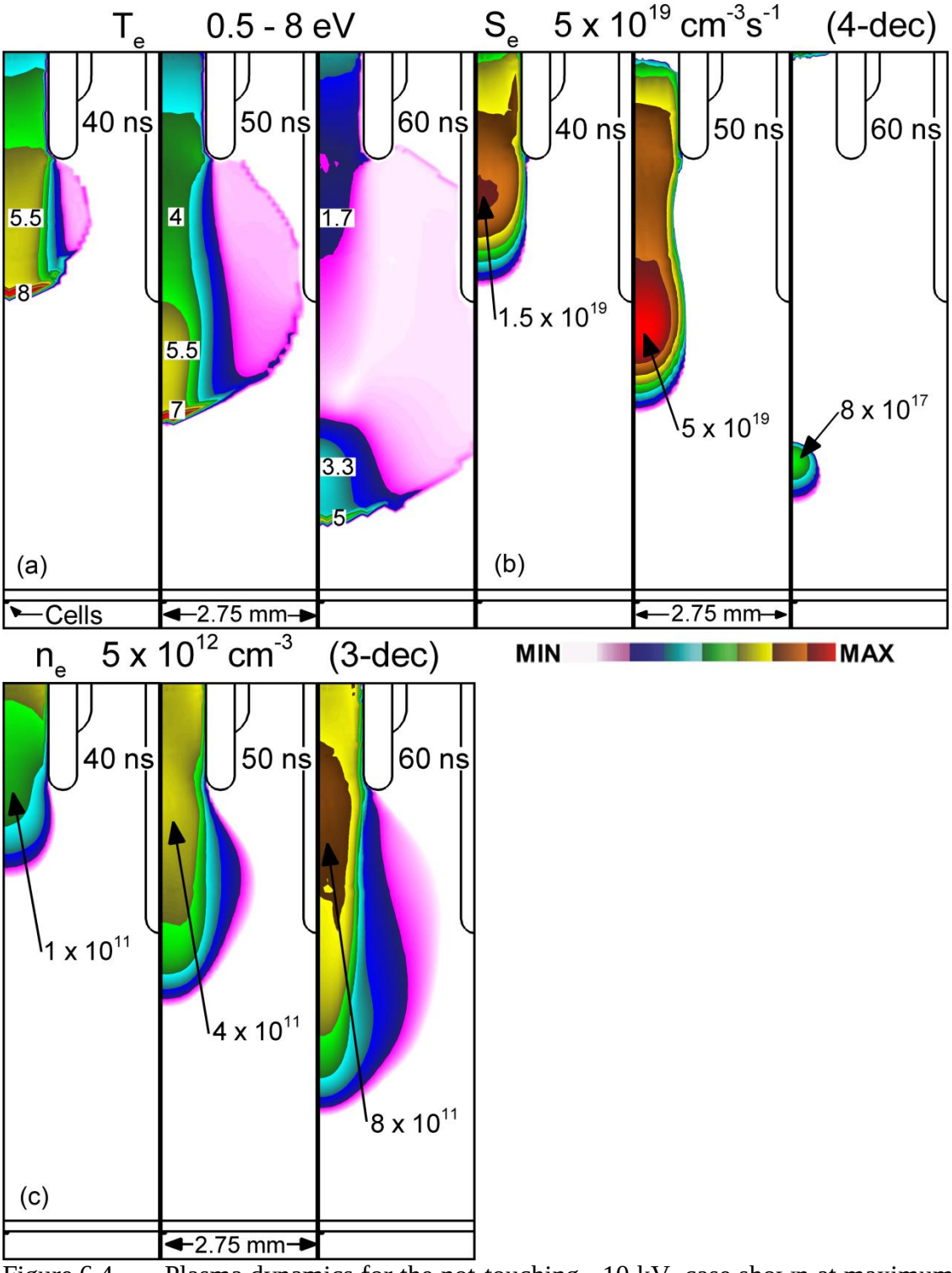

Figure 6.4 Plasma dynamics for the not-touching, -10 kV, case shown at maximum potential at 40 and 50 ns and at zero applied voltage at 60 ns. (a) Electron temperature T_e from left to right at 40, 50 and 60 ns on a linear scale between 0.5 – 8 eV. (b) The electron impact ionization source S_e, at 40, 50 and 60 ns using a log-scale over five decades. (c) Electron density at 40, 50 and 60 ns from left to right using a three decade log-scale.

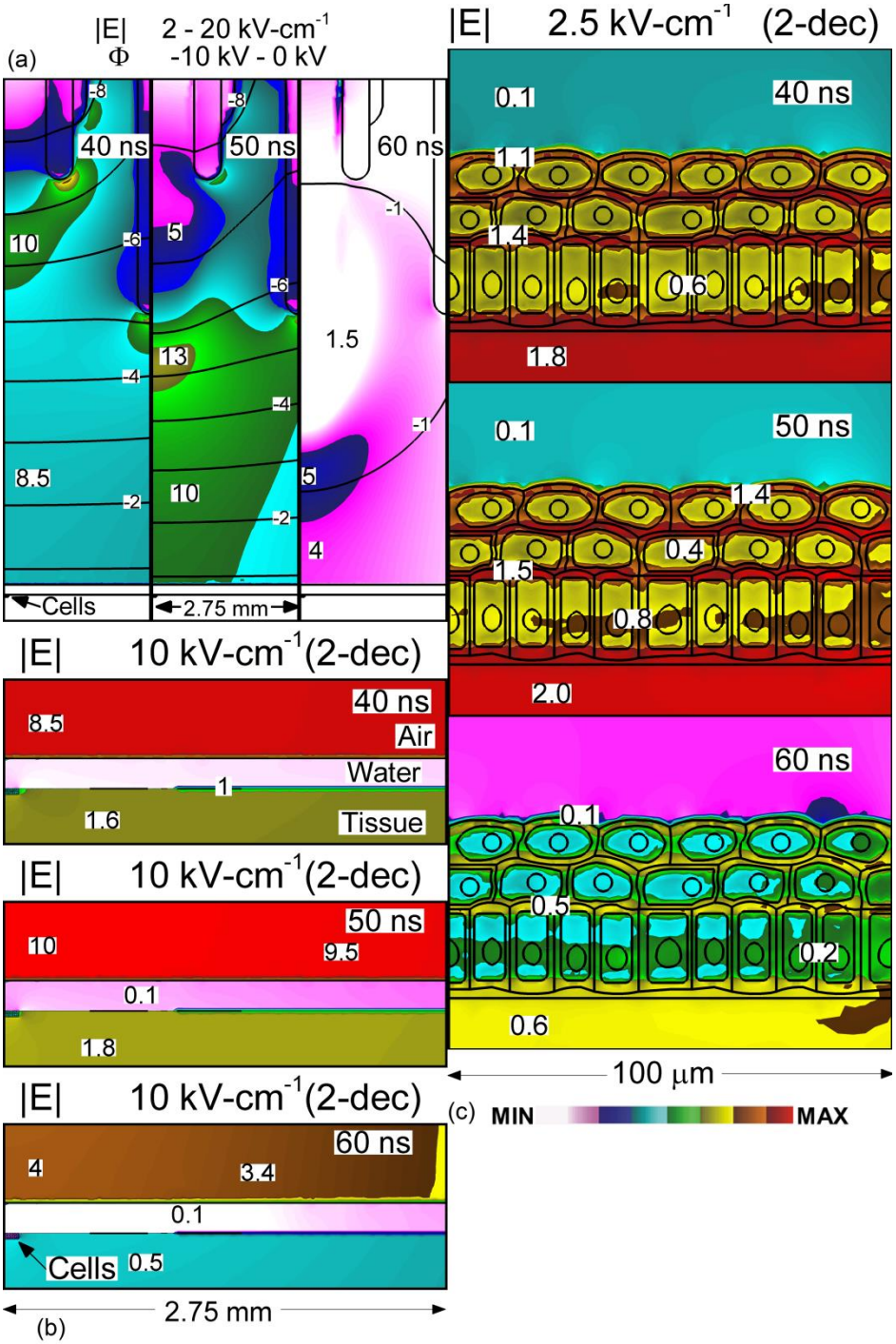

Figure 6.5 Magnitude of electric field for the not-touching, -10 kV, case shown at 40, 50 and 60 ns. (a) Electric field using a linear scale from 2 – 20 kV/cm with potential contours representing one kV changes. (b) Electric field at the air – water layer – tissue interface from top to bottom at 40, 50, and 60 ns using a log-scale over two decades. (c) Electric field magnitude at the water layer – cell membrane interface, within the cell structure, and in the tissue below the cells shown using a log-scale over two decades.

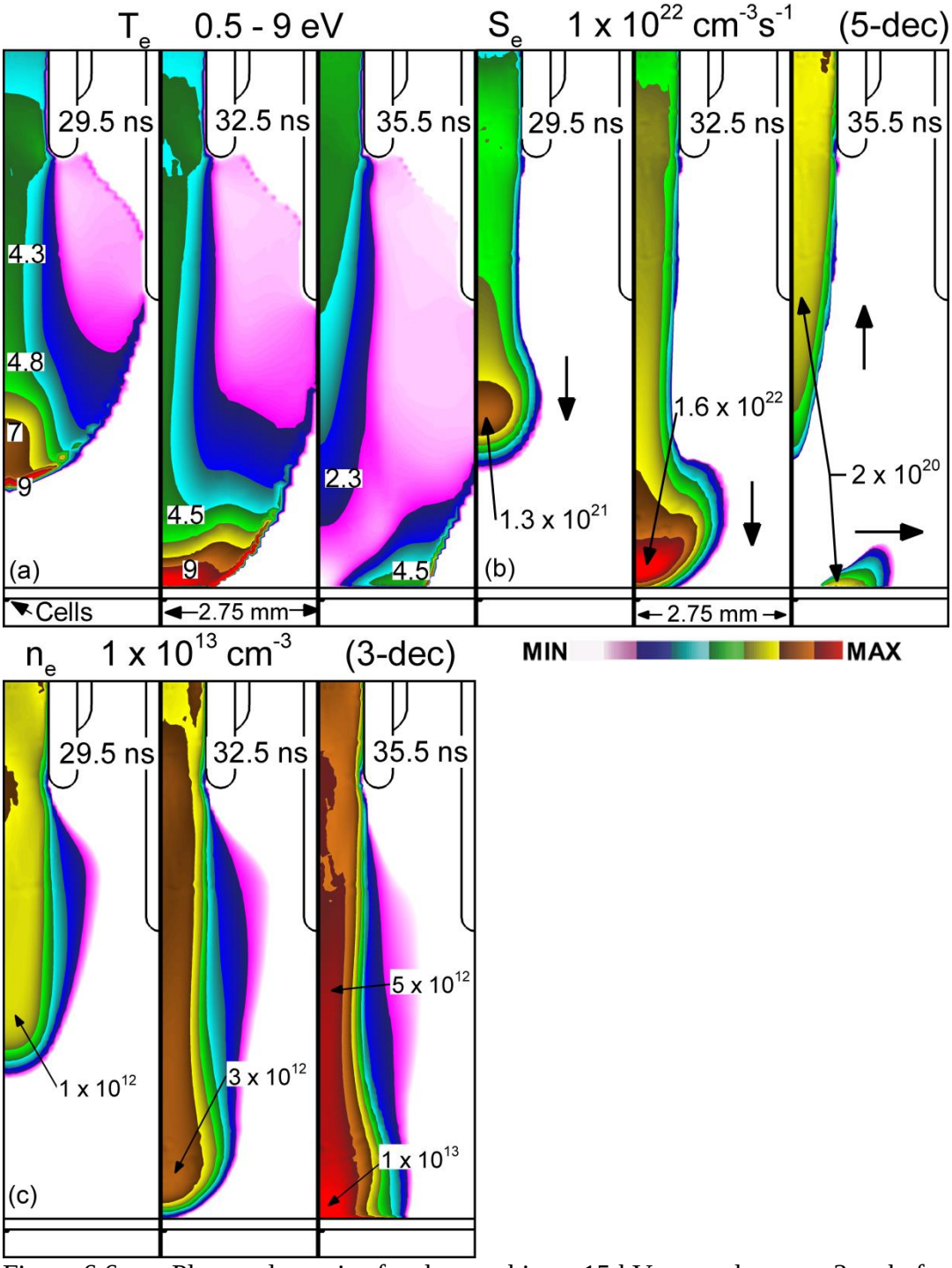

Figure 6.6 Plasma dynamics for the touching, -15 kV, case shown at 3 ns before touching, at touching, and 3 ns after touching. (a) Electron temperature T_e, using a linear scale from 0.5 – 9 eV with direction of the propagation shown by arrows within the frame. (b) The electron impact ionization source S_e, using a log-scale over five decades. The restrike and surface ionization wave at 35.5 ns are noticeable in both (a) and (b). (c) Electron density n_e, using a log-scale over three decades. The formation of the conduction channel is apparent at 35.5 ns.

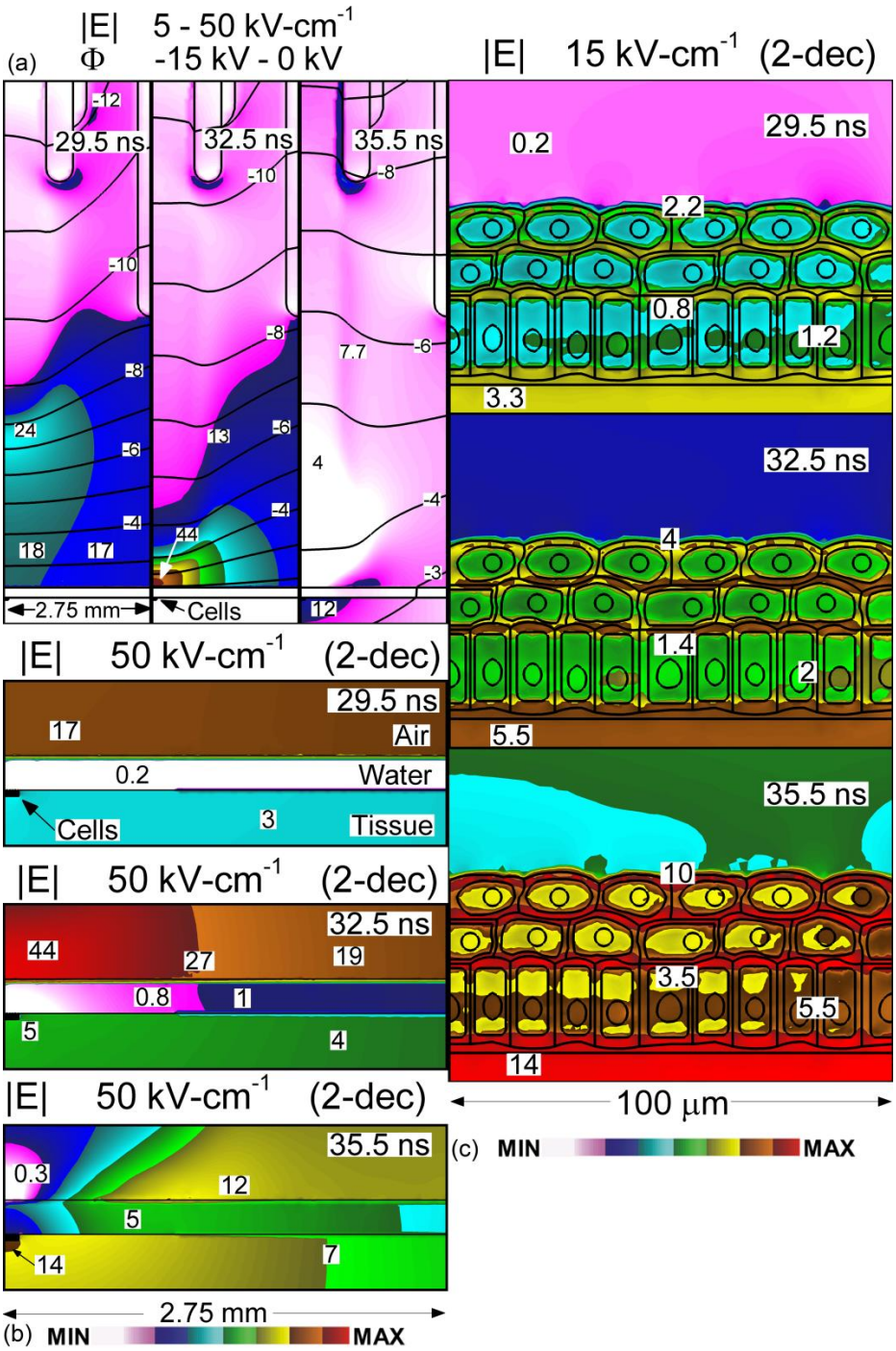

Figure 6.7 Magnitude of electric field for the touching, -15 kV, case shown at 3 ns before touching, at touching, and 3 ns after touching. (a) Electric field within the using a linear scale from 5 – 50 kV/cm with potential contours representing one kV changes. (b) Electric field at the air – water layer – tissue interface from top to bottom at 3 ns before, at, and 3 ns after touching using a log-scale from a maximum of 50 kV/cm over two decades. (c) Electric field magnitude at water layer – cell membrane interface, within the cell structure, and in the tissue below the cells shown from a maximum of 15 kV/cm on a log-scale over two decades.

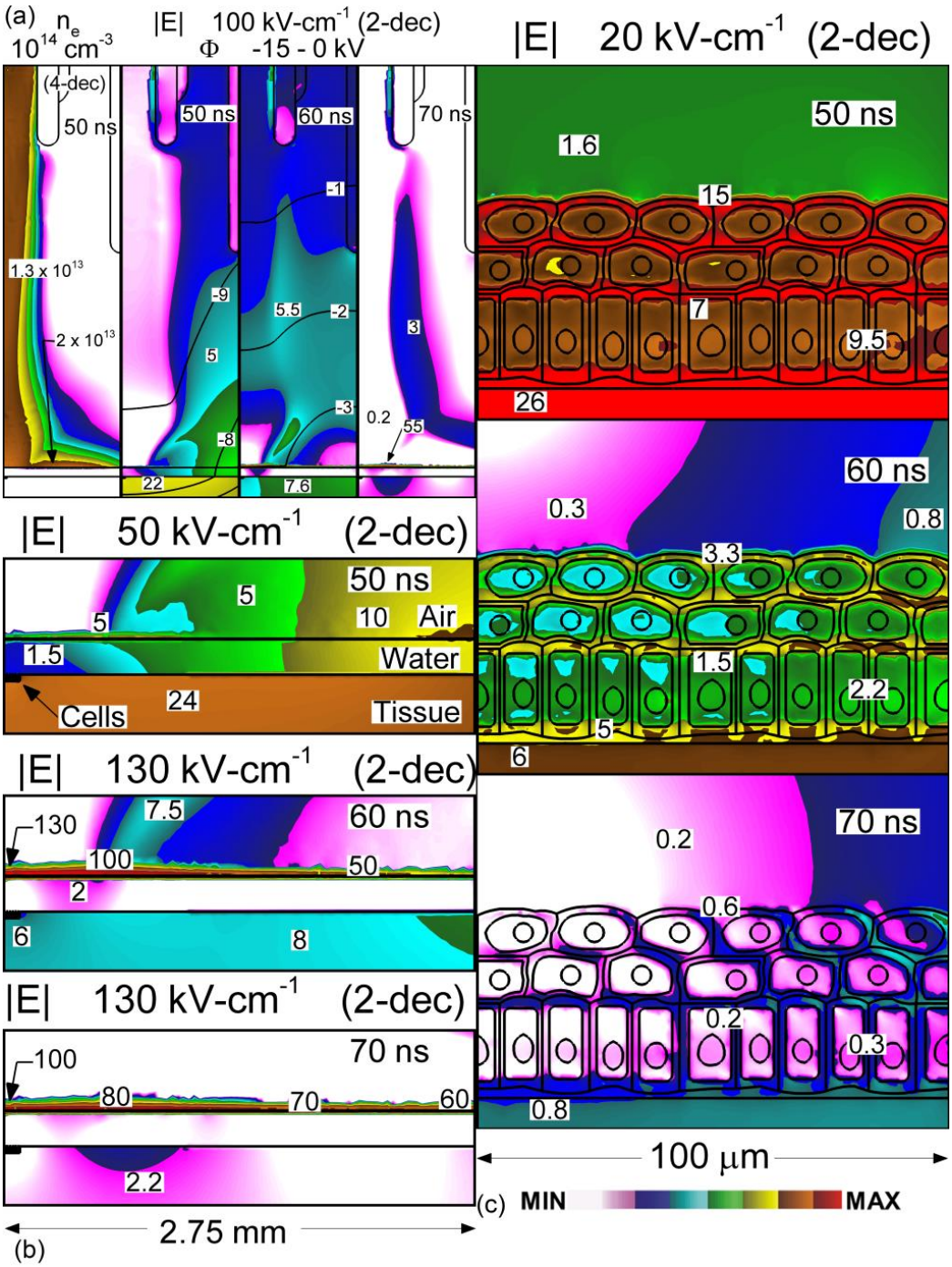

Figure 6.8 The discharge dynamics at the end of the pulse. Corresponding to the maximum extent of the pulse at 50 ns, the end of the pulse fall at 60 ns, and 10 ns into the afterglow at 70 ns. (a) The electron density in the left frame at 50 ns on a log-scale over four decades. The magnitude of the electric field and potential contours at 50, 60 and 70 ns. The contours represent one kV and the field is shown using a log-scale from 100 kV/cm over two decades. (b) The electric field at the air – water layer – tissue interface. (c) The magnitude of the electric field at the water layer – cell interface at the maximum extent of the pulse (50 ns), pulse fall (60 ns) and afterglow (70 ns).

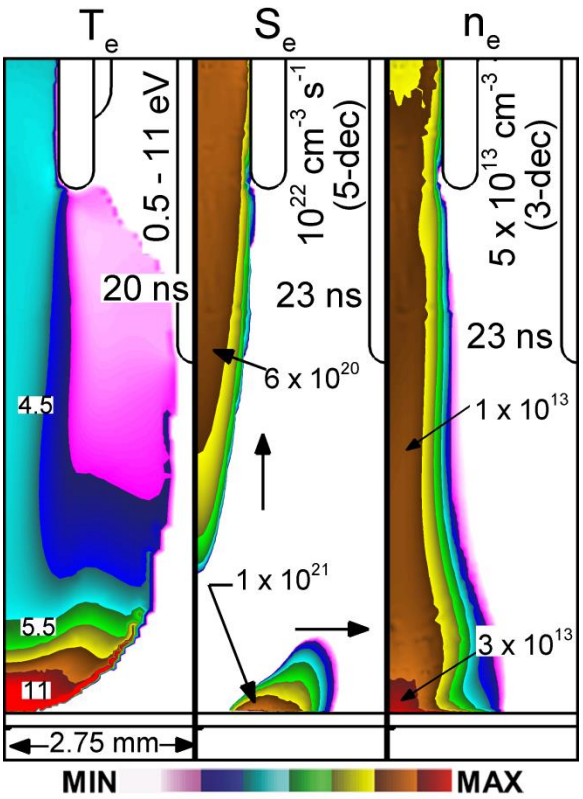

Figure 6.9 The critical discharge dynamics of the touching, -20 kV, case. From left to right, electron temperature T_e, using a linear scale from 0.5 – 11 eV at moment guided ionization wave touches the water layer, the electron impact ionization source S_e, using a log-scale over five decades with arrows indicating direction of restrike and surface ionization wave at 3 ns after touching, and electron density n_e, using a log-scale over three decades at 3 ns after touching.

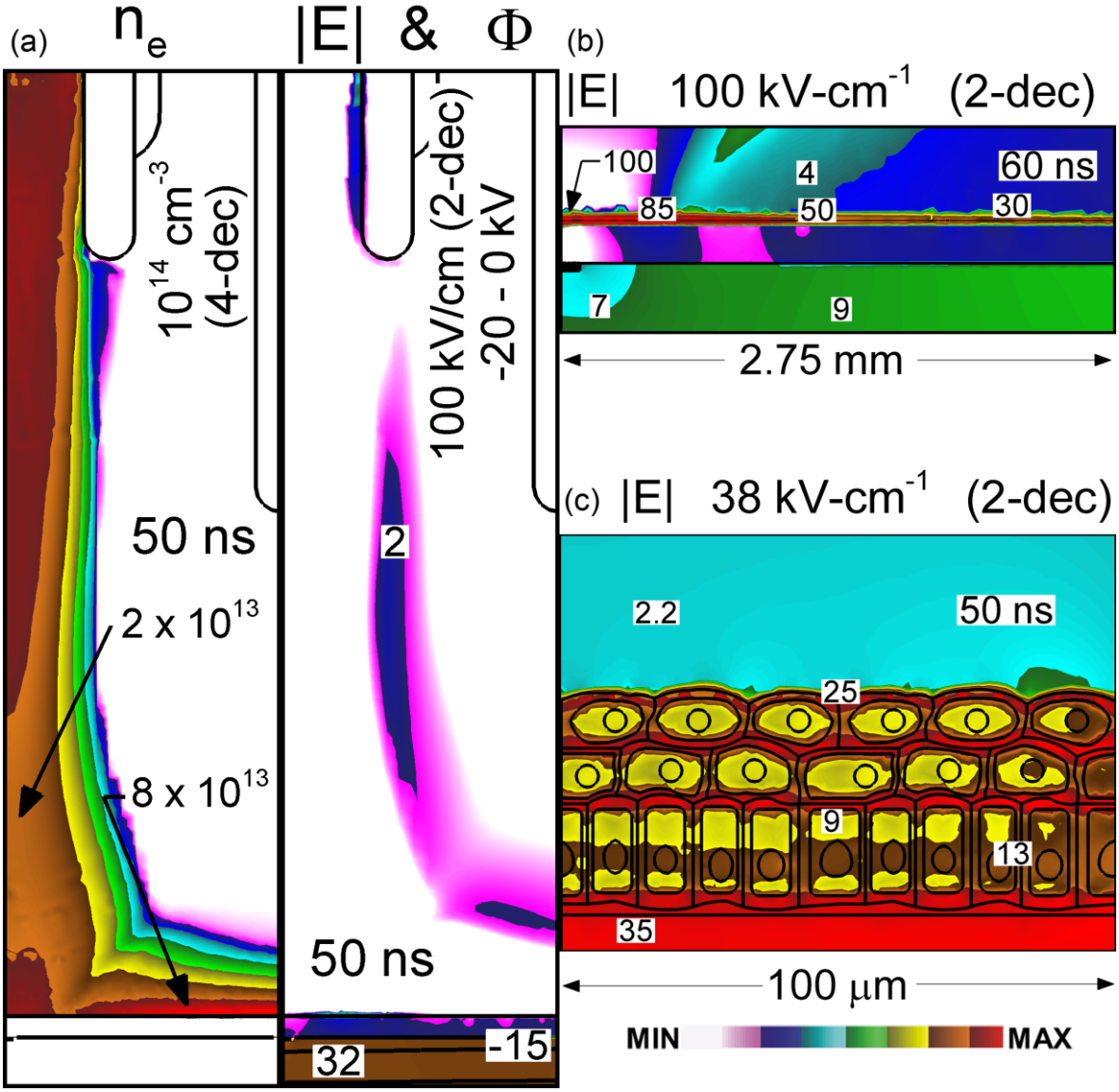

Figure 6.10 The discharge dynamics of the end of the -20 kV pulse shown at the maximum extent of the pulse (50 ns) and the end of the pulse fall (60 ns). (a) The conduction channel represented by the connection of the electrons from the water layer surface to the pin electrode and the spread of the electrons across the surface of the water layer is shown in the left frame at 50 ns. The magnitude of the electric field at 50 ns shown using a log-scale from 100 kV/cm over two decades. (b) The magnitude of the electric field at the air – water layer – tissue interface highlights the formation of an electric field on the surface of the water layer at 60 ns shown using a log-scale over two decades from 100 kV/cm. (c) The magnitude of the electric field at the water layer – cell membrane interface, within the cell, and in the tissue beneath the cells from a maximum of 38 kV/cm over two decades using a log-scale at 50 ns.

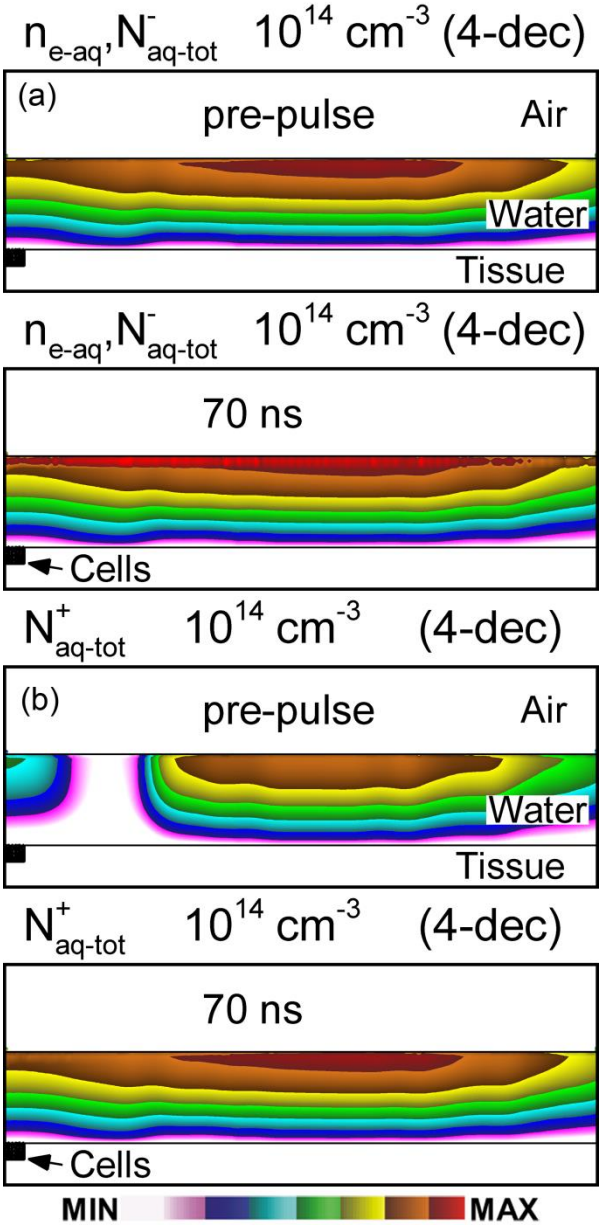

Figure 6.11 The concentration of aqueous ions 50 ms after the completion of the first pulse and immediately prior to the second -15 kV pulse (top frame) and at the end of the second -15 kV pulse (70 ns). (a) Concentration of aqueous electrons and anions and (b) concentration of aqueous cations from 10^{14} cm^{-3} using a log-scale over four decades.

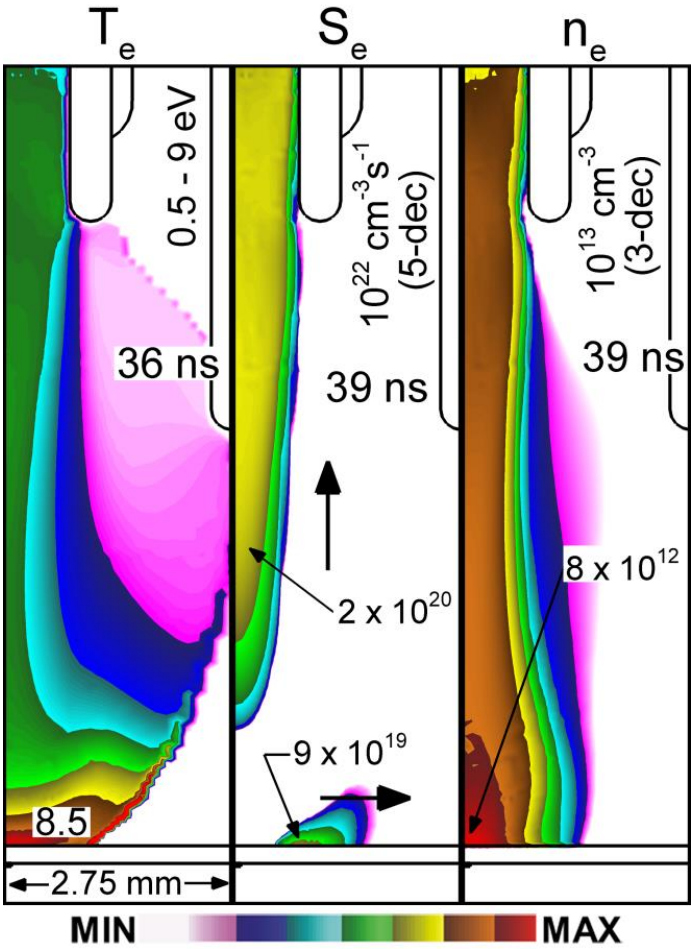

Figure 6.12 The critical discharge dynamics of a second -15 kV pulse touching a conductive, 200 µm thick, water layer. From left to right, electron temperature T_e, using a linear scale from 0.5 – 9 eV at the time of touch, 36 ns. the electron impact ionization source S_e, using a log-scale over five decades with arrows indicating direction of restrike and surface ionization wave at 39 ns (3 ns after touch), and electron density n_e, at 39 ns using a log-scale over three decades.

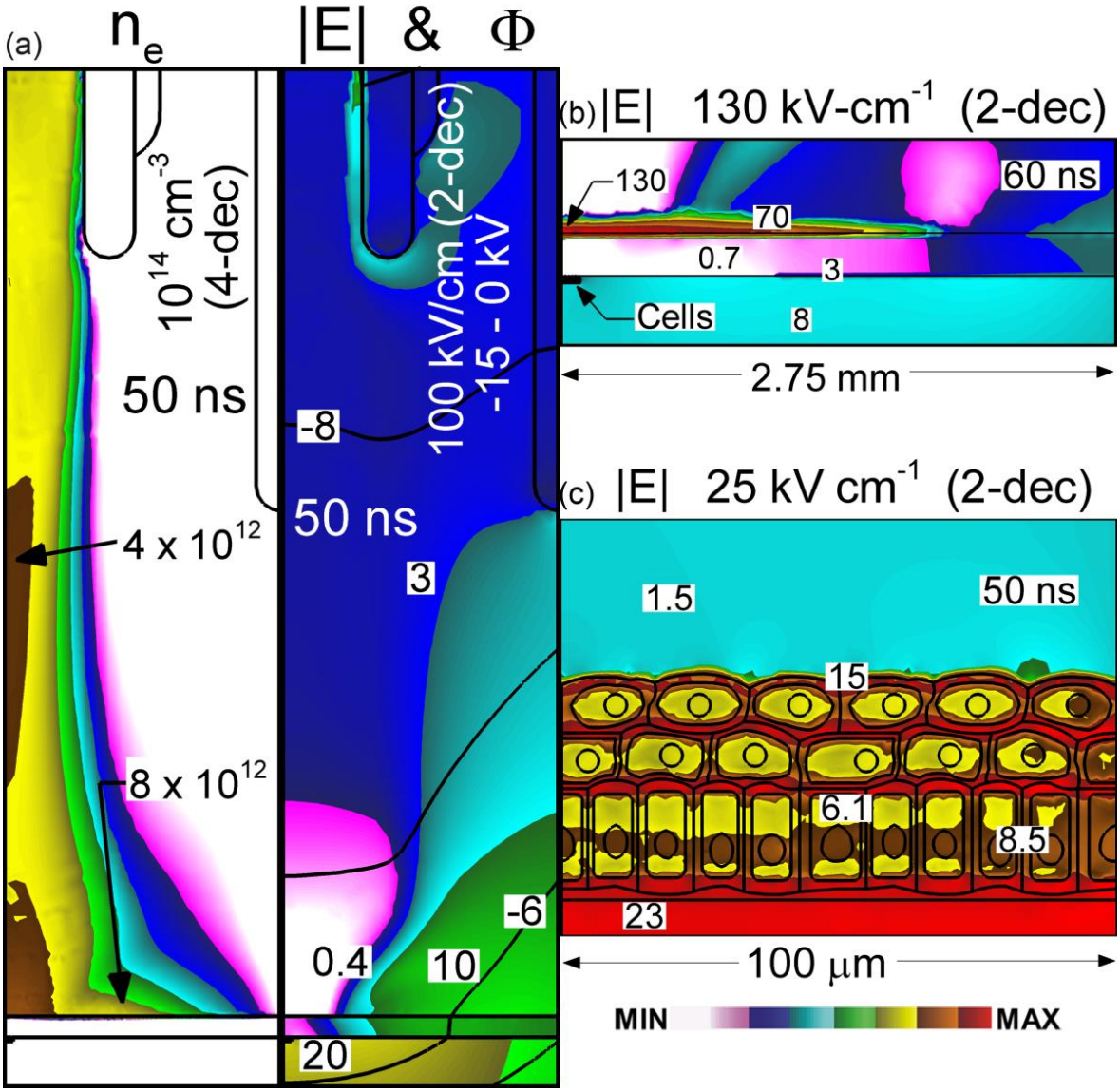

Figure 6.13 The discharge dynamics at the end of the second pulse. Corresponding to the maximum extent of the pulse at 50 ns and the end of the pulse fall at 60 ns. (a) The electron density in the left frame is shown on a log-scale over four decades at lower levels than those of the first pulse at 50 ns. The magnitude of the electric field and potential contours are shown at 50 ns for the plasma region. The contours represent one kV and the field is shown using a log-scale from 100 kV/cm over two decades. (b) The electric field at the air-water layer-tissue interface highlighting the effect of surface charging and the resulting surface electric field created at 60 ns using a log-scale from 130 kV/cm over two decades. (c) The magnitude of the electric field at the water layer-cell interface at the extent of the pulse (50 ns) also using a log-scale from 25 kV/cm over two decades.

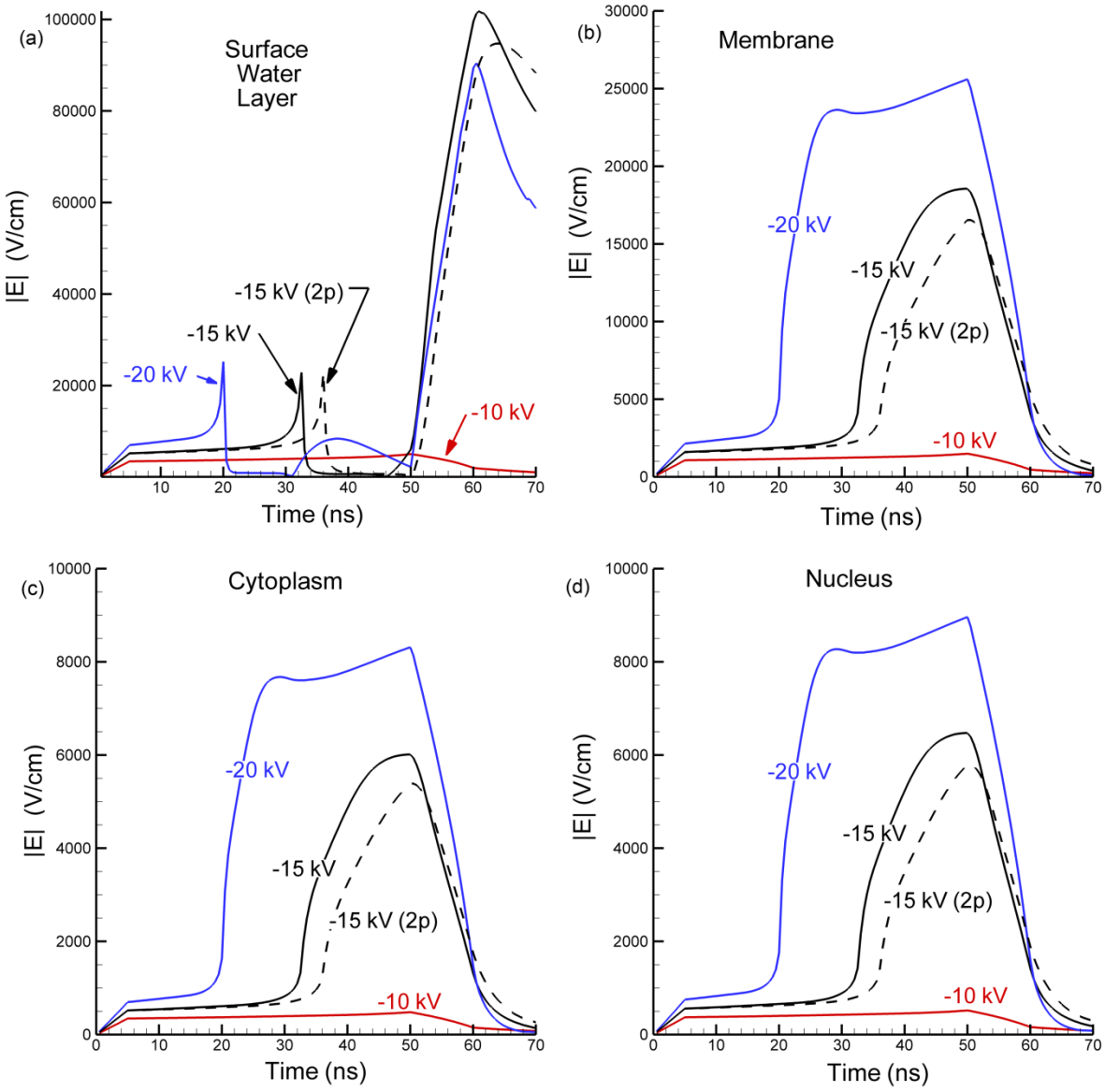

Figure 6.14 The magnitude of the electric field as it changes with time at four locations for the -10 kV, -15 kV (1st and 2nd pulses) and -20 kV cases. (a) At the surface of the water layer, 10 μm from the centerline. The locations for the membrane, cytoplasm and nucleus are indicated in Fig. 6.2(b). (b) In the membrane. (c) In the cytoplasm. (d) In the nucleus.

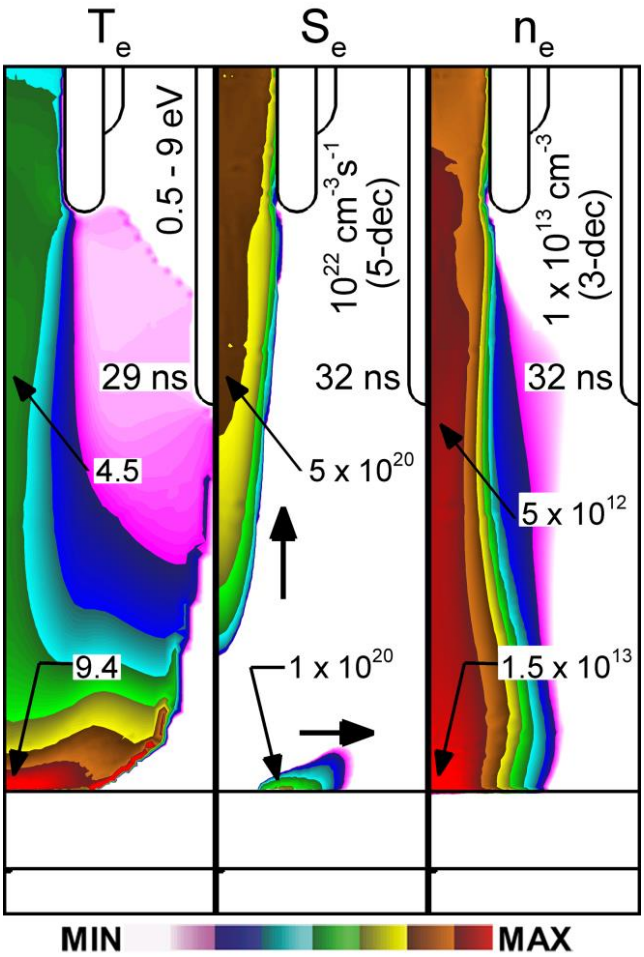

Figure 6.15 The critical discharge dynamics of the touching, -15 kV, case touching a 1 mm thick water layer. From left to right, electron temperature T_e, using a linear scale from 0.5 – 9 eV at the moment of touching, 29 ns, the electron impact ionization source S_e, using a log-scale over five decades with arrows indicating direction of restrike and surface ionization wave at 3 ns after touching (32 ns), and electron density n_e, at 32 ns using a log-scale over three decades.

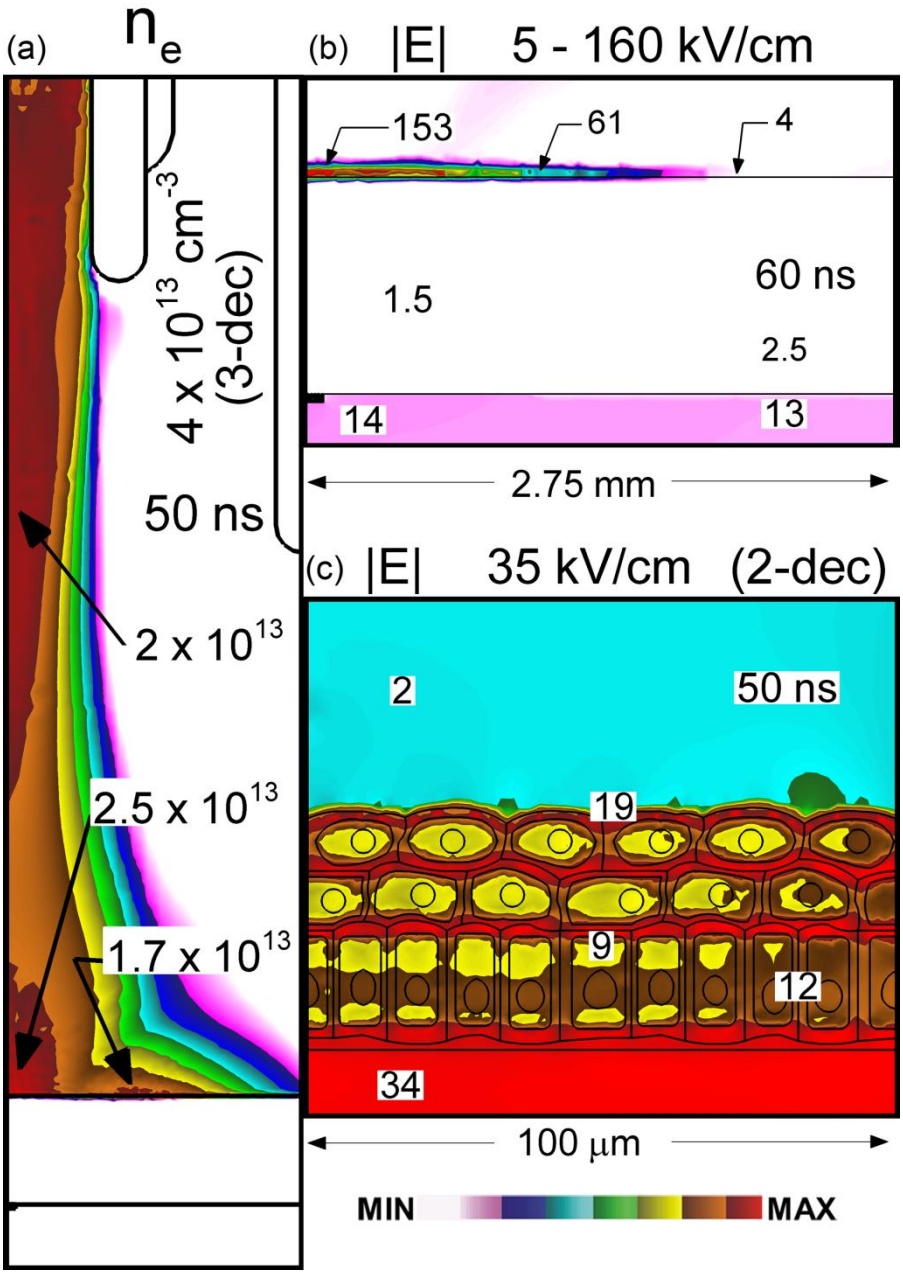

Figure 6.16 The discharge dynamics of the end of the -15 kV pulse onto a 1 mm thick water layer shown at the maximum extent of the pulse (50 ns) and the end of the pulse fall (60 ns). (a) The conduction channel and spread of electrons across the surface of the water layer using a log-scale from 4×10^{13} cm^{-3} over three decades. (b) The magnitude of the electric field at the air – water layer – tissue interface highlights the formation of an electric field on the surface of the water layer at 60 ns shown from 5 – 160 kV/cm using a linear-scale. (c) The magnitude of the electric field at the water layer – cell membrane interface, within the cell, and in the tissue beneath the cells at 50 ns from a maximum of 35 kV/cm over two decades using a log-scale.

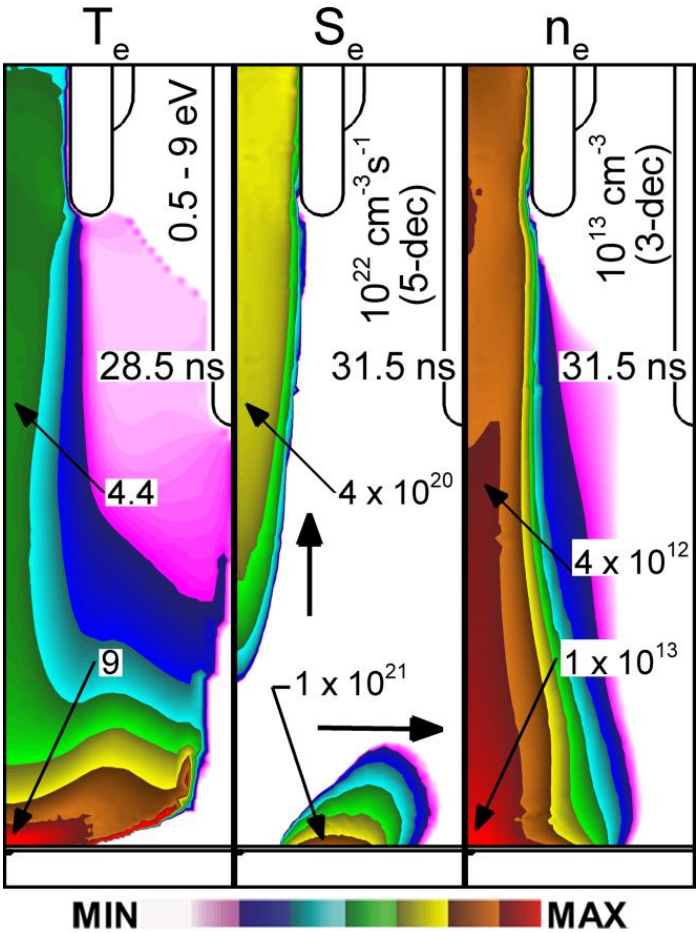

Figure 6.17 The critical discharge dynamics of the touching, -15 kV, case touching a 50 μm thick water layer. From left to right, electron temperature T_e, using a linear scale from 0.5 – 9 eV at the moment of touch (28.5 ns), the electron impact ionization source S_e, using a log-scale over five decades with arrows indicating direction of restrike and surface ionization wave at 3 ns after touch (31.5 ns), and electron density n_e, at 31.5 ns using a log-scale over three decades.

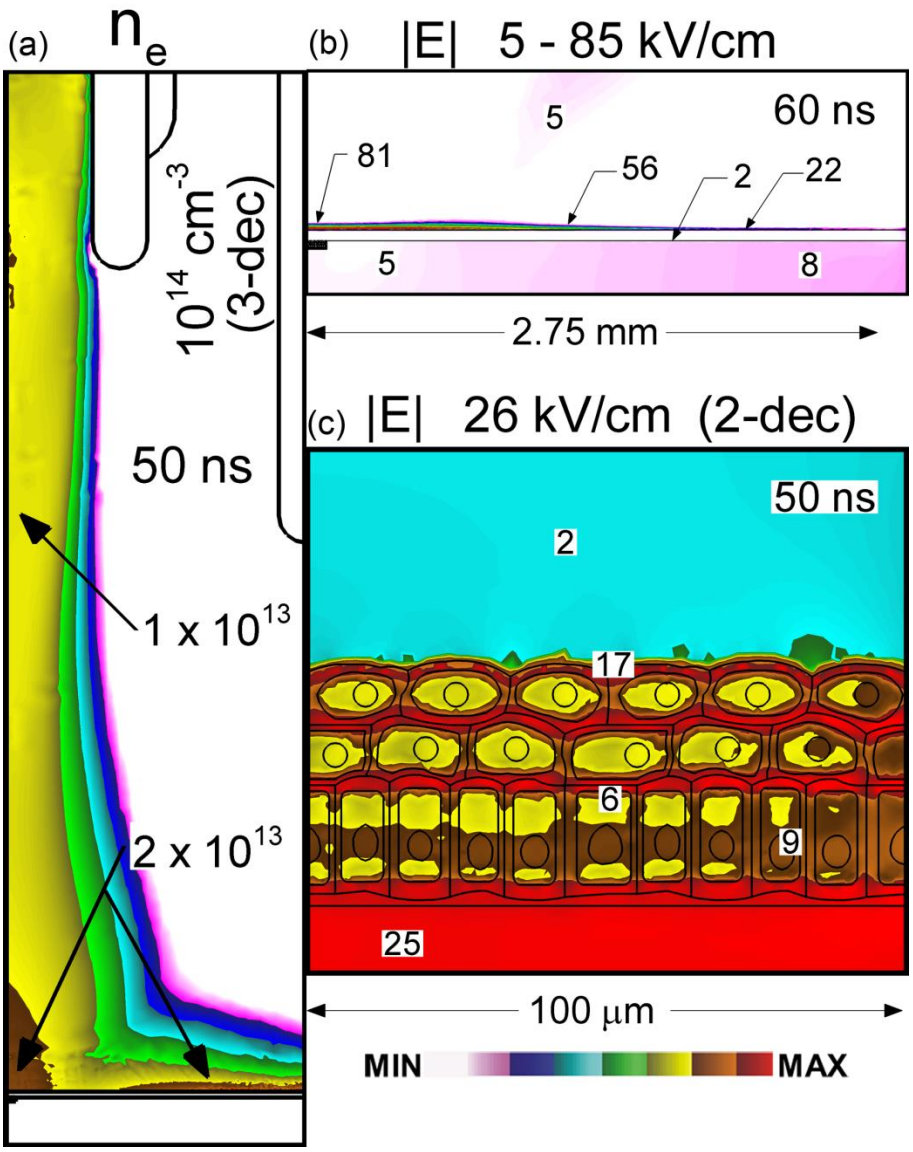

Figure 6.18 The discharge dynamics of the end of the -15 kV pulse onto a 50 μm thick water layer shown at the maximum extent of the pulse (50 ns) and the end of the pulse fall (60 ns). (a) The conduction channel and spread of electrons across the surface of the water layer using a log-scale from 1×10^{14} cm^{-3} over three decades. (b) The magnitude of the electric field at the air – water layer – tissue interface highlights the formation of an electric field on the surface of the water layer at 60 ns shown from 5 – 85 kV/cm using a linear-scale. (c) The magnitude of the electric field at the water layer – cell membrane interface, within the cell, and in the tissue beneath the cells at 50 ns from a maximum of 26 kV/cm over two decades using a log-scale.

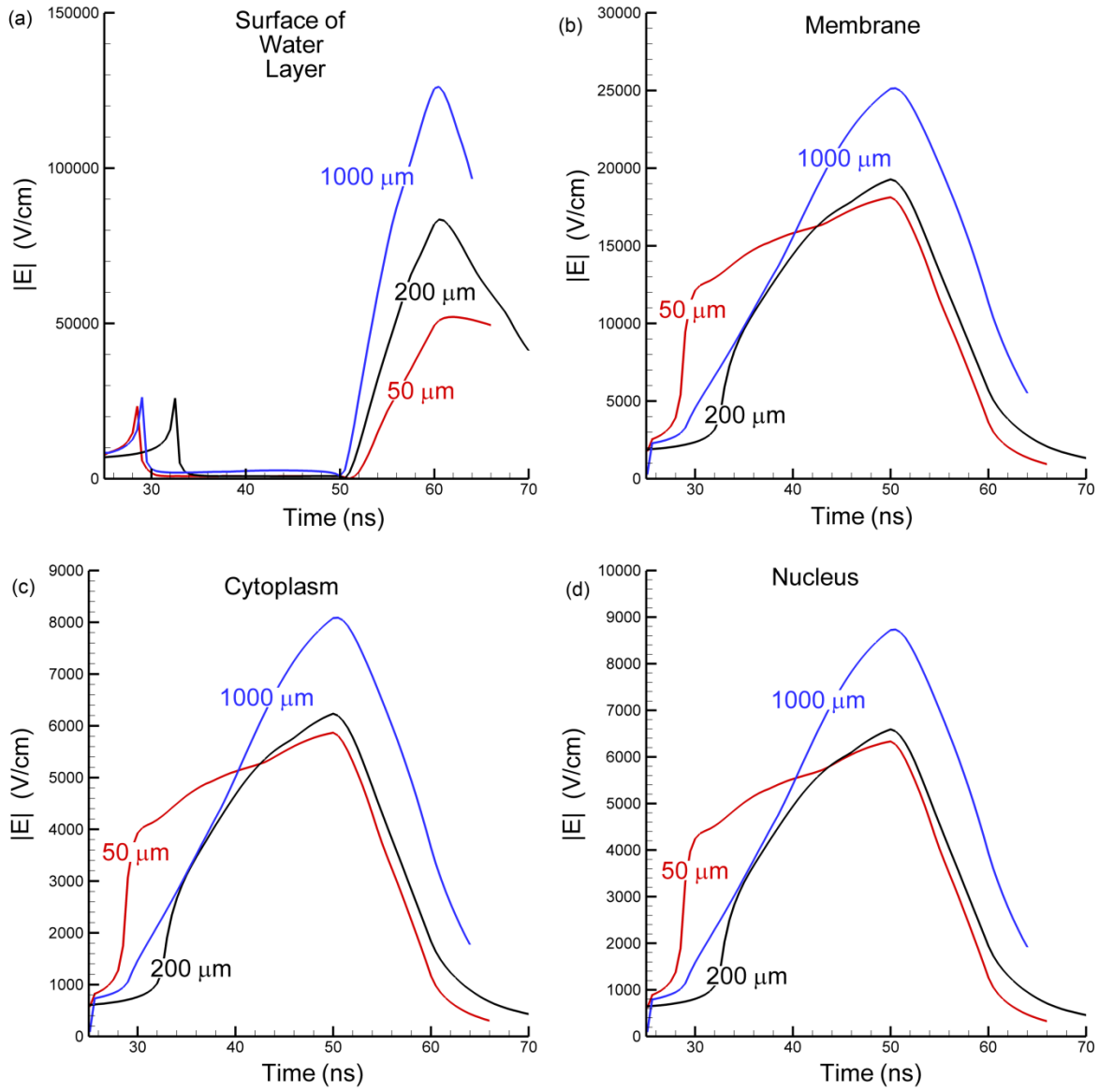

Figure 6.19 The magnitude of the electric field as it changes with time at four locations for the 50 μm, 200 μm, and 1 mm thick water layer cases. (a) At the surface of the water layer, 10 μm from the centerline. The locations for the membrane, cytoplasm and nucleus are indicated in Fig. 6.2(b). (b) In the membrane. (c) In the cytoplasm. (d) In the nucleus.

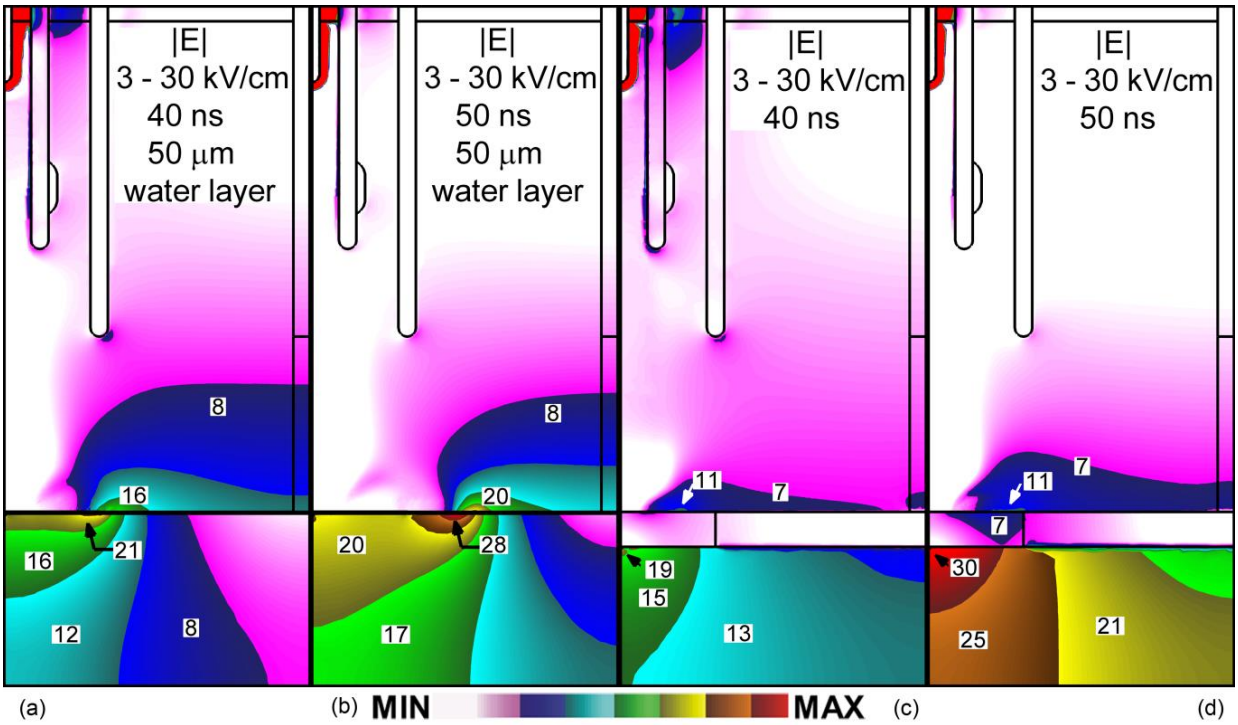

Figure 6.20 Comparing the development and propagation of the electric field in and through the tissue beneath the water layer for the 50 μm and the 1 mm thick water layer cases at 40 and 50 ns. A grounded plate exists beneath the tissue at the bottom of the computational domain. (a) 50 μm at 40 ns. (b) 50 μm at 50 ns showing the lateral spread of the electric field through the tissue but beneath the water layer forming a connection with the surface ionization wave. (c) 1 mm at 40 ns. (d) 1 mm at 50 ns showing the penetration of the field through the tissue to the ground plate and spread through the tissue. Each figure uses a linear scale showing 3 – 30 kV/cm to highlight the electric field within the tissue.

6.7 References

[1] M. Laroussi, I. Alexeff, and W. Kang, "Biological Decontamination by Non-thermal Plasmas", IEEE Trans. Plasma Sci., **28**, 184 (2000).

[2] M. Laroussi, M. Kong, G. Morfill, and W. Stolz, *Plasma Medicine: Applications of Low-Temperature Gas Plasmas in Medicine and Biology*, (Cambridge, Cambridge University Press, 2012), pp. 156-174.

[3] G. Fridman, G. Friedman, A. Gutsol, A.B. Shekter, V.N. Vasilets, and A. Fridman, "Applied Plasma Medicine", Plasma Process. Polym., **5**, 503 (2008).

[4] M. Keidar, A. Shashurin, O. Volotskova, M. Stepp, P. Srinivasan, A. Sandler, B. Trink, "Cold atmospheric plasma in cancer therapy", Physics of Plasmas, **20**, 057101 (2013).

[5] D.B. Graves, "The emerging role of reactive oxygen and nitrogen species in redox biology and some implications for plasma applications to medicine and biology", J. Phys. D: Appl. Phys., **45**, 263001 (2012).

[6] J.C. Weaver, "Electroporation of Cells and Tissues", IEEE Trans. Plasma Sci., **28**, 24 (2000).

[7] S.B. Dev, D.P. Rabussay, G. Widera, and G.A. Hofmann, "Medical Applications of Electroporation", IEEE Trans. Plasma. Sci., **28**, 206 (2000).

[8] K.H. Schoenbach, F.E. Peterkin, R.W. Allen, and S.J. Beebe, "The Effect of Pulsed Electric Fields on Biological Cells: Experiments and Applications", IEEE Trans. Plasma Sci., **25**, 284 (1997).

[9] K.H. Schoenbach, S.J. Beebe, E.S. Buescher, "Intracellular Effect of Ultrashort Electrical Pulses", Bioelectromagnetics, **22**, 440 (2001).

[10] K.H. Schoenbach, S. Katsuki, R.H. Stark, E.S. Buescher, S.J. Beebe, "Bioelectrics – New Applications for Pulsed Power Technology", IEEE Transactions on Plasma Science, **30**, 293 (2002).

[11] S.J. Beebe, P.M. Fox, L.J. Rec, K. Somers, R.H. Stark, K.H. Schoenbach, "Nanosecond Pulsed Electric Field (nsPEF) Effects on Cells and Tissues: Apoptosis Induction and Tumor Growth Inhibition", IEEE Trans. Plas. Sci., **30**, 286 (2002).

[12] R.P. Joshi and K.H. Schoenbach, "Bioelectric Effects of Intense Ultrashort Pulses", Critical Reviews in Biomedical Engineering, **38**, 255 (2010).

[13] P.T. Vernier, Y. Sun, L. Marcu, C.M. Craft, and M.A. Gundersen, "Nanoelectropulse-induced phosphatidylserine translocation", Biophys. J., **86**, 4040 (2004).

[14] T.B. Napotnik, Y-H. Wu, M.A. Gundersen, D. Miklavcic, and P.T. Vernier, "Nanosecond Electric Pulses Cause Mitochondrial Membrane Permeabilization in Jurkat Cells", Bioelectromagnetics, **33**, 257 (2012).

[15] K. Morotomi-Yano, H. Akiyama, K. Yano, "Nanosecond pulsed electric fields activate MAPK pathways in human cells", Archives of Biochemistry and Biophysics, **515**, 99 (2011).

[16] P.T. Vernier, Y. Sun, L. Marcu, C.M. Craft, and M.A. Gundersen, "Nanosecond pulsed electric fields perturb membrane phospholipids in T lymphoblasts", FEBS Letters, **572**, 103 (2004).

[17] B. Alberts, A. Johnson, J. Lewis, M. Raff, K. Roberts, P. Walter, *Molecular Biology of THE CELL*, 5th Ed., (New York, Garland Science, Taylor & Francis Group, 2008) pp. 651-669.

[18] M. Laroussi, "Low-Temperature Plasmas for Medicine?", Trans. Plasma Sci., **37**, 714 (2009).
[19] R.A. Rhoades, D.R. Bell, *Medical Physiology: Principles for Clinical Medicine* 4th ed. (Baltimore, Williams & Wilkins, 2012), pp. 167-177.
[20] N.Y. Babaeva and M.J. Kushner, "Intracellular electric fields produced by dielectric barrier discharge treatment of skin", J. Phys. D: Appl. Phys., **43**, 185206 (2010).
[21] Y.A. Chizmadzhev, V.G. Zarnitsin, J.C. Weaver, and R.O. Potts, "Mechanism of electroinduced ionic species transport through a multilamellar lipid systems", Biophys. J., **68**, 749 (1995).
[22] Y. Feldman, I. Ermolina, and Y. Hayashi, "Time domain dielectric spectroscopy study of biological systems", IEEE Trans. Dielectr. Electr. Insul., **10**, 728 (2003).
[23] I. Ermolina, Y. Polevaya, Y. Feldman, B. Ginzburg, and M. Schlesinger, "Study of normal and malignant white blood cells by time domain dielectric spectroscopy", IEEE Trans. Dielectr. Electr. Insul., **8**, 253 (2001).
[24] S.A. Norberg, W. Tian, E. Johnsen, M.J. Kushner, "Atmospheric Pressure Plasma Jets Interacting with Liquid Covered Tissue: Touching and Not-touching the Liquid", J. Phys. D: Appl. Phys., **47**, 475203 (2014).

Chapter 7 Summary and Future Work

Atmospheric pressure plasma jets have been widely adopted for medical applications. This thesis focused on characterizing the dynamics of the discharge formation, the propagation of the ionization wave, the impact of the ionization wave upon multiple reactive and non-reactive surfaces, the formation of reactive oxygen and nitrogen species in both the gaseous and liquid regions, and finally the impact of the discharge created fields on cellular structure through a reactive liquid layer of varying thicknesses and conductivities. By using the 2-D hydrodynamic simulation platform, *nonPDPSIM*, more is understood about these devices and their interaction with medically relevant surfaces. Summary is discussed in Sec. 7.1 followed by future works in Sec. 7.2. The author's publication list and conference presentations are located in Sec. 7.3.

7.1 Summary

For this section, I will quickly summarize each chapter and synthesize the results discussed throughout this thesis. In Chapter 3, APPJ into humid air, production of RONS in an O_2 seeded He plasma jet flowing into atmospheric pressure humid air was discussed for different voltage, flow rate, repetition rate and O_2 admixture. Several trends emerged in the analysis of the development of RONS over 30 discharge pulses. The first was the importance of residence time on the reaction hierarchy. A second trend was that over a range of mole fractions, less oxygen in the initial mixture increases the inventory of RONS produced over 30 discharge pulses. A third trend was that although higher voltages do deposit more energy, a significant

effect of increasing voltage was that the faster, more intense ionization wave penetrates further into the plume. Lastly, the total elapsed time was important to accurately characterize the development of RONS. This chapter, as well as a large portion of Chapter 2, is the source of a publication accepted to Plasma Sources Science and Technology.

In Chapter 4, the topic of modeling the APPJ onto dielectric or metal surfaces was intended to be a bridge going from analysis of the effluent into the ambient air to analysis of plasma jet interaction with more medically relevant surfaces in subsequent chapters. This work was necessary as it served as a baseline for comparing the plasma jet interaction with various materials. By changing only the relative permittivity of the material targeted by the APPJ, significant effects on the dynamics of the discharge, production of charged and reactive species and the behavior of the electric field are realized. Increasing the permittivity increases the speed of the ionization wave to the surface, increases the electron density, and subsequent ion density. A lower permittivity allowed more penetration of the electric field into the material to nearly 1.5 times higher magnitudes beneath the surface. Analyzing the fall of the pulse revealed the development of the ion matrix electric field at the edge of the conductive channel as well as the presence of an electric field on the treated surface.

As Chapter 4 was written to be a bridge, many of the future work ideas were conducted in Chapters 5 and 6 with a reactive water layer covering tissue and cell structure. Chapter 4 is in preparation for submission and will be submitted shortly after the defense.

In Chapter 5, the APPJ interacted with a water layer covering tissue with the effect of the effluent touching or not-touching the water layer considered. One of the major distinctions in producing active aqueous species in water layers over tissues by plasma jets is whether the visible electron-ion plasma plume touches the surface of the water. This immediate proximity of

the plasma to the liquid enables photolysis, direct charge exchange reactions with H_2O_{aq}, and direct solvation of electrons. Not-touching plasmas do receive fluxes of gas phase ions in the form of an ion-ion plume; however these fluxes can be orders of magnitude smaller than in the touching cases. The convection and diffusion of neutral species to the liquid is also a source of predominantly neutral aqueous species. The formation of aqueous reactivity by neutral species is much less sensitive to touching or not-touching conditions as discussed in Chapter 5. The delivery of these neutral species to the water is more sensitive to fluid dynamics within the plasma region than for the ions. This chapter was published in Journal of Physics D: Applied Physics in 2014 and named a "Highlight Paper 2014" in the Low Temperature Plasma section.

In the last chapter, the APPJ interacted with a water layer covering tissue containing cell structure and the effect of the electric field onto the cells was analyzed. Certain results are clear, if the ionization wave does not touch the surface of the water layer, there is little chance of any electrical effect on the cell. Another clear result is the variability of the experimental conditions; if a displacement current is formed through the tissue to ground beneath the electric fields in the cells grow considerably. The short duration pulse and relatively high electric field promote the possibility of intracellular electromanipulation.

The coupling of electric fields, UV radiation, and the production of reactive and charged gas and aqueous species by the plasma jet are unique aspects of plasma medicine. Each has shown individually the ability to promote healing. The implications of this research culminate in the ability to control RONS production based on the desired end state of treatment. If a medical technician is treating a patient for vasodilation, a higher pulse repetition frequency with the plasma jet creating a conductive channel with the surface, regulated by a ballast resistor and temperature feedback control, will produce more NO and N_xO_y that are critical for treatment. If

hydrogen peroxide is desired, a low pulse repetition rate, low (0.1 or 0.2%) fraction of O_2, and water vapor naturally occurring or introduced above the treated surface are the optimum conditions. Plasma activated water could be used to "paint" a dry wound or flush a wet wound prior to treatment with a plasma jet to enhance production of critical aqueous species through the thin liquid layer. Flexibility of treatment and the ability to optimize one aspect to promote the desired effect (i.e. more electric fields, more H_2O_2, more NO, less O_3) will carry this emerging field from an interesting idea to a necessary tool for medical professionals.

As referenced in Chapter 1, Graves wrote in his 2014 tutorial review, "The use of near-room temperature ('cold') gas discharges at atmospheric pressure for various biomedical applications is now well established, although not well understood." The results of my efforts have contributed to the understanding of the plasma discharge dynamics, formation of RONS, effect of electric fields in general plasma jet scenarios as well as specific insight into the formation of aqueous RONS in liquid layers above tissue and electrical effects on cellular structure.

7.2 Future Work

Plasma medicine combines the effects of ultraviolet light, photons, RONS (gaseous and aqueous) in addition to the electric field considered in bioelectronics. As more experiments in this field are conducted, the theories produced may cause adjustments from those of bioelectronics. In order to do that, however, improvements to the model must be made. Parallelization of the code would provide tremendous flexibility for more detailed analysis on the cellular level as well as increasing the complexity of the system level analysis. Continued refinement to the reaction mechanisms for both gaseous and aqueous species is critical.

Opportunities to increase the accuracy are emerging as more experimentalists are investigating the plasma – liquid interface.

Future work possibilities are nearly limitless in this emerging field. New atmospheric pressure plasma jet configurations are being introduced routinely. Varying the diameter of the dielectric tube, grounding the ring electrode, changing the orientation of powered and ring electrodes, varying the pulse shape, varying the humidity in the ambient air, and changing the admixture composition beyond O_2 have all been recently attempted and would benefit from computational modeling. Modeling a positive pulse to include analyzing the rise and fall to and from the positive pulse from the negative would provide insights into guided positive ionization waves. Attempts to optimize production of individual reactive species are on-going through those means listed above as well as the use of shielding gases. Each of these aspects presents an opportunity for more validation opportunities and each would be better understood through the use of computational modeling.

In the context of the work discussed in this thesis, an obvious future work opportunity is increasing the accuracy of the multiple pulse prediction by updating the plasma source function every 5 – 10 pulses. One of the computational simplifications was importing a source function at prescribed pulse repetition frequency. However, the original discharge was created by the propagation of the ionization wave into a pristine environment. Modeling another pulse solving the plasma calculations after 5 – 10 pulses would increase the accuracy of the model. There has also been recent work charting the effects of the plasma discharge on the flow characteristics – triggering turbulent behavior earlier compared to the base helium jet flowing into the ambient. Modeling this would require including the plasma calculations with the cumulative effects of charged species momentum and gas heating over a much longer time than the 100 ns currently

modeled. This would greatly increase the computational demand and time required for completion of the submitted case.

Based on the inclusion of a treated surface, additional future works could including conductivity of treated materials, surface reactions (especially for treatment of polymers), the development of RONS after the conduction channel is established into the afterglow as well as the effect of multiple pulses for this baseline configuration. Multiple groups are interested in the production of OH from the water vapor above a wet surface. Including the recirculation of flow to increase the diffusion of air into the helium stream should increase the amount of aqueous RNS produced within the water layer. The production of plasma-activated-water (PAW) is another potential opportunity and subsequent pulsing of the cells immersed in PAW could then be modeled.

Future work possibilities with the cellular structure are limitless. Opening the field of bio-chemistry into the reaction mechanism is another possibility. In a more realistic scenario (for this author), analyzing a reactive path through the cells to study the communication through the membranes and into the underlying cell interior for liposomes, first, and then additional substances to mimic the behavior of enzymes and proteins in the cytoplasm. For a long time, atmospheric pressure plasma coupled physics in the understanding the plasma discharge dynamics and chemistry for production of reactive oxygen and nitrogen species. Now, the field of plasma medicine requires both physics and chemistry (in both gaseous and aqueous species) but also biology as we now need to move beyond viewing the components of the cell as dielectrics.

7.3 Publications

Research both presented in this thesis and conducted, but not included in this thesis, during the author's time at the University of Michigan has resulted in the following conference presentations and peer-reviewed journal articles. In the list of conferences, the presenter's name is underlined.

Refereed Journal Articles:

[1] Norberg, S., Johnsen, E., Kushner, M.J., "Helium atmospheric pressure plasma jets touching dielectric and metal surfaces", preparing for submission, 2015.

[2] Norberg, S., Johnsen, E., Kushner, M.J., "Formation of reactive oxygen and nitrogen species by repetitive negatively pulsed helium atmospheric pressure plasma jets propagating into humid air", Plasma Sources Sci. Technol. accepted, 2015.

[3] Schmidt-Bleker, A., Norberg, S., Winter, J., Johnsen, E., Reuter, S., Weltman, KD, Kusher, M.J., "Propagation mechanisms of guided streamers in plasma jets: the influence of electronegativity of the surrounding gas", Plasma Sources Sci. Technol. accepted, 2015.

[4] Norberg, S., Tian, W., Johnsen, E., Kushner, M.J., "Atmospheric pressure plasma jets interacting with liquid covered tissue: touching and not-touching the liquid", J. Phys. D: Appl. Phys. 47, 475203 (2014).

Conference Proceedings and Presentations:

[1] Norberg, S., Tian, W., Lietz, A., and Kushner, M.J., "Strategies for customizing reactive fluxes in plasma treatment of liquid covered tissue", 2nd International Workshop of Plasma for Cancer Treatment, Nagoya, Japan, 16-17 March 2015.

[2] Tian, W., Norberg, S., Lietz, A., Johnsen, E., Kushner, M.J., "Liquid transformed activation energy: how controlling plasma parameters translates to chemically active species in thin liquid layers", COST Action TD1208, Barcelona, Spain, 23-26 February 2015.

[3] Norberg, S., Tian, W., Johnsen, E., Kushner, M.J., "Variability in plasma activation of thin water layers by direct and remote plasma sources", 67th Gaseous Electronics Conference, Raleigh, NC, 3-7 November 2014.

[4] Norberg, S., Tian, W., Johnsen, E., Kushner, M.J., "Multiple pulses from plasma jets onto liquid covered tissue", 67th Annual Gaseous Electronics Conference, Raleigh, NC, 4 November 2014.

[5] Norberg, S., Johnsen, E., Kushner, M.J., "Plasma jet interactions with wet cells", Michigan Institute for Plasma Science and Engineering Symposium, Ann Arbor, MI, 8 October 2014 (poster).

[6] Norberg, S., Tian, W., Johnsen, E., Kushner, M.J., "Atmospheric pressure plasma jets contacting liquid layers", Gordon Research Seminar/Conference, North Smithfield, RI, 27 July 2014 (poster).

[7] Norberg, S., Tian, W., Johnsen, E., and Kushner, M.J., "Plasma-jets onto liquid surfaces: remote and touching configurations", 2014 ESCAMPIG XXII, Griefswald, Germany, 15-19 July 2014 (poster).

[8] Norberg, S., Tian, W., Johnsen, E., Kushner, M.J., "Controlling plasma jets with gas shields and their interactions with water covered tissue", 5th International Conference on Plasma Medicine, Nara, Japan, 20 May 2014.

[9] Tian, W., Norberg, S., Babaeva, N., and Kushner, M.J., "Progress and needs in modeling of plasma interactions with tissue", 5th International Conference on Plasma Medicine, Nara, Japan, May 2014

[10] Norberg, S., Tian, W., Kushner M., "Plasma Jet interactions with wet and dry tissue", International Workshop of Plasma for Cancer Treatment, Washington, DC, 25 March 2014, (poster).

[11] Norberg, S., Schmidt-Bleker, A., Winter, J., Reuter, S., Johnsen, E., Kushner, M., "Controlling reactive oxygen and nitrogen species production by atmospheric pressure plasma jets using gas shields", 66th Annual Gaseous Electronics Conference, Princeton, NJ, 30 September 2013.

[12] Norberg, S., Johnsen, E., Kushner, M., "Reactive oxygen and nitrogen species produced by repetitive pulses in atmospheric pressure plasma jets", IEEE Pulsed Power and Plasma Science Conference, San Francisco, CA, 17 June 2013.

[13] Norberg, S., Babaeva, N., Kushner, M., "Optimizing pulse waveforms in plasma jets for reactive oxygen species production", 65th Annual Gaseous Electronics Conference, Austin, TX, 22 October 2012.

APPENDIX I LIST OF REACTIONS

RXN NUM	Reaction[c,e,f,g,h,i]	A[a,j]	n	E	Ref.
	electron impact				
1	$e + He \rightarrow He + e$				b
2	$e + He \rightarrow He^* + e$				b
3	$e + He \rightarrow He^+ + e + e$				b
4	$e + He^* \rightarrow He^* + e$				b
5	$e + He^* \rightarrow He + e$				b
6	$e + He^* \rightarrow He^+ + e + e$				b
7	$e + N_2 \rightarrow N_2 + e$				b
8	$e + N_2 \rightarrow N_2(v) + e$				b
9	$e + N_2 \rightarrow N_2^* + e$				b
10	$e + N_2 \rightarrow N_2^{**} + e$				b
11	$e + N_2 \rightarrow N + N + e$				b
12	$e + N_2 \rightarrow N_2^+ + e + e$				b
13	$e + N_2(v) \rightarrow N_2(v) + e$				b
14	$e + N_2(v) \rightarrow N_2 + e$				b
15	$e + N_2(v) \rightarrow N_2^* + e$				b
16	$e + N_2(v) \rightarrow N_2^+ + e + e$				b
17	$e + N_2^* \rightarrow N_2^* + e$				b
18	$e + N_2^* \rightarrow N_2 + e$				b
19	$e + N_2^* \rightarrow N_2^+ + e + e$				b
20	$e + N_2^* \rightarrow N_2(v) + e$				b
21	$e + N_2^{**} \rightarrow N_2 + e$				b
22	$e + N \rightarrow N + e$				b
23	$e + N \rightarrow N^* + e$				b
24	$e + N \rightarrow N^* + e$				b
25	$e + N \rightarrow N^+ + e + e$				b
26	$e + N^* \rightarrow N^* + e$				b
27	$e + N^* \rightarrow N + e$				b
28	$e + N^* \rightarrow N^+ + e + e$				b
29	$e + O_2 \rightarrow O_2 + e$				b
30	$e + O_2 \rightarrow O^- + O$				b
31	$e + O_2 \rightarrow O_2^* + e$				b
32	$e + O_2 \rightarrow O_2^*1S + e$				b
33	$e + O_2 \rightarrow O + O + e$				b

34	$e + O_2 \rightarrow O^* + O + e$				b
35	$e + O_2 \rightarrow O_2^+ + e + e$				b
36	$e + O_2 \rightarrow O + O^+ + e + e$				b
37	$e + O_2^*1S \rightarrow O_2^*1S + e$				b
38	$e + O_2^*1S \rightarrow O^- + O$				b
39	$e + O_2^*1S \rightarrow O_2^* + e$				b
40	$e + O_2^*1S \rightarrow O_2 + e$				b
41	$e + O_2^*1S \rightarrow O + O + e$				b
42	$e + O_2^*1S \rightarrow O^* + O + e$				b
43	$e + O_2^*1S \rightarrow O_2^+ + e + e$				b
44	$e + O_2^*1S \rightarrow O + O^+ + e + e$				b
45	$e + O_2^* \rightarrow O_2^* + e$				b
46	$e + O_2^* \rightarrow O^- + O$				b
47	$e + O_2^* \rightarrow O_2^*1S + e$				b
48	$e + O_2^* \rightarrow O_2 + e$				b
49	$e + O_2^* \rightarrow O + O + e$				b
50	$e + O_2^* \rightarrow O^* + O + e$				b
51	$e + O_2^* \rightarrow O_2^+ + e + e$				b
52	$e + O_2^* \rightarrow O + O^+ + e + e$				b
53	$e + O \rightarrow O + e$				b
54	$e + O \rightarrow O^* + e$				b
55	$e + O \rightarrow O^* + e$				b
56	$e + O \rightarrow O^+ + e + e$				b
57	$e + O^* \rightarrow O^* + e$				b
58	$e + O^* \rightarrow O + e$				b
59	$e + O^* \rightarrow O^+ + e + e$				b
60	$e + O_3 \rightarrow O^- + O_2$				b
61	$e + O_3 \rightarrow O_2^- + O$				b
62	$e + H_2O \rightarrow H_2O + e$				b
63	$e + H_2O \rightarrow O^- + H_2$				b
64	$e + H_2O \rightarrow OH^- + H$				b
65	$e + H_2O \rightarrow H + OH + e$				b
66	$e + H_2O \rightarrow O + H + H + e$				b
67	$e + H_2O \rightarrow H_2O^+ + e + e$				b
68	$e + H_2O \rightarrow H^+ + OH + e + e$				b
69	$e + H_2 \rightarrow H + H + e$				b
70	$e + H_2 \rightarrow H + H + e$				b
71	$e + NO \rightarrow NO^+ + e + e$				b
72	$e + He^+ \rightarrow He23S$	6.76×10^{-12}	-0.5	0	[1]
73	$e + e + He^+ \rightarrow He23S + e$	2.69×10^{-26}	-4	0	[2,3]
74	$e + e + He_2^+ \rightarrow He23S + He + e$	4.50×10^{-27}	-4	0	[2,3]
75	$e + e + He_2^+ \rightarrow He_2^* + e$	1.35×10^{-26}	-4	0	[2,3]
76	$e + He_2^+ \rightarrow He23S + He$	1.60×10^{-9}	-0.5	0	[4]

77	$e + N_2^+ \rightarrow N^* + N$	2.00×10^{-7}	-0.5	0		[5,6]
78	$e + N_4^+ \rightarrow N_2 + N_2$	2.00×10^{-7}	-0.5	0		[5]
79	$e + O^+ \rightarrow O^*$	5.30×10^{-12}	-0.5	0		[7,8]
80	$e + e + O^+ \rightarrow O^* + e$	5.12×10^{-27}	-4.5	0		[7,8]
81	$e + O_2^+ \rightarrow O + O$	1.20×10^{-8}	-0.7	0		[7,9]
82	$e + O_2^+ \rightarrow O^* + O$	8.88×10^{-9}	-0.7	0		[7,9]
83	$e + H_2O^+ \rightarrow OH + H$	6.60×10^{-6}	-0.5	0		[5,10]
84	$e + H_2O^+ \rightarrow O + H + H$	2.88×10^{-6}	-0.5	0		[5,10]
85	$e + H_2O^+ \rightarrow O + H_2$	2.52×10^{-6}	-0.5	0		[5,10]
86	$e + H_3O^+ \rightarrow H_2O + H$	2.00×10^{-7}	-0.5	0		[5,10]
87	$e + H_5O_2^+ \rightarrow H_2O + H_2O + H$	2.00×10^{-7}	-0.5	0	d	[5]
88	$e + NO^+ \rightarrow N + O$	2.00×10^{-7}	-0.5	0	d	[5]
	electron ion three-body recombination					
89	$e + He^+ + M \rightarrow He^* + M$	1.20×10^{-33}	-4	0		[1]
90	$e + He_2^+ + M \rightarrow He^* + He + M$	1.30×10^{-28}	-1	0		[3]
91	$e + O_2 + M \rightarrow O_2^- + M$	2.00×10^{-31}	-1	0		[5,11,12,60]
92	$e + O_2^* + M \rightarrow O_2^- + M$	1.00×10^{-29}	0	0	d	[12,13]
93	$e + NO^+ + M \rightarrow NO + M$	3.12×10^{-23}	-1.5	0		[14]
	Reactions with He					
94	$He^* + He^* \rightarrow He^+ + He + e$	4.50×10^{-10}	0.5	0		[2,3]
95	$He^* + He^* \rightarrow He_2^+ + e$	1.05×10^{-9}	0.5	0		[2,3]
96	$He^* + He_2^* \rightarrow He^+ + He + He + e$	2.25×10^{-11}	0.5	0		[3]
97	$He^* + He_2^* \rightarrow He_2^+ + He + e$	1.28×10^{-10}	0.5	0		[2,3]
98	$He^+ + He + M \rightarrow He_2^+ + M$	1.10×10^{-31}	-0.38	0		[15]
99	$He^* + He + M \rightarrow He_2^* + M$	2.00×10^{-34}	0	0		[3,16]
100	$He(2^3S) + He(2^3S) \rightarrow He + He^+ + e$	1.50×10^{-9}	0.5	0		[3,2]
101	$He(2^3S) + O_2 \rightarrow O_2^+ + He + e$	2.54×10^{-10}	0.5	0		[3,17]
102	$He(2^3S) + O_3 \rightarrow O_2^+ + O + He + e$	2.54×10^{-10}	0.5	0		[3,17]
103	$He(2^3S) + O_2^*1S \rightarrow O_2^+ + He + e$	2.54×10^{-10}	0.5	0		[3,17]
104	$He_2^* + He_2^* \rightarrow He^+ + He + He + He + e$	2.25×10^{-11}	0.5	0		[2,3]
105	$He_2^* + He_2^* \rightarrow He_2^+ + He + He + e$	1.28×10^{-10}	0.5	0		[2]
106	$e + He_2^* \rightarrow He + He + e$	1.00×10^{-7}	0	0	d	[5]
	Ion-ion neutralization					
107	$O^- + N_2^+ \rightarrow N_2 + O$	3.00×10^{-6}	0	0		[5]
108	$O^- + N^+ \rightarrow N + O$	3.00×10^{-6}	0	0	d	[5]
109	$O^- + N_4^+ \rightarrow N_2 + N_2 + O$	3.00×10^{-6}	0	0	d	[5]
110	$O^- + O_2^+ \rightarrow O_2 + O$	3.00×10^{-6}	0	0		[5,19]
111	$O^- + O^+ \rightarrow O + O$	3.00×10^{-6}	0	0	d	[5]
112	$O^- + H_2O^+ \rightarrow H_2O + O$	3.00×10^{-6}	0	0		[5,19]
113	$O^- + NO^+ \rightarrow NO + O$	3.00×10^{-6}	0	0		[5]
114	$O^- + He^+ \rightarrow O + He$	2.00×10^{-7}	-1	0		[7,18,61]
115	$O^- + He_2^+ \rightarrow O + He + He$	3.00×10^{-6}	0	0	d	[12,14,60]
116	$O^- + H_3O^+ \rightarrow O + H_2O + H$	1.00×10^{-7}	0	0		[14]

117	$O^- + H_5O_2^+ \rightarrow O + H_2O + H_2O + H$	2.00×10^{-6}	0	0	d	[12,14,60]
118	$O^- + O_2^+ \rightarrow O + O + O$	1.00×10^{-7}	0	0		[14,12]
119	$O^- + N^+ \rightarrow O + N$	2.00×10^{-7}	-0.5	0		[14,20]
120	$O^- + N_2^+ \rightarrow O + N + N$	1.00×10^{-7}	0	0		[14,12]
121	$O^- + NO^+ \rightarrow O + N + O$	1.00×10^{-7}	0	0		[14,12]
122	$O^- + NO^+ \rightarrow O + NO$	2.00×10^{-7}	-0.5	0		[14,20]
123	$O^- + H^+ \rightarrow H + O$	2.00×10^{-7}	-0.5	0		[14]
124	$O^- + H_2O^+ \rightarrow O + OH + H$	1.00×10^{-7}	0	0		[14]
125	$O^- + NO^+ + M \rightarrow O + NO + M$	2.00×10^{-25}	-2.5	0		[13,12]
126	$O^- + NO^+ + M \rightarrow NO_2 + M$	2.00×10^{-25}	-2.5	0		[13,12,21]
127	$O^- + O^+ + M \rightarrow O_2 + M$	1.20×10^{-25}	0	0		[5]
128	$O^- + N^+ + M \rightarrow NO + M$	1.20×10^{-25}	0	0		[5]
129	$O^- + He^+ + M \rightarrow O + He + M$	2.00×10^{-25}	-2.5	0		[19]
130	$O^- + O_2^+ + M \rightarrow O + O_2 + M$	2.00×10^{-25}	-2.5	0		[19]
131	$O_2^- + N_2^+ \rightarrow N_2 + O_2$	2.00×10^{-6}	0	0		[5,11]
132	$O_2^- + N^+ \rightarrow N + O_2$	2.00×10^{-6}	0	0		[5,19]
133	$O_2^- + N_4^+ \rightarrow N_2 + N_2 + O_2$	2.00×10^{-6}	0	0		[5]
134	$O_2^- + O_2^+ \rightarrow O_2 + O_2$	2.00×10^{-6}	0	0		[5,19]
135	$O_2^- + O^+ \rightarrow O + O_2$	2.00×10^{-6}	0	0		[5,19]
136	$O_2^- + H_2O^+ \rightarrow H_2O + O_2$	2.00×10^{-6}	0	0		[5,19]
137	$O_2^- + NO^+ \rightarrow O_2 + NO$	2.00×10^{-6}	0	0		[5,19]
138	$O_2^- + He^+ \rightarrow O_2 + He$	2.00×10^{-7}	-1	0		[18]
139	$O_2^- + He_2^+ \rightarrow O_2 + He + He$	2.00×10^{-6}	0	0	d	[12,14,60]
140	$O_2^- + H_3O^+ \rightarrow O_2 + H_2O + H$	1.00×10^{-7}	0	0		[14]
141	$O_2^- + H_5O_2^+ \rightarrow O_2 + H_2O + H_2O + H$	2.00×10^{-6}	0	0	d	[12,14,60]
142	$O_2^- + O_2^+ \rightarrow O_2 + O + O$	1.00×10^{-7}	0	0		[14,22]
143	$O_2^- + N^+ \rightarrow O_2 + N$	2.00×10^{-7}	-0.5	0		[14,20]
144	$O_2^- + N_2^+ \rightarrow O_2 + N + N$	1.00×10^{-7}	0	0		[14,12]
145	$O_2^- + NO^+ \rightarrow O_2 + N + O$	1.00×10^{-7}	0	0		[14,22]
146	$O_2^- + NO^+ \rightarrow O_2 + NO$	2.00×10^{-7}	-0.5	0		[14,22]
147	$O_2^- + H^+ \rightarrow H + O_2$	2.00×10^{-7}	-0.5	0		[14]
148	$O_2^- + H_2O^+ \rightarrow O_2 + OH + H$	1.00×10^{-7}	0	0		[14]
149	$O_2^- + NO^+ \rightarrow N + O + O + O$	1.00×10^{-7}	0	0		[12,13]
150	$O_2^- + NO^+ + M \rightarrow NO_3 + M$	2.00×10^{-25}	-2.5	0		[12,13]
151	$O_2^- + NO^+ + M \rightarrow O_2 + NO + M$	2.00×10^{-25}	-2.5	0		[12,13,21]
152	$OH^- + O^+ \rightarrow O + OH$	2.00×10^{-7}	-0.5	0		[14]
153	$OH^- + O_2^+ \rightarrow OH + O_2$	2.00×10^{-7}	-0.5	0		[14]
154	$OH^- + O_2^+ \rightarrow OH + O + O$	1.00×10^{-7}	0	0		[14]
155	$OH^- + N_2^+ \rightarrow OH + N_2$	2.00×10^{-7}	-0.5	0		[14]
156	$OH^- + N_2^+ \rightarrow OH + N + N$	1.00×10^{-7}	0	0		[12,14]
157	$OH^- + NO^+ \rightarrow OH + N + O$	1.00×10^{-7}	0	0		[14]
158	$OH^- + NO^+ \rightarrow OH + NO$	2.00×10^{-7}	-0.5	0		[14]
159	$OH^- + H^+ \rightarrow H + OH$	2.00×10^{-7}	-0.5	0		[14]

160	$OH^- + H_2O^+ \rightarrow H_2O + OH$	2.00×10^{-7}	-0.5	0		[14]
161	$OH^- + H_2O^+ \rightarrow OH + OH + H$	1.00×10^{-7}	0	0		[14]
162	$OH^- + H_3O^+ \rightarrow OH + H_2O + H$	1.00×10^{-7}	0	0		[14]
163	$OH^- + N^+ \rightarrow OH + N$	2.00×10^{-7}	-0.5	0	d	[14]
164	$OH^- + N_4^+ \rightarrow N_2 + N_2 + OH$	2.00×10^{-7}	-0.5	0	d	[14]
165	$OH^- + He^+ \rightarrow OH + He$	2.00×10^{-7}	-1	0	d	[12,14,60]
166	$OH^- + He_2^+ \rightarrow OH + He + He$	3.00×10^{-6}	0	0	d	[12,14,60]
167	$OH^- + H_5O_2^+ \rightarrow OH + H_2O + H_2O + H$	2.00×10^{-6}	0	0	d	[12,14,60]
168	$OH^- + NO^+ + M \rightarrow OH + NO + M$	2.00×10^{-25}	-2.5	0		[12,13]
169	$OH^- + NO^+ + M \rightarrow HNO_2 + M$	2.00×10^{-25}	-2.5	0		[12,13]
	ion molecule reactions					
170	$O^- + O_2 \rightarrow O_2^- + O$	1.50×10^{-20}	0	0	d	[13,23]
171	$O^- + O_2^*1S \rightarrow O + O_2 + e$	6.90×10^{-10}	0.5	0		[7]
172	$O^- + O \rightarrow O_2 + e$	1.90×10^{-10}	0	0		[7,24]
173	$O^- + O_3 \rightarrow O_2 + O_2 + e$	3.01×10^{-10}	0.5	0		[7,24]
174	$O^- + O_3 \rightarrow O_2^- + O_2$	1.02×10^{-11}	0.5	0		[7,24]
175	$O_2^- + O \rightarrow O_3 + e$	1.50×10^{-10}	0	0		[14,22]
176	$O_2^- + O \rightarrow O^- + O_2$	3.30×10^{-10}	0	0		[14,22]
177	$O_2^- + O_2^* \rightarrow e + O_2 + O_2$	2.00×10^{-10}	0	0		[14,22]
178	$N_2^+ + O_2 \rightarrow NO + NO^+$	1.00×10^{-17}	0	0		[13,25,26]
179	$O_2^+ + N_2 \rightarrow NO + NO^+$	1.00×10^{-17}	0	0		[13,12,27]
180	$O^- + N \rightarrow NO + e$	2.60×10^{-10}	0	0	d	[14,22]
181	$O^- + N_2^* \rightarrow N_2 + O + e$	1.90×10^{-9}	0	0		[14,22]
182	$O^- + O_2 \rightarrow O_3 + e$	1.00×10^{-12}	0	0		[14,28]
183	$O^- + O_2^* \rightarrow O_3 + e$	3.00×10^{-10}	0	0		[14,22]
184	$O^- + O_3 \rightarrow O_2 + O_2 + e$	3.00×10^{-10}	0	0		[14,22]
185	$O^- + NO \rightarrow NO_2 + e$	2.60×10^{-10}	0	0		[14,22]
186	$O^- + H_2 \rightarrow H_2O + e$	7.00×10^{-10}	0	0		[14,22]
187	$O^- + O_2^* \rightarrow O_2^- + O$	1.00×10^{-10}	0	0		[14,22]
188	$O^- + H_2 \rightarrow OH^- + H$	3.30×10^{-11}	0	0		[14,22]
189	$O^- + H_2O \rightarrow OH^- + OH$	1.40×10^{-9}	0	0		[14,22]
190	$O_2^- + N_2 \rightarrow N_2 + O_2 + e$	1.90×10^{-12}	0.5	4990		[14,22]
191	$O_2^- + N \rightarrow NO_2 + e$	5.00×10^{-10}	0	0		[14,22]
192	$O_2^- + N_2^* \rightarrow N_2 + O_2 + e$	2.10×10^{-9}	0	0		[14,22]
193	$O_2^- + O_2 \rightarrow O_2 + O_2 + e$	2.70×10^{-10}	0.5	5590		[14,22]
194	$O_2^- + O_3 \rightarrow O_3 + O_2 + e$	6.00×10^{-10}	0	0		[14,28]
195	$O_2^- + H \rightarrow HO_2 + e$	1.40×10^{-9}	0	0		[14,19]
196	$OH^- + O \rightarrow HO_2 + e$	2.00×10^{-10}	0	0		[14,19]
197	$OH^- + H \rightarrow H_2O + e$	1.80×10^{-9}	0	0		[14,22]
198	$N^+ + O_2 \rightarrow NO^+ + O$	2.70×10^{-10}	0	0		[14,29]
199	$N^+ + O_2 \rightarrow O^+ + NO$	3.60×10^{-11}	0	0		[5,11]
200	$N^+ + O_2 \rightarrow O_2^+ + N$	3.10×10^{-10}	0	0		[5,11]
201	$N^+ + H_2O \rightarrow H_2O^+ + N$	1.19×10^{-9}	0	0		[14,30]

202	$N^+ + H_2O \rightarrow NO^+ + H_2$	2.10×10^{-10}	0	0		[14,30]
203	$N^+ + NO \rightarrow NO^+ + N$	9.00×10^{-10}	0	0		[5,11]
204	$N_2^+ + O \rightarrow NO^+ + N$	1.40×10^{-10}	0	0		[14,20]
205	$N_2^+ + O \rightarrow NO^+ + N^*$	1.80×10^{-10}	-1	0		[14,20]
206	$N_2^+ + N_2 + M \rightarrow N_4^+ + M$	6.80×10^{-29}	-1.64	0		[13,31,32]
207	$O^+ + N + M \rightarrow NO^+ + M$	1.00×10^{-29}	0	0		[14,22]
208	$O^+ + N_2 + M \rightarrow NO^+ + N + M$	1.00×10^{-29}	0	0		[14,22]
209	$O^+ + O + M \rightarrow O_2^+ + M$	1.00×10^{-29}	0	0		[14,22]
210	$O^+ + O_2 \rightarrow O_2^+ + O$	2.10×10^{-11}	-0.5	0		[14,22]
211	$O^+ + O_3 \rightarrow O_2^+ + O_2$	1.00×10^{-10}	0	0		[14,20]
212	$O^+ + N^* \rightarrow N^+ + O$	1.30×10^{-10}	0	0		[14,22]
213	$O^+ + H_2O \rightarrow H_2O^+ + O$	3.20×10^{-9}	0	0		[14,22]
214	$O^+ + NO \rightarrow NO^+ + O$	1.70×10^{-12}	0	0		[5,11]
215	$O_2^+ + N \rightarrow NO^+ + O$	1.50×10^{-10}	0	0		[14,33]
216	$O_2^+ + NO \rightarrow NO^+ + O_2$	4.60×10^{-10}	0	0		[5,11]
217	$H^+ + O \rightarrow O^+ + H$	3.80×10^{-10}	0	0		[14,22]
218	$H^+ + O_2 \rightarrow O_2^+ + H$	1.17×10^{-9}	0	0		[14,33]
219	$H^+ + NO \rightarrow NO^+ + H$	1.90×10^{-9}	0	0		[14,22]
220	$H^+ + H_2O \rightarrow H_2O^+ + H$	8.20×10^{-9}	0	0		[14,33]
221	$H_2O^+ + N \rightarrow NO^+ + H_2$	1.90×10^{-10}	0	0		[14,33]
222	$H_2O^+ + O \rightarrow O_2^+ + H_2$	5.50×10^{-11}	0	0		[14,26]
223	$H_2O^+ + H_2 \rightarrow H_3O^+ + H$	7.60×10^{-10}	0	0		[14,33]
224	$OH^- + O \rightarrow HO_2 + e$	4.00×10^{-10}	0	0		[13,21]
225	$H^+ + H_2O \rightarrow H_3O^+$	5.00×10^{-10}	0	0	d	[60]
226	$H_2O^+ + H_2O \rightarrow H_3O^+ + OH$	1.70×10^{-9}	0	0		[14,22]
227	$H_3O^+ + H_2O \rightarrow H_5O_2^+$	5.00×10^{-10}	0	0	d	[13,29,12]
	charge exchange					
229	$He^+ + N \rightarrow He + N^+$	1.60×10^{-9}	0	0	d	[7]
230	$He^+ + O \rightarrow O^+ + He$	3.30×10^{-11}	0.5	0	d	[7,60]
231	$He^+ + H \rightarrow H^+ + He$	5.00×10^{-10}	0	0	d	[7]
232	$He_2^+ + N \rightarrow N^+ + He + He$	1.20×10^{-9}	0	0	d	[7]
233	$He_2^+ + O \rightarrow O^+ + He + He$	1.00×10^{-9}	0	0		[60]
234	$He_2^+ + H \rightarrow H^+ + He + He$	2.00×10^{-9}	0	0	d	[7]
235	$N^+ + O_2 \rightarrow O_2^+ + N$	3.10×10^{-10}	0	0		[5,11]
236	$N^+ + O \rightarrow O^+ + N$	1.00×10^{-12}	0	0		[13,12,19]
237	$N^+ + N \rightarrow N + N^+$	1.00×10^{-12}	0	0		[13]
238	$N_2^+ + N \rightarrow N^+ + N_2$	5.00×10^{-12}	0	0	d	[13]
239	$N_2^+ + N^* \rightarrow N^+ + N_2$	1.00×10^{-10}	0	0		[13,34]
240	$N_2^+ + O_2 \rightarrow O_2^+ + N_2$	5.10×10^{-11}	0	0		[5,11]
241	$N_4^+ + O_2 \rightarrow O_2^+ + N_2 + N_2$	2.40×10^{-10}	0	0		[14,29]
242	$N_2^+ + NO \rightarrow NO^+ + N_2$	3.90×10^{-10}	0	0		[14,29]
243	$N_2^+ + O \rightarrow O^+ + N_2$	1.00×10^{-11}	-0.5	0		[14,22]
244	$N_2^+ + H_2O \rightarrow H_2O^+ + N_2$	2.30×10^{-9}	0	0		[14,22]

245	$N_4^+ + N_2 \rightarrow N_2^+ + N_2 + N_2$	2.10×10^{-10}	0	-121		[14,22]
246	$N_4^+ + N \rightarrow N^+ + N_2 + N_2$	1.00×10^{-11}	0	0		[14,22]
247	$N_4^+ + NO \rightarrow NO^+ + N_2 + N_2$	3.90×10^{-10}	0	0		[14,29]
248	$N_4^+ + H_2O \rightarrow H_2O^+ + N_2 + N_2$	3.00×10^{-9}	0	0		[14,22]
249	$N_4^+ + O \rightarrow O^+ + N_2 + N_2$	2.50×10^{-10}	0	0		[14,22]
250	$H_2O^+ + O_2 \rightarrow O_2^+ + H_2O$	4.30×10^{-10}	0	0		[14,22]
251	$H_2O^+ + NO \rightarrow NO^+ + H_2O$	4.60×10^{-10}	0	0		[14,29]
252	$O^+ + O_2 \rightarrow O_2^+ + O$	1.90×10^{-11}	0	0		[5,11]
253	$O^+ + O \rightarrow O + O^+$	1.00×10^{-12}	0	0		[7]
254	$O_2^+ + O_2 \rightarrow O_2 + O_2^+$	1.00×10^{-9}	0.5	0		[7,35]
255	$He^+ + N_2 \rightarrow N_2^+ + He$	1.30×10^{-9}	0	0		[24]
256	$He^+ + O_2 \rightarrow O_2^+ + He$	3.30×10^{-11}	0.5	0		[7,24]
257	$He^+ + O_2^* \rightarrow O_2^+ + He$	3.30×10^{-11}	0.5	0		[7]
258	$He^+ + H_2O \rightarrow H_2O^+ + He$	5.00×10^{-10}	0	0		[24]
259	$He^+ + NO \rightarrow NO^+ + He$	1.60×10^{-9}	0	0		[24]
260	$He^+ + He \rightarrow He + He^+$	1.00×10^{-9}	0.5	0		[7,35]
261	$He_2^+ + N_2 \rightarrow N_2^+ + He + He$	1.20×10^{-9}	0	0		[24]
262	$He_2^+ + O_2 \rightarrow O_2^+ + He + He$	1.00×10^{-9}	0	0		[24]
263	$He_2^+ + H_2O \rightarrow H_2O^+ + He + He$	2.00×10^{-9}	0	0	d	[7,24]
264	$He_2^+ + NO \rightarrow NO^+ + He + He$	1.30×10^{-9}	0	0		[24]
	Penning					
265	$He^* + N \rightarrow He + N^+ + e$	1.50×10^{-10}	0	0	d	[2]
266	$He^* + O \rightarrow He + O^+ + e$	1.50×10^{-10}	0	0	d	[2]
267	$He^* + H \rightarrow He + H^+ + e$	1.50×10^{-10}	0	0	d	[2]
268	$He^* + NO \rightarrow He + NO^+ + e$	1.50×10^{-10}	0	0	d	[2]
269	$He^* + N_2 \rightarrow He + N_2^+ + e$	1.50×10^{-10}	0	0	d	[2]
270	$He^* + O_2 \rightarrow He + O_2^+ + e$	1.50×10^{-10}	0	0	d	[2]
271	$He^* + H_2O \rightarrow He + H_2O^+ + e$	1.50×10^{-10}	0	0	d	[2]
272	$He_2^* + N \rightarrow He + He + N^+ + e$	1.50×10^{-10}	0	0	d	[2]
273	$He_2^* + O \rightarrow He + He + O^+ + e$	1.50×10^{-10}	0	0	d	[2]
274	$He_2^* + H \rightarrow He + He + H^+ + e$	1.50×10^{-10}	0	0	d	[2]
275	$He_2^* + NO \rightarrow He + He + NO^+ + e$	1.50×10^{-10}	0	0	d	[2]
276	$He_2^* + O_2 \rightarrow He + He + O_2^+ + e$	1.50×10^{-10}	0	0	d	[2]
277	$He_2^* + N_2 \rightarrow He + He + N_2^+ + e$	1.50×10^{-10}	0	0	d	[2]
278	$He_2^* + H_2O \rightarrow He + He + H_2O^+ + e$	1.50×10^{-10}	0	0	d	[2]
	Quenching					
279	$O^* + O_3 \rightarrow O_2 + O + O$	1.20×10^{-10}	0	0		[3,7]
280	$O^* + O_3 \rightarrow O_2 + O_2$	5.04×10^{-10}	0	0		[3,7]
281	$O^* + O_2^* \rightarrow O + O_2$	1.00×10^{-11}	0	0		[36]
282	$O^* + O \rightarrow O + O$	1.00×10^{-11}	0	0	d	[7,9]
283	$O^* + N_2 \rightarrow O + N_2$	1.80×10^{-11}	0	-107		[5]
284	$O^* + O_2 \rightarrow O + O_2$	3.80×10^{-11}	0	0		[5,11]
285	$O^* + H_2O \rightarrow OH + OH$	2.00×10^{-10}	0	0		[5,11]

286	$O^* + H_2O \rightarrow O + H_2O$	1.20×10^{-11}	0	0		[5,11]
287	$O^* + H_2O \rightarrow H_2 + O_2$	2.30×10^{-12}	0	0		[5]
288	$O^* + NO \rightarrow O_2 + N$	8.50×10^{-11}	0	0		[5]
289	$O^* + NO_2 \rightarrow O_2 + NO$	1.40×10^{-10}	0	0		[14]
290	$O_2^*1S + O_2^*1S \rightarrow O_2^* + O_2$	3.60×10^{-17}	0.5	0		[3,7]
291	$O_2^*1S + O_2 \rightarrow O_2^* + O_2$	3.60×10^{-17}	0.5	0		[3,7]
292	$O_2^*1S + O_2 \rightarrow O_2 + O_2$	4.00×10^{-18}	0.5	0		[3,7]
293	$O_2^*1S + O \rightarrow O_2^* + O$	7.20×10^{-14}	0.5	0		[3,7]
294	$O_2^*1S + O \rightarrow O_2 + O$	8.00×10^{-15}	0.5	0		[3,7]
295	$O_2^*1S + O_3 \rightarrow O + O_2 + O_2$	7.33×10^{-12}	0.5	0		[3,7]
296	$O_2^*1S + O_3 \rightarrow O_2^* + O_3$	7.33×10^{-12}	0.5	0		[3,7]
297	$O_2^*1S + O_3 \rightarrow O_2 + O_3$	7.33×10^{-12}	0.5	0		[3,7]
298	$O_2^*1S + He \rightarrow O_2^* + He$	1.00×10^{-17}	0.5	0		[3,7]
299	$O_2^* + O_2 \rightarrow O_2 + O_2$	2.20×10^{-18}	0	0		[36]
300	$O_2^* + O_2^* \rightarrow O_2^*1S + O_2$	9.00×10^{-17}	0	560		[3,7]
301	$O_2^* + O_2 \rightarrow O + O_3$	2.95×10^{-21}	0	0		[36]
302	$O_2^* + O_3 \rightarrow O_2 + O_2 + O$	9.96×10^{-11}	0	3050	d	[7,37]
303	$O_2^* + He \rightarrow O_2 + He$	8.00×10^{-21}	0.5	0		[36]
304	$N^* + N_2 \rightarrow N + N_2$	2.40×10^{-14}	0	0		[5,11]
305	$N_2^* + N_2 \rightarrow N_2 + N_2$	1.90×10^{-12}	0	0		[5,38]
306	$N_2^* + O_2 \rightarrow O + O + N_2$	1.50×10^{-12}	0	0		[5,38,56]
307	$N_2^* + O_2 \rightarrow O_2 + N_2$	2.80×10^{-11}	0	0		[5,38]
308	$N_2^* + NO_2 \rightarrow NO + O + N_2$	1.00×10^{-12}	0	0		[5,38]
309	$N_2^* + H_2 \rightarrow N_2 + H_2$	2.60×10^{-11}	0	0		[5,38]
310	$N_2(v) + N_2 \rightarrow N_2 + N_2$	1.00×10^{-15}	0	0	d	[21]
311	$N_2(v) + N \rightarrow N_2 + N$	1.00×10^{-16}	0	0	d	[21]
312	$N_2(v) + O_2 \rightarrow N_2 + O_2$	1.00×10^{-15}	0	0	d	[21]
313	$N_2(v) + O \rightarrow N_2 + O$	1.00×10^{-16}	0	0	d	[21]
314	$N_2(v) + H_2O \rightarrow N_2 + H_2O$	1.00×10^{-15}	0	0	d	[21]
	Three-body neutral recombination					
315	$O + O_2 + M \rightarrow O_3 + M$	3.40×10^{-34}	-1.2	0		[36]
316	$O + O + M \rightarrow O_2 + M$	1.18×10^{-33}	0	0		[19,36]
317	$O + O + M \rightarrow O_2^* + M$	9.88×10^{-35}	0	0		[19,36]
318	$N + N + M \rightarrow N_2 + M$	3.90×10^{-33}	0	0	d	[21]
319	$N + O + M \rightarrow NO + M$	5.46×10^{-33}	0	-155		[36]
320	$NO + O + M \rightarrow NO_2 + M$	1.00×10^{-31}	-1.6	0		[36]
321	$NO + O + O_2^* \rightarrow NO_2 + O_2^*$	1.00×10^{-31}	-1.6	0		[36]
322	$NO + O + O_3 \rightarrow NO_2 + O_3$	1.00×10^{-31}	-1.6	0		[36]
323	$NO + O + O \rightarrow NO_2 + O$	1.00×10^{-31}	-1.6	0		[36]
	Higher temperature critical reactions					
324	$O + O_3 \rightarrow O_2 + O_2$	8.00×10^{-12}	0	2060		[5,39]
325	$O_3 + M \rightarrow O_2 + O + M$	1.56×10^{-9}	0	11490		[7,40]
326	$N_2 + M \rightarrow N + N + M$	4.29×10^{-10}	0	86460	d	[36]

327	$O_2 + M \rightarrow O + O + M$	5.17×10^{-10}	0	58410	d	[36]
	NO and N_xO_y reactions					
328	$N + O_2 \rightarrow NO + O$	4.40×10^{-12}	1	3270		[36]
329	$N + O_3 \rightarrow NO + O_2$	5.00×10^{-16}	0	0		[36]
330	$N + NO_2 \rightarrow NO + NO$	1.33×10^{-12}	0	-220		[13]
331	$N + OH \rightarrow NO + H$	4.70×10^{-11}	0	0		[36]
332	$NO + O_3 \rightarrow O_2 + NO_2$	1.40×10^{-12}	0	1310		[36]
333	$NO + O_2^* \rightarrow O_2 + NO$	3.50×10^{-17}	0	0		[36]
334	$NO + O_2^* \rightarrow O + NO_2$	4.88×10^{-18}	0	0		[36]
335	$N^* + O_2 \rightarrow NO + O$	1.22×10^{-11}	0	317		[36]
336	$N^* + O_2 \rightarrow NO + O^*$	6.00×10^{-12}	0.5	0		[14,12]
337	$N^* + NO \rightarrow N_2 + O$	6.30×10^{-11}	0	0		[5,11]
338	$N^* + NO_2 \rightarrow NO + NO$	1.50×10^{-12}	0	0		[5,11]
339	$N_2^{**} + O \rightarrow NO + N$	5.00×10^{-10}	0	0		[41]
340	$N_2^* + O \rightarrow NO + N$	5.00×10^{-10}	0	0		[41]
341	$O + N_2^* \rightarrow NO + N^*$	1.00×10^{-12}	0	0		[13]
342	$O + NO_2 \rightarrow NO + O_2$	6.50×10^{-12}	0	-120		[13,42,43]
343	$O + NO_3 \rightarrow O_2 + NO_2$	1.00×10^{-11}	0	0		[5,11]
344	$O^* + NO_2 \rightarrow NO + O_2$	3.00×10^{-10}	0	0		[13,44,5]
345	$O_2^* + N \rightarrow O + NO$	2.00×10^{-14}	0	600		[13,12]
346	$O_2^*1S + N \rightarrow O + NO$	2.50×10^{-10}	0	0		[45]
347	$O_3 + N \rightarrow NO + O_2$	5.00×10^{-16}	0	0		[13,11,26]
348	$O_3 + N^* \rightarrow NO + O_2$	1.00×10^{-10}	0	0		[13,46]
349	$O_3 + N_2^* \rightarrow NO + NO + O$	8.40×10^{-12}	0	0		[13,47,48]
350	$O_3 + N_2^{**} \rightarrow NO + NO + O$	8.40×10^{-12}	0	0		[13]
351	$NO_2 + O_2^* \rightarrow O_2 + NO_2$	5.00×10^{-18}	0	0		[36]
352	$NO_2 + O \rightarrow O_2 + NO$	4.21×10^{-12}	0	-273		[36]
353	$NO_2 + O + M \rightarrow NO_3 + M$	9.00×10^{-32}	-2	0		[36]
354	$N + NO \rightarrow N_2 + O$	3.14×10^{-11}	0	0		[36]
355	$O + NO + M \rightarrow NO_2 + M$	1.00×10^{-31}	0	0		[36]
356	$H + NO_2 \rightarrow NO + OH$	1.28×10^{-10}	0	0		[36]
357	$NO + HO_2 \rightarrow NO_2 + OH$	8.80×10^{-12}	0	0		[36]
	OH and HO_2 reactions					
358	$H + O_2 + M \rightarrow HO_2 + M$	5.40×10^{-32}	0	0		[36]
359	$OH + O \rightarrow H + O_2$	3.50×10^{-11}	0	0		[36]
360	$O + HO_2 \rightarrow OH + O_2$	2.90×10^{-11}	0	200		[5,39]
361	$OH + OH \rightarrow O + H_2O$	1.03×10^{-12}	1.4	-200		[5,49]
362	$OH + O_3 \rightarrow HO_2 + O_2$	1.90×10^{-12}	0	1000		[5,50]
363	$HO_2 + O_3 \rightarrow OH + O_2 + O_2$	1.40×10^{-14}	0	600		[5,50]
364	$O + OH \rightarrow H + O_2$	2.30×10^{-11}	0	-110		[5,49]
365	$OH + H_2 \rightarrow H_2O + H$	7.70×10^{-12}	0	2100		[5,49]
366	$O^* + H_2 \rightarrow OH + H$	1.10×10^{-10}	0	0		[5,50]
367	$HO_2 + OH \rightarrow H_2O + O_2$	8.00×10^{-11}	0	0		[5]

368	$O + H_2 \rightarrow OH + H$	1.60×10^{-11}	0	4570	[5,50]
369	$H + HO_2 \rightarrow H_2O + O$	9.40×10^{-12}	0	0	[5,50]
370	$O + H + M \rightarrow OH + M$	1.62×10^{-32}	0	0	[5,51]
371	$H + H + M \rightarrow H_2 + M$	4.80×10^{-33}	0	0	[5,11]
372	$H + HO_2 \rightarrow OH + OH$	2.80×10^{-10}	0	440	[5,49]
373	$H + O_3 \rightarrow OH + O_2$	1.40×10^{-10}	0	480	[5,39]
374	$H + HO_2 \rightarrow H_2 + O_2$	1.10×10^{-10}	0	1070	[5,49]
375	$H_2 + O_2 \rightarrow H + HO_2$	2.40×10^{-10}	0	28500	[5,49]
376	$H + O_2 \rightarrow OH + O$	1.65×10^{-9}	-0.9	8750	[5,49]
377	$H_2O + H \rightarrow H_2 + OH$	5.24×10^{-12}	1.9	9265	[5,49]
378	$H_2O + O \rightarrow OH + OH$	1.26×10^{-11}	1.3	8605	[5,49]
379	$OH + M \rightarrow O + H + M$	4.00×10^{-9}	0	50000	[5,49]
380	$OH + O_2 \rightarrow O + HO_2$	3.70×10^{-11}	0	26500	[5,49]
381	$OH + H \rightarrow O + H_2$	5.21×10^{-11}	0.67	518	[5,10]
382	$HO_2 + M \rightarrow H + O_2 + M$	2.39×10^{-8}	-1.18	24360	[5,49]
	Path to H_2O_2				
383	$OH + OH + M \rightarrow H_2O_2 + M$	6.90×10^{-31}	-0.8	0	[5,39]
384	$HO_2 + HO_2 \rightarrow H_2O_2 + O_2$	8.05×10^{-11}	-1	0	[21,60]
385	$HO_2 + H_2O \rightarrow H_2O_2 + OH$	4.65×10^{-11}	0	16477	[36]
386	$H_2 + HO_2 \rightarrow H_2O_2 + H$	5.00×10^{-11}	0	13110	[5,49]
387	$HO_2 + HO_2 + M \rightarrow H_2O_2 + O_2 + M$	1.90×10^{-33}	0	-980	[5,39]
388	$H + H_2O_2 \rightarrow H_2 + HO_2$	8.00×10^{-11}	0	4000	[5,49]
389	$H + H_2O_2 \rightarrow H_2O + OH$	4.00×10^{-11}	0	2000	[5,49]
390	$O_2 + H_2O_2 \rightarrow HO_2 + HO_2$	9.00×10^{-11}	0	19965	[5,49]
391	$O + H_2O_2 \rightarrow OH + HO_2$	1.40×10^{-12}	0	2000	[5,49]
392	$O^* + H_2O_2 \rightarrow H_2O + O_2$	5.20×10^{-10}	0	0	[13,52,21]
393	$OH + H_2O_2 \rightarrow H_2O + HO_2$	2.90×10^{-12}	0	160	[5,50]
394	$H_2O_2 \rightarrow OH + OH$	1.96×10^{-9}	-4.86	26800	[36,60]
	Path to NxOy and HNOx				
395	$NO + NO_2 \rightarrow N_2O_3$	7.90×10^{-12}	0	0	[36]
396	$NO + HO_2 \rightarrow ONOOH$	6.09×10^{-11}	0	0	[36]
397	$NO + NO + O_2 \rightarrow NO_2 + NO_2$	2.00×10^{-38}	0	0	[36]
398	$NO + NO_2 + M \rightarrow N_2O_3 + M$	3.10×10^{-34}	0	0	[36]
399	$NO + NO_3 \rightarrow NO_2 + NO_2$	1.60×10^{-11}	0	-150	[5,39]
400	$NO + NO_2 + H_2O \rightarrow HNO_2 + HNO_2$	5.55×10^{-34}	0	0	[36]
401	$NO + OH + M \rightarrow HNO_2 + M$	6.00×10^{-31}	0	0	[36]
402	$NO + HO_2 \rightarrow HNO_3$	4.76×10^{-11}	0	0	[36]
403	$NO + HO_2 + M \rightarrow HNO_3 + M$	2.00×10^{-30}	0	0	[36]
404	$NO_2 + OH + O_2 \rightarrow HNO_3 + O_2$	1.70×10^{-30}	0	0	[36]
405	$NO_2 + OH + H_2O \rightarrow HNO_3 + H_2O$	1.70×10^{-30}	0	0	[36]
406	$NO_2 + HO_2 \rightarrow HNO_2 + O_2$	1.20×10^{-12}	0	0	[5,36]
407	$NO_2 + OH \rightarrow ONOOH$	4.10×10^{-11}	0	0	[36]
408	$NO_2 + OH + M \rightarrow ONOOH + M$	3.37×10^{-30}	0	0	[36]

409	$NO_2 + OH \rightarrow HO_2 + NO$	3.03×10^{-11}	0	3360		[5,36]
410	$NO_2 + OH \rightarrow HNO_3$	4.10×10^{-11}	0	0		[36]
411	$NO_2 + O_3 \rightarrow NO + O_2 + O_2$	1.00×10^{-18}	0	0		[5,53]
412	$NO_2 + O_3 \rightarrow O_2 + NO_3$	1.40×10^{-12}	0	2470		[13,46,48]
413	$NO_2 + NO_2 \rightarrow N_2O_4$	1.00×10^{-12}	0	0		[36]
414	$NO_2 + NO_2 + M \rightarrow N_2O_4 + M$	1.40×10^{-33}	0	0		[36]
415	$NO_3 + NO_2 \rightarrow N_2O_5$	1.90×10^{-12}	0	0		[36]
416	$NO_3 + NO_2 + M \rightarrow N_2O_5 + M$	3.60×10^{-30}	0	0		[36]
417	$NO_3 + NO_3 \rightarrow NO_2 + NO_2 + O_2$	1.20×10^{-15}	0	0		[5,11]
418	$NO_3 + OH \rightarrow HO_2 + NO_2$	2.60×10^{-11}	0	0		[5,54]
419	$NO_3 + HO_2 \rightarrow NO_2 + OH + O_2$	3.60×10^{-12}	0	0		[5,54]
420	$NO_3 + HO_2 \rightarrow HNO_3 + O_2$	9.20×10^{-12}	0	0		[5,54]
421	$NO_3 + NO_2 \rightarrow NO_2 + NO + O_2$	8.21×10^{-14}	0	1480		[5,36]
422	$NO_3 + M \rightarrow NO + O_2 + M$	1.94×10^{-12}	0	1610	d	[5]
423	$N_2O_3 + H_2O \rightarrow HNO_2 + HNO_2$	1.93×10^{-17}	0	0		[36]
424	$N_2O_4 + H_2O \rightarrow HNO_2 + HNO_3$	1.33×10^{-18}	0	0		[36]
425	$N_2O_5 + H_2O \rightarrow HNO_3 + HNO_3$	2.00×10^{-21}	0	0		[36]
426	$N_2O_5 + H_2O + H_2O \rightarrow HNO_3 + HNO_3 + H_2O$	1.80×10^{-39}	0	0		[36]
427	$N_2O_5 + H_2O \rightarrow ONOOH + ONOOH$	2.00×10^{-21}	0	0		[36]
428	$HNO_2 + O \rightarrow NO_2 + OH$	2.00×10^{-11}	0	3000		[5,36]
429	$HNO_2 + OH \rightarrow NO_2 + H_2O$	1.80×10^{-11}	0	390		[5,39]
430	$HNO_3 + OH \rightarrow NO_3 + H_2O$	1.50×10^{-14}	0	-650		[5,50]
431	$HNO_3 + NO \rightarrow HNO_2 + NO_2$	7.37×10^{-21}	0	0		[5,55]
	Radiation					
432	$N_2^{**} \rightarrow N_2$	2.00×10^{8}	0	0	d	[21,22]
433	$N_2^{**} \rightarrow N_2^{*}$	2.00×10^{8}	0	0	d	[21,22]
434	$He_2^{*} \rightarrow He + He$	1.00×10^{7}	0	0	d	
435	$O_2 \rightarrow O_2^{+} + e$	1.00×10^{-15}	0	0	d	
436	$N_2 \rightarrow N_2^{+} + e$	1.00×10^{-15}	0	0	d	
437	$He(2^3P) \rightarrow He(2^3S)$	1.02×10^{7}	0	0		[36]
438	$He(3P) \rightarrow He(2^3S)$	9.47×10^{6}	0	0		[36]
439	$He(3P) \rightarrow He(2^1S)$	1.34×10^{7}	0	0		[36]
440	$He(3S) \rightarrow He(2^3P)$	1.55×10^{7}	0	0		[36]
441	$He(3S) \rightarrow He(2^1P)$	1.83×10^{7}	0	0		[36]
442	$He(2^1P) \rightarrow He$	1.20×10^{6}	0	0		[36]

[a] Units are $cm^{-3}s^{-1}$ for two-body reactions and $cm^{-6}s^{-1}$ for three-body reactions and s^{-1} for radiative

[b] Boltzmann solver with cross section data from [57-59]

[c] M represents N_2, O_2, H_2O, and He

[d] estimate based on reference indicated

[e] He^* represents $He(2^1S)$, $He(2^1P)$, $He(2^3S)$, $He(2^3P)$, He(3S), and He(3P)
[f] N_2^* represents $N_2(A^3\Sigma)$ and $N_2(B^3\Pi)$
[g] N_2^{**} represents $N_2(C^3\Pi)$ and higher states
[h] O_2^* is $O_2(a^1\Delta)$
[i] O_2^*1S is $O_2(^1\Sigma)$
j reaction rates are of the form:
$k = A(T_g/300)^n exp(-E/T_g)$ for neutrals and
$k = AT_e^n exp(-E/T_e)$ for charged species

Appendix I References

[1] M.A. Biondi in G. Bekefi "Principles of Laser Plasmas", Wiley, New York, 1976.
[2] R. Deloche, P. Monchicourt, M. Cheret and F. Lambert, PRA **13**, 1140 (1976).
[3] K. Niemi, J. Waskoenig, N. Sadeghi, T. Gans, and D. O'Connell, Plasma Sources Sci. Technol. **20**, 055005 (2011).
[4] A. W. Johnson and J. B. Gerardo, PRA **5**, 1410 (1972).
[5] R. Dorai, PhD Thesis Department of Chemical Engineering, University of Illinois at Urbana-Champaign (2002).
[6] J. B. A. Mitchell, Phys. Rpts. **186**, 215 (1990).
[7] D.S. Stafford and M.J. Kushner, J. Appl. Phys. **96,** 2451 (2004).
[8] G. Bekefi, Radiation Processes in Plasmas, Wiley, New York, 1966.
[9] B. F. Gordiets, C. M. Ferreira, V. L. Guerra, J. Loureiro, J. Nahorny, D. Pagnon, M. Touzeau, and M. Vialle, IEEE Trans. Plasma Sci. **23**, 750 (1995).
[10] B.R. Rowe, F. Vallee, J.L. Queffelec, J.C. Gomet, and M. Morlais, J. Phys. Chem. **88**, 845 (1988).
[11] J. C. Person and D. O. Ham, Radiat. Phys. Chem. **31**, 1 (1988).
[12] I.A. Kossyi, A.Yu Kostinsky, A.A. Matveyev, and V.P. Silakov, Plasma Sources Sci. Technol. **1**, 207 (1992).
[13] W. Van Gaens and A. Bogaerts, J. Phys. D: Appl. Phys. **46**, 275201 (2013).
[14] Y. Sakiyama, D.B. Graves, H-W. Chang, T. Shimizu, and G. Morfill, J. Phys. D: Appl. Phys. **45**, 425201 (2012).
[15] R. Johnsen, A. Chen and M. A. Biondi, J. Chem. Phys. **73**, 1717 (1980).
[16] F. Emmert, H.H. Angermann, R. Dux, H. Langhoff, J. Phys. D: Appl. Phys. **21**, 667 (1988).
[17] J.M. Pouvesle, A. Khacef, J. Stevefelt, H. Jahani, V.T. Gylys, and C.B. Collins, J. Chem. Phys. **88** 3061 (1988).
[18] D. K. Bohme, N. G. Adams, M. Mosesman, D. B. Dunkin, and E. E. Ferguson, J. Chem. Phys. **52**, 5094 (1970).
[19] R. E. Olson, J. R. Peterson, and J. Moseley, J. Chem. Phys. **53**, 3391 (1970).
[20] H. Matzing, Adv. Chem. Phys. **80**, 315–402 (2007).
[21] F.J. Gordillo-V´azquez, J. Phys. D: Appl. Phys. **41**, 234016 (2008).
[22] M. Capitell, C.M. Ferreira, B.F. Gordiets, and A. Osipov, Plasma Kinetics in Atmospheric Gases, Springer, Berlin, 2000.
[23] J. Lowke and R. Morrow, IEEE Trans. Plasma Sci. **23**, 661 (1995).
[24] Y. Ikezoe, S. Matsuoka, M. Takebe, and A. Viggiano, Gas Phase Ion-Molecule Reaction Rate Constants Through 1986 (Ion Reaction Research Group of the Mass Spectroscopy Society of Japan, Tokyo, Japan, 1987).
[25] E.E. Ferguson, At. Data Nucl. Data Tables **12**, 159–78 (1973).
[26] O. Eichwald, M. Yousfi, A. Hennad, and M.D. Benabdessadok, J. Appl. Phys. **82**, 4781 (1997).
[27] D. Albritton, At. Data Nucl. Data Tables **22**, 1–89 (1978).
[28] A. Cenian, A. Chernukho, and V. Borodin, Contrib. Plasma Phys. **35**, 273 (1995).
[29] L.W. Sieck, J.T. Herron, and D.S. Green, Plasma Chem. Plasma Process. **20**, 235 (2000).

[30] K.R. Stalder, R.J. Vidmar, G. Nersisyan, and W.G. Graham, J. Appl. Phys. **99,** 093301 (2006).
[31] A. Bogaerts, Spectroc. Acta B **64**, 126–40 (2009).
[32] A.N.B. Bhoj, Multiscale simulation of atmospheric pressure pulsed discharges used in polymer surface functionalization, PhD Thesis, University of Illinois, 2006.
[33] V.G. Anicich, J. Phys. Chem. Ref. Data **22**, 1469 (1993).
[34] A. Sankaran and M.J. Kushner, J. Appl. Phys. **92**, 736 (2002).
[35] H. W. Ellis, M. G. Thackston, E. W. McDaniel, and E. A. Mason, At. Data Nucl. Data Tables **31**, 113 (1984).
[36] NIST Chemical Kinetics Database, Standard Reference Database 17, Version 7.0 (Web Version), Release 1.6.8 Data Version 2013.03, http://kinetics.nist.gov/kinetics/index.jsp
[37] R. Atkinson, D. L. Baulch, R. A. Cox, J. R. F. Hampson, J. A. Kerr, M. J. Rossi, and J. Troe, J. Phys. Chem. Ref. Data **26**, 1329 (1997).
[38] L. G. Piper, J. Chem. Phys. **87**, 1625 (1987).
[39] R. Atkinson, D. L. Baulch, R. A. Cox, R. F. Hampson, Jr., J. A. Kerr, and J. Troe, J. Phys. Chem, Ref. Data, **18**, 881 (1989).
[40] B. Eliasson and U. Kogelschatz, Brown Boveri Technical Report LKR 86-11 C, (1986).
[41] I. Shkurenkov, D. Burnette, W. Lempert, and I. Adamovich, Plasma Sources Sci. Technol. **23**, 065003 (2014).
[42] J. Woodall, M. Ag´undez, A.J. Markwick-Kemper, and T.J. Millar, Astronom. Astrophys. **466**, 1197–204 (2007).
[43] I.A. Soloshenko, V.V. Tsiolko, S.S. Pogulay, A.G. Terent'yeva, V.Y. Bazhenov, A.I. Shchedrin, A.V. Ryabtsev, and A.I. Kuzmichev, Plasma Sources Sci. Technol. **16**, 56 (2007).
[44] A.C. Gentile, Kinetic processes and plasma remediation of toxic gases, PhD Thesis, University of Illinois, 1995.
[45] M. Uddi, N. Jiang, I. Adamovich, and W. Lempert, J. Phys. D: Appl. Phys. **42**, 075205 (2009).
[46] J.T. Herron and D.S. Green, Plasma Chem. Plasma Proc. **21**, 459 (2001).
[47] J.T. Herron, J. Phys. Chem. Ref. Data, **28**, 1453 (1999).
[48] J.T. Herron, Plasma Chem. Plasma Proc. **21**, 581 (2001).
[49] W. Tsang and R. F. Hampson, J. Phys. Chem. Ref. Data **15**, 1087 (1986).
[50] S. Mukkavilli, C. K. Lee, K.Varghese, and L. L. Tavlarides, IEEE Trans. Plasma Sci. **16**, 652 (1988).
[51] R. K. Bera and R. J. Hanrahan, J. Appl. Phys. **62**, 2523 (1987).
[52] D.X. Liu, P. Bruggeman, F. Iza, M.Z. Rong, and M.G. Kong, Plasma Sources Sci. Technol. **19**, 025018 (2010).
[53] J. Hjorth, J. Notholt, and G. Restelli, Int. J. Chem. Kin. **24**, 51 (1992).
[54] A. Mellouki, G. Le Bras, and G. Poulet, J. Phys. Chem. **92**, 2229 (1988).
[55] R. Svensson and E. Ljungström, Int. J. Chem. Kin. **20**, 857 (1988).
[56] N.A. Popov, J. Phys. D: Appl. Phys. **44**, 285201 (2011).
[57] A. V. Phelps, "Tabulations of Collision Cross Sections and Calculated Transport and Reaction Coefficients for Electron Collisions with O2", JILA Information Center Report No. 28, 1985.
[58] Y. Itikawa, "Cross Sections for Electron Collisions with Water Molecules", J. Phys. Chem. Ref. Data **34**, 1 (2005).

[59] Y. Itikawa, M. Hayashi, A. Ichimura, K. Onda, K. Sakimoto, K. Takayanagi, M. Nakamura, H. Nishimura, and T. Takayanagi, "Cross Sections for Collisions of Electrons and Photons with Nitrogen Molecules" J. Phys. Chem. Ref. Data **15,** 985 (1986).
[60] D.X. Liu, P. Bruggeman, F. Iza, M.Z. Rong, and M.G. Kong, "Global model of low-temperature atmospheric-pressure He + H_2O plasmas", Plasma Sources Sci. Technol. **19**, 025018 (2010).
[61] D.X. Liu, M.Z. Rong, X.H. Wang, F. Iza, M.G. Kong, and P. Bruggeman, "Main Species and Physicochemical Processes in Cold Atmospheric-pressure He + O_2 Plasmas", Plasma Process. Poly. **7**, 846 (2010).

APPENDIX II AUTHOR'S BIOGRAPHY

Seth Norberg is a Lieutenant Colonel in the United States Army. He earned his B.S. (1995) and M.S. (2005) in Mechanical Engineering from The Ohio State University. Upon graduating with a Ph.D. from the University of Michigan in Mechanical Engineering in 2015, LTC Norberg will join the faculty at the United States Military Academy at West Point, New York, as an Assistant Professor in the Department of Civil and Mechanical Engineering.